Massive filamentary clouds and their role in star formation

Dissertation

zur

Erlangung des Doktorgrades (*Dr. rer. nat.*)

der

der Mathematisch-Naturwissenschaftlichen Fakultät

der

Rheinischen Friedrich–Wilhelms–Universität, Bonn

vorgelegt von

Michael Mattern

aus

Wertheim, Deutschland

Bonn 2018

Angefertigt mit Genehmigung der Mathematisch-Naturwissenschaftlichen Fakultät
der Rheinischen Friedrich–Wilhelms–Universität Bonn

1. Referent: Prof. Dr. Karl M. Menten
2. Referent: Prof. Dr. Pavel Kroupa
Tag der Promotion: 04.04.2019
Erscheinungsjahr: 2019

Abstract

by Michael Mattern

for the degree of

Doctor rerum naturalium

Filamentary structures are ubiquitous in the interstellar medium of the Milky Way. They are observed at a large range of size-scales from $\sim$ 1 pc within star-forming and quiescent molecular clouds to $\sim$ 100 pc representing molecular clouds themselves. Therefore, filamentary structures play an important role in the early phases of star formation. Filaments in nearby ($<$ 500 pc) molecular clouds were found to be thermally stable against gravitational collapse, and therefore, the fragmentation time-scales are much shorter than the collapse time-scales, which allows the filament to fragment into star-forming clumps. However, the evolutionary scenario of filaments with masses significantly above the thermally critical value is virtually unknown. These massive filaments are found throughout the entire Galaxy, where they channel the gas from large, Galactic to small, star-forming scales.

In this thesis we use various survey observations to investigate the evolution of massive filamentary molecular clouds. Here we first concentrate on the hundred-parsec-scale, massive Nessie filament. We aim to characterize the fragmentation of the cloud covering size-scales in the range $\sim$ 0.1–100 pc and to connect the smallest scales to its star-forming potential. Further, we will analyze the kinematics of Nessie to reveal its continuity in position-position-velocity (ppv) space, which is essential to confirm Nessie as a single physical object, and to study the gas motions along and across the filament. For the fragmentation characterization we combine near- and mid-infrared data to derive a high-resolution dust extinction map, from which we extract the cloud fragments at different size-scales. The characteristics are then compared with predictions from gravitational fragmentation models. We find that the median nearest-neighbor separations of the fragments at all scales are similar to the ones predicted for a filament that exhibits a Larson-like scaling between size-scale and velocity dispersion. The kinematic information of Nessie is provided by the ^{13}CO(2 – 1) and C^{18}O(2 – 1) molecular lines of the SEDIGISM (Structure, Excitation, and Dynamics of the Inner Galactic Inter Stellar Medium) survey. Although Nessie shows several morphological differences along the filament it is observed as a continuous structure in ppv space.

In the second part of the thesis we analyze the kinematics of 283 filamentary molecular cloud candidates in the Galactic Plane, that were previously identified in the ATLASGAL (APEX Telescope Large Area Survey of the Galaxy) dust continuum data. The ^{13}CO(2 – 1) and C^{18}O(2 – 1) data of the SEDIGISM survey allows us to analyze the kinematics of these targets and to determine their

physical properties. To do so, we developed an automated algorithm to identify all velocity components along the line- of-sight correlated with the ATLASGAL dust emission, and derive size, mass, and kinematic properties for all velocity components. We find two-third of the filament candidates are coherent structures in ppv space. Also, we find a correlation between the observed mass per unit length and the velocity dispersion of the filament of $m \propto \sigma_{\rm v}^2$. We show that this relation can be explained by a virial balance between self-gravity and pressure. Another possible explanation could be radial collapse of the filament, but the observation can exclude infall motions close to the free-fall velocity.

List of publications related to this doctoral thesis

"SEDIGISM: Structure, excitation, and dynamics of the inner Galactic interstellar medium"
F. Schuller, T. Csengeri, J. S. Urquhart, A. Duarte-Cabral, P. J. Barnes, A. Giannetti, A. K. Hernandez, S. Leurini, **M. Mattern**, S. N. X. Medina, C. Agurto, F. Azagra, L. D. Anderson, M. T. Beltrán, H. Beuther, S. Bontemps, L. Bronfman, C. L. Dobbs, M. Dumke, R. Finger, A. Ginsburg, E. Gonzalez, T. Henning, J. Kauffmann, F. Mac-Auliffe, K. M. Menten, F. M. Montenegro-Montes, T. J. T. Moore, E. Muller, R. Parra, J. P. Perez-Beaupuits, A. Pettitt, D. Russeil, Á. Sánchez-Monge, P. Schilke, E. Schisano, S. Suri, L. Testi, K. Torstensson, P. Venegas, K. Wang, M. Wienen, F. Wyrowski, A. Zavagno; 2017, A&A, 601, A124

"Structure and Fragmentation of a high line-mass filament: Nessie"
M. Mattern, J. Kainulainen, M. Zhang, H. Beuther; 2018, A&A, 616, A78

"SEDIGISM: The Kinematics of ATLASGAL filaments"
M. Mattern, J. Kauffmann, T. Csengeri, J. S. Urquhart, S. Leurini, F. Wyrowski, A. Giannetti, P. J. Barnes, H. Beuther, L. Bronfman, A. Duarte-Cabral, T. Henning, J. Kainulainen, K. M. Menten, E. Schisano, and F. Schuller; 2018, A&A, 619, A166

Acknowledgements

First and foremost I want to thank my parents Elfriede and Richard Mattern and the rest of my family who supported me for every step in my life, so the little farmer boy, that I liked to be, could follow its dream to the stars.

I also want to say Thank You to Prof. Dr. Karl M. Menten and Dr. Friedrich Wyrowski who supported me throughout my PhD and gave me the opportunity to develop my own ideas and research leading to this thesis.

Further, I want to thank all my colleagues for their help with all these little technical or scientific problems and questions that appeared throughout the years. Especially, I want to mention Jens Kauffmann, James Urquhart, and Timea Csengeri, who were a big support for my publications.

Also, I want to thank the members of my promotion committee, Prof. Dr. Pavel Kroupa who followed my thesis work as second referee, and Prof. Dr. Simon Stellmer and PD Dr. Ines Gütgemann who kindly agreed to complete the committee.

I also want to thank my office former and current mates, and all the other doctoral candidates who were open for discussions (scientific or not) and became friends over the time. A special thanks goes also to my non astronomer friends that I found here in Bonn.

Last but not least I want to thank a special person who made me work harder and enjoy life more at the same time. Thank you for being with me.

Contents

List of Figures

List of Tables

Nomenclature

Frequently Used Symbols

b	Galactic latitude
g	Gravitational acceleration
G	Gravitational constant
c	Speed of light
δ	Declination
h	Planck's constant
k_{B}	Boltzmann's constant
σ	Dispersion
l	Longitude
L	Luminosity
μ	Mean molecular weight
m	Line-mass (mass per unit length)
M	Mass
ν	Frequency
n	Numerical density
P	Pressure (or period)
d	Distance
r	Radius
t	Time
T	Temperature
v	Speed
V	Volume
Ω	Solid angle

Numerical Constants

π	$= 3.14156$
$1\,\mathrm{rad}$	$= 57.296\,\mathrm{degrees}$
e	$= 2.7183$
$\log e$	$= 0.4343 = \ln(10)^{-1}$

Physical Constants

Speed of light	$c = 2.9979 \times 10^{8}\,\mathrm{m\,s^{-1}}$
Gravitational constant	$G = 6.670 \times 10^{-11}\,\mathrm{m^{3}\,kg^{-1}\,s^{-2}}$
Planck's constant	$h = 6.626 \times 10^{-27}\,\mathrm{erg\,s}$
Coulomb's constant	$k = 1$
Boltzmann's constant	$k_{\mathrm{B}} = 1.381 \times 10^{-16}\,\mathrm{erg\,deg^{-1}}$
Stefan–Boltzmann constant	$\sigma = 5.6704 \times 10^{-5}\,\mathrm{erg\,cm^{-2}\,s^{-1}\,K^{-4}}$
Electron mass	$m_{\mathrm{e}} = 9.110 \times 10^{-28}\,\mathrm{g}$
Proton mass	$m_{\mathrm{p}} = 1.673 \times 10^{-24}\,\mathrm{g}$

Astronomical Constants

Astronomical unit ($1\,\mathrm{AU}$)	$= 1.496 \times 10^{13}\,\mathrm{cm}$
Parcec ($1\,\mathrm{pc}$)	$= 3.086 \times 10^{18}\,\mathrm{cm}$
Julian light year ($1\,\mathrm{ly}$)	$= 9.460730472 \times 10^{17}\,\mathrm{cm}$
Julian year ($1\,\mathrm{yr}$)	$= 3.15576 \times 10^{7}\,\mathrm{sec}$
Solar mass ($1\,\mathrm{M_{\odot}}$)	$= 1.989 \times 10^{33}\,\mathrm{g}$
Solar radius ($1\,\mathrm{R_{\odot}}$)	$= 6.960 \times 10^{10}\,\mathrm{cm}$
Solar luminosity ($1\,\mathrm{L_{\odot}}$)	$= 3.9 \times 10^{33}\,\mathrm{erg\,s^{-1}}$
Absolute magnitude of the Sun (M_{V})	$= 4.77$
Apparent magnitude of the Sun (m_{V})	$= -26.7$
Effective temperature of the Sun (T_{eff})	$= 5770\,\mathrm{K}$

Chapter 1

Introduction

Stars are an essential part of the Universe. They contribute to its evolution in two different ways. First, they are the most efficient way to create atoms that are heavier than the primordial hydrogen and helium. These are needed to build complex molecules, ices, dust and finally, planets and life. Second, stars, especially those of higher mass, inject kinetic energy and momentum into the interstellar medium (ISM) primarily via stellar winds and super novae explosions. This stellar feedback influences the energetics and distribution of the ISM and can trigger or prevent the formation of new stars. Therefore, it is necessary to understand the complete life cycle of a star. While most phases have been studied for a long time, the paradigm of early phases of star formation was shifted in the last decade, when new instruments revealed a new view on the structures of gas and dust.

1.1 Formation of molecular clouds

At the beginning of the star formation process is the interstellar medium which is composed out of different gas phases (McKee & Ostriker, 1977). Simplifying there exists an ionized, a neutral, and a molecular phase. These phases are observed to have distinct temperatures and densities, and can be separated by the three forms of hydrogen (HII , HI and H_2). Additionally, the ISM is enriched with dust particles, small grains (size of ~ 0.1 μm) composed of silicates and carbon compounds and surrounded by ice mantles, that contribute about 1% of the mass of the medium.

The largest parts of the ISM are heated and ionized by energetic ultraviolet (UV) radiation emitted predominantly from massive stars. However, stars are formed in the coldest and densest phase of the ISM, in molecular clouds. To create molecular clouds it is necessary to concentrate and cool the diffuse atomic ISM. Several processes can contribute to the condensation of such a cloud, for example cloud-cloud collisions (e.g., Oort, 1954), gravitational instabilities (e.g., Goldreich & Lynden-Bell, 1965),thermal instabilities (e.g., Field, 1965), magnetic instabilities (e.g., Parker, 1966), spiral arm interaction (e.g., Roberts, 1969), turbulent flows (e.g., Ballesteros-Paredes et al., 1999), or colliding flows from stellar feedback (e.g., Koyama & Inutsuka, 2000). All of these processes may increase the density of the ISM to > 100 cm^{-3}, where it shields itself from the energetic radiation. Without photo-electric heating of dust grains by UV radiation, cooling becomes dominant through radiation from metals like carbon, oxygen or nitrogen. Therefore, the gas cools down, and becomes predominantly molecular. Finally, the gas reaches temperatures of about 10–20 K and densities up to 10^5 cm^{-3} (Dobbs et al., 2014).

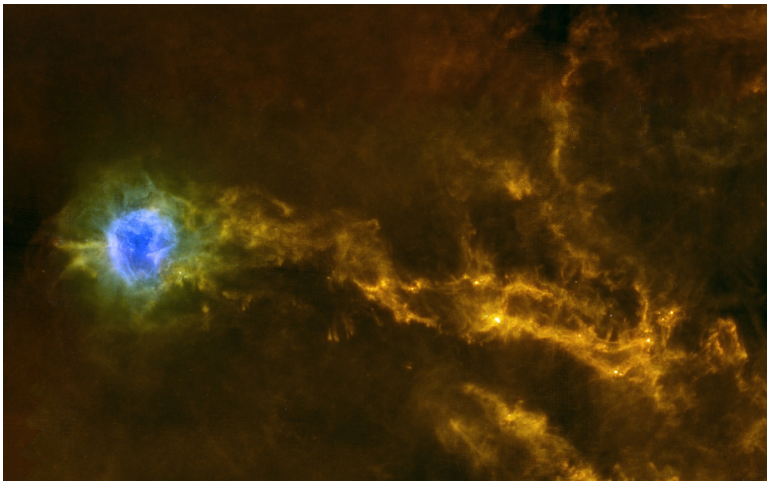

Figure 1.1: Composite 3-color image of IC 5146 (red: SPIRE 500 μm and 350 μm, green: SPIRE 250 μm and PACS 160 μm, blue: PACS 70 μm, Arzoumanian et al., 2011)

For a long time these molecular clouds were mostly assumed to be almost spherical and local variances in the density distribution cause the formation of small (~ 0.1 pc) gravitational unstable condensations, in which the later phases of star formation happen. Although elongated structures were observed since the 1980s (e.g., Schneider & Elmegreen, 1979; Bally et al., 1987; Abergel et al., 1994) only since the results of the Herschel satellite it was shown, that almost all molecular clouds inhabit linear structures, or are themselves formed in a linear way (e.g., André et al., 2010; Arzoumanian et al., 2011; André et al., 2014). These linear structures, where the extend in one spatial direction is larger than the other direction by a factor of at least three, were then called filaments.

1.2 Filaments

Interstellar filaments are generally defined as linear structures with an aspect ratio of at least three and a clearly enhanced density compared to the surrounding ISM. However, depending on the study, the ratio might be larger or the density is replaced by the column density as a criteria for continuum observations.

Filamentary structures have been observed at different wavelengths in various tracers, like dust emission, dust extinction, or molecular line emission (e.g. CO, HNC, N_2H^+). Also, filaments have been observed all over in the interstellar medium (e.g., Schneider & Elmegreen, 1979; Molinari et al., 2010; André et al., 2010; Schisano et al., 2014; Ragan et al., 2014; Li et al., 2016) covering wide ranges of masses ($\sim 1 - 10^5\,M_\odot$) and lengths ($\sim 0.1 - 100$ pc) (e.g., Bally et al., 1987; Jackson et al., 2010; Arzoumanian et al., 2011; Hernandez et al., 2012; Hacar et al., 2013; Kirk et al., 2013; Palmeirim et al., 2013; Li et al., 2016; Kainulainen et al., 2013; Beuther et al., 2015; Kainulainen et al., 2017; Abreu-Vicente et al., 2016; Zucker et al., 2017).

Filaments are seen in quiescent and star-forming clouds, in which a significant fraction of pre-stellar cores are located (André et al., 2010; Molinari et al., 2010), but also whole filamentary molecular clouds have been observed. This wide range of size scales and masses suggests that the processes of filament formation, evolution and fragmentation might also differ over the spectrum of observed structures. For example, most filaments in nearby (< 500 pc) clouds are found to have a mass per unit length (line-mass) that corresponds to its thermally critical value (André et al., 2010; Arzoumanian et al., 2011, 2013), which describes the line-mass that can be supported against gravitational collapse by the thermal motion of the gas. This critical line-mass, $m_{\rm crit}$, can be derived from the sound speed, c_s, of the medium, which is related to the gas temperature, by $m_{\rm crit} = 2c_s^2/G$ (Ostriker, 1964), where G is the gravitational constant. Furthermore, these filaments show a width that strongly peaks around 0.1 pc and therefore, is conjecture to be a general a property of filaments (Arzoumanian et al., 2011; André et al., 2014; Arzoumanian et al., 2018). Additionally, Hacar et al. (2013) revealed that filaments in the Taurus molecular cloud, which were found supercritical by a factor of a few based on dust continuum data, are bundles of about critical fibers. Later analyses of the massive ($m_{\rm obs} >> m_{\rm crit}$) filaments in the Orion cloud showed similar substructures, but in a more complex morphology (Hacar et al., 2018). However, it remains unknown whether all massive filaments are a collection of (roughly) critical filamentary sub-structures.

Recently, the longest and most massive structures, the so called giant molecular filaments (GMFs), came into focus of research, as these filaments seem to follow the spiral arms of the Milky Way. The first structure of this kind identified was the Nessie filament (Jackson et al., 2010). Nessie, initially presented as a 80 pc long infrared dark filament, was later discussed to be even longer, about 200 pc in the 'extended' version, and about 500 pc as 'optimistic' Nessie (Goodman et al., 2014). Given the large size and the possible association with the Scutum-Centaurus spiral arm, the idea was raised that GMFs are the 'bones of the Galaxy' and build the gaseous skeleton of the Milky Way. To further elucidate this, several studies to identify GMFs where conducted Ragan et al. (2014); Zucker et al. (2015); Abreu-Vicente et al. (2016); Wang et al. (2015, 2016). However, the identification methods and GMF criteria vary in these studies. These identified GMFs where found to be located in or close to spiral arms as well as in inter-arm regions. Further it was shown that longer GMFs have a tendency of being associated with a spiral arm (Zucker et al., 2015), and that spiral arm GMFs have a higher dense gas mass fraction than inter-arm GMFs (Abreu-Vicente et al., 2016).

Similar extended filamentary structures where also found in simulations of a Galactic disk (Dobbs & Pringle, 2013; Smith et al., 2014). However, while Smith et al. (2014) resolves the long filaments within the spiral arms of their simulation, Dobbs & Pringle (2013) see the filaments emerging from the spiral arm into the inter-arm region as so called spurs. In further analysis of the simulation of Dobbs & Pringle (2013), Duarte-Cabral & Dobbs (2016) and Duarte-Cabral & Dobbs (2017) show that GMFs could be formed by Galactic shear in the following way: giant molecular clouds are formed in the potential of the spiral arm, eventually leave the arm, and are stretched along the

Galactic rotation in the inter-arm region. Therefore, the elongated structure will align with the shape of the next spiral arm. The longest extent of a filament would then be reached at the center of the spiral potential before entering the arm. Furthermore, Duarte-Cabral & Dobbs (2017) show that these structures would only locally be gravitationally bound, but are to some extend pressure confined over their whole length with star formation appearing only in the densest parts. Also, the filament would eventually be disrupted by the feedback of star formation or differences in the forces cause by the shear.

Therefore, this evolutionary model for GMFs provides a possible origin for shorter, 'normal' filamentary molecular clouds. However, there are several possible scenarios for the formation of filaments with lengths of a few pc. Generally, simulations of supersonic turbulence have shown that gas gets compressed into sheet-like and filamentary structures (Vazquez-Semadeni, 1994; Padoan et al., 2001), where dense parts collapse when gravity is included in the simulation (Ostriker et al., 1999; Ballesteros-Paredes et al., 1999; Klessen & Burkert, 2000; Bonnell et al., 2003; Low et al., 2004; Tilley & Pudritz, 2004; Krumholz et al., 2007). The source for supersonic turbulence in the ISM can be supernovae, stellar winds from massive stars, expanding HII regions, cloud cloud collisions, radiation pressure, or galactic spiral shocks, which can form giant molecular clouds. To form a filament, two planar shock waves created by supersonic turbulence need to intersect. The intersection of two planes is a linear structures, hence a filament (Pudritz & Kevlahan, 2013). The formation of the filament is not dependent on gravity. However, only if the filament is massive enough to be gravitationally bound, it can further evolve to form stars. Gravitationally unbound filaments will be eventually dispersed by the turbulence. Additionally, magnetic fields can support or prevent the formation of filaments dependent on their strength and orientation. These can also influence accretion flows along and radially onto the filament, which has been seen in observations and simulations (Schneider et al., 2010; Peretto et al., 2013, 2014; Henshaw et al., 2014; Smith et al., 2015). In general, the formation and evolution of filaments is a highly dynamical process.

In the further evolution of filaments, fragmentation occur into about equally spaced clumps, which are the sites of star formation. Theoretical predictions of gravitational fragmentation models are developed for near-equilibrium cylinders, which are typically derived from linear perturbations applied on a static initial configuration (Jeans, 1902; Chandrasekhar & Fermi, 1953; Inutsuka & Miyama, 1992). These models predict a periodic pattern with a specific wavelength, which is not scale-dependent. However, the fragmentation pattern depends on the density of the filament and therefore, filaments with different densities have different fragmentation wavelengths.

Two commonly used fragmentation models are the spherical Jeans' instability model (Jeans, 1902) and the fragmentation of an infinitely long, self-gravitating cylinder (Chandrasekhar & Fermi, 1953; Inutsuka & Miyama, 1992). For both models the fragmentation wavelength, λ_f, is dependent on the sound speed, c_s, within the medium and its density, ρ, where $\lambda_f \propto c_s$ and $\lambda_f \propto \rho^{-\frac{1}{2}}$. However, Jeans' fragmentation uses the average density of the structure and the density in the cylinder model fragmentation

is derived from the central density. Therefore, to compare both models it is necessary to know the radial profile of the filament, which is also topic of current studies.

As we know, observed structures are more complex than the static initial configuration of these models. However, evaluating the model for different conditions is one way to approach complex configurations like non-isothermal, or turbulent filaments.

Many studies on the various processes of filament formation, evolution and fragmentation have been carried out within the last decade. However, our understanding of these processes arises only from a relatively limited sample of structures. This includes mainly nearby star-forming regions, e.g. Orion, Musca and Taurus (Bally et al., 1987; Takahashi et al., 2013; Hacar et al., 2016; Kainulainen et al., 2015, 2017), and prominent infrared dark structures, e.g., "Nessie" and G11.11−0.12 (Johnstone et al., 2003; Pillai et al., 2006; Schneider et al., 2010; Jackson et al., 2010; Kainulainen et al., 2013; Henshaw et al., 2014). This selection of structures is mainly based on observational issues. Nearby (< 500 pc) sources can be spatially resolved down to ~ 0.1 pc with single dish telescopes in the sub-millimeter range and infrared dark sources are generally bright in dust and molecular line emission. However, the increasing capabilities of the observing facilities allow the analysis of further filaments.

Recently conducted surveys of the Galactic plane, like Hi-GAL (Molinari et al., 2010), or ATLASGAL (Schuller et al., 2009), have a spatial resolution to allow an unbiased search for filamentary structures. To do so, several algorithms have been developed like filfinder (Koch & Rosolowsky, 2015), or have been adjusted for this purpose, like DisPerSE (Sousbie, 2011). As a result, there are three catalogues of filaments identified on continuum data Schisano et al. (2014); Koch & Rosolowsky (2015); Li et al. (2016). Additionally, extremely long filaments were visually identified (Wang et al., 2015, 2016; Ragan et al., 2015; Zucker et al., 2015; Abreu-Vicente et al., 2016), also including the mid-infrared GLIMPSE survey (Churchwell et al., 2009), which shows filamentary structures in extinction.

1.3 Observations

Within this thesis, we will make use of different observational data. Most of these data were obtained in previously conducted surveys. Here I want to give a brief introduction to the observed molecular line and dust emission and introduce the used surveys, which are ATLASGAL (APEX Telescope Large Area Survey of the Galaxy, Schuller et al., 2009), ATLASGAL+PLANCK (ATLASGAL combined with PLANCK, Csengeri et al., 2016), and SEDIGISM (Structure, Excitation and Dynamics of the Inner Galactic InterStellar Medium, Schuller et al., 2017). For more detailed information I refer to the standard literature, like 'Tools of Radio Astronomy' by Rohlfs & Wilson (2004)

1.3.1 Molecular lines

In the coldest and densest regions of the Galaxy, atoms can form molecules. Because of the binding of the atoms molecules can have additional to the electronic states also

vibrationally and rotationally excited states. Generally, the emission emerging from the transition of molecules between the different excited states creates a specific spectrum that can be used to to identify the molecules in the ISM. This spectrum is shifted by the Doppler-effect due to relative motions between the molecules and the observer, allowing to measure the kinematics of the emitting regions. Transitions between the electronic states will emit in the ultra-violet and optical frequency range, vibrational transitions emit in the infra-red, and rotational transitions in the millimeter and sub-millimeter range. However, under the cold conditions of star forming regions typically only the rotational transitions will be excited.

The most abundant molecule in the universe is the molecular hydrogen (H_2), which is difficult to observe because of it does not have a dipole moment due to its symmetry. The second most abundant molecule is carbon monoxide (CO) and therefore, is often used to trace the molecular gas, when the abundance ratios are known (a typical CO-to-H_2 ratio is 10^{-4}, Bolatto et al., 2013; Giannetti et al., 2017). As a diatomic molecule, CO provides simple transition spectra, where the transition energies between the different rotational states E_J can be derived by

$$E_J = \frac{\hbar^2}{2\mu r^2} J(J+1) \tag{1.1}$$

where J is the quantum number of the lower state, $\hbar = h/2\pi$ with h the Planck-constant, $\mu = \frac{m_1 m_2}{m_1+m_2}$ is the reduced mass, with the masses m_1 and m_2 of the constituting atoms, and r the distance between the atoms. The lowest energy levels are only 5.5 K above the ground state and easy excited under typical temperatures of 10 – 20 K in the cloud.

In addition, the low critical density of CO and its isotopologs due to their low dipole moments allows observations of molecular gas with densities of about 10^3 cm^{-3}. However, towards the densest regions the main isotopolog of carbon monoxide, $^{12}C^{16}O$ is mostly optically thick, and hence, it will not trace all the gas in the line-of-sight. Therefore, we will use the $^{13}C^{16}O$ and $^{12}C^{18}O$ isotopologs, which have an abundance about 60 and 560 times lower than $^{12}C^{16}O$ (Wilson & Rood, 1994) and a correspondingly lower optical depth which allows to measure the number of molecules on a given line-of-sight (column density).

1.3.1.1 SEDIGISM

The SEDIGISM survey (Structure, Excitation and Dynamics of the Inner Galactic InterStellar Medium) (Schuller et al., 2017) is a spectrometric survey of the frequency range from 217 GHz to 221 GHz. It covers the inner Galactic plane between $-60° \leq \ell \leq 18°$ and $|b| \leq 0.5°$. The observations were performed with the SHeFI heterodyne receiver (Vassilev et al., 2008) at the APEX 12 m telescope in the years from 2013 to 2016. The survey was designed to primarily target the $^{13}CO(2-1)$ and $C^{18}O(2-1)$ molecular lines with a spectral resolution of 0.25 km s^{-1} and a spacial resolution 30″. At this resolution the average root-mean-square (RMS) noise of the survey is 0.9 K (T_{MB}) with a pixel-size of 9.5″. Therefore, the SEDIGISM survey extends the Galactic

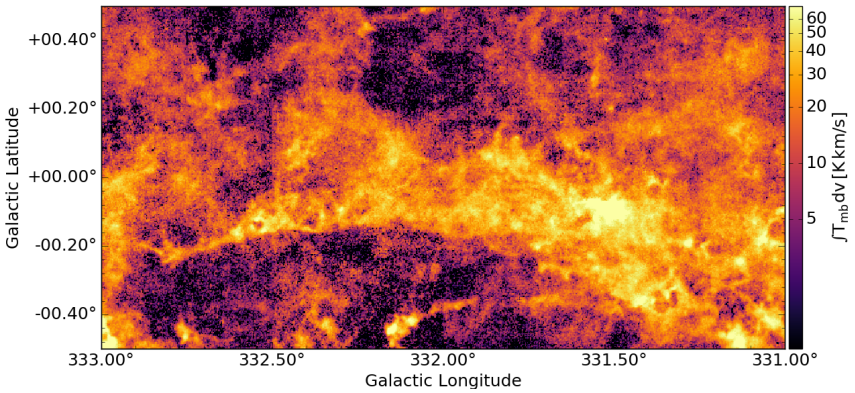

Figure 1.2: Total integrated ^{13}CO(2 – 1) intensity map of a SEDIGISM field.

Ring Survey (GRS, 0.21 km s^{-1}, 46″ Jackson et al., 2006) over the rest of the inner Galactic plane. The data will be released to the public.

1.3.2 Thermal dust continuum

Every body in the universe emits thermal radiation specific for its temperature. This is also the case for the dust in the ISM. As previously mentioned, dust makes up about 1% of mass of the ISM in the Milky Way. The dust particles are heated by high energetic ultraviolet radiation and emit this energy over the frequency spectrum of a modified blackbody (Planck-function), as so-called gray-body, $I_\nu(T) = B_\nu(T) \cdot (1 - e^{-\tau_\nu})$, where $\tau_n u$ is the optical depth at the observed frequency ν, and $B_\nu(T) = \varepsilon \cdot \frac{2h\nu^3}{c^2} 1/(e^{\frac{h\nu}{kT}} - 1)$ is the Planck-function, where ν is the frequency of the emission, T is the dust temperature, h is the Planck's constant, c is the speed of light, and k_B is the Boltzmann's constant (Dent et al., 1998). The dust temperature in the ISM is typically 10 – 100 K, which leads to significant emission in the wavelengths between 10 μm and 1000 μm. As the thermal dust emission is optically thin for most of the ISM, it is an ideal tracer for the column density of the medium. As such, several dust emission surveys have been conducted, of which I now want to introduce: the ATLASGAL and PLANCK survey, and their combination.

1.3.2.1 ATLASGAL

The APEX Telescope Large Survey of the Galaxy (ATLASGAL) was conducted by Schuller et al. (2009) with the Large APEX Bolometer Camera (LABOCA) at 870 μm between 2007 and 2010 at the Atacama Pathfinder Experiment (APEX) telescope (Güsten et al., 2006) located on the Chajnantor plateau in Chile. With the 12 m antenna of the APEX telescope the spatial resolution of the survey is 19.2″ (6.0″ per pixel). The survey covers the inner Galactic plane between $-80° \leq \ell \leq 60°$ and $|b| \leq 1.5°$. Because of the relatively short wavelength the ATLASGAL survey is most sensitive to the cold dust, and it traces mainly the high molecular hydrogen column

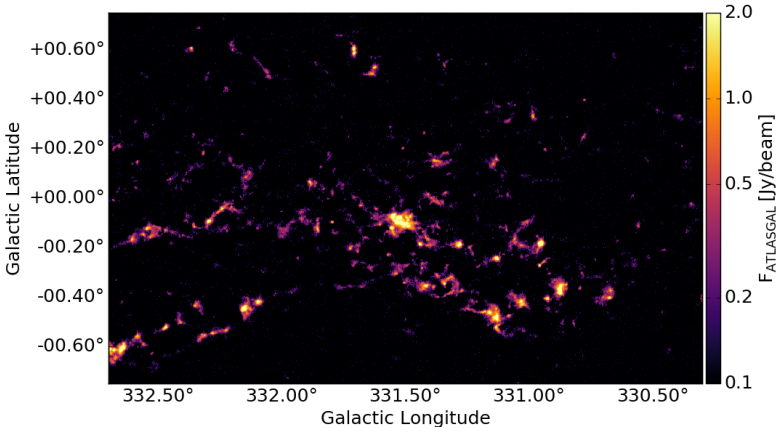

Figure 1.3: ATLASGAL dust continuum map.

density regions ($N_{\mathrm{H_2}} \geq 1.0 \times 10^{22}$ cm^{-2}) of the ISM. The sensitivity of the survey is in the range of 40–70 mJy/beam for the 1σ RMS noise.

As the ATLASGAL survey traces the high column density gas at a modest spatial resolution, it is ideal to identify the densest, most massive structures in the inner Galaxy. This was done in three different approaches, which will be discussed in Section 1.4. However, there are also caveats to the ATLASGAL data. One is the missing large scale low column density emission due to sky noise subtraction. Therefore, we are not able to see the large-scale structures that might connect the dense condensations and put them into a larger picture of star formation. Another caveat is the general lack of information in a third dimension, which is true for all continuum data. Without such radial velocity data it is not possible to separate the emission from two or more distinct sources along a given line-of-sight. This is especially a problem towards the Galactic center, where the gas is more dense and the line-of-sight passes through multiple spiral arms.

1.3.2.2 ATLASGAL + PLANCK

As mentioned before, the ATLASGAL data is missing the large scale dust emission due to sky noise subtraction. To address this Csengeri et al. (2016) combined the ATLASGAL data with data observed by the PLANCK space mission. PLANCK's main objective was to observe the cosmic microwave background all over the sky. However, to achieve this, it is also necessary to measure all foreground emission. Therefore, PLANCK observed the sky with the HFI instrument at several frequencies including 353 GHz (850 μm) with a spatial resolution of 4.8′ (Lamarre et al., 2010; Planck Collaboration et al., 2014).

The combination of the two datasets is performed in the Fourier domain following the method of Weiß et al. (2001). The combined ATLASGAL+PLANCK survey data is sensitive to a wide range of spatial scales at a resolution of 21″ covering the same region as the original ATLASGAL data on the same pixel grid. However, the additional large

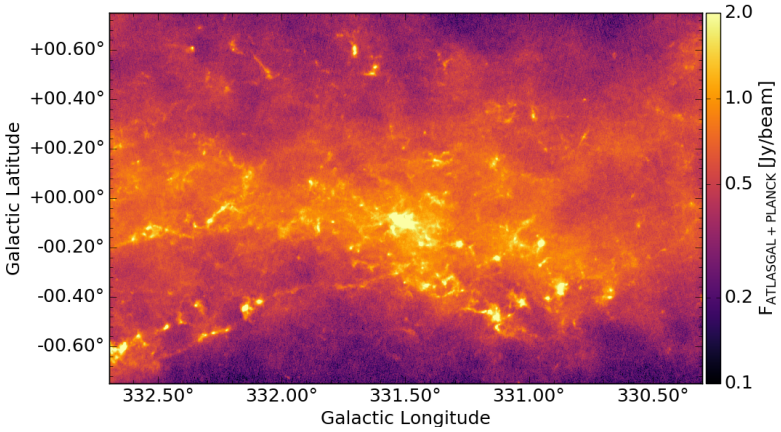

Figure 1.4: ATLASGAL + Planck dust continuum map.

scale emission leads to a larger line-of-sight confusion, especially towards the Galactic mid-plane. Therefore, mass estimates based on these data might need to corrected for foreground and background emission.

1.4 Catalogs

1.4.1 The ATLASGAL sample of filaments

As discussed before, the ATLASGAL dust emission traces the small scale high column density gas. Therefore, Li et al. (2016) used the data to identify all filamentary structures in the survey. To do so, they used the DisPerSE (Discrete Persistent Structures Extractor, Sousbie, 2011) algorithm. This algorithm is optimized for the identification of large spatially coherent structures by following the ridges of lowest intensity gradients, and has been successfully used to trace filaments in previous studies (e.g., Hill et al., 2011; Arzoumanian et al., 2011). Thereby the algorithm is sensible to the noise level. Therefore, the ATLASGAL data was smoothed to a spatial resolution of $42''$.

The identified structures do not all fit the definition of a filament as given before, as the data has no information on the velocity coherence. Therefore, this study can only provide a catalog of filament candidates. Additionally, the found structures vary in their morphology and complexity from roundish clumps to large web-like structures. To select the filament candidates, Li et al. (2016) defined a filament as single elongated linear structure with relatively few branches with an aspect ratio of at least 3, that is clearly resolved across its length and width. Despite the preferred interest in the filamentary structures, the remaining structures were also separated in different categories. Therefore, all structures were categorized through visual inspection into six groups: unresolved clumps, marginally resolved elongated structures, filaments, networks of filaments, complexes, and unclassified structures. This classification resulted in a finding of 517 filament candidates.

The biggest caveat of this method is the missing velocity information, which leads

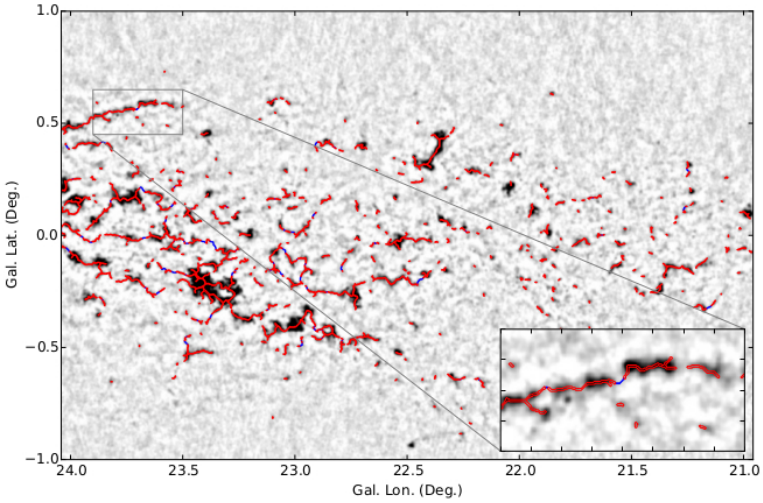

Figure 1.5: Structures identified by the DisPerSE algorithm (red lines, Sousbie, 2011) on top of ATLASGAL dust emission (gray scale). (Li et al., 2016)

to line-of-sight projection effects. Physically unconnected structures emit towards the same line-of-sight, which creates a stronger signal and can connect extended structures in the projected plane. Therefore, morphologies towards regions of high column densities, like the Galactic center, are likely to be more complex. This can be seen in the drop of the number identified structures towards the Galactic center (Li et al., 2016). Furthermore, this catalog of filament candidates is unlikely to be complete because of the limited sensitivity and resolution. However, because the large coverage of the Galactic plane, which includes structures at a wide range of distances, it is likely to include the full range of sizes and masses of filamentary type structures.

1.4.2 ATLASGAL clump catalogs

As high-mass stars have a large impact on the dynamics of the ISM through different types of feedback, like high energy radiation, outflows, or super novae, it is essential to understand there formation. As mentioned before, the ATLASGAL data traces the highest column density gas in the Galaxy and therefore, is ideal to identify the densest and most massive clumps, which are likely to form high-mass stars. As a result there are two clump catalogues based on different extraction methods from ATLASGAL.

The Compact Source Catalogue (CSC) catalogue from Contreras et al. (2013) and Urquhart et al. (2014) was produced by using the SExtractor code (Bertin & Arnouts, 1996) on the ATLASGAL data. The sources were identified as emission peaks over a threshold three times the local rms noise with a covered area larger than one beam. This way, 10163 massive, dense clumps were identified, which include all cold dense clumps (< 25 K) with masses ≥ 1000 $M_\odot$ at a heliocentric distance of ≤ 20 kpc. Several follow up studies were performed on this catalog, where Urquhart et al. (2018) provides distances and evolutionary phases for most of the sources. The sources of the GaussClump Source Catalog (GCSC) from Csengeri et al. (2014) were identified by the

GaussClump algorithm (Stutzki & Guesten, 1990; Kramer et al., 1998), which is fitting a two dimensional Gauss to every intensity peak above $5\sigma_{\rm rms}$. Leading to a catalog of 10861 sources, which are complete to $> 99\%$ above a $\sigma_{\rm rms}$ threshold. The catalogs have a significant overlap, however, about 1600 CSC sources are associated with two or more GCSC sources, as the Gauss fit can separate close sources more likely, and about 2500 CSC sources have no counterpart in the GCSC catalog as their peak intensity is below the $5\sigma_{\rm rms}$ threshold. In this theses I will make use of both catalogs in different studies.

1.4.3 Hi-GAL clump catalog

The Hi-GAL clump catalog (Molinari et al., 2016) is based on the Hi-GAL dust continuum survey (Molinari et al., 2010) performed with the Herschel Space Observatory at wavelength of 70, 160, 250, 350 and 500 μm in the region of $68^\circ > l > -70^\circ$ and $|b| \leq 1^\circ$. In these five bands 123210, 308509, 280685, 160972, and 85460 compact sources have been identified using the CuTEx algorithm, which analyses the local intensity variations and selects sources above a $2\sigma_{\rm rms}$ local noise threshold. For 100922 sources associations in the different band could be found, allowing analysis of their properties and evolutionary phase (Elia et al., 2017).

1.5 Motivation and Outline

As discussed before, filamentary structures are found ubiquitously in the ISM and cover a large range of size scales. Many mechanisms are discussed to explain the formation of these structures in a theoretical and numerical simulation context, while observational constraints are still being established. Nearby filaments are found to be mostly thermally stable and fragmenting into clumps; these can be described by cylindrical or spherical fragmentation patterns. However, this process leads only to the formation of low-mass stars. It remains unclear whether high-mass stars can be formed through fragmentation of massive filaments. Therefore, it will be necessary to understand the complete life-cycle of massive filaments. In particular, the following questions need to be answered: what are the processes responsible for the filament formation? Are they different from one filament to another? Are massive filaments stable against gravitational collapse or are they transient objects, which channel the gas motion radially onto and along its length? Does fragmentation of massive filaments lead to the formation of high-mass stars?

Recent surveys covering the inner Galactic Plane with different tracers not only reveal the ubiquity of filamentary structures in the ISM, but also allow to study these filaments. In particular, survey data allows to study the largest structures, GMFs, which can be longer than 1°, as well as a significant number of 'average' massive filaments.

In this thesis I will use data of several surveys to investigate the formation, evolution and fragmentation of the first GMF identified, the massive Nessie filament. In Chapter 2 I will use combined near- and mid-infrared dust extinction measurements

to analyze the fragmentation characteristics of this archetypal structure and its star formation rate. I then study in Chapter 3 the kinematics of the extended Nessie using SEDIGISM molecular line data and their correlation with massive clumps identified from dust continuum data to reveal the variation of star formation along this GMF. Chapter 4 shows the capabilities of analyzing ATLASGAL identified filaments with the SEDIGISM survey based on this survey's science demonstration field, which is then extended to the whole survey in Chapter 5 to study the kinematics and gravitational stability. I then summarize and draw conclusions in Chapter 6 and give an outlook for the continuation of these studies in Chapter 7.

Chapter 2

Structure and fragmentation of a high line-mass filament: Nessie

The following Chapter is based on a study performed for my Master Thesis at the University of Heidelberg. Parts that are a direct result of the Master Thesis and contributions of co-authors are marked by footnotes. The Chapter is published under M. Mattern, J. Kainulainen, M. Zhang and H. Beuther, 2018, A&A, 616, A78.

2.1 Introduction

Star formation is an important process in the evolution of galaxies and the Universe. It plays a crucial role in gas-to-stars conversion through parameters such as star-forming rate (SFR) and star-formation efficiency (SFE), and the initial mass function (e.g., McKee & Ostriker, 2007; Hennebelle & Falgarone, 2012; Padoan et al., 2014). Star formation takes place in dense regions of molecular clouds, which appear to be commonly composed of filamentary structures (Schneider & Elmegreen, 1979; Arzoumanian et al., 2011; Hacar et al., 2013; Schisano et al., 2014; Li et al., 2016; Kainulainen et al., 2017; Stutz & Gould, 2016, see André et al. 2014 for a review). Filaments are observationally defined as any elongated structures with an aspect ratio larger than approximately five and a clearly higher density than their surroundings (Myers, 2009). Given the link between filamentary structures and star formation, the processes driving the formation and evolution of filaments are linked with SFR and SFE. However, these processes are still not well understood.

Specifically, the physics of filament fragmentation is not well known. This is mostly because determining the basic characteristics of filaments is observationally challenging, as the cold molecular hydrogen is invisible to observations. Therefore, different tracers and techniques are needed to determine its distribution and properties (e.g., Lombardi & Alves, 2001; Goldsmith et al., 2008; Goodman et al., 2009; André et al., 2014). Each of the techniques is sensitive to different density regimes and has different spatial resolution. For studies of the structures related to star formation, the resolution should clearly resolve the Jeans' length. This is about 0.1 pc for typical conditions of a molecular cloud (gas temperature $T = 15$ K, average density $\overline{n}(\mathrm{H}) = 10^5$ cm^{-3}). This currently limits the observations to mostly nearby (< 500 pc) clouds. Interferometric observations can increase this resolution further, but they have their own caveats (e.g., spatial filtering, slow mapping speed).

However, the nearby clouds that can be systematically mapped in high-enough resolution are mainly low-mass clouds, containing mostly low line-mass filaments (mass

per unit length of $(M/l) \lesssim$ a few $\times 10$ $M_\odot$) forming almost exclusively low-mass stars. An exception to this is the integral shaped filament in the Orion A cloud (at distance 414 pc, Menten et al., 2007) whose fragmentation has been analyzed in high resolution using interferometric data (e.g., Takahashi et al., 2013; Teixeira et al., 2016; Kainulainen et al., 2017). In general, however, our current observational picture of filaments is mostly built by data on low-mass clouds. Filaments that have much higher line masses ($(M/l) \gg 100$ $M_\odot$), and may also be able to form high-mass stars, have been identified in numbers, but they are typically located at farther distances (e.g., Jackson et al., 2010; Hernandez et al., 2012; Busquet et al., 2013; Kainulainen et al., 2013; Ragan et al., 2014; Wang et al., 2014; Beuther et al., 2015; Abreu-Vicente et al., 2016; Henshaw et al., 2016; Li et al., 2016; Wang et al., 2016). Modern facilities are only just approaching the ability to study them systematically at a resolution that resolves the Jeans' scale.

Recently, Kainulainen & Tan (2013) developed a dust-extinction-based method that allows studying infrared dark molecular clouds at a resolution of $\sim 2''$ over a wide dynamic range of column densities, using a combination of near- and mid-infrared observations (see also Lombardi & Alves, 2001; Kainulainen et al., 2011; Butler & Tan, 2012). This method allows us to analyze the internal structure of clouds up to several kpc distance at ~ 0.1 pc resolution, enabling fragmentation studies of high line-mass filaments.

With the high-resolution mapping technique in hand, we can address a basic question related to filament fragmentation: What are the fragmentation characteristics of massive filaments and are they in agreement with gravitational fragmentation models?

In this paper, we take advantage of the high resolution provided by the Kainulainen & Tan (2013) extinction-mapping technique and analyze the fragmentation characteristics of a ~ 100 pc-long, high line-mass filamentary cloud known as "Nessie" (Jackson et al., 2010). It is supposedly located within the Scutum-Centaurus Arm of the Milky Way (Goodman et al., 2014; Ragan et al., 2014; Zucker et al., 2015; Abreu-Vicente et al., 2016). The high resolution allows us to characterize the cloud structure and to gauge the fragmentation processes over a wide range of scales (~ 0.1 pc – 100 pc). We use the dust extinction mapping technique in conjunction with the near-infrared (NIR) data from the ESO/VISTA telescope and mid-infrared (MIR) data from the *Spitzer* satellite. We subsequently analyze the derived column density map with a hierarchical structure-identification technique and examine the fragmentation of the cloud over multiple size-scales. The results are then compared with theoretical models and other clouds in the literature. Finally, we compare our identified small-scale structures to clumps identified in low-resolution (~ 20") dust emission maps by Csengeri et al. (2014). This demonstrates how structures identified from data with ten times lower resolution are seen to fragment when viewed in finer detail.

2.2 Data

2.2.1 Infrared data and data reduction

We employ NIR imaging data from the VVV (VISTA Variables in the Via Lactea) survey (Saito et al., 2012) at the 4.1 m VISTA telescope of the Paranal Observatory. The calibrated and reduced data are publicly available in the ESO archive. Specifically, we used the J, H, K_S spectral bands of the tiles d069 and d068. For each filter band there are two $t_{\rm exp} = 80\ s$ exposures and additionally there are 8 and 12 $t_{\rm exp} = 16\ s$ exposures of tiles d069 and d068 in the K_S band, respectively. The pixel size of the images is 0.34" $\times$ 0.34". Detailed information about the observations can be found in Table A.1 in the appendix. We stacked the observations and performed point-spread-function (PSF) photometry with the daophot package (Stetson, 1987) using the Image Reduction and Analysis Facility (IRAF) software. The PSF model was created from bright isolated stars with the model radius of $r_{\rm PSF} = 1.5$". The different spatial resolutions of the single-observation epochs has no significant effect on the photometry as we show in Appendix A.2. The daophot algorithm identifies and extracts extended sources and cosmic rays, and we expect only a very low contamination of the data by galaxies because we are looking through the galactic mid-plane. The zero-point magnitudes were defined by comparing the resulting magnitudes of the stars with the corresponding stars of 2MASS, that are flagged as good photometric quality (Skrutskie et al., 2006; Cutri et al., 2003). This resulted in zero-points $\mathrm{J_{zpt}} = 21,21$ mag, $\mathrm{H_{zpt}} = 21,22$ mag, and $\mathrm{K_{S,zpt}} = 20,88$ mag. The resulting data show the expected shape in the NIR color-color scatter plot (Fig. 2.1), with a bump for the main sequence stars and an elongated distribution for stars with varying reddening. We also tested the photometry measurements for completeness by adding artificial stars. We could identify all artificial stars up to a magnitude of about $\mathrm{J_{com}} = 16.5$ mag, $\mathrm{H_{com}} = 15.5$ mag, and $\mathrm{K_{S,com}} = 15.0$ mag.

We also employ MIR 8 μm imaging data from the *Spitzer*/GLIMPSE survey, data release 5 (Benjamin et al., 2003; Churchwell et al., 2009). The pipeline-reduced (S13.2.0 1v04) images were retrieved from the IRSA[1] database and used as such. The 8 μm image has a spatial resolution of $2.4''$ and a pixel size of $1.2''$ times $1.2''$. The used tile is centered around $RA = 16:43:14.08$, $DEC = -16:00:15.92$. The effective integration time of the tile is 1.2 s.

2.2.2 ATLASGAL data

We also use data from the APEX telescope large area survey of the galaxy (ATLASGAL, Schuller et al., 2009) for a comparison with our extinction data. The survey was obtained by the Millimeter and Submillimeter Group of the Max-Planck-Institut für Radioastronomie from 2007 to 2010 at the Atacama Pathfinder Experiment (APEX) located on Chajnantor in Chile. The survey instrument was the Large APEX Bolometer Camera (LABOCA) observing at 870 μm, which traces the thermal dust emis-

[1] `http://irsa.ipac.caltech.edu/data/SPITZER/GLIMPSE/`

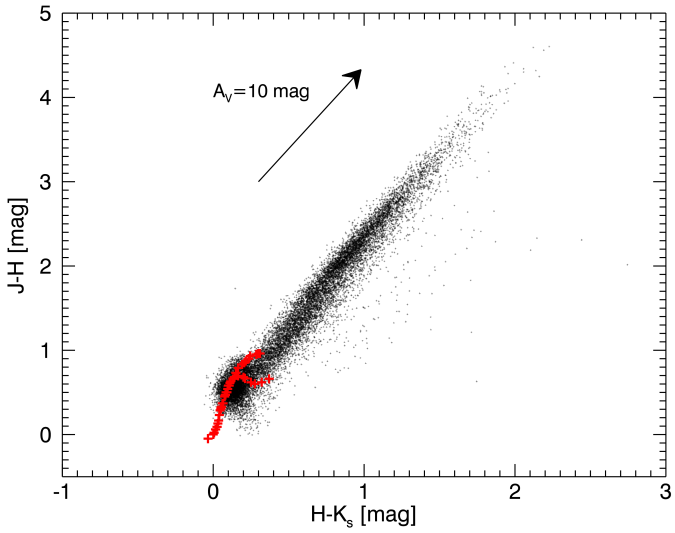

Figure 2.1: NIR color-color diagram of all sources in the mapped area extracted from the VVV survey with the photometric errors lower than 0.02 mag. The blue crosses indicate non-reddened intrinsic colors of stars (Bessell & Brett, 1988). The arrow shows the reddening for an extinction of $A_V = 10$ mag

.

sion. The resolution of the survey is $\Omega = 19.2$" with a sensitivity in the range of $40 - 70$ mJy/beam. The maps covering the Nessie filament are centered at $l = -22.5°$, $b = 0.0°$ and $l = -19.5°$, $b = 0.0°$ and were observed on August 18 and 21 of 2007. The flux per beam, F_ν, of the ATLASGAL map can be used to estimate the hydrogen column density $N(H_2)$ under the assumptions of a constant gas-to-dust ratio of $R = 100$ and a dust opacity of $\kappa_{345\,\mathrm{GHz}} = 1.85$ cm^2 g^{-1}, which was extrapolated by Schuller et al. (2009) based on the work of Ossenkopf & Henning (1994),

$$N(H_2) = \frac{F_\nu R}{B_\nu(T_d)\Omega\kappa_\nu\mu_{H_2}m_H} \tag{2.1}$$

$B_\nu(T_d)$ is the Planck function at the dust temperature T_d, m_H is the mass of a hydrogen atom, and μ_{H_2} the mean molecular weight of the interstellar medium with respect to hydrogen molecules, which is 2.8 (Kauffmann et al., 2008).

Csengeri et al. (2014) have identified clump-like structures from the ATLASGAL data using two-dimensional (2D) Gaussian fitting (Gauss Clump Source Catalog, GCSC). It provides the position, peak flux F'_ν and integrated flux S_ν, the half maximum major and minor axes and the position angle of the clumps. We then calculated the masses of the clumps from (Schuller et al., 2009):

$$M = \frac{S_\nu R\, d^2}{B_\nu(T_d)\kappa_\nu}, \tag{2.2}$$

where R is the gas-to-dust ratio and d the distance towards the clump.

2.3 Extinction mapping technique[2]

We employ the technique from Kainulainen & Tan (2013), which is based on combining extinction maps made at two wavelength regimes: in NIR using NICER (Near-Infrared Color Excess Revisited, Lombardi & Alves, 2001) and in MIR using the absorption against the Galactic background (e.g., Peretto & Fuller, 2009; Butler & Tan, 2012). Below, the implementation of the two techniques is explained in detail.

2.3.1 NICER method

We use the NICER method in conjunction with JHK_S photometric data of the VVV survey. The method is based on NIR color measurements of stars shining through the molecular cloud and comparison of those with stars of a reference field that is (optimally) free from extinction. The observed reddening towards the cloud region is used to estimate the extinction by adopting a wavelength dependent reddening law. The extinction values towards each star are then used to derive a spatially smoothed dust extinction map.

This method is straightforward when applied for nearby clouds ($d < 500$ pc, e.g., Lombardi et al., 2006; Froebrich et al., 2007; Juvela et al., 2008; Goodman et al., 2009; Kainulainen et al., 2009), where the contamination due to stars between the cloud and the observer is small. The extinction towards more distant clouds might be underestimated because of these (mostly unreddened) foreground stars, especially in high-extinction regions where the fraction of foreground sources is high (Lombardi, 2005). The foreground stars do not trace the dust reddening caused by the cloud, but only the reddening along the line of sight until the cloud. Therefore, foreground sources should be removed as accurately as possible, which is challenging in practice because of the degeneracy between the intrinsic colors of stars and reddening caused by extinction.

The subtraction of the foreground is also necessary for the reference field (see, Kainulainen et al., 2011). Due to diffuse dust in the Galactic plane, stars in the reference field, located at the same distance as stars behind the cloud, are redder than the ones at closer distance. Therefore, foreground stars shift the mean color of the reference field towards blue, which leads to an overestimation of the extinction. For the implementation of the NICER method we have to find a reliable way to remove the effect of the foreground stars. This is described in the following.

First, we derive a "dirty" extinction map using arbitrary reference colors and use this map to identify low- and high-extinction regions. The low-extinction region (Fig. 2.2; $338.39^\circ < l < 338.58^\circ; -0.36^\circ < b < -0.21^\circ$) is then used as a control field to estimate the reference colors, indicating the average star colors without dust reddening by the cloud. In the regions of high extinction, identifying foreground stars is simple: they appear as a distinct feature in the frequency distribution of individual extinction measurements (cf., Kainulainen et al., 2011). For regions of lower extinction the feature

[2]I used the same method as for the work described in my Master thesis, but here we used improved data.

is less distinct, but under the assumption of uniformly distributed foreground stars the position and width of the frequency distribution remains the same; this fact can be used to statistically subtract the contribution of foreground stars to the reference field colors. To do this, we fit a Gaussian function, $G_{\rm fg}$, to the peak of the foreground stars in the extinction histogram $H(A_V)$ (Fig. 2.3) and subtract these stars in a statistical sense from the distribution. To achieve this, we add a weighting term ($W_{\rm fg}(\widehat{A}_V^{(n)})$, see Fig. 2.3) into the original NICER method. This weighting term suppresses the contribution of stars that might be foreground stars, and it is calculated in the following way

$$W_{\rm fg}(\widehat{A}_V^{(n)}) = \frac{H(A_V) - G_{\rm fg}}{H(A_V)}. \tag{2.3}$$

The weighting term is introduced into Eq. (15) of Lombardi & Alves (2001) as shown here:

$$W^{(n)} = \frac{W(\theta - \theta^{(n)}) \cdot W_{\rm fg}(\widehat{A}_V^{(n)})}{\mathrm{Var}(\widehat{A}_V^{(n)})}, \tag{2.4}$$

where $W^{(n)}$ is the weighting of the nth star, $W(\theta - \theta^{(n)})$ is the weight for the distance between the actual location θ and the location of the nth star $\theta^{(n)}$, $W_{\rm fg}(\widehat{A}_V^{(n)})$ is the foreground weight based on the estimated extinction of the nth star, and $\mathrm{Var}(\widehat{A}_V^{(n)})$ is variance of the estimated extinction of the nth star.

With this method the contribution of foreground stars was subtracted statistically from the mean color of the reference field to calculate an estimate of the mean color of the stars in the background of the cloud. The statistical subtraction is done in the JHK-color-color space, where the density of foreground stars was subtracted from the density of the reference field stars in each color-color bin. Subsequently, the foreground-corrected number of stars per bin was calculated from the resulting density in the reference field. The foreground-corrected mean color was calculated from this sample of stars, which is also the estimate of the background color. The JHK-color-color histograms of the reference field before and after correction are shown in Appendix A.3.

With the foreground-corrected reference color and the method for extracting foreground sources, the "true" NIR extinction map was calculated. The spatial resolution of the map is given by the width of the Gaussian smoothing function that is used to smooth the pencil-beam measurements towards the stars onto the map grid. The pixel size is chosen following the surface number density of background sources so that even in high-extinction regions, where the density is lower, each pixel covers at least two stars. For the VVV data we concluded that a pixel size of 24" is sufficient, which leads to a beam width of 48".

2.3.2 Mid-infrared extinction measurement[3]

We use the MIR imaging data from the GLIMPSE survey to estimate extinction through the cloud at 8 μm. Generally, the technique is based on the extinction of

[3]The mid-infrared extinction measurement was performed by a co-author.

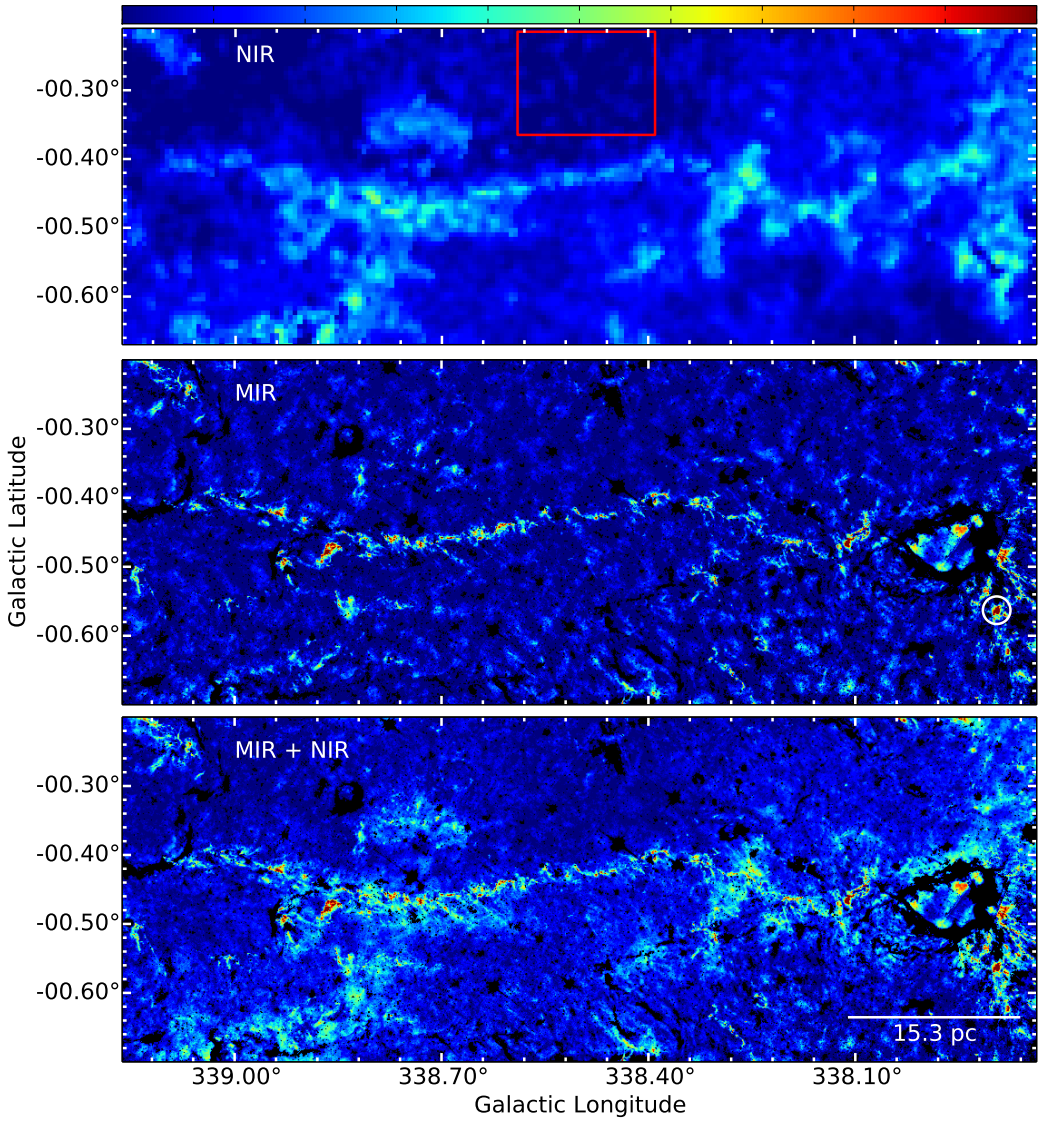

Figure 2.2: Extinction maps of Nessie derived using the NIR data of the VVV survey (top), MIR data of the *Spitzer* Space Telescope (center) and their combination (bottom). The black areas indicate regions of bright MIR emission that hampers extinction mapping. The red rectangle marks the area used for estimating the reference colors for the NICER method. The white circle marks the high-extinction region used to estimate the MIR foreground emission.

the diffuse MIR emission from the Galactic plane by the dust of the cloud (see, e.g., Johnstone et al., 2003; Peretto & Fuller, 2009; Butler & Tan, 2012). If we consider a simplistic geometry in which the intensity of radiation behind the cloud is I_0, the intensity right in front of the cloud is $I_1 = I_0 e^{-\tau_8}$, in which τ_8 refers to the optical depth at the *Spitzer* 8 μm band. An observer detects the intensity $I_{\mathrm{obs},1}$, which in addition to I_1 contains the intensity I_{fg} that is emitted from between the cloud and

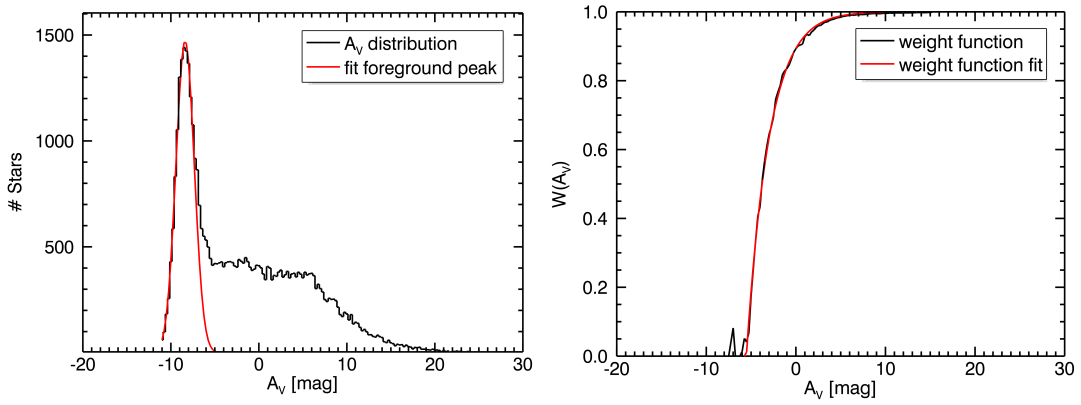

Figure 2.3: **Left:** The black line shows a histogram of the calculated extinction from a high-extinction region. The red line marks the Gaussian fitted to the peak of foreground stars. **Right:** The black line shows the empirical weighting function, which is derived as shown in Eq. 2.3. The red line shows the fitted function, which is then introduced into the weighting function of the NICER method (Eq. 2.4).

the observer, that is, $I_{\rm obs,1} = I_1 + I_{\rm fg}$. A line-of-sight off the cloud does not exhibit extinction and the observed intensity is $I_{\rm obs,0} = I_0 + I_{\rm fg}$. Combining these relations, one can solve the optical depth

$$\tau_8 = \ln \frac{I_{\rm obs,0} - I_{\rm fg}}{I_{\rm obs,1} - I_{\rm fg}}. \tag{2.5}$$

Thus, the optical depth along the line of sight can be estimated through measurements of the off-cloud and foreground intensities.

Various approaches have been used in the past to estimate the off-cloud and foreground intensities (see, e.g., Johnstone et al., 2003; Peretto & Fuller, 2009; Ragan et al., 2009; Butler & Tan, 2012). We follow an approach similar to Butler & Tan (2012) to which we refer for a thorough description and discussion; we describe here only the implementation of the technique in our case. The off-cloud intensity is estimated using a median-filtered 8 μm map. Prior to the filtering, the most prominent dark features are masked from the map by using a threshold intensity of 46 MJy sr^{-1}. The filter size defines the upper limit of the structures the map is sensitive to. However in our case, we will later combine the MIR-derived map with the NIR-derived map that probes spatial scales larger than 24″. Therefore, the filter function width is not a crucial choice for us, as long as there is some overlap of scales probed by the MIR and NIR maps. Following the discussion in (Ragan et al., 2009), we chose the filter width of 3′.

The foreground intensity is estimated with the help of the pixels with lowest intensities (i.e., highest extinctions) in the 8 μm data. If several independent high-extinction regions show similar intensities, one can assume that such locations are opaque and the intensity towards them is a reasonable estimate of the foreground intensity. The smallest intensities detected in the cloud area are $I_{\rm obs,1} = 24.6$ MJy sr^{-1}. There are three independent locations in the cloud where the intensity is within $2\sigma_{\rm rms}$ of this value (the

rms noise, $\sigma_{\rm rms}$, of the GLIMPSE data is $\sim$0.6 MJy sr^{-1}, Reach et al., 2005). One of them (l, $b = 337.895°$, $-0.563°$) is extended, containing tens of pixels, which indicates that the region is indeed saturated. The number of saturated regions is relatively low given the large extent of the cloud on the sky; it would be preferable to have numerous saturated regions along the cloud. Regardless, we adopt the value of 24 MJy sr^{-1} for the foreground intensity. We note that the resulting fraction of foreground emission, that is, $I_{\rm fg}/I_{\rm obs,0} \approx 45\%$, well in the range of the foreground intensities typically determined for IRDCs (e.g., Butler & Tan, 2012).

Following the estimation of the off-cloud and foreground intensities, Eq. 2.5 is used to compute an optical depth map for Nessie. Finally, the map is converted into units of visual extinction by adopting the ratio between 8 μm and V band optical depths (based on Cardelli et al., 1989; Ossenkopf & Henning, 1994, see Kainulainen & Tan 2013)

$$A_{\rm V} = 33.6\tau_8. \tag{2.6}$$

The resulting extinction map is shown in Fig. 2.2.

2.3.3 Combined near- and mid-infrared extinction measurement

We have now derived the NIR and MIR extinction maps; both show some advantages and disadvantages. The NIR data are sensitive to low column densities, but are at low resolution. The MIR data are at good resolution, but are much less sensitive. Therefore, we now want to combine them and use the NIR data to recalibrate the MIR data, thus gaining high spatial resolution of the MIR data while imposing the good calibration of the NIR data on them. The combination of NIR and MIR extinction maps follows the scheme described in Kainulainen & Tan (2013). The combined maps deliver a higher dynamic range of extinction compared to maps computed from NIR or MIR data alone (Fig. 2.2). The correlation between the two maps is shown in Appendix A.4.

The combined map is then converted to molecular hydrogen column density by applying the conversion of Savage et al. (1977); Bohlin et al. (1978); Rachford et al. (2002):

$$N({\rm H_2}) = A_V \cdot 0.94 \cdot 10^{21} {\rm cm^{-2}\,mag^{-1}}, \tag{2.7}$$

using a typical reddening constant of $R_V = 3.1$ (Schultz & Wiemer, 1975) and assuming all hydrogen atoms are in molecular form.

2.4 Results

2.4.1 Distance determination

The foreground star density measurements (see Sect. 2.3.1) allow us to estimate the distance of Nessie independently of previous, kinematic distance estimates. We can compare the measured surface density of foreground stars with a distance-dependent stellar surface density model of the Galaxy. We used the Besançon Galactic stellar

distribution model (Robin et al., 2003) to estimate the distance; see Fig. 2.4. For a more detailed description of the method see Kainulainen et al. (2011); Ioannidis & Froebrich (2012). The most important input parameter of the stellar distribution model is the extinction caused by diffuse interstellar dust. We used the measurements by Marshall et al. (2006) to estimate the mean extinction along the line of sight towards Nessie. For an estimate of the uncertainty we also estimated the minimum and maximum extinction, which indicate the upper and lower limits of the surface density (Fig. 2.4). We neglected other, potentially significant uncertainties in our distance calculations such as the uncertainty of the measured number surface density of the foreground stars or of the stellar distribution model. Therefore, the uncertainty of the distance is underestimated and it is more likely to be on the order of 15 % corresponding to $\Delta d \approx 0.5$ kpc (Kainulainen et al., 2011).

The result of our distance estimate is $d_{\mathrm{extinction}} = 3.5 \pm 0.5$ kpc, which is in agreement with the kinematic distance estimations of Jackson et al. (2010), $d_{\mathrm{HCN}} = 3.1$ kpc. We find also dynamical distance measurements from Wienen et al. (2015) for 14 ATLASGAL sources likely embedded in the Nessie cloud. Their distances range between 3.0 kpc and 3.5 kpc, which is also in agreement with our estimate. The distance of ~ 3.5 kpc suggests that Nessie is associated with the Scutum-Centaurus spiral-arm of the Milky Way as suggested by Goodman et al. (2014) and Ragan et al. (2014).

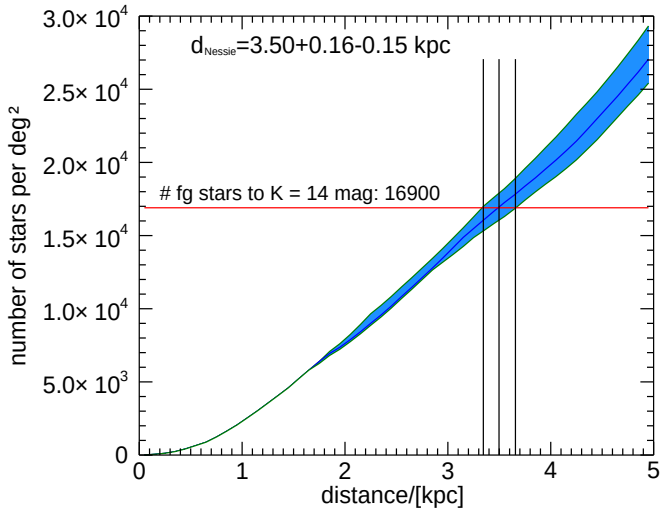

Figure 2.4: Predicted stellar surface density based on the Besançon stellar distribution model (Robin et al., 2003). The blue area indicates the uncertainty arising from the scatter in the diffuse extinction measurements. The horizontal line represents the measured foreground star surface density and the vertical lines the resulting estimates of the distance and its uncertainty.

2.4.2 The large-scale structure

The combined NIR and MIR extinction map of the Nessie cloud is shown in Fig. 2.5 and zoom-ins in Figs. 2.6, 2.7, and 2.8. For comparison, Fig. 2.2 shows the NIR-based map, MIR-based map, and their combination.

The filament has a length of $\sim 1.1^\circ$ following the central, dense main axis (neglecting inclination) and a perpendicular width of $\sim 0.05^\circ$. This corresponds to a physical size of 67 pc $\times$ 3 pc at a distance of $d = 3.5$ kpc. The width of the extinction structures, defined at the column density contours of about $A_V = 3$ mag, varies along the filament. This can be seen in the zoomed-in map of Nessie (Fig. 2.6). In the region in the range $338.57^\circ < l < 338.95^\circ$ the low-column-density material is located only towards the south of the dense main axis, in the range $338.23^\circ < l < 338.30^\circ$ towards north and south, and the rest of the filament shows almost no surrounding low column density material. These two low-column-density regions also show some less dense structures, which are mainly orientated almost perpendicular to the main filament.

We need to identify which structures that we see in the map are actually part of Nessie. This is difficult because we miss information about the line-of-sight velocities of the structures. However, the Nessie filament was confirmed as a velocity coherent structure by Jackson et al. (2010). Additionally, some areas lack the MIR extinction data and cannot be used in the further analysis, such as the HII -bulb at $(l; b) = (337.95^\circ; -0.46^\circ)$ (Fig. 2.5), which is part of Nessie in Jackson et al. (2010). Therefore, the map needs to be cropped to the Nessie filament. To do this, we introduce a polygon around the cloud (see Fig. 2.5). The area selection is mainly based on physical inspection of the derived column density map with orientation on the $A_V = 3$ mag contour and the observations published by Jackson et al. (2010).

We derive an estimate of the total cloud mass from the column density map, given by:

$$M_{\mathrm{Nessie}} = \sum_{i,j} (N(\mathrm{H_2})_{i,j}) \cdot p^2 \cdot m_{\mathrm{H}} \cdot \mu_{\mathrm{H_2}}, \tag{2.8}$$

where $N(\mathrm{H_2})_{i,j}$ is the column density of the (i, j) pixel of the map, $p = \tan(1.2") \cdot d_{\mathrm{Nessie}}$ is the physical size of a pixel, m_{H} is the mass of the hydrogen atom, and $\mu_{\mathrm{H_2}} = 2.8$ the mean molecular weight of the interstellar medium (Kauffmann et al., 2008). The total mass of the Nessie cloud within the polygon (Fig. 2.5) is $M_{\mathrm{Nessie}} = 4.2 \cdot 10^4$ $\mathrm{M_\odot}$.

From the length and mass, we calculate the mean line-mass of the filament (mass per unit length along the main axis of the filament). The mean line-mass of Nessie is $(M/l) = 627$ $\mathrm{M_\odot\,pc^{-1}}$. As we neglected an inclination of the filament, which would increase its length, the derived line-mass is an upper limit. We note that there are variations in the line mass along the filament, both at large scales due to the varying amount of diffuse extinction and at small scales due to the substructure of the cloud.

2.4.3 Fragmentation analysis

We analyzed fragmentation of Nessie simultaneously over a wide range of spatial scales using an algorithm explained in Kainulainen et al. (2014), which employs wavelet filter-

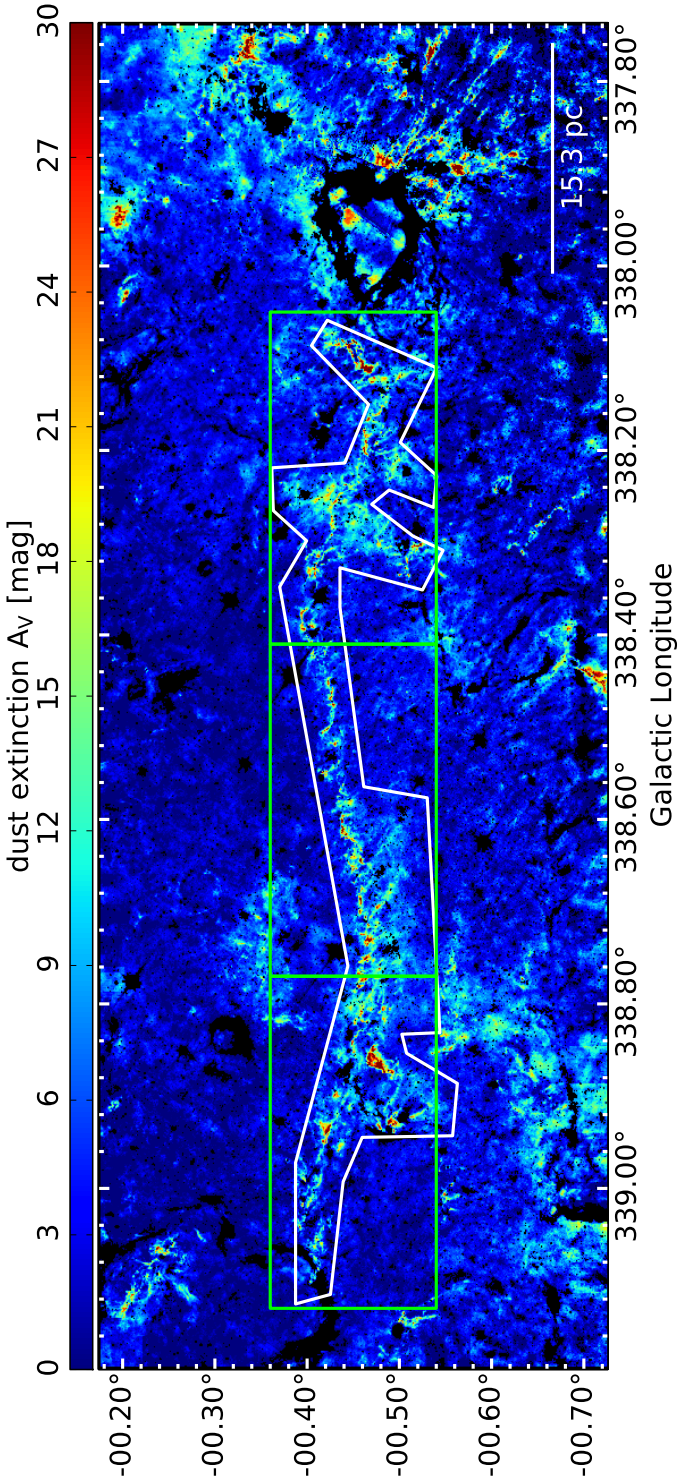

Figure 2.5: Column density map of the Nessie filament. The white polygon marks the area chosen for the mass estimate of the cloud. The green rectangles show the positions of the zoom-ins shown in Figs. 2.6, 2.7, and 2.8.

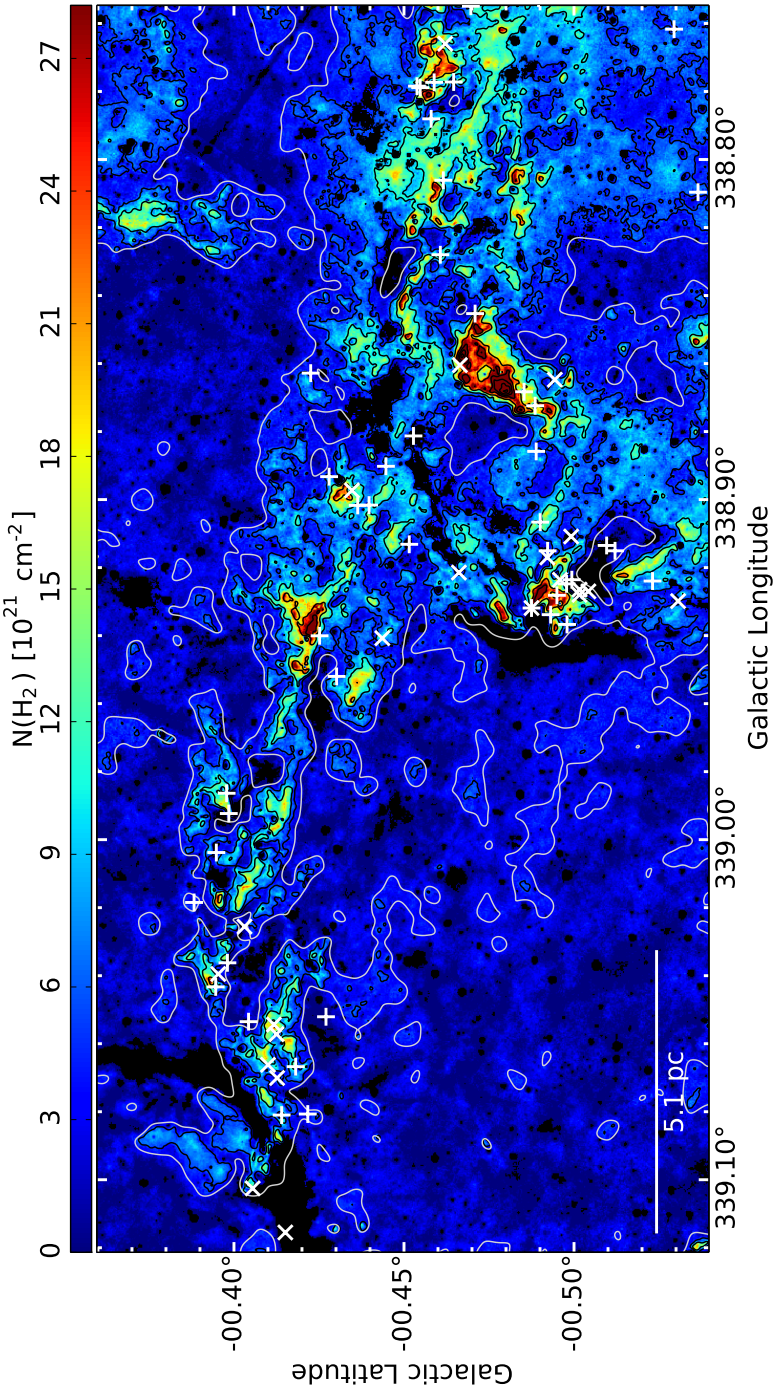

Figure 2.6: Zoom-in number one of the column density map (Fig. 2.5). The black contours indicate the levels of $5, 10, 20, 30, 40, 50, 60 \cdot 10^{21}$ cm^{-2}. The white contour indicates the smoothed $A_V = 3$ mag level. Additionally, the Class1 ('x') and Class2 ('+') YSOs are marked in white.

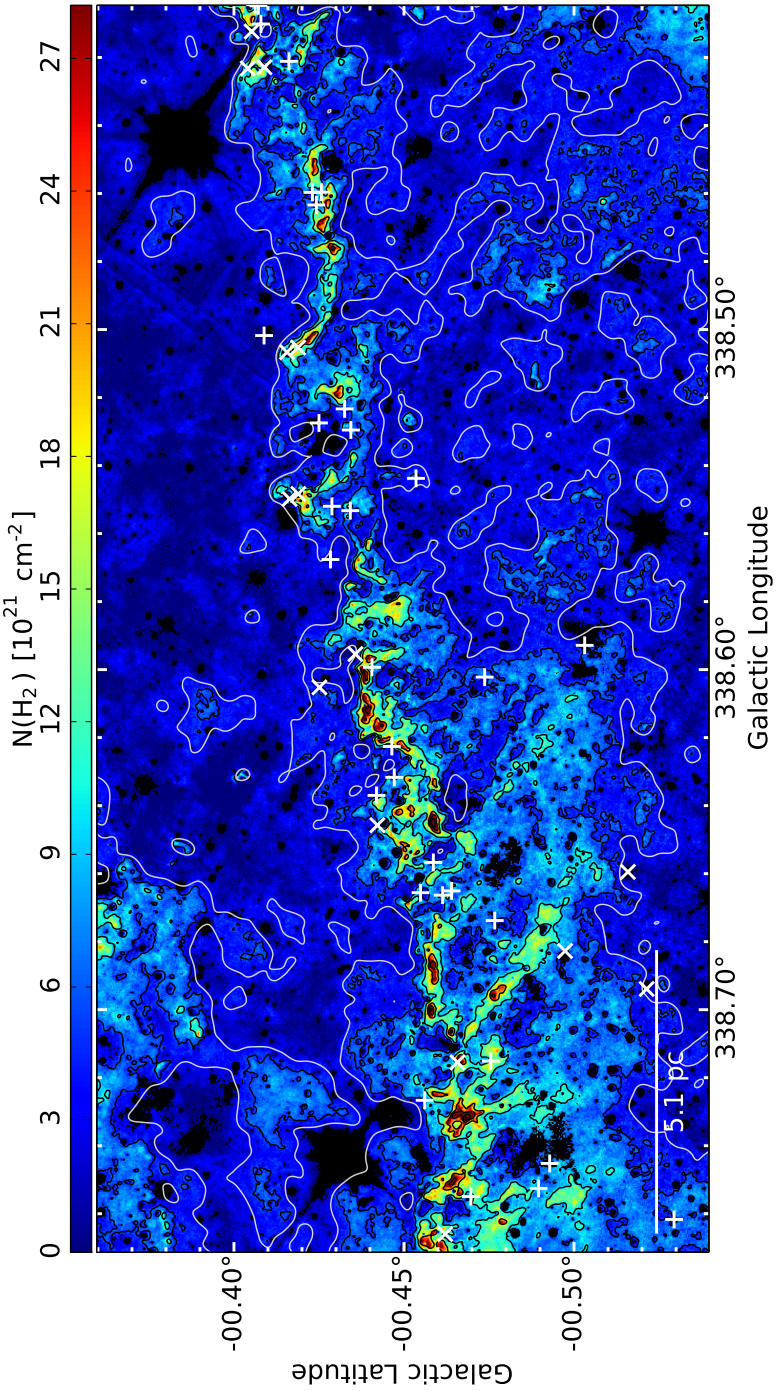

Figure 2.7: Zoom-in number two of the column density map (Fig. 2.5).The black contours indicate the levels of $5, 10, 20, 30, 40, 50, 60 \cdot 10^{21}$ cm^{-2}. The white contour indicates the smoothed $A_V = 3$ mag level. Additionally, the Class1 ('x') and Class2 ('+') YSOs are marked in white.

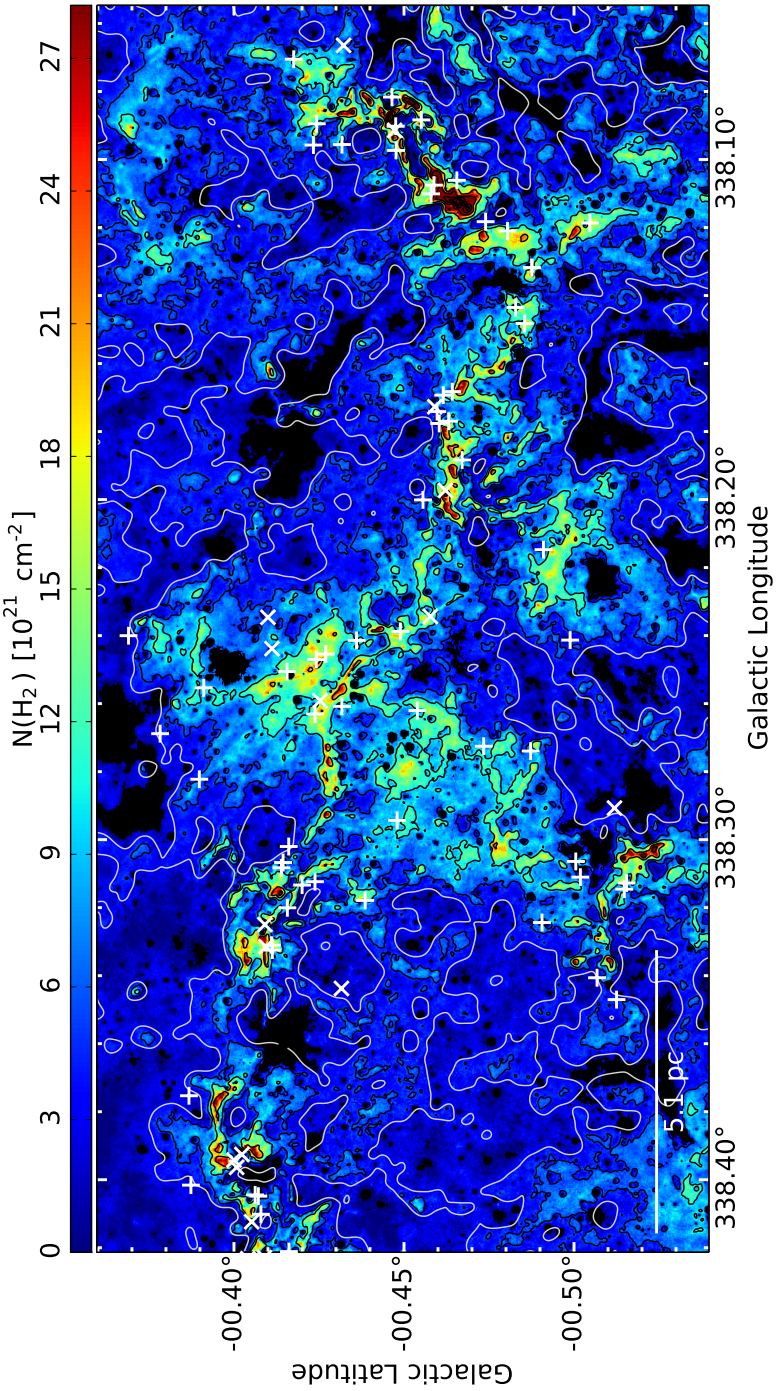

Figure 2.8: Zoom-in number three of the column density map (Fig. 2.5). The black contours indicate the levels of $5, 10, 20, 30, 40, 50, 60 \cdot 10^{21}$ cm^{-2}. The white contour indicates the smoothed $A_V = 3$ mag level. Additionally, the Class1 ('x') and Class2 ('+') YSOs are marked in white.

ing to identify structures at various spatial scales. In short, the algorithm uses a spatial filtering algorithm based on the à Trous wavelet transform (Starck & Murtagh, 2002) to decompose the column density map into scale-maps that describe structure at different scales. The different scales are defined as 2^i pixels, with $2 \leq i \leq 8$, where the limits are given by the pixel size for small scales and the cloud size for large scales. Individual structures are then identified from each scale map using the clumpfind-2D algorithm (Williams et al., 1994). This provides the position, the size in x and y direction, and the total amount of column density of the structures $N(\mathrm{H})_{\mathrm{tot}}$.

For reliable detection of structures, it is necessary to estimate the noise level of each scale map. The noise level is estimated as the standard deviation σ of an (almost) extinction-free area. The size of the area corresponds to the size-scale of the largest scale map. To test the robustness of the structure identification, we tested the clumpfind-2D algorithm for contour level separations of $1.5\sigma, 3\sigma, 4\sigma$ and 5σ with the lowest level at 3σ. The results do not show a significant difference and we chose the level separation of 3σ.

The numbers of structures identified at each scale using the chosen technique are listed in Table 2.1. The number of structures increases towards smaller scales, but drops significantly for the smallest scales ($i = 2$, see Table 2.1). This behavior was seen for all tested algorithm parameters and therefore is not likely to be an artifact. In the data these smallest structures trace only the densest clumps, which are predominantly located along the dense spine of the filament, but not in the surrounding low-column-density gas. This suggests that only in the densest parts is the filament able to fragment into the smallest scales.

Table 2.1 shows the properties of structures at each scale i: the total number of identified structures N_{strc}, the total mass of these structures $\sum(M_{\mathrm{strc}})$, the median hydrogen number density $\widetilde{n}(\mathrm{H})$, and the median separation $\widetilde{s}$. The sum of the masses over all scales, including scale $i > 8$, results in a total cloud mass of about $M^{\mathrm{scales}}_{\mathrm{Nessie}} = 4.9 \cdot 10^4 \mathrm{M}_\odot$. This is slightly higher than the mass derived from the combined column density map (see Section 2.4.2). The difference is a consequence of the spatial filtering algorithm used, which may not accurately reproduce the true shapes of the structures.

We include in the fragmentation analysis all structures identified at scales $i = 2$ – 8 and only include structures within the Nessie filament area (see the polygon in Fig. 2.5). We computed the projected nearest neighbor distances of the structures. The separation distributions of the scales $i = 2, 3$ are shown in Fig. 2.9. They are non-Gaussian in shape and we adopt the median separation as a diagnostic of the separations (given in Table 2.1).

For the fragmentation analysis an estimate of the structure density is interesting; we estimate this from the outputs of the clumpfind-2D algorithm. The size of a structure was given by clumpfind-2D as the number of pixels, N_{pix}, in the FWHM area. For the calculation of the structure volume we assume the shape of a prolate spheroid, that has been found to be among the shapes that best quantify the structures at the scales we are looking at (e.g., Kainulainen et al., 2014). The depth of the prolate spheroids is estimated as the shorter of the projected x and y dimensions. Therefore, the volume

of a fragment is

$$V = 4/3\ \pi \cdot x \cdot y \cdot \min\{x, y\}. \tag{2.9}$$

The average column density, $\overline{N}(H)$, is given by: $\overline{N}(\mathrm{H}) = N(\mathrm{H})_{\mathrm{tot}}/N_{\mathrm{pix}}$, and therefore, the hydrogen number density of one structure is: $n(H) = \overline{N}(\mathrm{H}) \cdot \pi \cdot x \cdot y/V$. The median number density and the 95% interval for structures at each scale are shown as a function of their median separation in Fig. 2.10.

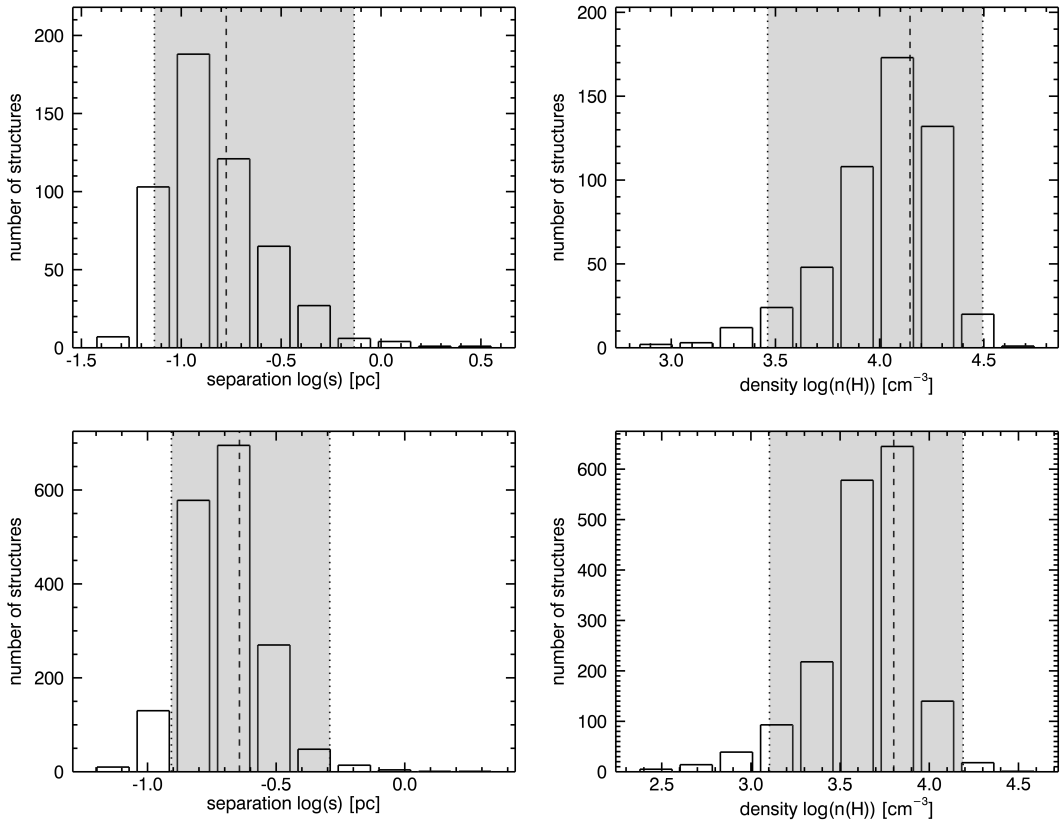

Figure 2.9: Distributions of the separations (left) and densities (right) of the structures identified from the scale maps $i = 2$ (top) and $i = 3$ (bottom). The dashed line indicates the median and the dotted lines the 95% quantiles of each distribution.

Additionally, we estimated the median separation and density from the HNC molecular line observations of Jackson et al. (2010). We used the shown positions to estimate their separation at the distance of $d = 3.5$ kpc. The density was calculated assuming a spherical geometry with a radius of $r = \sqrt{\Omega/\pi}$, using the angular size Ω of the identified clumps, and their mass M. The hydrogen number density is given by:

$$n(H) = \frac{M}{\mu_{\mathrm{H}} m_{\mathrm{H}} (4/3\,\pi r^3)}, \tag{2.10}$$

where $\mu_{\mathrm{H}} = 1.4$ is the mean molecular weight of the interstellar medium with respect to atomic hydrogen and m_{H} is the mass of a hydrogen atom.

We estimated the uncertainty of the median separations and median mean densities using bootstrapping, because their probability distributions are not Gaussian (see Fig. 2.9). For the separation and mean density on every scale, we drew a new sample of values from among the observed values of separations and mean densities. This new sample had the same amount of data points as originally detected at that scale. We then calculated the median of these new simulated samples. The resulting distribution of the median values then estimates the sampling function of the observed median and was used to estimate the uncertainty using the standard deviation. The uncertainties vary between 1 and 14% for the separation and between 1 and 25% for the density on scales of $i = 3$ and $i = 8$. The uncertainty values of all scales are given in Table 2.1.

The scatter shown in the separation density plot represents the 95% quantiles of the measured parameters. Large uncertainties, which are neglected here, are the opacity at different wavelengths (J, H, K, 8 μm) and their ratios contributing in the extinction measurement and the conversion factor from extinction to column density. For measuring masses, the uncertainty of the distance, as discussed before, also introduces a significant contribution. For more detail, see Kainulainen et al. (2011); Kainulainen & Tan (2013).

The density-separation relation (Fig. 2.10) shows a clear decrease of the mean densities for larger separations. We perform a linear least-square-fit in the log-log space to the data, which represents a power law of the form $\widetilde{n}(\mathrm{H}) = A \cdot \widetilde{s}^{\,p}$ as $log(\widetilde{n}(\mathrm{H})) = p \cdot log(\widetilde{s}) + log(A)$. The resulting parameters are $p = -0.96 \pm 0.05$ and $log(A) = 3.22 \pm 0.02$, which is $A = 1669^{+91}_{-86}\,\mathrm{cm}^{-3}$. The fitted model is shown as a black line in figure 2.10.

A commonly used fragmentation model is the spherical Jeans' instability model (Jeans, 1902), where the separation is linked to the mean density $\overline{\rho}$ via the Jeans' length

$$l_J = c_s(\pi/(G\overline{\rho}))^{1/2}, \tag{2.11}$$

where c_s is the sound speed within the medium, and G the gravitational constant. We compute the prediction from this assuming a gas temperature of $T = 15$ K. At all scales, the observed mean separations are in agreement with the Jeans' scale within a factor of approximately three. However, for the smallest scales, $i = 2 - 4$, the measurements are systematically below the predicted relationship and for the largest scales, the measurements are systematically above (see the discussion about the slope of the relationship later in this section).

A shallower slope of the Jeans' fragmentation can be achieved by assuming a non-isothermal medium (e.g., Takahashi et al., 2013). The innermost dense ($\sim 10^4$ cm^{-3}) regions of the cloud are shielded from the interstellar radiation field and therefore, can reach temperatures down to 10 K. As the surrounding low-density gas ($\sim 10^2$ cm^{-3}) is exposed to the radiation, we assume a higher temperature of 20 K. This leads to a slope of about -1.7, which still does not solve the systematic deviations from the observation.

Another commonly used model describes the fragmentation of an infinitely long, self-gravitating cylinder (Chandrasekhar & Fermi, 1953; Inutsuka & Miyama, 1992). This model predicts the separation, λ, depending on the scale-height H =

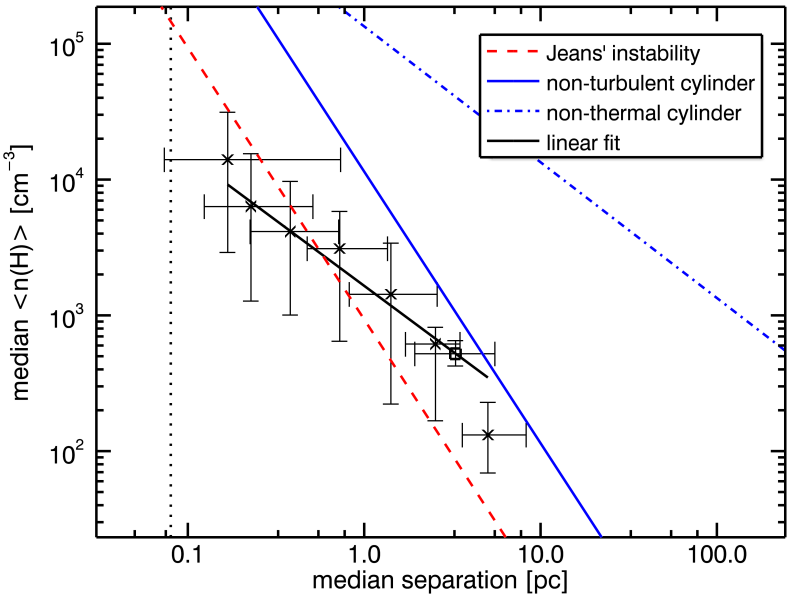

Figure 2.10: Median number density of structures at different spatial scales as a function of their median separation. Measurements of this study are marked with crosses. The square marks the data point derived from HNC observations of Jackson et al. (2010). The error bars show the 95% quantiles of both measurements. The blue lines indicate the scale dependency of an infinitely long cylinder in the non-turbulent case (solid), and non-thermal case (dash-dotted), and the dashed red line indicates the scale dependency of Jeans' fragmentation. The black line shows a power-law fit to the data.

$\sigma_{\rm v}(4\pi G\rho_c)^{-1/2}$, where ρ_c is the central density of a filament in virial equilibrium, $\sigma_{\rm v}$ the velocity dispersion of the medium, and G the gravitational constant. In the case of a non-turbulent medium, the velocity dispersion $\sigma_{\rm v}$ is given by the sound speed c_s within the medium (we assume $T = 15$ K to calculate the sound speed). In the regime of the filament radius, $R \gg H$, the separation is given by $\lambda = 22\ H$. If we assume a central density at the largest scale of $n_c(H) \approx 10^3$ cm^{-3}, then we derive a scale-hight of $H \approx 0.15$ pc. This is smaller than the typical radius of Nessie, $R \approx 1.5$ pc (see Section 2.4.2). Therefore, the separation is predicted to be

$$\lambda = 22 \cdot c_s(4\pi G\rho_c)^{-1/2}, \tag{2.12}$$

which is shown in Fig. 2.10 and is in agreement with the measurements within a factor of approximately three for scales larger than $i = 5$, but systematically above the measured densities. However, the model predicts central densities while we derived mean densities, and therefore, the model predicts an upper limit of the mean densities.

The above models describe fragmentation in non-turbulent medium. However, observations show that high-line-mass filaments have a non-thermal line width (Jackson

et al., 2010; Kainulainen et al., 2013), which is higher than the sound speed c_s in the non-turbulent case. Larson (1981) found a relation between the size of a molecular cloud and its observed line width. Such a line width-size relation might also apply to the structures observed here, and therefore we adopted a typical relation of $\sigma_{\rm v} = 0.72\ {\rm km\,s^{-1}} \cdot (\lambda/1\ {\rm pc})^{0.5}$ (Solomon et al., 1987; Heyer & Brunt, 2004; Pillai et al., 2006; Shetty et al., 2012; Colombo et al., 2015), where the line width $\sigma_{\rm v}$ depends on the observed size scale λ. The non-thermal line width exceeds non-turbulent motion, given by the sound speed c_s, at large scales. But the line-width-size relation can also be partially explained by the non-isothermal behavior of the gas.

$$\lambda^{0.5} = 22 \cdot 0.72\ {\rm km\,s^{-1}} (4\pi G \rho_c)^{-1/2}, \tag{2.13}$$

where ρ_c is the central density of a filament in virial equilibrium, and G the gravitational constant (Fig. 2.10).

Therefore, the relation between the central density and the separation is $\rho_c \propto \lambda^{-1}$, which is in agreement with the observed slope of $p = -0.96 \pm 0.05$. However, again we have to mention that the model predicts central densities while we derived mean densities. Additionally, without information about the kinematics of the cloud, we cannot constrain the scaling velocity of the line-width-size relation.

Table 2.1: Results of the fragmentation analysis.

Scale i	Scale [pc]	$N_{\rm strc}$	$\sum(M_{\rm strc})$ [10^3 M$_\odot$]	$\overline{M}_{\rm strc}$ [M$_\odot$]	$\widetilde{n}$(H)^a [10^3 cm^{-3}]	$\sigma(\widetilde{n}({\rm H}))$ [10^3 cm^{-3}]	$\widetilde{s}^b$ [pc]	$\sigma(\widetilde{s})$ [pc]	$\lambda_{\rm J}$ [pc]
>8	>5.2	1	34.5						
8	5.2	11	4.0	373	0.13	0.04	5.0	0.8	2.7
7	2.6	31	3.2	108	0.61	0.05	2.5	0.2	1.2
6	1.3	72	2.4	33.2	1.4	0.12	1.4	0.1	0.81
5	0.65	242	2.0	8.28	3.1	0.12	0.73	0.02	0.55
4	0.33	903	1.9	2.06	4.1	0.07	0.38	0.004	0.48
3	0.16	1751	1.2	0.66	6.3	0.08	0.23	0.002	0.38
2	0.08	523	0.20	0.40	14.2	0.47	0.17	0.004	0.26

Notes. $^{(a)}$ Median of the mean density of the identified structures. $^{(b)}$ Median of the separation between identified structures

2.4.4 Comparison with ATLASGAL

We briefly describe how the parsec-scale structures identified in Nessie from ATLASGAL data (resolution of 18″, Schuller et al., 2009) break down into substructures when extinction data offer about ten times higher resolution. For this, we considered the 16 sources from the ATLASGAL GCSC catalog (Csengeri et al., 2014) that are likely embedded in the cloud. We calculated the number of structures within the FWHM ellipse of the ATLASGAL sources at the two smallest scales ($i = 2, 3$) of the extinction map (see Fig. 2.11). We also estimated the mass of the ATLASGAL clumps by adopting Eq.

(2.2) and assuming a dust temperature of $T_{\rm d} \approx 15$ K. These masses are then compared to the total mass of the small-scale structures. The resulting ratios are shown in Table 2.2.

In particular, we found that, on average, the number of small-scale structures within the half power ellipse of the clump is $\overline{N}_{\rm strc,2} = 2.9$ and $\overline{N}_{\rm strc,3} = 2.8$. These contain 2% and 6% of the mass of the ATLASGAL clump. The half power ellipses of the clumps and the $i = 2$ structures identified within the clumps are shown in Fig. A.6 overlaid on the extinction map. While half of the ATLASGAL clumps are clearly associated with high-extinction peaks, the four most massive ones (> 500 M$_\odot$) in particular contain no or only low-extinction peaks. This is dominantly because of the caveats of the extinction mapping technique. The massive clumps commonly exhibit MIR emission of polycyclic aromatic hydrocarbons (PAHs) in the 8 μm band (Benjamin et al., 2003); this interferes with the extinction mapping procedure. Also bright foreground stars cause a lack of MIR extinction and influence our results. In total, this likely leads to an underestimated number of substructures per clump and to underestimation of some of their masses. This also shows that our method is excellent for identifying the youngest and densest regions, but it starts to fail as soon as star formation progresses and the regions show strong MIR emission.

Table 2.2: ATLASGAL GCSC clumps (Csengeri et al., 2014) likely embedded in the Nessie cloud.

Name	Size ["]	PA [°]	$M_{\rm clump}$ [M$_\odot$]	$N_{\rm strc,\ 2}$	$M_{\rm strc,\ 2}$ [M$_\odot$]	$\frac{M_{\rm strc,\ 2}}{M_{\rm clump}}$	$N_{\rm strc,\ 3}$	$M_{\rm strc,\ 3}$ [M$_\odot$]	$\frac{M_{\rm strc,\ 3}}{M_{\rm clump}}$
G338.9380-0.4231:	46 x 20	-12	221	4	3.15	0.014	4	12.33	0.056
G338.9362-0.4808:	28 x 22	52	197	2	1.36	0.007	1	4.69	0.024
G338.9371-0.4919:	41 x 34	134	1094	3	3.27	0.003	2	10.77	0.010
G338.9275-0.5018:	39 x 26	102	523	0	0.00	0.000	3	7.77	0.015
G338.8688-0.4796:	32 x 23	71	248	5	4.34	0.018	1	15.63	0.063
G338.7790-0.4591:	39 x 23	-24	176	4	3.97	0.022	4	15.95	0.090
G338.7314-0.4691:	32 x 19	90	116	3	4.76	0.041	3	13.14	0.114
G338.5519-0.4190:	27 x 24	71	134	2	2.57	0.019	4	7.65	0.057
G338.4236-0.4101:	28 x 26	111	292	0	0.00	0.000	2	2.20	0.008
G338.3937-0.4053:	42 x 31	72	632	2	2.22	0.004	3	10.43	0.016
G338.3923-0.3972:	34 x 19	16	124	2	1.75	0.014	3	9.91	0.080
G338.3271-0.4096:	36 x 27	-20	534	4	3.72	0.007	3	11.02	0.021
G338.1991-0.4642:	27 x 25	36	181	2	2.61	0.014	3	10.09	0.056
G338.1122-0.4632:	41 x 25	62	202	6	8.27	0.041	5	20.46	0.101
G338.0892-0.4474:	30 x 25	65	147	3	6.57	0.045	1	16.08	0.109
G338.3048-0.5223:	47 x 22	95	216	4	4.21	0.019	3	15.57	0.072
mean:			315	2.88	3.30	0.017	2.81	11.48	0.056
stddev:			261	1.63	2.16	0.014	1.17	4.66	0.037

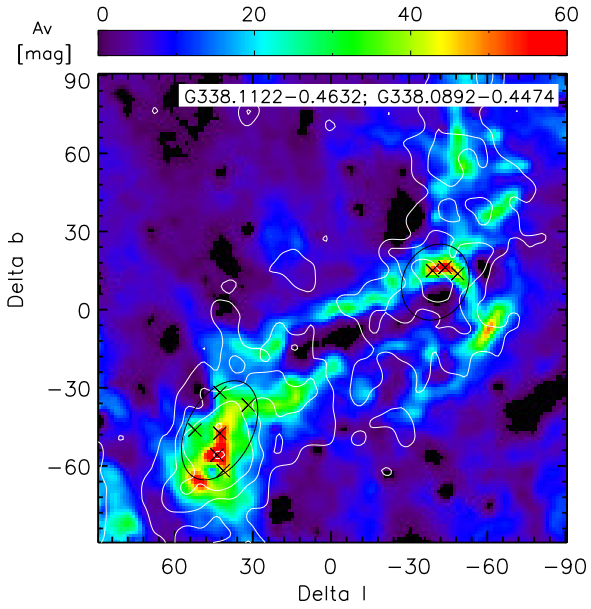

Figure 2.11: Combined NIR and MIR extinction map ($l = 338.10°, b = -0.45°$) overlaid with the half power contour of two ATLASGAL GCSC sources (black ellipses) and their covered sources identified with clumpfind-2D from the scale 2 map. The white lines show the contours of the ATLASGAL emission.

2.5 Discussion

2.5.1 Scale-dependent fragmentation of Nessie

In the following, we discuss the scale-dependent fragmentation of Nessie (Fig. 2.10) in the context of the analytic gravitational fragmentation models. We showed that the upper limit of the average line-mass of Nessie is $(M/l) = 627\ \mathrm{M_\odot\,pc^{-1}}$. For a thermally supported filament at a temperature of $T = 15$ K, the critical line-mass is $(M/l)_{\mathrm{crit}} = 20\ \mathrm{M_\odot\,pc^{-1}}$. Thus, the filament is clearly thermally supercritical. There are no analytic theories that would self-consistently explore the evolution of such highly thermally super-critical filaments.

In the absence of directly applicable models, a common approach in the recent literature is to assume that the non-thermal motions provide a straightforward, idealized supporting force for the filament, increasing its critical line-mass (e.g., Jackson et al., 2010; Hernandez et al., 2012; Busquet et al., 2013; Beuther et al., 2015). This commonly leads to a conclusion that the line-masses of high-line-mass filaments are close to their critical line-masses. This is also true for Nessie. Jackson et al. (2010) showed that the non-thermal motions in Nessie increase the critical line mass to $(M/l)_{\mathrm{vir}} = 525\ \mathrm{M_\odot\,pc^{-1}}$, which is similar to our observed value.

Building on the above agreement, observations are commonly compared to the pre-

dictions of gravitational fragmentation models developed for near-equilibrium cylinders. These models typically proceed from a static initial configuration with a linear perturbation analysis. In short, such models predict a periodic fragmentation pattern with a specific wavelength, that is, the fragmentation pattern predicted by the models is not scale-dependent. However, the fragmentation wavelength depends on the density of the filaments as described by Eqs. 2.13, 2.12, and 2.11; filaments with different densities have different fragmentation wavelengths. This should be kept in mind when interpreting the relationship between the data and models presented in Fig. 2.10.

In this context, the observed slope of the mean density-separation relationship in Nessie is in agreement with that of a non-thermal, self-gravitating cylinder that has a Larson-like line-width-size relation ($\sigma_v \propto \lambda^{0.5}$, Larson, 1981; Solomon et al., 1987; Heyer & Brunt, 2004; Shetty et al., 2012; Colombo et al., 2015). As the cloud shows non-thermal velocity dispersions (Jackson et al., 2010), this relation could be a result of turbulent motions within the cloud, but also systematic motions, such as collapse, could affect the line width. The observed median nearest-neighbor separations of the fragments are within a factor of two of the predictions of the isothermal and non-isothermal Jeans' fragmentation (Jeans, 1902). However, the slope is significantly steeper than the observed one. Additionally, on the large scales, the separations are also in agreement with the fragmentation model of a non-turbulent, self gravitating, infinitely long cylinder Chandrasekhar & Fermi (1953); Inutsuka & Miyama (1992), but again the slope of the model is significantly steeper than observed. We note that the cylindrical models predict central densities, which can only be seen as upper limits for the derived mean densities.

Previously, a change of fragmentation mode between large and small scales has been seen at the size-scale of $\sim$ 0.5pc, for example, in the studies of the young high-mass cloud G11.11-0.12 (Kainulainen et al., 2013), the Taurus cloud (Hacar et al., 2013), and the integral-shaped filament in Orion (Teixeira et al., 2016; Kainulainen et al., 2017). While we do not detect one in Nessie, the data are in agreement with the presence of such a feature, that is, we cannot rule it out (c.f., Fig. 2.10). One possible explanation for the change of fragmentation modes could be changing influence of the environment (Pon et al., 2011). While on large scales, fragmentation is driven by the characteristics of the cylindrical, filamentary structure, the smaller scales approach a more spherical shape, which is independent of larger scales. Also, recent numerical simulations have explored possibilities to explain scale-dependent fragmentation through dynamical processes (e.g., Clarke et al., 2017; Gritschneder et al., 2017).

2.5.2 Star formation potential[4]

Ultimately, one would like to link the fragmentation in Nessie to star formation. To take the first step towards this, we estimated the young stellar object (YSO) content of Nessie using publicly available multi-band photometric catalogs. The detailed methods used to identify the YSOs and estimate the SFR are explained in Zhang et al. (2018).

[4]The identification of YSOs and the calculation of the resulting star formation rate was performed by a co-author.

Here we give a short description of the method.

For the YSO selection, we used NIR data (we did the PSF photometry on VVV images, VISTA Variables in the Via Lactea, Saito et al., 2012), *S*pitzer GLIMPSE (Galactic Legacy Mid-Plane Survey Extraordinaire, Benjamin et al., 2003; Churchwell et al., 2009) and MIPSGAL (Multiband Imaging Photometer Galactic Plane Survey, Carey et al., 2009; Gutermuth & Heyer, 2015) archival catalogs, the AllWISE catalog (Wide-field Infrared Survey Explorer, Wright et al., 2010), the Herschel Hi-GAL catalog (Herschel infrared Galactic Plane Survey, Molinari et al., 2010, 2016), the Red MSX source catalog (Midcourse Space Experiment, Lumsden et al., 2013, used to include massive protostars), and the methods from Gutermuth et al. (2009); Koenig & Leisawitz (2014); Saral et al. (2015); Robitaille et al. (2008); Veneziani et al. (2013). Our YSO selection scheme uses the SEDs of sources from 1 to 500 μm and can efficiently mitigate the effects of contamination. In Nessie, we finally obtain 298 sources with the excessive IR emission, of which 35 are classified as AGB candidates using the multi-color criteria.

Considering the distance of Nessie, it is necessary to correct the flux densities of the YSO candidates for extinction. We use the method suggested by Fang et al. (2013); Zhang et al. (2015) to estimate the foreground extinction towards each YSO candidate and de-redden their photometry. Here we also give a short description of this method.

1 For the sources with J, H, K_S detections, the extinction is obtained by employing the JHK$_S$ color-color diagram. Figure 2.12 shows the J-H versus H-K$_S$ color-color diagram of the YSO candidates in Nessie. Given the different origins of intrinsic colors of YSO candidates, the color-color diagram is divided into three subregions. In region 1, the intrinsic color of $[J\text{-}H]_0$ is simply assumed to be 0.6; in region 2, the intrinsic color of a YSO is obtained from the intersection between the reddening vector and the locus of main sequence stars (Bessell & Brett, 1988); and in region 3, the intrinsic color is derived from where the reddening vector and the classical T Tauri star (CTTS) locus (Meyer et al., 1997) intersect. The extinction values of YSO candidates are then estimated from observed and intrinsic colors with the extinction law of Xue et al. (2016).

2 For other sources (outside these three regions or without detections in JHK$_S$ bands), their extinction is estimated with the median extinction values of surrounding Class II sources that have extinction measurements in step 1.

Using the de-reddened SEDs, we re-classify the YSO candidates into Class I, Flat, and Class II sources based on their spectral indices and bolometric temperatures (Greene et al., 1994; Chen et al., 1995). Figure 2.12 shows the $K_S - [8.0]$ versus J-H color-color diagrams before and after de-reddening for Class I+Flat and Class II sources in Nessie.

Although we have removed some contamination during the YSO selection process, our YSO candidates in Nessie are still contaminated by the foreground and background sources.

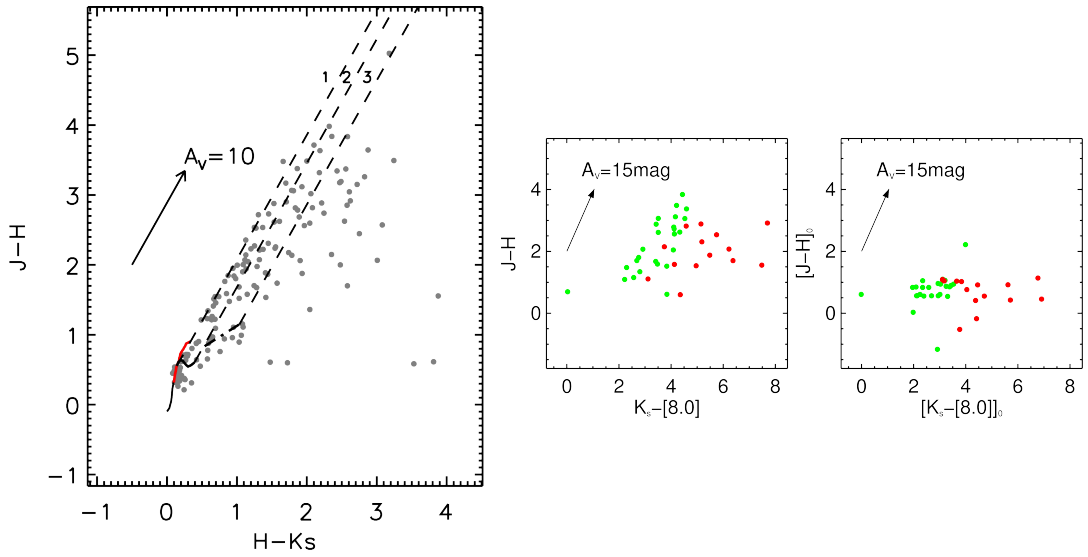

Figure 2.12: **Left:** The H-K_S vs. J-H color–color diagram for the YSO candidates in Nessie. The solid curves show the intrinsic colors for the main sequence stars (black) and giants (red; Bessell & Brett, 1988), and the dash–dotted line is the locus of T Tauri stars from Meyer et al. (1997). The dashed lines show the reddening direction, and the arrow shows the reddening vector. The extinction law we adopted is from Xue et al. (2016). We note that the dashed lines separate the diagram into three regions marked with numbers 1, 2, and 3 in the figure. We use different methods to estimate the extinction of YSO candidates in different regions (see the text for details). **Right:** The observed (*left*) and de-reddened (*right*) $K_S - [8.0]$ vs. J-H color-color diagrams for Class I+Flat (red) and Class II (green) sources in Nessie. The black arrows show the extinction vectors.

The foreground contamination mainly includes the foreground AGBs and the foreground YSOs which are associated with the molecular clouds that are located between us and Nessie. We use the A_V values of YSOs obtained previously and the 3D extinction map (Marshall et al., 2006) to isolate the foreground contamination. Based on the distance of Nessie, we can estimate the foreground extinction in different lines of sight towards Nessie with the 3D extinction map. If the extinction value of a YSO is lower than the corresponding foreground extinction of Nessie, this YSO would have a high probability of being a foreground contamination. We checked the YSOs in Nessie and marked the possible foreground contamination using this method. The fraction of foreground contamination in Nessie is 10% in Class I+Flat sources and 9% in Class II sources.

Our YSOs are also contaminated by background sources, including extragalactic objects, background AGBs, and background YSOs which are associated with the molecular clouds that are located behind Nessie. We think that the extragalactic contamination is not important in our YSOs because we are observing through the Galactic plane. Many background AGBs have been removed using the multi-color criteria dur-

ing the YSO identification process. The residual contamination of background AGBs is estimated with the control fields. We select five nearby fields with weak CO emission as the control fields and apply the YSO selection scheme to all the control fields to select YSOs. Assuming that there is no YSOs in each control field, all selected 'YSOs' in the control fields are actually contamination by AGBs (if neglecting the extragalactic contamination). With an assumption of a uniform distribution for AGB stars, we can estimate the number of residual background AGBs in the Nessie using the mean value of the surface density of background AGBs in five control fields. Combining the numbers of background AGBs identified by color criteria and estimated using control fields, we found that the fraction of background contamination is 22% in Class I+Flat sources and 11% in Class II sources. We note that we did not try to eliminate the contamination from background YSOs because they are difficult to remove without the information of radial velocities of YSOs.

After removing the contamination, we obtain 51 Class I and flat spectrum objects and 137 Class II sources in Nessie. In order to calculate the SFR, we must estimate the total mass of YSOs in Nessie. In this work, we use different methods to estimate the total mass of Class I+Flat and Class II populations:

- We use the de-reddened photometry of Class II sources in Nessie to estimate the flux completeness. Figure 2.14 shows the K_S absolute magnitude histogram of Class II sources in Nessie. We simply adopt the peak position of histogram as the completeness of K_S band (~ 1 mag). Figure 2.13 shows the $M_{K_S} - M_*$ relation for Class II sources constructed from YSO models presented by Robitaille et al. (2006). Using this relation, we transfer the K_S band completeness to the mass completeness of $1.48 \pm 0.65\ M_\odot$. Assuming a universal IMF (Kroupa, 2001), we estimated the number of Class II sources to be 1282^{+1228}_{-614} and the total mass of Class II sources to be $698.4^{+711.8}_{-355.9}\,M_\odot$.

- For Class I+Flat sources, we used the observed luminosity functions constructed by Kryukova et al. (2012) as the template to estimate the total number of Class I+Flat sources. We calculate the bolometric luminosities of Class I+Flat sources using the trapezoid rule to integrate over the finitely sampled de-reddened SEDs (Dunham et al., 2008, 2015). Figure 2.14 shows the the de-reddened luminosity function of Class I+Flat sources in Nessie and the corresponding luminosity completeness, which is calculated with the method suggested by Kryukova et al. (2012), is also marked with the red line. As a comparison, we also plot the luminosity function of Class II sources in Nessie. Assuming a universal luminosity function, we estimate the total number of Class I+Flat sources in Nessie to be 185^{+52}_{-51}. Assuming the average mass of 0.5 solar mass for each Class I/Flat source, we estimated the total mass of Class I+Flat sources to be $92.7^{+25.8}_{-25.7}\,M_\odot$.

Adopting the lifetime of Class II sources, 2 Myr (Evans II et al., 2009), as the star formation time-scale, we obtain SFR $= 389^{+364}_{-182}\,M_\odot\,\mathrm{Myr}^{-1}$ for Nessie. The SFE within the star-forming time-scale is estimated by the total mass of YSOs, $M_{\rm YSOs}$, and the gas mass of Nessie, $M_{\rm Nessie}$, SFE $= M_{\rm YSOs}/(M_{\rm Nessie} + M_{\rm YSOs}) = 0.018^{+0.017}_{-0.008}$. The

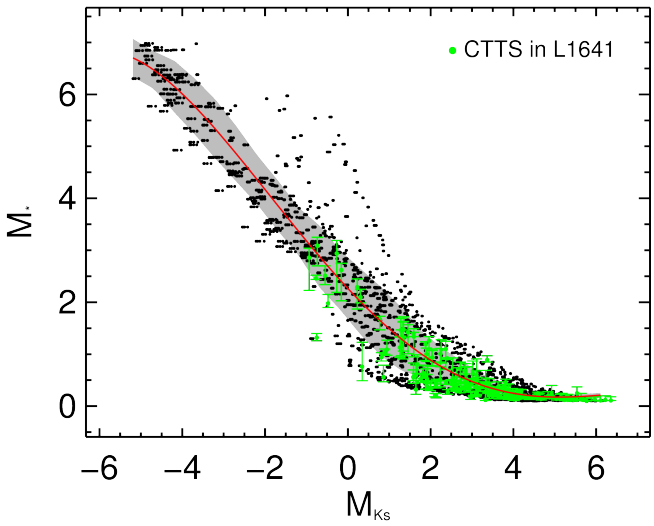

Figure 2.13: The relation between stellar mass and K_S absolute magnitude of Class II sources. The black dots represent the Robitaille et al. (2006) Stage 2 models with $0.001 < M_{\rm disk}/M_* < 0.01$, $0.08 < M_* < 7\,M_\odot$, and $30° <$ inclination angle $< 60°$. The red curve shows the robust polynomial fitting while the gray region shows the 1σ uncertainty of the fitting. The CTTS in L1641 from Fang et al. (2013) are marked with green filled circles. Most of CTTS are located in the gray region, which confirms that this $M_{K_S} - M_*$ relation for Class II sources is consistent with the observational results.

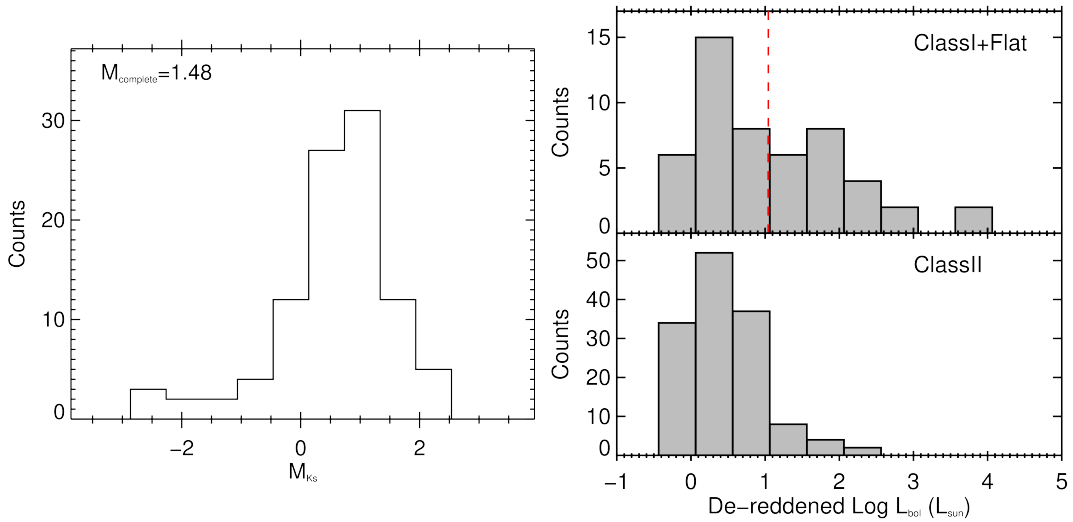

Figure 2.14: **Left:** K_S absolute magnitude (M_{K_S}) histogram of Class II sources in Nessie. **Right:** De-reddened luminosity functions of Class I+Flat (top panel) and Class II (bottom panel) sources in Nessie. The red vertical line shows the de-reddened luminosity completeness.

uncertainty is mainly from the uncertainty of transferring K_s magnitudes to stellar masses and the small number of observed Class I and Class II sources. To place these

values in context, the SFR of Nessie is comparable to those of the most active nearby star forming regions like Perseus (150 $M_\odot\,\mathrm{Myr}^{-1}$), Orion A (715 $M_\odot\,\mathrm{Myr}^{-1}$) and Orion B (159 $M_\odot\,\mathrm{Myr}^{-1}$; all values from Lada et al., 2010).

It is immediately interesting to compare this direct SFR estimate to other measures commonly linked with the star formation potential of molecular clouds. One such measure is the mass of dense gas in the cloud (e.g., Kainulainen et al., 2009; Lada et al., 2010). Specifically, Lada et al. (2010) found that in the Solar Neighborhood clouds (distance $\lesssim 500$ pc), SFRs correlate best with the mass above a column density threshold of $A_V \approx 7.3$ mag. Adopting this threshold results in the dense gas mass of $M_{\mathrm{dg}} = 8.7 \cdot 10^3$ $M_\odot$ in Nessie. Following the prescription of Lada et al. (2010) for the Solar Neighborhood clouds, the SFR of $4.6 \cdot 10^{-8}$ $\mathrm{yr}^{-1} \cdot M_{\mathrm{dg}} = 400$ $M_\odot\,\mathrm{Myr}^{-1}$ follows. This is in agreement with the SFR derived from the YSOs; in Nessie the mass of dense gas above $A_V \approx 7.3$ mag is a reasonable predictor of the SFR.

Yet another measure commonly connected with SFR is the dense core population of the molecular clouds (e.g., Motte et al., 1998; Alves et al., 2007; Marsh et al., 2016). To analyze this population in Nessie, we can take advantage of the high spatial resolution of our column density map: we can directly count the cores that might form stars or multiple stellar systems and estimate their mass. The mass enclosed in the dense structures smaller than ~ 0.1 pc is likely to take part in star formation processes. Therefore, the number of structures at the smallest scale of the wavelet-filtered map ($i = 2, \sim 0.08$pc) provides a first-order estimate for the number of stars forming in the cloud in the near future. To account for possible accretion processes during the collapse of a core, we assume that the gas at the scales $i = 2$ and $i = 3$ (size $<$ 0.16 pc) can participate in the collapse. This will then give an upper limit for the mass available for star formation. The mass of stars formed by these cores is then estimated by assuming an SFE of 30% (e.g., Alves et al., 2007; Rathborne et al., 2009; André et al., 2010). This results in the stellar mass of $M_{i=2,3} = 409$ $M_\odot$. Adopting again the star formation time of $t_{\mathrm{SF}} \approx 2$ Myr leads to a SFR of $M_*/t_{\mathrm{SF}} = 205$ $M_\odot\,\mathrm{Myr}^{-1}$ for the Nessie cloud. This estimate is within a factor of two of the values derived previously. We can also simply use the number of detected cores to gain a crude estimate of the star formation potential. If we assume that each structure at scale $i = 2$ will form at least one star, Nessie will form 523 stars. This is within a factor of two of the actual number of (completeness corrected) Class I and II sources. If we further divide the total mass in the cores in Nessie by 523, the predicted average mass of a star of 0.78 $M_\odot$ follows; this is relatively close to the mean stellar mass of 0.5 $M_\odot$ of the initial mass function (e.g., Kroupa, 2002). Altogether, the above considerations suggest that the dense core population identified from Nessie using the approach of this paper is a reasonable proxy of Nessie's star formation potential.

2.6 Conclusions

We analyzed the column density structure of the (projected) 67 pc long filamentary Nessie cloud using a combined NIR and MIR extinction-mapping method on data of

the VVV survey and 8 μm *Spitzer*/GLIMPSE images. Our results are as follows:

1. We derived a high-resolution (~ 0.03 pc), high dynamic range ($N(H_2) = 3$ – $100 \cdot 10^{21}$ cm^{-2}) column density map for Nessie and estimated the distance towards it to be $d = 3.5$ kpc based on NIR source-counts. The mass of Nessie is $4.2 \cdot 10^4$ M$_\odot$, considering regions above $N(H_2) \gtrsim 3 \cdot 10^{21}$ cm^{-2}. This leads to a mean line-mass of about 627 M$_\odot$ pc^{-1}.

2. We analyzed the fragmentation of the cloud across a wide range of scales in the range 0.1 – 10 pc and detected fragmentation at all scales. We characterize the fragments and find that their masses decrease and densities increase as a function of size-scale. At the smallest scale, the typical masses of the fragments are 0.4 M$_\odot$ and mean densities are $\sim 10^4$. The mean densities of the fragments decrease with their nearest-neighbor separations, following approximately a power-law with an exponent of -0.96 ± 0.05. The previous determination of the 4 pc fragmentation length by Jackson et al. (2010) is in agreement with this relationship, however, our data show that determining the fragmentation length at any one particular scale does not capture the full, scale-dependent picture of fragmentation in Nessie.

3. In the context of analytic gravitational fragmentation models, the observed nearest-neighbor separations are within a factor of two of the Jeans' length at all size-scales. However, the slope of the observed mean density – separation relationship is significantly shallower than the scale-dependency of the Jeans' length. The observed relationship is in agreement with a gravitationally fragmenting near-equilibrium cylinder that is supported by non-thermal motions that exhibits a Larson-like velocity-size scaling, that is, a power-law with an exponent of 0.5. This scaling could result, for example, from turbulent motions in the cloud, because the cloud shows clearly non-thermal velocity dispersions (Jackson et al., 2010).

4. We estimated the SFR of Nessie to be 389 M$_\odot$ Myr^{-1} based on the number of identified YSOs in the cloud. An estimate based on the number of $\sim$ 0.1 pc-scale column density "cores" yields 205 M$_\odot$ Myr^{-1}. We also estimate the SFR based on the total amount of dense gas ($A_V > 7.3$ mag; Lada et al. 2012) in the cloud, resulting in 400 M$_\odot$ Myr^{-1}. These results suggest that both the number of dense cores and the amount of dense gas above $A_V > 7.3$ mag are relatively good proxies of the star-forming content of Nessie. We further derive the SFE of 0.018 for Nessie. These numbers indicate that the star-forming content of Nessie is similar to the Solar neighborhood giant molecular clouds like Orion A.

5. The ATLASGAL clumps identified in Nessie typically harbor two to three small-scale structures (< 0.16 pc). These structures contain about 7 % of the mass of the parental clump. However, this is a lower limit as the extinction mapping is susceptible for incompleteness arising from MIR bright objects, such as foreground stars, and warm/hot gas.

We showed that the filamentary Nessie cloud has scale-dependent fragmentation characteristics. These characteristics are in agreement with some of the predictions of gravitational fragmentation models. However, self-consistent scale-dependent fragmentation models are needed to gain understanding of the structure and evolution of filamentary clouds.

Acknowledgments

We thank the referee for constructive comments. M. M. is supported for this research through a stipend from the International Max Planck Research School (IMPRS) for Astronomy and Astrophysics at the Universities of Bonn and Cologne. The work of J. K. was supported by the Deutsche Forschungsgemeinschaft priority program 1573 ("Physics of the Interstellar Medium"). This project has received funding from the European Union's Horizon 2020 research and innovation program under grant agreement No 639459 (PROMISE). H. B. acknowledges support from the European Research Council under the Horizon 2020 Framework Program via the ERC Consolidator Grant CSF-648505. M. Z. acknowledges support from the National Natural Science Foundation of China (grants No. 11503086). This research has made use of the NASA/ IPAC Infrared Science Archive, which is operated by the Jet Propulsion Laboratory, California Institute of Technology, under contract with the National Aeronautics and Space Administration.
This work is based on observations made with ESO Telescopes at the La Silla Paranal Observatory under programme ID 179.B-2002. The ATLASGAL project is a collaboration between the Max-Planck-Gesellschaft, the European Southern Observatory (ESO) and the Universidad de Chile. It includes projects E-181.C-0885, E-078.F-9040(A), M-079.C-9501(A), M-081.C-9501(A) plus Chilean data.

Chapter 3

The extended Nessie filament

3.1 Introduction

After we showed that the classical Nessie filament is undergoing hierarchical fragmentation towards mainly low-mass star formation, we now want to investigate the large scale molecular structure of Nessie. The study of Goodman et al. (2014) investigated the possibility that Nessie is considerably more extended than previously shown by Jackson et al. (2010). The "extended" and "optimistic" Nessie filament have a length of approximately 200 pc and 500 pc, respectively, which is about 20 – 50 times longer than the average massive filament studied in Chapter 5. Goodman et al. (2014) showed a line connecting elongated mid-infrared extinction structures and line-of-sight velocity information from the HOPS survey (Purcell et al., 2012) towards single pointings within these structures. However, this is not enough to confirm the structure as continuous, for which a more dense coverage of spectroscopic tracers is needed. For the "classical" Nessie Jackson et al. (2010) showed that every position seen in HNC(1 – 0) has a velocity of -38 ± 3.4 km s^{-1}, and therefore, confirmed the classical Nessie to be continuous in position-position-velocity (ppv) space. This continuity in ppv space is not prove of cloud being a single physical object (Clarke et al., 2018), but it is a necessary condition. With the ^{13}CO(2 – 1) and C^{18}O(2 – 1) emission data of the SEDIGISM survey (Schuller et al., 2017) we are able to investigate the kinematics of the extended and optimistic Nessie and our final goal is to discuss whether these are also continuous structures in ppv space along its larger extent.

In addition, we also try to identify signatures that hint on the formation of this extremely long filament. In the recent years several such giant molecular filaments (GMFs) have been identified using different approaches (Ragan et al., 2014; Zucker et al., 2015; Wang et al., 2015, 2016; Abreu-Vicente et al., 2016). However, the processes leading to the formation and driving the evolution of GMFs are not understood. Because of the size of these structures the driving processes must come from Galactic scales. Indeed, high-resolution Galactic simulations of Smith et al. (2014) and Dobbs (2015) allowed the formation of structures similar to the observed GMFs.

Smith et al. (2014) find extremely long CO bright filaments within the spiral arms, which is in agreement with the description of the Nessie filament as "bone of the Galaxy" by Goodman et al. (2014). Additionally, long filaments are seen in the Galactic interarm regions, of which large parts are likely to be CO dark. This would suggest, that the found shorter CO bright filaments are parts of longer CO dark structures, that are sufficiently shielded from UV radiation. However, while this simulation includes the chemical evolution of the gas, it does not include self-gravity, stellar feedback, or

magnetic fields.

The simulation of Dobbs (2015) also include self-gravity and stellar feedback, but only simple H_2 and CO formation and the long filaments are analyzed in Duarte-Cabral & Dobbs (2016) and Duarte-Cabral & Dobbs (2017). They find long filamentary molecular structures exclusively in the inter-arm regions, while the spiral arms are populated with giant molecular clouds. Following two giant filaments over a time of 11 Myr, they suggest the following evolutionary path: gas clouds exiting the arm are stretched by galactic shear into GMFs, which are not gravitationally bound as a whole, but are pressure confined. However, dense parts within the GMFs can be locally gravitationally bound and form stars. The feedback of local star formation or differential forces over the filament can lead to separation or destruction of the GMFs. When the structures eventually reach the gravitational potential of the next spiral arm, they become more well defined and align with the arm, which should be the most prominent phase. This would explain the observations of GMFs being located around spiral arms. At last the gas of the GMFs will be reorganized into highly sub-structured giant molecular cloud complexes within the gaseous spiral arm.

This is the first analyses of the kinematics of the entire region. We will analyze the morphologies and properties of the extended Nessie filament using ^{13}CO(2 – 1) and C^{18}O(2 – 1) to test the two models. Therefore, we reprocess the SEDIGISM data in Chapter 3.2, then analyze the data and derive different gas properties (Chapter 3.3), show the results in Chapter 3.4, and discuss them in Chapter 3.5 before we draw a conclusion from this study.

3.2 Data

We make use of the ^{13}CO(2 – 1) and C^{18}O(2 – 1) SEDIGISM data introduced in Chapter 1.3. However, to increase the SNR of the data we smoothed the beam to 40″ (30″ originally), reaching an average 1σ noise level of 0.5 K km s^{-1}. This lower resolution limits the ability to resolve the small-scale ($>$ 0.6 pc) inner dense structure of the filament, but enables us to study the low column density gas surrounding the dense structure. This compliments our previous work on the small scale structure of extinction mapping with the classical Nessie. Additionally, we make use of the (high-mass) clump catalogs based on ATLASGAL dust emission (Contreras et al., 2013; Urquhart et al., 2014, 2018) and Herschel dust emission (Hi-GAL, Molinari et al., 2010; Elia et al., 2017), as well as the HII region catalog of Anderson et al. (2014).

3.3 Method

To identify the velocity range that corresponds to the Nessie filament we assume that the ^{13}CO(2 – 1) emission is optically thin and traces the kinematics of the gas, which is most likely true for the extended diffuse parts of the filament. We then average all ^{13}CO spectra of the extended Nessie area, which we take from the work of Goodman et al. (2014). Based on the resulting spectrum (Fig. 3.1) we identified a velocity

interval of $-45.0\ \mathrm{km\,s^{-1}}$ – $-30.0\ \mathrm{km\,s^{-1}}$, thus covering $\sim 15\ \mathrm{km\,s^{-1}}$, corresponding to the molecular emission of the extended Nessie. This interval is now the limit for the identification of the emission peak in every pixel. Here we use the same method as in Mattern et al. (2018), where we define the velocity range of the corresponding ^{13}CO emission as that between which the emission of from the brightest peak is above the 1σ noise level of this pixel. Furthermore, we only consider components with an SNR ≥ 5 in their integrated intensity. Based on these identified emission intervals we calculate the zeroth, first, and second order moment of the emission. The resulting moment maps (Fig. 3.2) are the basis for the following analysis.

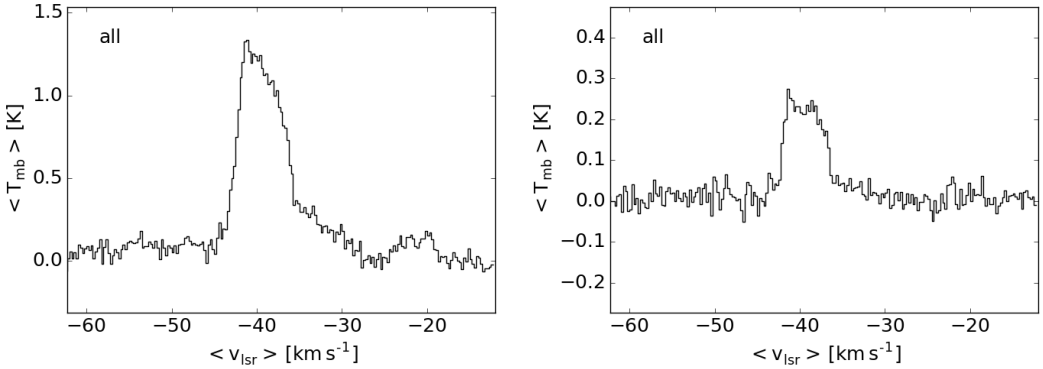

Figure 3.1: Average spectra of the ^{13}CO **(left)** and C^{18}O **(right)** emission over the extended Nessie.

To identify filaments and simplify their analysis it is useful to find the skeleton (connected lines tracing the highest intensity structures) or the spine (the longest path through the skeleton). Filament finding algorithms are commonly used to identify the skeleton, which is then truncated to the spine. Finding a spine through the whole proposed extended Nessie would be the clearest proof of a continuous structure. However, the high dynamic range of ^{13}CO intensities does not allow an automated filament finding. Therefore, we decided to identify the filament spine visually based on the ^{13}CO first and second order moment maps and the dust extinction map of the classical Nessie from (Mattern et al., 2018, Chapter 2). The resulting skeleton and spine are shown in Figs. 3.2 and 3.3.

3.3.1 The extended Nessie

To confirm the velocity coherence of the extended Nessie filament, we plot the previously derived integrated intensity, peak velocity and velocity dispersion along the spine of the filament (Fig. 3.4). Looking at the intensity cut along the spine, we find two areas where the integrated intensity per beam is close to the detection limit of SNR ≥ 5. One area is at the end of the extended filament towards higher Galactic longitudes, marked as a in Fig. 3.4. Here, we see the gas to be diffuse and less confined compared to the rest of the structure. However, despite the low intensity, this part shows to be consistent extension of the filament. The other area is located within the classical

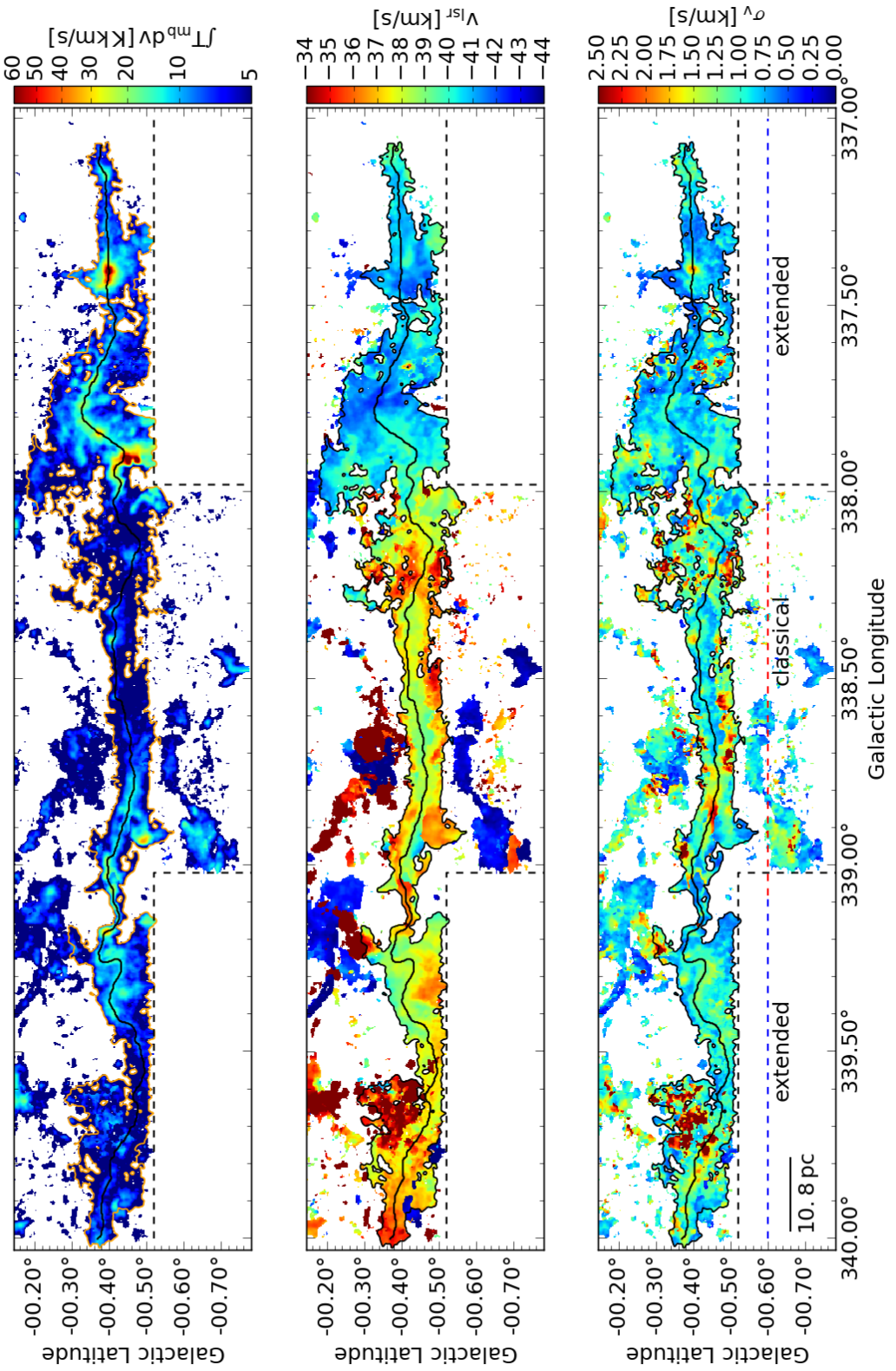

Figure 3.2: Moment maps of the extended Nessie filament derived from the ^{13}CO(2–1) SEDIGISM data. The contour indicates the outer limit of the filament, and the black line marks the spine of the filament.

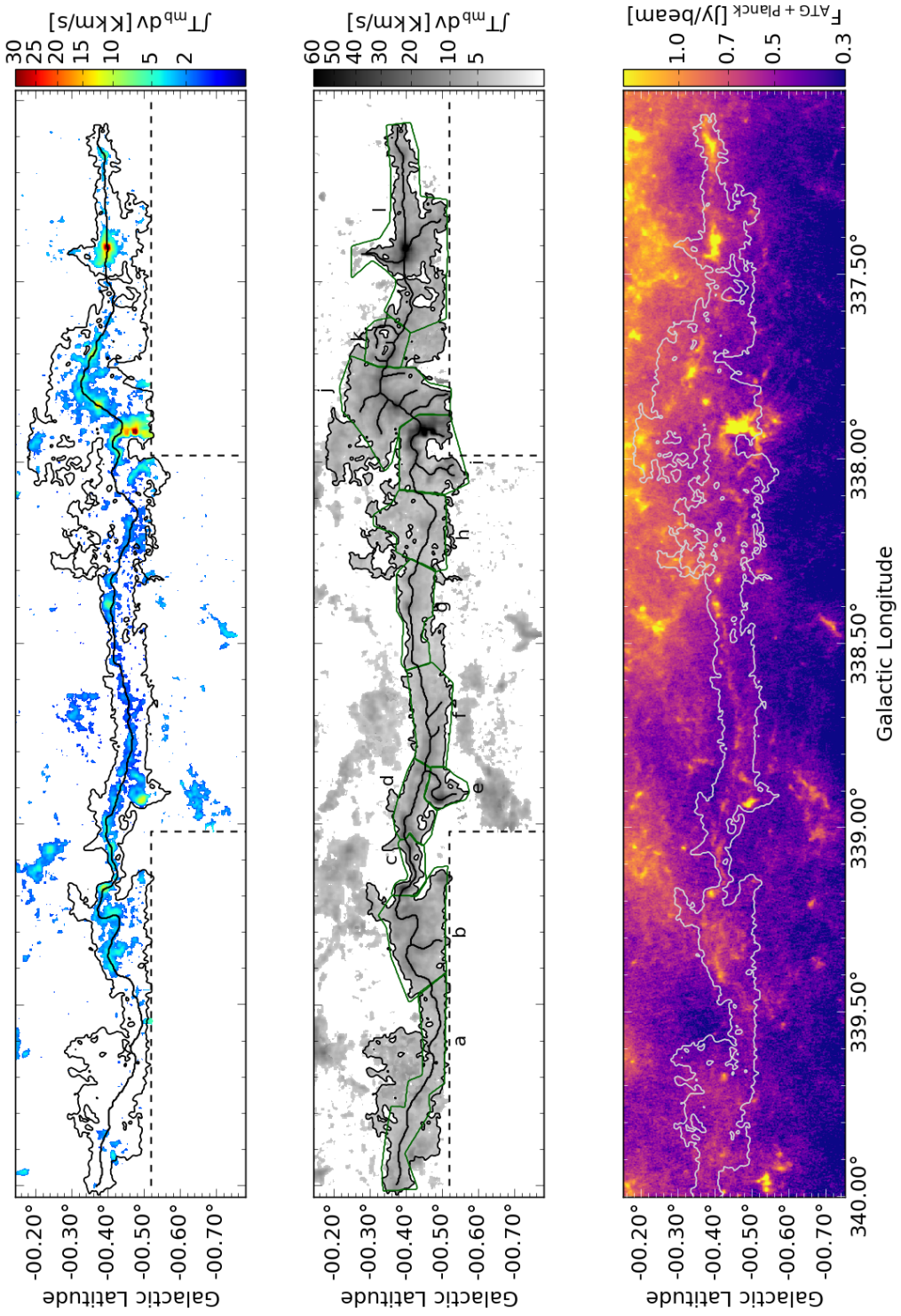

Figure 3.3: **Left:** Zeroth order moment map of the extended Nessie filaments derived from the $C^{18}O(2–1)$ SEDIGISM data. The contour indicates the outer limit of the filament, and the black line marks the spine of the filament. **Middle:** $^{13}CO(2–1)$ moment zero map of the extended Nessie overlaid with the skeleton and the outer limit of the filament (black contour). The green contours indicate the chosen sub-parts of Nessie named by letters from '*a*' to '*l*'. **Right:** ATLASGAL dust emission map of the extended Nessie filament with the outer contour of the integrated ^{13}CO emission.

Nessie between a Galactic longitude of 338.0° and 338.25° (i in Fig. 3.4). Here we know from the dust extinction data from Mattern et al. (2018) that the spine is narrow confined and therefore, we consider this part as well as continuous in intensity. The proximity to an expanded HII region suggest that the CO of this part is destroyed by UV radiation, but further investigation is needed to confirm this possibility.

Analyzing the peak velocities along the spine we find a continuous behavior, with only small local variations. In general, we find an increase of the peak velocities with Galactic longitude. To investigate this velocity gradient we compare the measurements to the line-of-sight velocities predicted by the Galactic rotation assuming the rotation curve of Brand & Blitz (1993). We calculate the derived the velocities for different distances from the Sun. In Fig. 3.4 the predicted velocities at 3.0 kpc, 3.1 kpc, and 3.2 kpc are indicated by the green, blue, and red lines. With this measurement we can give an estimate of the kinematic distance towards Nessie of $d = 3.1 \pm 0.1$ kpc, as it follows well the Galactic rotation curve.

In summary we see morphological changes along the filament, especially changes in intensity and radial extent, i.e. diffuse versus confined regions, suggesting a non-continuous structure. On the other hand, we find a continuous velocity structure with a large gradient following the Galactic rotation. Therefore, our findings support a picture where the extended Nessie is a continuous filamentary structure. In the following, we analyze its physical properties, like mass and length. To derive its mass we need to define an outer edge of the structure. Therefore, we use the contour of 5 $\mathrm{K\,km\,s^{-1}}$, which is about the set detection limit in the regions of the highest noise. Furthermore, we exclude structures with peak velocities outside the previously in the first order moment map identified range. The resulting limit is shown as black contour in Fig. 3.2.

To calculate the mass we use the ^{13}CO X-factor of $X_{^{13}\mathrm{CO}} = 1 \times 10^{21}$ $\mathrm{cm^{-2}\,(K\,km\,s^{-1})^{-1}}$ from Schuller et al. (2017) to derive the column densities of the structure, which was shown to be a valid estimate in Mattern et al. (2018) (Chapter 5). The mass is then derived by

$$M = \sum_x I_{^{13}\mathrm{CO}}(x) X_{^{13}\mathrm{CO}} A_x \mu m_\mathrm{p} \tag{3.1}$$

where M is the mass of the structure, $I_{^{13}\mathrm{CO}}(x)$ is the integrated ^{13}CO intensity at position x of the structure, A_x is the physical size of the pixel at position x, $\mu = 2.8$ is the mean molecular weight of the ISM (Kauffmann et al., 2008), and m_p the proton mass. For the extended Nessie filament we estimate a mass of $M_\mathrm{eN} = 1.89 \times 10^6$ $\mathrm{M_\odot}$.

Defining an accurate length of the filament is a not straight forward task. As a first approach the length can be defined as the extent of the spine, which would lead to an estimate of $l_\mathrm{spine} = 196.0$ pc for the extended Nessie. However, as shown before the morphology of the filament is not simply linear, but has branches, which contribute to the mass estimate. Therefore, the lengths of these branches needs to be taken into account as well. This leads to a total length over the skeleton of $l_\mathrm{skel} = 283.1$ pc, not accounting for a possible inclination angle. Also note, that these include only the

branches visually identified on the integrated ^{13}CO map, but there is the possibility of more branches, which are spatially not resolved.

Using the derived mass and the length over the skeleton we can derive the line-mass (mass per unit length) for the extended Nessie filament to be $m_{\mathrm{eN}} = 563\,\mathrm{M}_\odot\,\mathrm{pc}^{-1}$. This is similar to the measurements of the line-mass of the classical Nessie from (Mattern et al., 2018, Chapter 2, 555 $\mathrm{M}_\odot\,\mathrm{pc}^{-1}$ at 3.1 kpc). The derived properties are shown in Table 3.1.

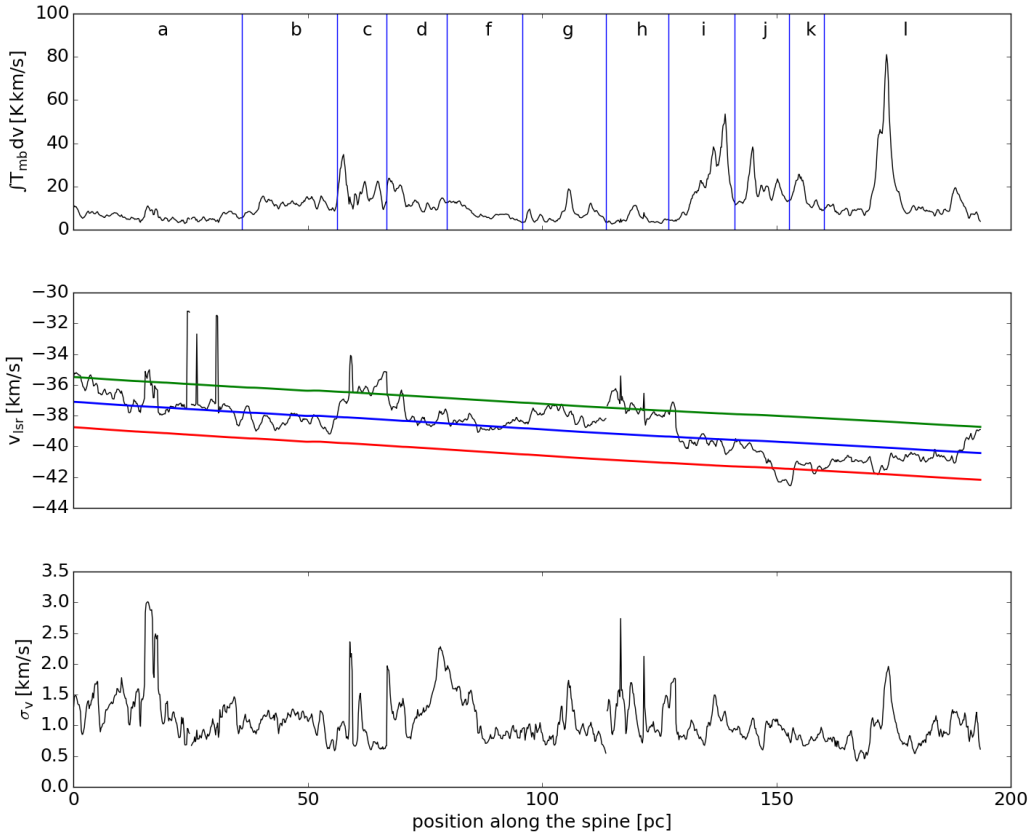

Figure 3.4: Integrated intensity (top), peak velocity (middle) and velocity dispersion (bottom) derived from the ^{13}CO(2–1) SEDIGISM data along the spine of the filament. The green, blue, and red lines plotted on top of the peak velocities indicate the predicted Galactic rotational velocities for distances from the sun of 3.0 kpc, 3.1 kpc, and 3.2 kpc, respectively.

3.3.2 Star formation within Nessie

In Mattern et al. (2018) the star formation rate of the classical Nessie filament was estimated to be about 371 $\mathrm{M}_\odot\,\mathrm{Myr}^{-1}$, which is comparable to those of the most active nearby star forming regions like Perseus and Orion. Also, it was shown that 16 high mass clumps (GCSC ATLASGAL clumps, Csengeri et al., 2014) are associated with the classical filament. We now want to follow up on the analysis of clumps associated

with the extended Nessie.

First, we identify the peaks in the integrated ^{13}CO and C^{18}O data, using a simple local maximum approach. In detail, we define a circular mask with diameter of twice the beamwidth, which we then apply to every pixel of the map. If the center of the mask is maximum of the masked area and exceeds a threshold of 10 K km s^{-1} for ^{13}CO and 3 K km s^{-1} for C^{18}O, then we mark this position as local peak. We find 102 ^{13}CO peaks and 81 C^{18}O peaks, of which 45 are associated within one beam. Almost all associated sources are located on the previously defined skeleton (Fig. 3.5). The differences for the other peaks arise most likely from the abundance difference of the two isotopes of about $n_{^{13}\mathrm{CO}}\,/n_{\mathrm{C}^{18}\mathrm{O}} = 8.7$ (Miettinen, 2012) and the therefore, different choice of identification thresholds. Also, because of the relatively low spatial resolution, elongated structures with one identified peak might contain a close series of clumps, that cannot be resolved spatially.

We know from Jackson et al. (2010); Goodman et al. (2014); Mattern et al. (2018) that the classical Nessie filament contains two expanding HII regions. Investigating the GLIMPSE 8 μm mid-infrared emission (Churchwell et al., 2009) in the area of the extended Nessie we find multiple bright round or shell-like regions, which typically indicate photodissociation regions, hence HII shells, around massive stars. Therefore, we overlay the HII shells from the catalog of Anderson et al. (2014) on the integrated ^{13}CO map. As the velocity information is only given for a few sources in this region, we discard only the sources with a deviating velocity and show the rest in Fig. 3.5. The HII regions of Anderson et al. (2014) are categorized in three groups, which are 'known', if a radio counterpart and a radio recombination line or Hα emission is detected, 'candidate', if only the counterpart is detected, and radio quiet, without a radio counterpart. We find 7 evolved shells coinciding with the ^{13}CO emission, of which 2 are the ones surrounding the classical Nessie (G337.957-00.474, G339.134-00.377). The other five are located at 337.404°; −0.404°, 337.428°; −0.401°, 337.684°; −0.343°, 337.843°; −0.372°, and 337.922°; −0.463°. Additionally, we find at least 8 radio quiet HII regions correlated with peaks identified on the CO maps, which are at a Galactic longitude of about 338.400°, 338.925°, 339.178°, 338.2°, 338.48°, and 4 in the dense region around a Galactic longitude of 337.4°. However, a clear association to Nessie would need additional velocity information.

HII regions indicate the latest phases of high-mass star formation. The earlier phases are embedded in dense clumps, which were identified based on ATLASGAL (Schuller et al., 2009) and Herschel Hi-GAL data (Molinari et al., 2010) and analyzed (Elia et al., 2017; Urquhart et al., 2018). These studies not only estimated the masses, luminosities, and distances, but also identified the evolutionary stages of the clumps. We now identify the clumps of both catalogs, that are likely to be associated with the extended Nessie filament. Therefore, we use the position and line-of-sight velocity (33 km s^{-1} $< v_{\mathrm{lsr}} <$ 45 km s^{-1}) for the ATLASGAL catalog, and the position and distance (2.9 kpc $< d <$ 3.3 kpc) for the Hi-GAL catalog, as the velocities are not given. This allows to identify 47 ATLASGAL clumps and 48 Hi-GAL clumps in the extended Nessie, which are shown in Fig. 3.5.

We find that several of these sources are associated with the previously identified

^{13}CO and C^{18}O peaks of the integrated intensity map. However, while we find counterparts for all except of two ATLASGAL clumps, there is a larger lack of counterparts for Hi-GAL sources. Inspection of ^{13}CO and C^{18}O maps around the sources without counterpart reveals that they are located at peaks where the molecular gas intensity does not exceed the threshold or in extended high intensity regions, where single peaks cannot be resolved. Furthermore, we find some of the evolved sources of the two catalogs also correlate with the location of radio quiet HII regions.

In general, we find clumps concentrating in distinct parts of the filament, and in these towards the skeleton of Nessie. Together with the differences seen in the intensity and peak velocity distributions, we decided to separate the filament into different parts. We then analyze these parts separately and investigate their individual correlations with the shown star formation tracers.

3.3.3 Different CO morphologies over the extended Nessie

The extended Nessie filament shows several morphological differences in CO gas which allows us to separate it into different parts, which are indicated in Fig. 3.3. The most obvious are three areas, where the spine is located around HII shells (parts *c*, *i*, *k*) with two of them enclosing the classical Nessie (*c*, *i*). In part *d* in the classical Nessie, we find a segment that shows a velocity gradient perpendicular to the elongation of the filament, which separates it from the rest. Next to it we find a side branch of the long filament (part *e*), that covers three ATLASGAL clumps, and therefore, shows active star formation. The rest of the classical Nessie we split in three parts: one the more extended part, which shows branches in the dust extinction data of (Chapter 2, part *f*), part *g* shows a single narrow filament without branches in the extinction data, but is barely resolved in the SEDIGISM ^{13}CO data, and part *h* is, as previously mentioned, barely detected in ^{13}CO. The extension towards lower galactic longitudes is separated in three parts, one of them the earlier mentioned region influenced by stellar feedback (*k*), which separates the others. Part *j* is the section with the largest radial extent in Nessie, which shows signs of fragmentation in CO. In part *l* we find a structure with medium radial extent and dominated by a central dense region, from which also two branches, one to each side, are identified. The higher longitude extension is more homogeneous, but the outer part seems to be only diffuse gas and is at the limit of the ^{13}CO sensitivity. Therefore, we also split this part. The more dense part *b* shows a more curved spine than in the rest of the filament.

We derive the mass, M, length over the skeleton, $l(d)$, covered area, A, and the average velocity dispersion, $\sigma_{\rm v}$ for each part separately. In order to compare their physical properties we then calculate the surface density, $\Sigma = M/A$, the observed, $m_{\rm obs} = M/l(d)$, and the non-thermal critical line-mass $m_{\rm nt} = 2\sigma_{\rm v}/G$. However, it needs to be mentioned that the skeleton of the structures is not necessarily complete and therefore, the observed line-mass would be overestimated, which might be the case specifically for regions *b*,*h*, and *j*, as they show a large radial extent of ^{13}CO emission. The results of these measurements are shown in Table 3.1.

Additionally, we measure the closest distance of each pixel to the spine of each

part. Therefore, we can show the distribution of intensity, peak velocity and velocity dispersion dependent on the radial distance. Here we choose to use negative distances for representing pixels with Galactic longitudes below the spine, except for part *k*. As the spine of part *k* describes a circle we choose the inner part to be at negative distances. We then use the radial intensity distribution to estimate the mean full width at half maximum (FWHM) of the spine after subtracting the low intensity envelope using a linear fit to the most outer values. The resulting FWHMs are presented in Table 3.1.

3.4 Results

3.4.1 Comparison of physical properties

After separating the extended filament in several parts based on observed morphological differences we now will analyze each part in more detail. In particular, we compare the morphology observed in ^{13}CO and C^{18}O with separately identified objects like high-mass clumps from the ATLASGAL catalog (Urquhart et al., 2018) and the HiGAL catalog (Elia et al., 2017), and HII regions from the catalog of Anderson et al. (2014), which is shown in Figs 3.5 and 3.6. Additionally, we show the resulting measurements of the parameters of each part and the whole structure in Table 3.1.

Table 3.1: Table of the derived physical properties for each part and the total extended Nessie.

Part	M	l	$l(d)$	$m_{\rm obs}$	$\sigma_{\rm v}$ [a]	$m_{\rm vir}$	$<\Sigma>$	FWHM	$N_{\rm ATG}$ [b]	$N_{\rm HG}$ [c]
	$M_\odot$	$'$	pc	$M_\odot$/pc	km/s	$M_\odot$/pc	$M_\odot$/pc^2	pc		
a	12960	38.54	34.8	372	1.18	647	114	2.09	0 (0)	3 (1)
b	19948	29.22	26.3	758	0.97	437	181	2.60	4 (2)	10 (3)
c	4930	11.39	10.3	479	0.86	344	243	0.90	3 (3)	0 (0)
d	8479	15.65	14.1	601	1.27	750	184	1.39	1 (1)	4 (2)
e	5267	10.73	9.7	543	0.94	411	221	1.07	3 (2)	1 (1)
f	9512	24.77	22.3	427	1.33	822	129	2.19	2 (1)	7 (5)
g	6721	19.85	17.9	375	0.99	456	109	1.69	4 (4)	0 (0)
h	7606	14.96	13.5	563	1.30	786	93	2.22	3 (3)	4 (4)
i	22825	30.90	27.9	818	1.08	542	277	1.22	9 (2)	6 (3)
j	26526	43.57	39.3	675	0.90	377	196	1.84	4 (4)	0 (0)
k	7235	21.42	19.3	375	0.89	368	195	0.90	3 (3)	0 (0)
l	32584	54.57	49.2	662	0.81	305	201	1.25	11 (9)	13 (9)
all	188980	313.99	283.1	668	1.10	563	158	1.61	47 (34)	48 (28)

Notes. [(a)] Average second order moment of all pixels within the area. [(b)] Number of ATLASGAL sources within the area, and on the skeleton in brackets. [(c)] Number of Hi-GAL sources within the area, and on the skeleton in brackets.

3.4.1.1 Part *a*

Part *a* shows a large extent of diffuse gas ($<\Sigma_{\rm a}>= 114\,M_\odot\,{\rm pc}^{-2}$, FWHM$_{\rm a}$ = 2.09 pc), where the integrated ^{13}CO intensities do not exceed 12 K km s^{-1}. The chosen mask of

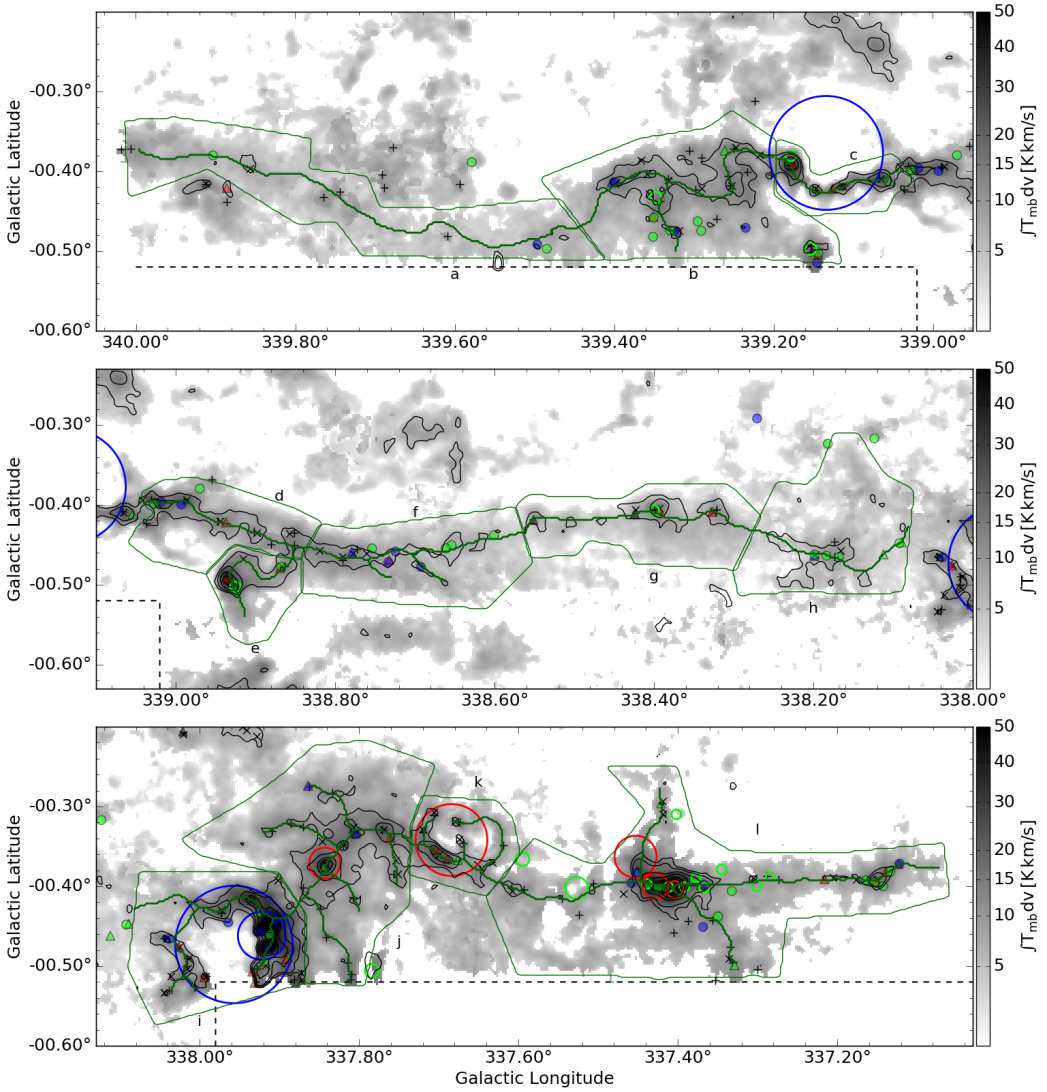

Figure 3.5: Integrated ^{13}CO intensity (zeroth order moment) maps overlaid with C^{18}O integrated intensity contours of 4, 7, 10, 15, 20 K km s^{-1}, and marks of ^{13}CO peaks (plus), C^{18}O peaks (x), ATLASGAL sources (triangle), Hi-GAL sources (filled circles), HII regions (rings) and the part limits (green contour).

this area avoids contamination from areas located around the Nessie structure, which show clearly different peak velocities. Therefore, the radial extent from -3 pc to 3 pc might be underestimated and therefore, also the mass ($M_{\rm a} \geq 12960$ M$_\odot$) and line-mass ($m_{\rm a} \geq 372$ M$_\odot$ pc^{-1}). In this area we find only three Hi-GAL clumps, which are not associated with any identified CO intensity peak. However, one ATLASGAL protostellar source (AGAL339.886-00.421) just outside the mask is associated with a ^{13}CO and C^{18}O peak and was observed to have the same peak velocity than the average of part *a*. In total, this indicates a low star formation activity.

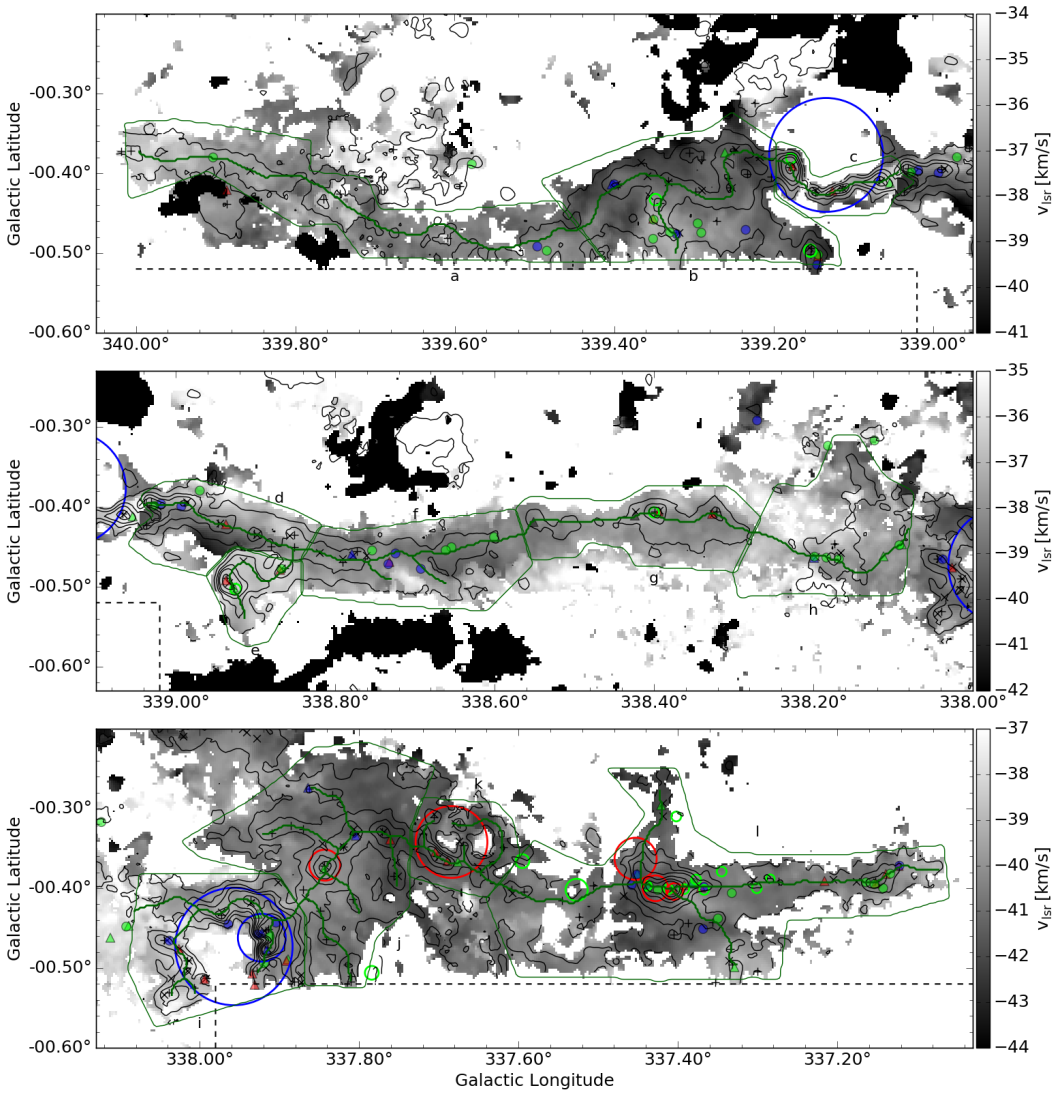

Figure 3.6: Peak velocity (first order moment) maps of ^{13}CO overlaid with ^{13}CO integrated intensity contours of 5, 10, 15, 20, 30, 40, 50K km s^{-1}, and marks of ^{13}CO peaks (plus), C^{18}O peaks (x), ATLASGAL sources (triangle), Hi-GAL sources (filled circles), HII regions (rings) and the part limits (green contour).

3.4.1.2 Part *b*

In part *b* the emission from part *a* continues coherently, but increases the intensity ($< \Sigma_b >= 181$ M$_\odot$ pc^{-2}) on the spine (FWHM$_b$ = 2.60 pc). Also, the spine of part *b* is more curved in the plane of the sky than the other parts of the Nessie spine, and it follows several peaks in the integrated intensity maps. We see four ATLASGAL clumps associated with CO peaks, where two are located on the skeleton. Further, three Hi-GAL sources are associated with the ATLASGAL clumps, three with other CO peaks and four do not have associations. Additionally, there are two compact HII regions

within part *b*, which both are aligned with bright CO emission, but only one has an ATLASGAL and Hi-GAL protostar association with a $40''$ (one beam) offset. The radial distribution of ^{13}CO intensities shows peaks at larger radii, which are also seen from the identified peaks on the CO maps and therefore, the assumed skeleton might not present the true morphology of the structure. Also the emission is truncated for Galactic latitudes below $-0.5°$ because of the edge of the observed data. Therefore, the mass of part *b* ($M_{\rm b} \geq 19948$ M$_\odot$) and the length over the skeleton ($l_{\rm b}(d) \geq 26.3$ pc) might be lower limits, leading to a line-mass of $m_{\rm b} \approx 756$ M$_\odot$ pc^{-1}. Furthermore, the distribution of the peak velocities indicates an average velocity gradient across the skeleton of about -0.2 km s^{-1} pc^{-1}.

3.4.1.3 Part *c*

For part *c* again we see a coherent transition from the previous part *b*. However, the radial extent is drastically reduced to a total width of about 2.5 pc with a FWHM$_{\rm c}$ = 0.90 pc and the CO intensities increase ($< \Sigma_{\rm c} >= 243$ M$_\odot$ pc^{-2}). This change is caused by the impact of an extended HII region (G339.134-00.377), which gives this part of the filament a compressed roundish shape. On the CO emission maps we could identify 4 peaks with three of them showing an ATLASGAL association (1 protostar, 2 YSOs) with slight offset to the peak location. Also one compact HII region is located at an $40''$ offset to one peak. With the higher intensities but lower radial extent we find a line-mass of $m_{\rm c} = 463$ M$_\odot$ pc^{-1} with a mass of $M_{\rm c} = 4906$ M$_\odot$ and a length of $l_{\rm c}(d) = 10.6$ pc. Towards part *d* we see a jump of about 4 km s^{-1} in the peak velocities for a small area. Such jumps are created because the used algorithm follows the highest intensity component within the given velocity range. However, as there is a coherent connection around this area, we interpret this area as line-of-sight contamination.

3.4.1.4 Part *d*

As stated before, the connection to part *c* shows some incoherent areas. While the change of peak velocity is more gradually in *d*, the integrated intensity shows a strong increase here. This indicates that the second bright velocity component merges with the one tracing the Nessie filament and cannot be resolved separately. In general, this part is again less confined (FWHM$_{\rm d} = 1.39$ pc) and again shows a radial velocity gradient, however, with about 1.2 km s^{-1} pc^{-1} it is steeper and orientated in opposite direction to part *b*. Within part d we find four Hi-GAL CO peak associations, one ATLASGAL CO association, and one more CO peak. Except for one Hi-GAL source, all sources are located on the center skeleton. We find a line-mass of $m_{\rm d} = 605$ M$_\odot$ pc^{-1} with a mass of $M_{\rm d} = 8596$ M$_\odot$ and a length of $l_{\rm d}(d) = 14.2$ pc.

3.4.1.5 Part *e*

Part *e* is only a side branch of the extended Nessie filament, but with a high surface density of $< \Sigma_{\rm e} >= 221\ M_\odot\, pc^{-2}$ and a confined spine with a FWHM$_{\rm e} = 1.07$. However, the line-mass $m_{\rm e} = 543$ M$_\odot$ pc^{-1} of this branch is in agreement the value of the

complete extended Nessie. This part shows a jump in peak velocity and intensity along one line towards the main spine, while there is a coherent connection along the skeleton. This part is dominated by one strong ^{13}CO emission peak, which is separated in two peaks in C^{18}O. Both C^{18}O peaks are associated with an ATLASGAL source, of which one is additionally associated with a compact HII region. Further, there is another less bright peak in both CO maps which is associated with an ATLASGAL and a Hi-GAL source. Part e also shows a especially flat distribution of peak intensities.

3.4.1.6 Part *f*

Now following again the spine of Nessie, we find that the spine is not the center of the radial extent of the emission (−4 pc to 2 pc), especially towards lower Galactic longitudes, with a width of $\mathrm{FWHM_f} = 2.19$ pc. Also, we identified two side branches towards lower Galactic latitudes, that branch off the spine in a similar angle. We identified four CO peaks, which are all located on the spine in the higher longitude half of the field. One peak is associated with an ATLASGAL source and one with a Hi-GAL source. Additionally, there are another six Hi-GAL and one ATLASGAL clump within the field, which have no CO peak association as the integrated intensity does not exceed the threshold. The average of radial distribution of the peak velocities shows a gradient of $-0.5\ \mathrm{km\,s^{-1}\,pc^{-1}}$ for the radii between −4 pc and −1 pc, is flat in the center (−1 pc to 1 pc), and increases with a rate of $2.0\ \mathrm{km\,s^{-1}\,pc^{-1}}$ towards the edge at 2 pc.

3.4.1.7 Part *g*

Part *g* shows a similar morphology as part f, but with a lower average intensity in both CO isotopes and the gas is more confined ($\mathrm{FWHM_g} = 1.69$ pc) on the non-centered spine. Therefore, we identified only two peaks in ^{13}CO and three in C^{18}O . We find four ATLASGAL sources within g, where three are associated with the ^{13}CO peaks and again one of these shows in addition alignment with a radio quiet HII region. The evolutionary stages of the sources are two massive star formation regions and two YSOs, one with the HII region. Therefore, this part is especially notable for its confined morphology and the low number of point sources, which are, however, further evolved than in the other regions. The average distribution of the peak velocities is also similar to part f, but with a shallower increase of about $1.0\ \mathrm{km\,s^{-1}\,pc^{-1}}$ for radii from 0 pc to 2 pc. Despite the confined appearance the line-mass ($m_\mathrm{g} = 375\ \mathrm{M_\odot\,pc^{-1}}$) is on the lower end of the parts, which shows, that the low intensity regions around the skeleton contribute significantly to the mass. This is also represented in the low surface density of $< \Sigma_\mathrm{g} >= 109\ M_\odot\, pc^{-2}$.

3.4.1.8 Part *h*

Part *h* shows only diffuse gas ($< \Sigma_\mathrm{h} >= 97\ M_\odot\, pc^{-2}$) in ^{13}CO , which does not follow the skeleton we chose in the beginning based on the dust extinction measurements in Chapter 2. However, in C^{18}O some part of the skeleton is traced by the emission.

Because of the generally diffuse gas we identified only two ^{13}CO and two C^{18}O peaks, of which one ^{13}CO peak can be associated with a Hi-GAL and an ATLASGAL source and one C^{18}O peak with one Hi-GAL source. Also, we find the radial distribution of intensities to be less confined than in other parts (FWHM$_{\rm h}$ = 2.22), but the variance of the peak velocities and velocity dispersions is lower around the skeleton than at larger radii. However, because of the large radial extent without a clear detectable filamentary structure the line-mass might be overestimated $m_{\rm h} \geq 786$ M$_\odot$ pc^{-1}.

3.4.1.9 Part *i*

Part *i* shows the next known extended HII region (G337.957-00.474) within the Nessie filament. A second, smaller HII region (G337.922-00.463) is indicated for this area by Anderson et al. (2014), which is, however not traced by the CO emission. The shell of the big HII region is not completely detected because of missing data at the edge of the survey. As the spine of this part follows the shape of the shell we can see that the intensity increases strongly from the inside of the shell and drops in a more shallow way to the outside. Also, we find the highest intensities towards the lower Galactic longitude side of the shell, and a low intensity gap towards higher Galactic longitudes. The distribution of peak velocities is relatively flat with a small increase again towards higher Galactic longitudes. In the shell we find nine ATLASGAL sources (5 YSOs, 2 protostellar, 2 quiescent), and six Hi-GAL sources (2 protostellar, 4 quiescent). All of them can be associated to a CO peak.

3.4.1.10 Part *j*

Part *j* shows the largest radial extent and the highest intensity for the surrounding gas, but the central filament is still well confined (FWHM$_{\rm j}$ = 1.84 pc) and shows about equally spaced peaks. This equal spacing is a hint on on-going fragmentation as discussed in Chapter 2. Because of the generally high intensity ($< \Sigma_{\rm j} >= 196\ M_\odot\, pc^{-2}$) we identified several ^{13}CO and C^{18}O peaks, however, only the central spine they are aligned. Also on the spine there are three ATLASGAL sources, which are associated to CO peaks, and one of them can be associated with a HII region candidate. There is one more ATLASGAL source located towards higher Galactic latitudes, which is aligned with a ^{13}CO peak. The large radial extent and high CO intensities lead to a mass of about $M_{\rm j} = 26526$ M$_\odot$. The ^{13}CO and C^{18}O emission contours indicate five side branches and therefore, the line-mass of $m_{\rm j} = 377$ M$_\odot$ pc^{-1}.

3.4.1.11 Part *k*

Part *k* shows two shell like structures located next to each other, however, only one is indicated as HII region candidate (G337.684-00.343). The lower galactic latitude side of the shells is in line with the spine of the extended Nessie. In the shell of the higher longitude HII region we find five aligned ^{13}CO – C^{18}O peaks, of which one is located in an elongated high intensity clump on the spine of Nessie. This elongated clump can be associated with three ATLASGAL sources (2 YSOs, 1 protostellar). The second

shell structure is less prominent and only a single position is detected in $C^{18}O$. Also, we do not find high-mass star formations signs in this shell and only two ^{13}CO and $C^{18}O$ peaks. Like the other extended shells also here the intensity is increasing strongly from the inside of the shell and decreases more shallow towards the surrounding with a confined spine of $FWHM_k = 0.90$ pc.

3.4.1.12 Part *l*

Most obvious in part *l* is a central peak which shows the highest integrated intensity in the extended Nessie filament. It is located in the intersection of the main spine and a side branch. In the rest of this part the integrated emission is concentrated on the skeleton and therefore, most CO peaks are also located on the skeleton. However, we find only two ^{13}CO – $C^{18}O$ associations, which can be explained by the brightness of the central peak that makes it difficult to identify peaks in the surrounding with our simple approach. Additionally, this part shows the most ATLASGAL (11) and HiGAL (14) associations of all parts, which are almost exclusively located on the skeleton, and 13 HII regions (10 radio quiet, 3 candidates), which can only partially be associated with the dust continuum clumps.

3.5 Discussion and Conclusions

We find the extended Nessie filament as a spatially continuous structure in the SEDIGISM ^{13}CO emission at a resolution of 40″. The SEDIGISM $C^{18}O$ emission traces the high column density parts of Nessie and therefore, shows a narrower radial extent than ^{13}CO and is not detected towards the regions of low ^{13}CO intensity leaving a spatially non continuous structure. The velocity structure is also continuous over most parts of the filament. The two exceptions are around Galactic longitudes of 339.1° and 338.0°, where the line-of-sight velocities are likely to be influenced by the neighboring HII regions G337.957-00.474 (and possibly G337.922-00.463) and G339.134-00.377 (part c, and i). As the two rapid changes in the velocity can be explained by the expanding HII shells we still consider the extended Nessie to be a single structure.

However, despite the continuity in ppv-space the morphology of the gas is constantly changing over the structure. The surface density of the regions is varying between 93 $M_\odot\,pc^{-2}$ and 277 $M_\odot\,pc^{-2}$ and indicate denser and more diffuse regions. We find the FWHM of the spine ranging from 2.6 pc in the diffuse parts to 0.9 pc in the parts around the HII shells. Some regions show velocity gradients across the filament spine, and some show the minimum velocity centered on the spine, while others are flat. While identifying the intensity peaks of the integrated ^{13}CO and $C^{18}O$ emission we find them concentrated on the skeleton in regions of higher surface density and an absence of peaks in low surface density regions. This is also true for the distribution of ATLASGAL and Hi-GAL high-mass clumps. In addition, the ATLASGAL sources are more likely to be located on the skeleton (72%, 58% for Hi-GAL sources) and are associated with the brightest peaks identified in CO, whereas Hi-GAL sources are associated with less bright CO peaks.

The existence of four expanding HII regions within and close to the extended Nessie filament (parts *c*, *i*, *k*) suggest that the O/B stars creating the shells were formed in the filament. Especially, the continuity in ppv-space on at least one side of the shell indicates that the line-of-sight position is similar to the one of the molecular gas. Additionally, we find several radio quiet HII regions correlated with bright CO peaks, however, because of the missing velocity information for the HII regions we cannot confirm an association. Furthermore, we find associations for 47 ATLASGAL and 48 Hi-GAL high-mass clumps at different evolutionary stages, which shows on-going high-mass star formation over large parts of the filament.

Another finding connected to the on-going high-mass star formation is that the shells of the expanded HII regions (parts c, i, k) also harbor high-mass clumps. These shells show confined (0.9 – 1.22 pc) high intensity ^{13}CO emission with surface densities among the highest values of Nessie (195 – 277 $M_\odot\,pc^{-2}$). Further part c, and k show each three almost equally spaced ATLASGAL sources located on the skeleton, of which two are in the YSO phase and one is in the protostellar phase. The equal spacing can hint on fragmentation processes, like the sausage instability discussed in the previous chapter. However, due to the low number of sources this is not a significant finding. The expanded shell in part i shows a more complex structure, which might be caused by the overlap of two HII regions (G337.957-00.474 and G337.922-00.463), but harbors with 15 ATLASGAL and Hi-GAL sources (ten on the skeleton) significantly more high-mass clumps. Therefore, 21 of 95 high-mass clumps (22%) are located in expanded HII shells, which cover only 12% of the area. This accumulation can be interpreted with two scenarios: star formation is triggered by the external pressure from the HII region onto the surrounding molecular gas, leading to a compression of the gas and increased density, which supports (high-mass) star formation. Alternatively, the high-mass clumps condensate out of an larger gas clump which is then dispersed by the most massive (fastest evolving) high-mass star and the gravitationally bound clumps are moved along with the gas. However, this scenario is unlikely because the radiation pressure and stellar winds of one star is not sufficient to move these massive objects.

Velocity gradients across the filament were observed in two parts, which can be interpreted as radial collapse, but two different parts show a minimum velocity at the spine contradicting this interpretation. Also, comparing the observed line-mass with the critical non-thermal (virial) value shows no conclusive correlation, however, the used skeleton must not be representative at every point and we find additional velocity components in the line-of-sight, which introduces some uncertainties.

Nevertheless, comparing our findings in the extended Nessie filament with the models of giant molecular filaments (GMFs) from Smith et al. (2014) and Duarte-Cabral & Dobbs (2017) we see several similarities. In particular, we find coherence in ppv-space, morphological differences along the filament, and on-going continuous (high-mass) star formation in localized parts of the molecular filament. However, these findings are predicted by both models and we do not find a clear observational signature for one of either models. Clearly, more studies are needed to understand the formation GMFs.

Further observations to differentiate the two proposed formation processes need to target the outer regions of GMFs with tracers of diffuse molecular, neutral and ionized

gas. This will reveal whether gas is constantly falling into the gravitational potential of the spiral arm, or exerts pressure onto the filament. To achieve a conclusive result it may also be necessary to derive the gas and dust temperatures throughout Nessie. The dust temperatures can be derived from the Herschel dust continuum maps. For the gas temperature we need observations of different transitions the same molecular tracer. From SEDIGISM we have the ^{13}CO(2 – 1) line and the public available ThrUMMS survey provides the ^{13}CO(1 – 0) line, however, at a spatial resolution of 72″. Alternatively, the newly commissioned LASMA receiver at the APEX telescope will be able to observe the ^{13}CO(3 – 2) line at a higher resolution of about 20″. With this data we will be able to also calculate the opacities of the gas and therefore, get a more precise estimate of the mass.

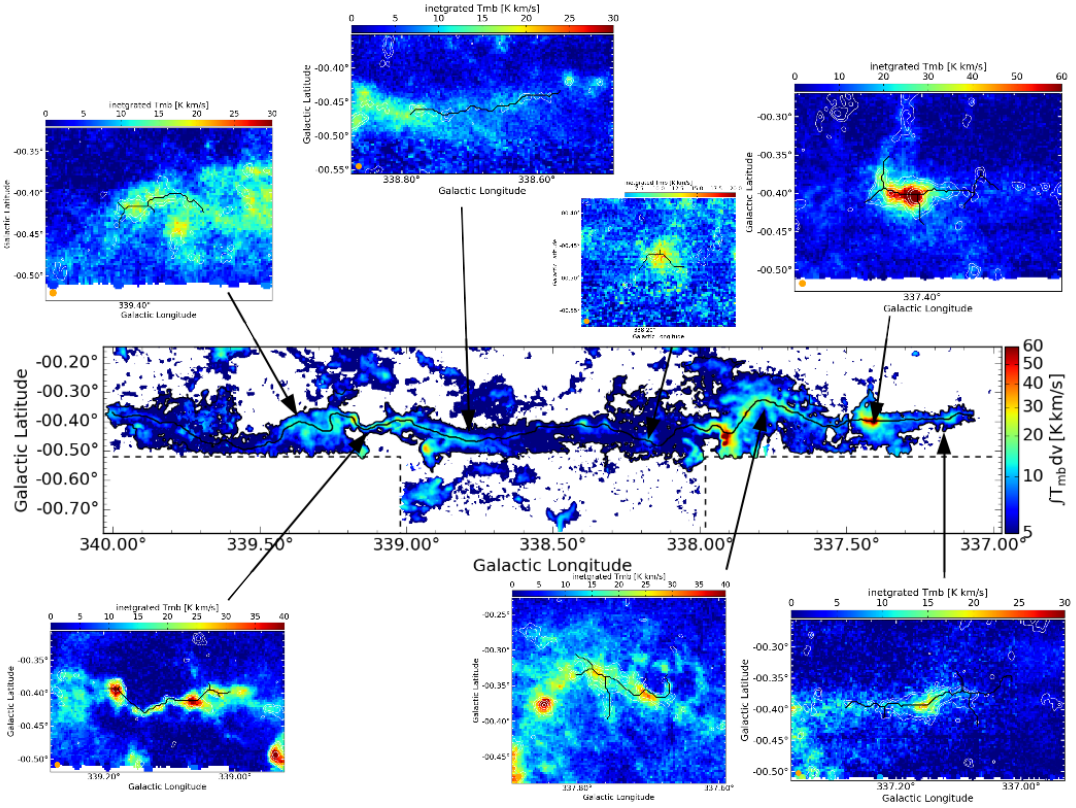

Figure 3.7: Comparison of filaments identified with the DisPerSE algorithm on ATLASGAL emission with the extended Nessie filament.

As we discussed in Chapter 3.3 it is not straight forward to find a continuous skeleton for such a long structure. Nevertheless, Li et al. (2016) applied the DisPerSE algorithm (Sousbie, 2011) to the ATLASGAL dust continuum data (Schuller et al., 2009) smoothed to a spatial resolution of 42″ to identify massive filamentary structures (see also Chapter 1.4.1). These massive filaments will be discussed in the following Chapters. However, as this also includes filaments within the extended Nessie area, we will briefly show how these compare to the findings of this study. To do so we

extract the SEDIGISM data around the 7 skeletons found to be associated within Nessie and integrate over the relevant velocity ranges (at maximum the range identified in Chapter 3.3). We then plot the skeletons and the ATLASGAL contours onto the integrated intensity maps and compare them to the integrated intensity map of the extended Nessie (Fig. 3.7). We find that the DisPerSE filaments cover only parts of the extended filament, which show a significant intensity in ATLASGAL and excludes the bright HII region at $l = 338.0°$ (probably categorized differently). This is only partially true for the ^{13}CO(2 – 1) SEDIGISM emission, where several bright regions are not covered by the DisPerSE skeletons. However, large parts of the extended Nessie could be recovered by applying a friends-of-friends analyses to the filaments from Li et al. (2016).

Table 3.2: Table of HII associations from the catalog of Anderson et al. (2014), where the Categories are Known, Candidate, and radio Quiet.

WISE Name	gl $^\circ$	gb $^\circ$	Cat.	R $''$	$v_{\rm lsr}$ km/s
G337.367-00.402	337.37	-0.40	Q	22.0	-
G337.377-00.389	337.38	-0.39	Q	22.0	-
G337.345-00.380	337.35	-0.38	Q	22.0	-
G337.301-00.400	337.30	-0.40	Q	22.0	-
G337.284-00.389	337.28	-0.39	Q	19.0	-
G337.402-00.310	337.40	-0.31	Q	22.0	-
G337.453-00.363	337.45	-0.36	C	95.0	-
G337.527-00.402	337.53	-0.40	Q	50.0	-
G337.428-00.401	337.43	-0.40	C	58.0	-41.9
G337.439-00.397	337.44	-0.40	Q	22.0	-41.9
G337.392-00.401	337.39	-0.40	Q	22.0	-41.4
G337.404-00.404	337.40	-0.40	C	38.0	-41.4
G337.412-00.401	337.41	-0.40	Q	22.0	-41.4
G337.684-00.343	337.68	-0.34	C	162.0	-
G337.595-00.366	337.60	-0.37	Q	31.0	-
G337.843-00.372	337.84	-0.37	C	70.0	-40.4
G337.957-00.474	337.96	-0.47	K	265.0	-
G337.784-00.507	337.78	-0.51	Q	31.0	-
G337.922-00.463	337.92	-0.46	K	108.0	-40.3
G338.400-00.407	338.40	-0.41	Q	23.0	-37.8
G339.348-00.434	339.35	-0.43	Q	26.0	-
G339.154-00.497	339.15	-0.50	Q	28.0	-
G339.134-00.377	339.13	-0.38	K	257.0	-
G338.925-00.504	338.93	-0.50	Q	24.0	-
G339.178-00.381	339.18	-0.38	Q	23.0	-

Table 3.3: Table of ATLASGAL associations.

ATLASGAL Name	gl $^\circ$	gb $^\circ$	$v_{\rm lsr}$ km/s	Evolution
AGAL337.123-00.372	337.12	-0.37	-39.7	Protostellar
AGAL337.139-00.382	337.14	-0.38	-39.3	Protostellar
AGAL337.152-00.394	337.15	-0.39	-40.1	MSF
AGAL337.216-00.391	337.22	-0.39	-41.1	Protostellar
AGAL337.329-00.499	337.33	-0.50	-39.8	Quiescent
AGAL337.371-00.399	337.37	-0.40	-41.4	YSO
AGAL337.382-00.394	337.38	-0.39	-41.5	YSO
AGAL337.392-00.396	337.39	-0.40	-41.0	YSO
AGAL337.406-00.402	337.41	-0.40	-41.4	MSF
AGAL337.421-00.296	337.42	-0.30	-42.4	YSO
AGAL337.438-00.397	337.44	-0.40	-41.3	YSO
AGAL337.451-00.382	337.45	-0.38	-42.4	YSO
AGAL337.676-00.367	337.68	-0.37	-41.9	YSO
AGAL337.689-00.366	337.69	-0.37	-41.5	YSO
AGAL337.704-00.354	337.70	-0.35	-41.8	YSO
AGAL337.761-00.339	337.76	-0.34	-41.2	YSO
AGAL337.804-00.334	337.80	-0.33	-41.2	YSO
AGAL337.844-00.376	337.84	-0.38	-40.4	MSF
AGAL337.864-00.274	337.86	-0.27	-41.5	Protostellar
AGAL337.889-00.489	337.89	-0.49	-40.0	YSO
AGAL337.891-00.491	337.89	-0.49	-40.0	YSO
AGAL337.916-00.477	337.92	-0.48	-39.6	YSO
AGAL337.922-00.456	337.92	-0.46	-38.7	MSF
AGAL337.927-00.432	337.93	-0.43	-39.5	
AGAL337.931-00.521	337.93	-0.52	-37.6	YSO
AGAL337.934-00.507	337.93	-0.51	-38.0	YSO
AGAL337.994-00.514	337.99	-0.51	-39.2	YSO
AGAL338.021-00.206	338.02	-0.21	-43.1	Protostellar
AGAL338.026-00.476	338.03	-0.48	-39.1	YSO
AGAL338.089-00.447	338.09	-0.45	-37.3	Protostellar
AGAL338.112-00.462	338.11	-0.46	-38.4	Quiescent
AGAL338.199-00.464	338.20	-0.46	-38.0	Protostellar
AGAL338.327-00.409	338.33	-0.41	-38.5	MSF
AGAL338.394-00.406	338.39	-0.41	-38.3	MSF
AGAL338.424-00.411	338.42	-0.41	-37.4	Protostellar
AGAL338.551-00.419	338.55	-0.42	-38.8	YSO
AGAL338.732-00.469	338.73	-0.47	-38.9	Quiescent
AGAL338.779-00.459	338.78	-0.46	-40.0	Quiescent
AGAL338.869-00.479	338.87	-0.48	-36.5	Quiescent

Table 3.3: Table of ATLASGAL associations continued.

ATLASGAL Name	gl °	gb °	$v_{\rm lsr}$ km/s	Evolution
AGAL338.927-00.501	338.93	-0.50	-37.0	YSO
AGAL338.937-00.422	338.94	-0.42	-39.5	Protostellar
AGAL338.937-00.492	338.94	-0.49	-36.9	MSF
AGAL339.054-00.412	339.05	-0.41	-35.9	Quiescent
AGAL339.126-00.422	339.13	-0.42	-37.2	YSO
AGAL339.144-00.504	339.14	-0.50	-39.6	Protostellar
AGAL339.176-00.391	339.18	-0.39	-37.6	YSO
AGAL339.261-00.374	339.26	-0.37	-39.0	Quiescent
AGAL339.351-00.457	339.35	-0.46	-36.1	Protostellar
AGAL339.403-00.414	339.40	-0.41	-38.3	MSF
AGAL339.886-00.421	339.89	-0.42	-37.7	Protostellar

Table 3.4: Table of Hi-GAL associations.

Hi-GAL Name	gl	gb	d	Evolution
	°	°	kpc	
HIGALBM337.1219-0.3717	337.12	-0.37	3.2	2
HIGALBM337.1334-0.3817	337.13	-0.38	3.2	1
HIGALBM337.1424-0.3999	337.14	-0.40	3.2	2
HIGALBM337.1534-0.3949	337.15	-0.39	3.2	2
HIGALBM337.1641-0.3925	337.16	-0.39	3.2	2
HIGALBM337.3323-0.4060	337.33	-0.40	3.0	1
HIGALBM337.3496-0.4379	337.35	-0.44	3.2	2
HIGALBM337.3673-0.3983	337.37	-0.40	3.0	2
HIGALBM337.3684-0.4510	337.37	-0.45	3.2	1
HIGALBM337.3802-0.3937	337.38	-0.39	3.0	1
HIGALBM337.4251-0.4022	337.43	-0.40	3.0	2
HIGALBM337.4367-0.3974	337.44	-0.40	3.1	2
HIGALBM337.4516-0.3829	337.45	-0.38	3.1	1
HIGALBM337.4581-0.3959	337.46	-0.40	3.1	2
HIGALBM337.9041-0.4431	337.90	-0.44	3.1	2
HIGALBM337.9118-0.4607	337.91	-0.46	3.1	2
HIGALBM337.9191-0.4940	337.92	-0.49	3.1	2
HIGALBM337.9272-0.4575	337.93	-0.46	3.1	2
HIGALBM337.9640-0.4453	337.96	-0.45	3.1	2
HIGALBM338.0379-0.4657	338.04	-0.47	3.0	2
HIGALBM338.0921-0.4480	338.09	-0.45	3.0	2
HIGALBM338.1233-0.3170	338.12	-0.32	3.3	2
HIGALBM338.1680-0.4654	338.17	-0.47	2.9	2
HIGALBM338.1818-0.3237	338.18	-0.32	2.9	2
HIGALBM338.1837-0.4636	338.18	-0.46	2.9	2
HIGALBM338.1987-0.4624	338.20	-0.46	2.9	2
HIGALBM338.2707-0.2920	338.27	-0.29	3.0	2
HIGALBM338.6006-0.4378	338.60	-0.44	3.0	2
HIGALBM338.6540-0.4506	338.65	-0.45	3.2	2
HIGALBM338.6613-0.4544	338.66	-0.45	3.2	2
HIGALBM338.6925-0.4777	338.69	-0.48	3.2	1
HIGALBM338.7243-0.4584	338.72	-0.46	3.2	2
HIGALBM338.7333-0.4717	338.73	-0.47	3.2	1
HIGALBM338.7537-0.4547	338.75	-0.45	3.2	2
HIGALBM338.8675-0.4776	338.87	-0.48	3.1	2
HIGALBM338.9698-0.3798	338.97	-0.38	3.1	2
HIGALBM338.9930-0.3996	338.99	-0.40	3.1	2
HIGALBM339.0185-0.3963	339.02	-0.40	3.1	1
HIGALBM339.0271-0.3987	339.03	-0.40	3.1	2

Table 3.4: Table of Hi-GAL associations continued.

Hi-GAL Name	gl	gb	d	Evolution
	$^\circ$	$^\circ$	kpc	
HIGALBM339.1439-0.5021	339.14	-0.50	3.1	2
HIGALBM339.1452-0.5149	339.15	-0.51	3.1	1
HIGALBM339.2349-0.4709	339.23	-0.47	3.3	1
HIGALBM339.2907-0.4745	339.29	-0.47	3.3	1
HIGALBM339.2951-0.4628	339.30	-0.46	3.3	2
HIGALBM339.3214-0.4764	339.32	-0.48	3.0	2
HIGALBM339.3298-0.4740	339.33	-0.47	3.0	2
HIGALBM339.3504-0.4582	339.35	-0.46	3.0	2
HIGALBM339.3511-0.4822	339.35	-0.48	3.0	2
HIGALBM339.3997-0.4138	339.40	-0.41	3.2	2
HIGALBM339.4844-0.4971	339.48	-0.50	3.1	1
HIGALBM339.4964-0.4918	339.50	-0.49	3.1	1
HIGALBM339.5785-0.3885	339.58	-0.39	3.0	2
HIGALBM339.9031-0.3801	339.90	-0.38	3.1	1

Chapter 4

Filaments in the SEDIGISM demonstration field

This chapter covers my contribution to content of Section 7.1 of the publication F. Schuller, T. Csengeri, J. S. Urquhart, A. Duarte-Cabral, P. J. Barnes, A. Giannetti, A. K. Hernandez, S. Leurini, M. Mattern, et al. (35 more) , 2017, A&A, 601, A124, and additional unpublished analysis.

As shown in the previous chapter, giant molecular filaments do not behave as a single entity, but rather as a chain of smaller filamentary structures. Additionally, it was shown that ^{13}CO is a good tracer for larger complexes of molecular gas. Therefore, we decided to visually inspect the SEDIGISM science demonstration field ($340.0° < l < 341.5°$) to identify different structures of ^{13}CO emission.

Generally, we find ^{13}CO emission only at velocities between -150 km s^{-1} and 0 km s^{-1}, which is agreement with what we expect from the Galactic rotation towards this sight line, and we find stronger emission from Galactic longitudes $b < 0°$ than $b > 0°$. To identify structures at different velocities we use an average spectra of the field and position-velocity plots, where we integrate over the Galactic latitude and longitude (Fig. 4.1). We find several complexes of emission which we then inspect in more detail to disentangle their structure.

In total, we find nine bigger complexes with each of them containing at least one filamentary structure. However, only two complexes show high intensity filamentary structures, which would indicate dense gas. These two complexes have peak velocities of around -45.0 km s^{-1} and -122.0 km s^{-1}, which corresponds to the highest intensity peak in the average spectrum of the field. While the -122.0 km s^{-1} complex shows only one high intensity structure, in the -45.0 km s^{-1} complex we find four high intensity filamentary structures, which are connected by low intensity gas. Furthermore, we can associate the found complexes with the spiral arms of the Milky Way using the 4-arm model of Pettitt et al. (2014), where the bright components align with the near Scutum-Centaurus and near 3-kpc arm and the other complexes with the near and far Norma arm, and the far 3-kpc arm (see Fig. 10 in Schuller et al., 2017).

In general, we find filamentary structures in every ^{13}CO complex with dense filaments located within less dense filamentary structures, where the size of the structure is dependent on the lower identification threshold. For a low threshold most structures seem to be connected by surrounding diffuse gas, which is likely to be associated to the spiral structure of the Galaxy. This confirms the ubiquity of filaments in the ISM and their hierarchical structure. The densest parts of the structures are also traced by C^{18}O emission.

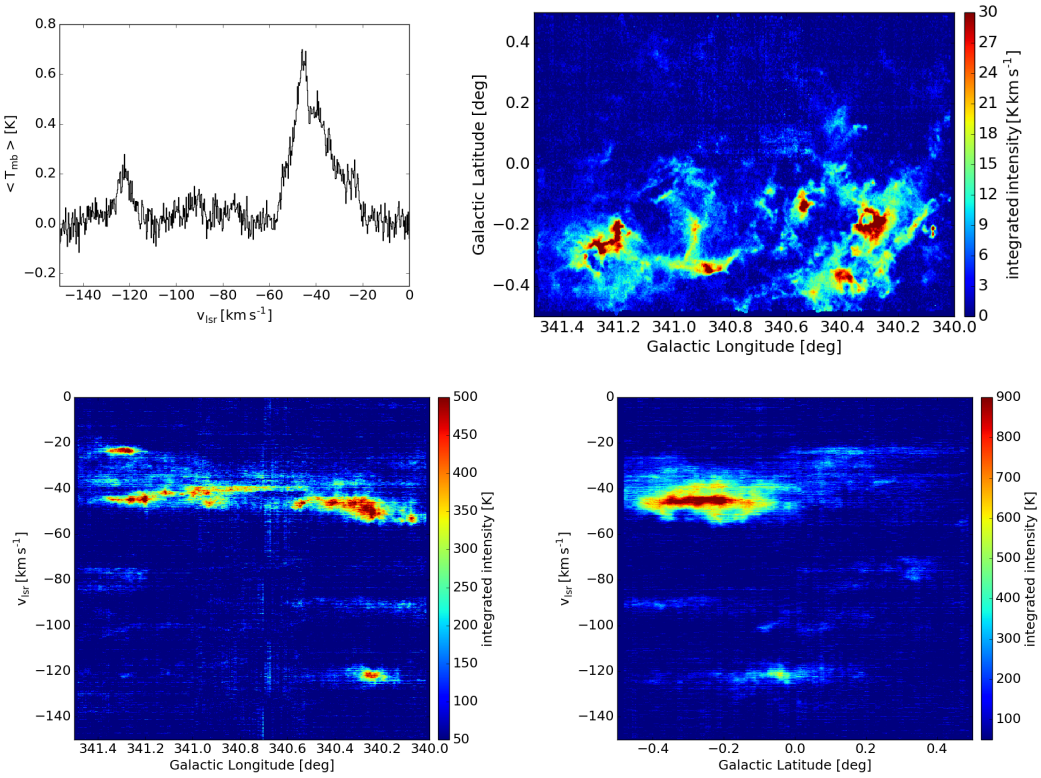

Figure 4.1: The SEDIGISM science demonstration field viewed in different perspectives. **Top Left:** Average spectra over the whole field. **Top Right:** ^{13}CO intensity integrated over the velocity range -49.0 km s^{-1}–-43.0 km s^{-1}. **Bottom Left:** Position-velocity plot of the science demonstration field integrated over the Galactic latitude. **Bottom Right:** Position-velocity plot of the science demonstration field integrated over the Galactic longitude.

For a more systemtical and unbiased study we use a catalog of previously identified filaments. Li et al. (2016) identified 517 filamentary structures in the ATLASGAL dust emission data, which traces dominantly dense gas. This catalog includes also seven structures that are part of the extended Nessie filament, which supports the conclusions from Chapter 3. Therefore, this catalog is likely to contain more fragments or complete giant molecular filaments and could be an ideal starting point to study them. However, the catalog of Li et al. (2016) does not include velocity informations and therefore, the structures might not be single filaments, but rather line-of-sight projections of several structures.

As the real structure of sources from the catalog of Li et al. (2016) is not known, we will refer to them now as filament candidates, while filament candidates with a confirmed coherent velocity will be called filaments. The new SEDIGISM survey is the ideal dataset to investigate the velocity coherence of the filament candidates. To show what we are able to do with the combination of the filamentary structures of Li et al.

(2016) and the ^{13}CO and C^{18}O lines of the survey, we performed a test study on the SEDIGISM science demonstration field, which is published in Schuller et al. (2017). Here I will give a summary of the work lead by myself.

Within the SEDIGISM science demonstration field Li et al. (2016) identified twelve filamentary structures, of which nine are filamentary candidates, and three are networks of filamentary candidates. To verify the velocity coherence of these twelve structures, we made use of the CO isotopologs observed by the survey. In particular, for each filament candidate we selected the spine of the skeleton identified in the dust emission, extracted the spectra along the spine, and analyzed the position-velocity diagrams along the spine. Additionally, we averaged the spectra located within a dilation box around the spine. For the diameter of the box we chose three SEDIGISM beams. From the average spectrum we derived the central velocity and velocity dispersion of the detected emission lines. We then derived integrated intensity maps of the ^{13}CO and C^{18}O lines for each identified velocity component, and compared them to the corresponding ATLASGAL dust emission maps to verify the correlation between the dust and molecular line emission.

We detected eleven of the twelve structures in the science demonstration field in the ^{13}CO data. The one undetected structure (G340.600+00.067) shows only weak dust emission and is located in the noisier area of the field. Ten of the detected structures have a coherent velocity component, which traces the main part of the spine identified in ATLASGAL (Fig. 4.2). We find multiple velocity components at all positions along the spine for the eleventh structure, and there is no single component that resamples the structure seen in ATLASGAL emission. Another six structures (G340.482-00.306, G340.511-00.471, G340.981-00.013, G341.415+00.244, G340.236-00.153, G341.306+00.339) show additional velocity components, which may contribute to the dust emission by line-of-sight projection. These projections are expected especially for more crowded regions. Therefore, we expect to see also a separation of structures or false classified structures. Within the demonstration field this is true for one filamentary network (G340.236-00.153), which splits into two networks for two different velocities. In Table 4.1, they are labeled as G340.236-00.153 at -50.9 km s^{-1} and G340.200-00.035 at -122.2 km s^{-1}.

Table 4.1: Catalog of the ATLASGAL filaments (top) and networks (bottom) in the First Science Field

Name	gl	gb	v	FWHM	$I_{\mathrm{int},^{13}\mathrm{CO}}$	A	d	$M_{13\mathrm{CO}}$	M_{dust}	l	$(m/l)_{obs}$	$(m/l)_{cr}$
	°	°	km/s	km/s	K*km/s	arcmin^2	kpc	10^3 M$_\odot$	10^3 M$_\odot$	pc	M$_\odot$/pc	M$_\odot$/pc
G340.305-00.388	340.305	-0.388	-48.9	8.7	21.4	46.1	3.8	4.9	16.4	23.61	208	2277
G340.318+00.079	340.318	+0.079	-111.7	4.5	3.9	15.3	6.2	0.8	1.0	11.15	70	349
G340.481-00.305	340.481	-0.305	-44.0	6.5	7.6	15.6	3.8	0.6	0.7	7.08	83	2970
G340.513-00.465	340.513	-0.465	-42.8	6.8	11.9	15.2	3.5	0.8	2.0	6.97	110	3178
G340.600+00.065	340.600	+0.065	-	-	-	18.0	-	-	-	-	-	-
G340.628-00.091	340.628	-0.091	-48.2	6.5	7.1	9.8	3.6	0.3	0.3	3.63	86	2680
G340.992-00.011	340.992	-0.011	-46.9	3.6	5.7	24.6	3.4	0.6	0.5	11.42	49	736
G341.246-00.267	341.246	-0.267	-44.4	3.4	16.9	44.6	3.6	3.4	12.2	21.34	158	712
G341.415+00.246	341.415	+0.246	-37.5	2.1	6.1	10.5	3.2	0.2	0.2	4.26	53	369
G340.236-00.153	340.236	-0.153	-51.3	7.3	15.3	201.1	3.8	15.3	29.1	-	-	2824
G340.941-00.319	340.941	-0.319	-46.0	4.5	11.4	82.2	3.6	4.2	7.7	-	-	1887
G341.306+00.339	341.306	+0.339	-78.3	4.0	9.6	30.4	5.2	2.7	4.2	-	-	1164

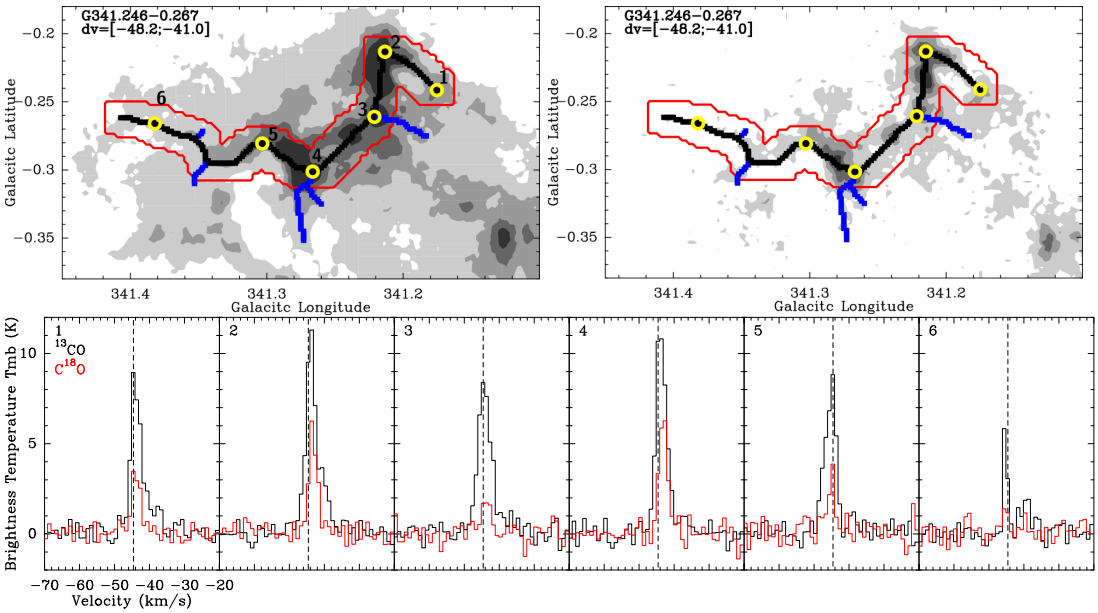

Figure 4.2: **Top Left:** Integrated ^{13}CO intensity map of G341.246-00.267. The spectra of the marked position are shown below. **Top Right:** Integrated C^{18}O intensity map. **Bottom:** ^{13}CO and C^{18}O spectra of the positions marked on the maps on top. (Schuller et al., 2017)

The ATLASGAL filament catalog provides also distance estimates and physical sizes for several sources, which we use to calculate the mass. Within the test field three filaments have assigned distances in the catalog. Additionally, we adopt for the networks the distances of ATLASGAL point sources (Wienen et al., 2015) that are most likely connected to the structures. First, we estimated the column densities of the eleven structures from the average ^{13}CO integrated intensity (Table 4.1) within the dilation box using the $X_{^{13}CO(2-1)}$ factor derived in Schuller et al. (2017). We then calculate the mass of each filament through the equation:

$$M(\mathrm{H_2}) = \sum_i N_i(\mathrm{H_2}) A_i \mu m_\mathrm{p} \tag{4.1}$$

where $N_i(\mathrm{H_2})$ is the $\mathrm{H_2}$ column density computed for pixel i, A_i the area of pixel i, $\mu = 2.8$ the mean molecular weight, and m_p the proton mass. As mentioned before, we find line-of-sight contamination for several sources. In the cases of G340.301-00.387 and G340.482-00.306 the projected structures have velocities red-shifted from the main velocity and contaminate the filament masses up to 20% and 34%, respectively. For the other sources the projected sources are clearly separated in velocity space.

One measurement of the gravitational stability of a filament is given by the comparison of the observed line-mass, m, with its critical value. The critical line-mass, m_{cr}, describes the maximum mass per unit length, that can be sustained against gravitational collapse by the thermal motions of the gas. An estimate of the thermal motions is given by the sound speed, c_s, of the medium, which is only dependent on the tem-

perature of gas. The critical line-mass is then given by $m_{cr} = 2c_s^2/G$ (Ostriker, 1964). However, turbulent motions of the gas can support this mechanism to counteract gravity and therefore, the sound speed can be replaced by the velocity dispersion, σ_v, of the medium ($m_{\rm vir} = 2\sigma_v^2/G$ Inutsuka & Miyama, 1997).

To measure the velocity dispersion of the filaments we fitted a Gaussian to the main component of the structures in the single spectra along the spine, minimizing the effect of velocity gradients along the filament. Here we only take the 7 detected filaments into account, as the filament networks are too complex to assign a representative length to derive a line-mass (Table 4.1). We find two filaments being sub-critical, three being critical, and two around the critical value, where the ratio of $m_{\rm obs}/m_{\rm vir}$ is ranging from 0.4 to 3.5. Previously, Hernandez et al. (2011) and Contreras et al. (2013) found values significantly below unity for different filamentary structures. From this we concluded that filaments might not be gravitationally bound globally, but form stars in the dense inner parts of the structure. However, our mass estimates include several uncertainties, like a factor of 2 for the $X_{^{13}CO(2-1)}$ value, and another factor 2 for opacity effects in the densest clumps embedded in the filaments (Hernandez et al., 2011).

Similar to the Li et al. (2016) catalog Schisano et al. (2014) and Schisano et al. (in prep.) identified filaments based on Hi-GAL dust emission maps at 70, 160, 250, 350, and 500 μm. These wavelength trace also the lower column density gas and therefore, the number of detected filaments per area is higher. Within the area of the science demonstration field there are 88 Hi-GAL filaments, which include all the filaments identified by Li et al. (2016).

The visual inspection of the data showed that the SEDIGISM survey is capable of revealing many filamentary structures at a wide range of column densities. The densest structures are likely to be also seen in dust continuum observations like ATLASGAL and Hi-GAL. However, low column density filamentary structures identified in continuum data may not be a single continuous structure in position-position-velocity space, but rather an artifact of line-of-sight projection. But even structures identified continuously in the position-position-velocity data of the survey may not translate into real three dimensional objects. Hence, a connection in velocity-space may not be indicating a connection in real space (Clarke et al., 2018).

After we were able to identify 7 filaments within the test field based on the ATLASGAL catalog, the whole SEDIGISM data will allow us to study even more filamentary structures. Additionally, we identified several filamentary structures by the visual inspection of the ^{13}CO data-cube of the test field not previously identified in dust surveys. These structures show generally low intensities, and therefore are not listed in other filament catalogs. This demonstrates the power of the SEDIGISM survey for filament identification. However, different identification approaches are needed to perform an unbiased search on the SEDIGISM survey. Therefore, we improved and extended the methods used in this test study and performed an analysis for all filament candidates of the Li et al. (2016) catalog, which is shown in the following chapter and published in Mattern et al. (2018).

Chapter 5

SEDIGISM: The kinematics of ATLASGAL filaments

This chapter is published under M. Mattern, J. Kauffmann, T. Csengeri, J. S. Urquhart, S. Leurini, F. Wyrowski, A. Giannetti, P. J. Barnes, H. Beuther, L. Bronfman et al. (6 more) , 2018, A&A, 619, A166. The Appendix of this Chapter is shown in Appendix B.

5.1 Introduction

Filamentary structures play an important role in the process of star formation. Observations at different wavelengths based on various tracers have revealed that filaments are ubiquitous in the interstellar medium (e.g., Schneider & Elmegreen, 1979; Molinari et al., 2010; André et al., 2010; Schisano et al., 2014; Ragan et al., 2014; Li et al., 2016). Filaments are seen in quiescent and star-forming clouds, in which a significant fraction of prestellar cores are located (André et al., 2010). Filamentary structures have wide ranges of masses ($\sim 1 - 10^5\,M_\odot$) and lengths ($\sim 0.1 - 100\,pc$) (e.g., Bally et al., 1987; Jackson et al., 2010; Arzoumanian et al., 2011; Hernandez et al., 2012; Hacar et al., 2013; Kirk et al., 2013; Palmeirim et al., 2013; Li et al., 2016; Kainulainen et al., 2013; Beuther et al., 2015; Kainulainen et al., 2017; Abreu-Vicente et al., 2016; Zucker et al., 2017).

The processes of filament formation and filament fragmentation to star-forming cores are not well understood. Because of the wide range of filament size scales and masses these processes might also differ among filaments. High-resolution magnetohydrodynamical simulations of molecular cloud evolution and filament formation show subsonic motions in the inner dense regions of filaments, but the surrounding low density gas is supersonic (Padoan et al., 2001; Federrath, 2016). Additionally, accretion flows along and radially onto the filament have been seen in observations and simulations (Schneider et al., 2010; Peretto et al., 2013, 2014; Henshaw et al., 2014; Smith et al., 2015). Therefore, the formation and evolution of filaments is a highly dynamical process and to constrain it is essential to study their kinematics.

Studies of filaments have targeted mainly sources in nearby star-forming regions, for example Orion, Musca and Taurus (Bally et al., 1987; Takahashi et al., 2013; Hacar et al., 2016; Kainulainen et al., 2015, 2017), where high resolution data (~ 0.01 pc, $0.1\ km\,s^{-1}$) reveals sub-structures like fibers (Hacar et al., 2013, 2018), or prominent mid-infrared extinction structures, like "Nessie" and infrared dark clouds like

G11.11−0.12 (Johnstone et al., 2003; Pillai et al., 2006; Schneider et al., 2010; Jackson et al., 2010; Kainulainen et al., 2013; Henshaw et al., 2014; Mattern et al., 2018). Detailed studies of these filaments led us to recognize their important role in star formation, and their internal structure, but studies of small samples do not allow to draw general conclusions. In particular the filaments towards the more distant, typically high-mass star forming regions have not yet been systematically studied. Therefore, it is necessary to study a large unbiased sample of filaments. Such studies have recently become feasible because of modern multiwavelength surveys, which cover the Galactic plane at high resolution and sensitivity.

Several catalogs of filamentary structures have been conducted in the last years, which can be divided in two groups. The filaments in the catalogs of Schisano et al. (2014); Koch & Rosolowsky (2015); Li et al. (2016) were identified from continuum data and therefore, miss the kinematic information, and might be affected by line-of-sight projection effects. The catalogs of Ragan et al. (2014); Zucker et al. (2015); Abreu-Vicente et al. (2016); Wang et al. (2015, 2016) concentrate on the longest filamentary structures in the Galaxy. While the identification methods and criteria vary in these studies, all filaments are tested for a velocity coherent behaviour.

In this study, we have targeted the largest catalog of filamentary structures published so far (Li et al., 2016), which is based on the ATLASGAL survey at 870μm (Schuller et al., 2009). As these structures were identified in continuum dust emission data, the scope of this work is to use the SEDIGISM data (Schuller et al., 2017) to assess their velocity structure. Because of the large number of targets, it is necessary to perform the analysis in a fully-automated way, which are also presented in this work.

In this paper, we will refer to the structures identified by Li et al. (2016) as filament candidates. After the analysis of their velocity structure we will refer to the velocity coherent structures in the filament candidates as filaments, where one filament candidate can consist of multiple filaments. Some of these filaments may not meet the definitions of a filament, as they seem to be composed of a chain of dense clumps, or a dense clump with an elongated low column density environment. However, since filaments fragment, these structures could represent a late phase of evolution and should not be ignored.

The structure of the paper is as follows: Section 5.2 introduces the survey data used in this study and the targeted catalog of filament candidates. The methods used to separate the velocity components of a given filament candidate and to derive its filament parameters are described in Section 5.3. In Section 5.4 we present the resulting statistics of the velocity separation and the interpretation of the kinematics. We then discuss in Section 5.5 the dependency of the filament mass with increasing radius, and the origin of the correlation found between the line-mass (mass per unit length) and velocity dispersion of the filaments. Finally, we summarize our results in Section 5.6.

5.2 Data and filament sample

5.2.1 Survey data

Within this paper, we will make use of three surveys: ATLASGAL (APEX Telescope Large Area Survey of the Galaxy, Schuller et al., 2009), ATLASGAL+PLANCK (ATLASGAL combined with PLANCK, Csengeri et al., 2016) and SEDIGISM (Structure, Excitation and Dynamics of the Inner Galactic InterStellar Medium, Schuller et al., 2017).

The ATLASGAL survey was conducted with the Large APEX Bolometer Camera (LABOCA) at 870 μm between 2007 and 2010 at the Atacama Pathfinder Experiment (APEX) telescope (Güsten et al., 2006) located on the Chajnantor plateau in Chile. The resolution of the survey is 19.2″ (6.0″ per pixel) with a 1σ RMS noise in the range of 40–70 mJy/beam. It covers the inner Galactic plane between $-80° \leq \ell \leq 60°$ and $|b| \leq 1.5°$. It is sensitive to the cold dust, and it traces mainly the high molecular hydrogen column density regions ($N_{\mathrm{H_2}} \geq 1.0 \times 10^{22}$ cm^{-2}) of the ISM.

As the ATLASGAL data is missing the large scale low column density emission due to sky noise subtraction, Csengeri et al. (2016) combined the survey with the data observed by the HFI instrument at 353 GHz (850 μm) with a resolution of 4.8′ on board the PLANCK satellite (Lamarre et al., 2010; Planck Collaboration et al., 2014). The combined ATLASGAL+PLANCK survey is sensitive to a wide range of spatial scales at a resolution of 21″ covering the same region as the original ATLASGAL data on the same pixel grid.

The SEDIGISM survey (Schuller et al., 2017) covers the inner Galactic plane between $-60° \leq \ell \leq 18°$ and $|b| \leq 0.5°$, which was observed from 2013 to 2016 with the SHeFI heterodyne receiver (Vassilev et al., 2008) at the APEX telescope. The prime targets of the survey are the ^{13}CO(2 – 1) and C^{18}O(2 – 1) molecular lines. The average root-mean-square (RMS) noise of the survey is 0.9 K (T_{MB}) at a velocity resolution of 0.25 km s^{-1}, an FWHM beam size of 30″, and a pixel-size of 9.5″. For this analysis we use the first data release (DR1, Schuller et al. in prep.).

5.2.2 The ATLASGAL sample of filaments

Based on ATLASGAL, Li et al. (2016) produced a catalog of filament candidates, which is the base for this study. The filaments were identified in the ATLASGAL only maps, after they were smoothed to a spatial resolution of 42″. The source extraction was performed with the DisPerSE (Discrete Persistent Structures Extractor, Sousbie, 2011) algorithm, which is optimized for the identification of large spatially coherent structures, and has been successfully used to trace filaments in previous studies (e.g., Hill et al., 2011; Arzoumanian et al., 2011). Because of the limited sensitivity and resolution (minimal mean column density $N_{\mathrm{H_2}} = 1.6 \times 10^{21}$ cm^{-2}), the resulting catalog is unlikely to be complete, however, as it covers a large fraction of the Galactic plane it is likely to include the full range of sizes and masses of filamentary type structures.

Not all of the identified structures are filamentary, but they cover a range of morphologies and complexity from roundish clumps to large web-like structures. Therefore,

the identified structures were categorized by Li et al. (2016) through visual inspection into six groups: unresolved clumps, marginally resolved elongated structures, filaments, networks of filaments, complexes, and unclassified structures. Here a filament was defined as single elongated linear structure with relatively few branches, an intensity clearly above the surrounding medium and an aspect ratio of at least 3, that is clearly resolved across its length and width. The high column densities found in the Galactic center region lead to a higher probability of identifying more complex structures. Therefore, the number of filament candidates in the catalog is lower towards the Galactic center. This classification resulted in a catalog of 517 filament candidates, providing the starting point of this study. For more details about the filament identification see Li et al. (2016). In the following, we will refer to the structures of the catalog as filament candidates, as they have been identified only in position-position space, which leaves the possibility of line-of-sight projection effects. One of the objectives of this study is to investigate their velocity coherence.

5.3 The automated filament analysis

The SEDIGISM survey covers the Galactic plane between $-60^\circ \leq \ell \leq 18^\circ$ and $|b| \leq 0.5^\circ$, which is only a part of the ATLASGAL survey. Therefore, we analyze the 283 filament candidates in the area covered by all three surveys described in section 5.2.1. This corresponds to $\sim 55\%$ of the total number of filaments, and can therefore be considered representative of such structures in the inner Galactic plane.

Because of the large number of filament candidates, it is necessary to use an automated approach to analyze them. However, as the sample is distributed over a large range of Galactic longitudes, it is unlikely to find homogeneous conditions in their surrounding material. Therefore, we choose a robust and efficient method to analyze the data in a systematic way, which leads to the following decisions for the analysis. We use the calculation of moments instead of multi-Gaussian fitting to identify the kinematics of the filaments. Also, we do not truncate or alter the skeletons of the filament candidates to fit the identified filaments more accurately, but rather neglect parts where we do not detect molecular gas. Therefore, there are two sets of pixels for a filament candidate used in the analysis: One that describes only the skeleton for the calculation of the kinematics and one that includes also the surrounding area within a dilation box with diameter of three beams used for the structure correlation. This approach results in larger uncertainties in the derived properties, but the homogeneous method enables the finding of correlations in the large scale properties of the filaments, which is the aim of this work.

From Li et al. (2016) we have a set of positions defining the skeleton of each filament, which trace the highest ATLASGAL intensities, that form the backbone of the structure. For each candidate we extract the data around the skeleton from the surveys using a rectangular box that is $5'$ larger on each side than the extrema of the skeleton points. This showed to be sufficient for the analysis of the most nearby < 2 kpc filaments, where the angular extend of the structure is the largest. We now describe the

analysis performed on every filament candidate.

5.3.1 The filament skeleton

For the analysis of each filament candidate we first have to transfer the skeleton coordinates (Fig. 5.1) onto the SEDIGISM grid. To do so, we check whether all positions of the skeleton are covered by the SEDIGISM observations, and remove the positions if they are not covered. This allows us to continue with structures that are partially truncated by the data limits. Then we overlay the skeleton coordinates on the pixel grid of the molecular line data. We mark the pixels within a dilation box around each pixel that covers a position of the DisPerSE skeleton as part of the new pixel skeleton. The size of the dilation box is set to be larger than the maximum distance between two neighboring skeleton points. Here a width of 1 pixel (9.5″) is sufficient. As the resulting skeleton mask might have a width larger than one pixel, we use the thinning algorithm of Gonzalez & Woods (1992) to truncate the pixel skeleton. The result is a "chain" of pixels which might have several branches (see Fig. 5.1).

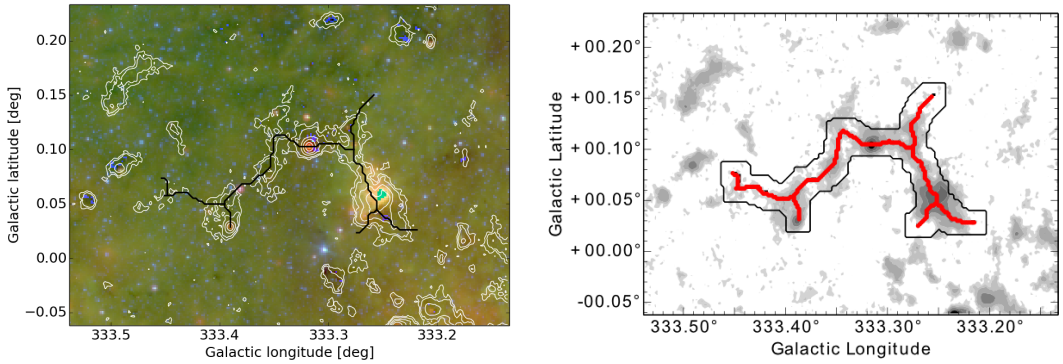

Figure 5.1: **Left:** ATLASGAL contours (0.05, 0.1, 0.2, 0.5, 1.0, 2.0 Jy/beam) and skeleton derived by DisPerSE for the filament candidate G333.297+00.073, overlaid on an infrared three color image of the field (red: MIPSGAL 24 μm; green: GLIMPSE 8.0 μm; blue GLIMPSE 3.6 μm. **Right:** Skeleton of the filament candidate G333.297+00.073 derived by DisPerSE on top of the ATLASGAL grayscale contour map. The black contour indicates the dilation box used for the correlation in Section 5.3.3.

5.3.2 Identification of velocity components

In order to investigate whether the filament candidates form a single structure in velocity, spectroscopic observations are indispensable. From a study of filaments in the SEDIGISM first science field (seven filament candidates in 1.5 deg^2, Schuller et al., 2017), we know that one can observe line emission at very different velocities towards one continuum structure due to projection effects through the Galactic plane. Therefore, we average all spectra located on the skeleton and identify the velocity ranges that show emission peaks in this spectrum. To identify the velocities we smooth the average

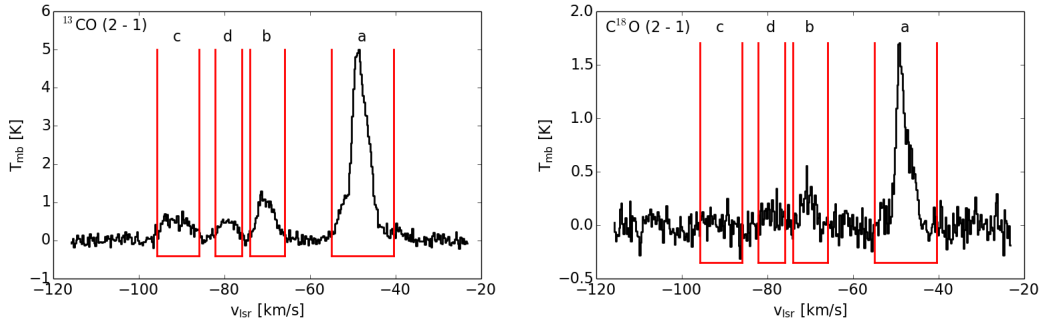

Figure 5.2: Average ^{13}CO **(left)** and C^{18}O **(right)** spectrum over the skeleton of filament candidate G333.297+00.073 (see Figs. 5.1 and 5.1). The red lines mark the identified emission intervals named by letters.

spectrum with a Gaussian kernel with a dispersion of four channels ($= 1\,\mathrm{km\,s^{-1}}$) to reduce the noise. In case the signal-to-noise ratio (S/N) is low, peak intensity $\leq 5\sigma$, we double the kernel width. We then define the velocity range of each spectral component in the averaged spectrum as that between which the emission attains more than the 1σ noise level. This leaves us with a minimum separation limit of $\delta v_{\mathrm{min}} = 2.5\ \mathrm{km\,s^{-1}}$, which is described in detail later on. Furthermore, we only consider components with an S/N ≥ 5 in their integrated intensity of the original data (for example, see Fig. 5.2).

We then define the ends of the velocity components where the emission peaks of the average spectrum exceeds the 1σ noise level, so the emission peak is not likely to be truncated, and accept only components with an integrated intensity S/N ≥ 5 (for example Fig. 5.2). The above procedure is only applied to the ^{13}CO data because of their higher S/N. The C^{18}O emission lines are narrower than the ^{13}CO data lines and so we use the same velocity ranges to calculate the moments in the C^{18}O data. Thereafter, we calculate the zeroth, first, and second "order" moment of each velocity component, that indicate the integrated intensity, peak velocity, and velocity dispersion, respectively, for both molecules. This gives us a first impression of the kinematics of the filament.

Separating the velocity components of a filament along the line-of-sight is a crucial part of this work. Therefore, the technique of identifying the velocity range of emission needs to be tested in a systematic way. We created a simulated data cube with an RMS noise per position of 1 K, typical for SEDIGISM, and include two filaments at the same 2D location, with the same velocity dispersion and intensity, but with different peak velocities. For the emission of the filaments, we assume a Gaussian line profile. We then vary the peak-to-peak velocity, the linewidth, and the intensity and analyze these cubes in exactly the same way as the observed data. From this modeling, we find for filaments with a signal-to-noise S/N > 4, which is typical for our ^{13}CO data (channel width 0.25 $\mathrm{km\,s^{-1}}$), that the minimal separated peak-to-peak velocity $(\delta v)_{\mathrm{min}}$ depends linearly on the velocity dispersion σ_{v} like,

$$(\delta v)_{\mathrm{min}} = 2\sigma_{\mathrm{v}} + 1\ \mathrm{km\,s^{-1}} \tag{5.1}$$

shown in Fig. 5.3. Emission lines with a velocity dispersion of $\sigma_v < 0.75$ km s^{-1} (3 channels) are not identified as an emission line. For filaments with low intensities (S/N ≤ 4) and for different intensities these limits must be degraded by $\Delta\sigma_v = 0.25$ km s^{-1} . We note, as the identification is done on the average spectrum over the filament skeleton, the velocity dispersion of an emission line can be larger than the intrinsic value because of velocity gradients along the skeleton. As a result, we are not resolving the kinematic substructure, like fibers ($\delta v \approx 1.0$ km s^{-1}, Hacar et al., 2013), but can determine the large scale kinematics of the filament.

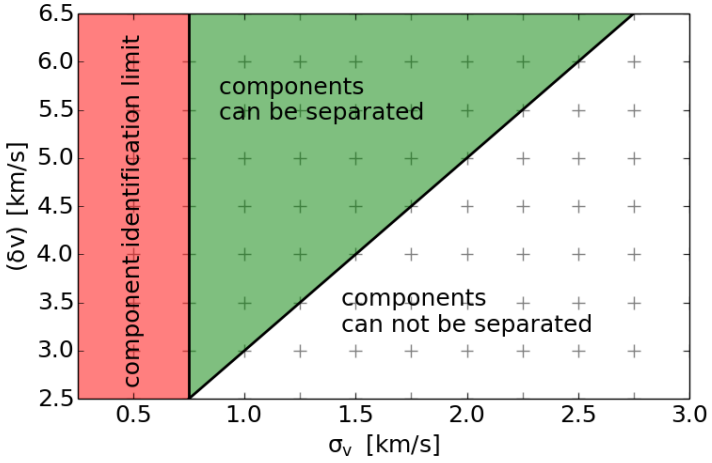

Figure 5.3: Component separation limits dependent on the velocity dispersion of the two velocity components. The crosses indicate the modeled data points

From previous studies (Schuller et al., 2017) we know that ^{13}CO is likely to be optically thick towards the densest regions, which might lead to effects like self-absorption, and could affect the separation method. As the abundance of C^{18}O is lower by ^{13}CO /C^{18}O = 8.3 (Miettinen, 2012), it is likely to be optically thin over the whole filament. During visual comparison of the ^{13}CO and C^{18}O spectra of all 604 ATLASGAL clumps within the filaments (position and velocity) optically thick ^{13}CO emission is seen in 76 clumps, corresponding to 13%. However, these clumps do not show a significant effect on the average spectrum over the whole skeleton. Hence, our method is unlikely to separate velocity components because of self-absorption features. Additionally, we conclude that the contribution of the dense core emission is small when compared to the emission integrated up over the whole filament.

In the next step we use the same method as for the average spectrum on every pixel, hence spectrum, along the skeleton within the identified velocity ranges. In this way we identify which part of the skeleton is detected in the different velocity components. Velocity components in which less than ten positions of the skeleton are detected in ^{13}CO are discarded, as these barely deviate from the noise, and we ensure a minimal elongated shape for all correlated structures (aspect ratio of 3 assuming a width of one beam). Additionally, we are able to detect multiple velocity components within the previously identified velocity range towards individual pixels. In the case where several

velocity components are found, we only keep the calculated moments for the one with highest intensity. This is done for the ^{13}CO and C^{18}O data. The separation of these subcomponents is limited by the smoothed velocity resolution. Also, we calculate the zeroth, first, and second "order" moments of skeleton pixels in each detected velocity component. With the first order measurements we potentially trace velocity gradients along the spine, but this is beyond the scope of this paper. However, the second order measurements, hence the velocity dispersion, of one pixel includes only the velocity gradient within one beam, which can be considered to be small. Therefore, the average over the skeleton pixels is a better estimate of the velocity dispersion of a filament than the value derived from the average spectrum and used in the further analysis. To check the results of these calculations we plot the derived moments on top of the position-velocity diagram of the filament candidate skeleton (Fig. 5.4). Additionally, we integrate over the velocity ranges of each velocity component; see Fig. 5.5.

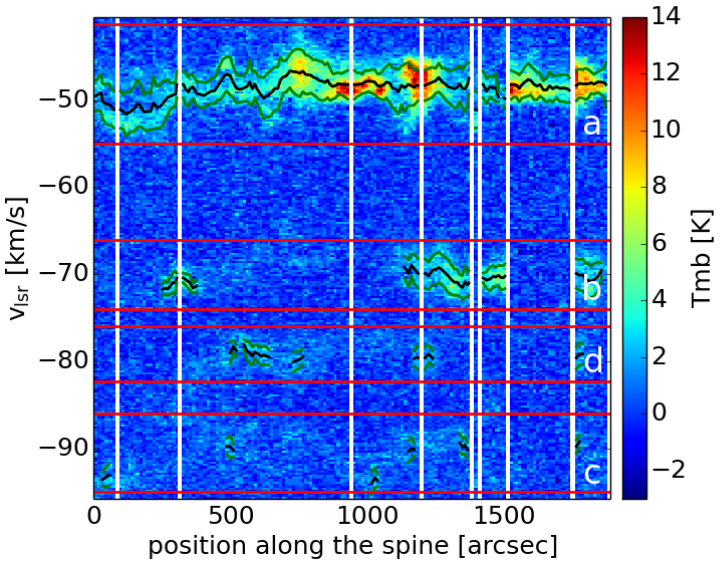

Figure 5.4: Position-velocity plot of the intensity along the skeleton of the filament candidate G333.297+00.073. The white stripes indicate the beginning/end of a skeleton branch. The first five branches show the longest connection through the skeleton from higher to lower galactic longitude and the last four are the branches to the side in the same direction. The horizontal red lines mark the identified emission intervals shown in Fig. 5.2 with intervals a, b, d, c from top to bottom. The jagged black and green lines mark the per pixel measured peak velocity and the 1σ interval of the detected emission peak.

5.3.3 Gas-dust correlation

We further estimate how much each velocity component contributes to the overall dust emission from a given filament candidate. We smooth and re-grid the ATLASGAL

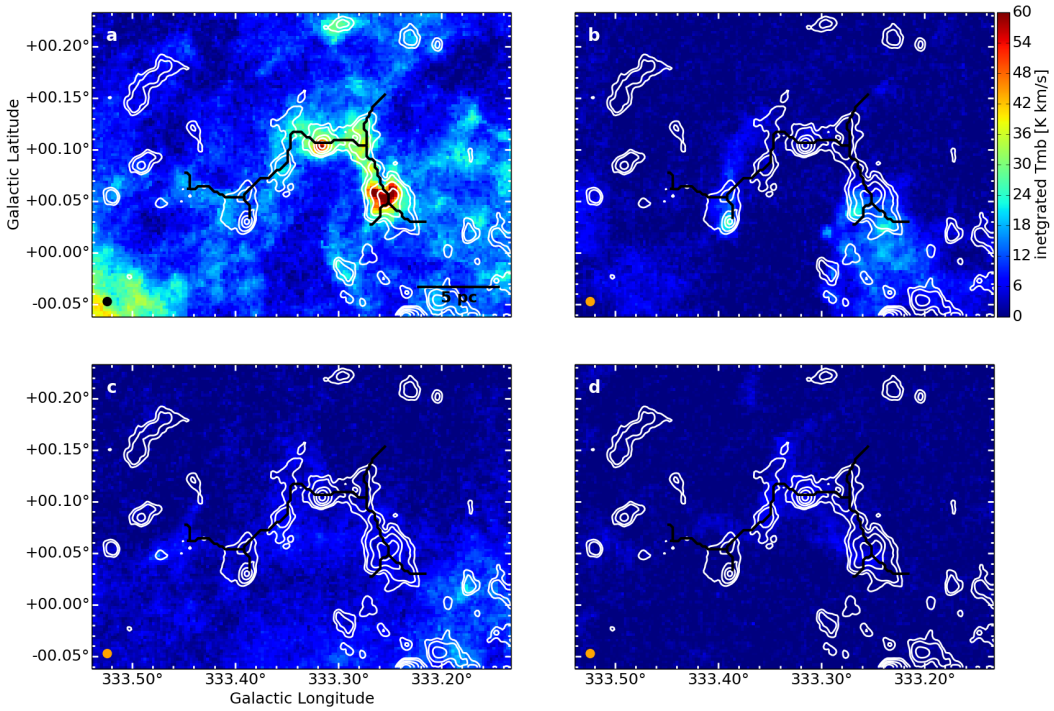

Figure 5.5: Integrated ^{13}CO(2 – 1) emission of the four velocity components of the filament candidate G333.297+00.073. The intensity was integrated over the velocity ranges −55.0 to −40.5 km s^{-1} (top left), −74.0 to −66.0 km s^{-1} (top right), −96.0 to −86.0 km s^{-1} (bottom left) and −82.5 to −76 km s^{-1} (bottom right). The beamsize is indicated by the circle in the lower left and the contours show the ATLASGAL [0.1, 0.2, 0.5, 1.0, 2.0] Jy/beam levels. The letters in the upper right refer to the marked intervals in Fig. 5.2.

maps, which were used for the candidate identification, to the resolution (30.1″) and pixel-grid (9.5″) of the SEDIGISM cubes. For comparison with the ^{13}CO integrated emission we restrict the maps (ATLASGAL and integrated ^{13}CO intensities per velocity component) to an area within a dilation box around the skeleton with a width of 3 beams (9 pixels), which covers the emission seen in ATLASGAL. We scale the ATLASGAL intensities with the minimum and maximum value to an interval of [0–1], using

$$I_s^{\rm dust} = \frac{I^{\rm dust} - \min(I^{\rm dust})}{\max(I^{\rm dust}) - \min(I^{\rm dust})} \tag{5.2}$$

where $I_s^{\rm dust}$ are the scaled ATLASGAL intensities, and $I^{\rm dust}$ the original ones, and min() and max() describe the minimal and maximal value of the pixel intensities within the dilation box. As the ATLASGAL emission traces only the small scale high density gas, the minimun value is typically around 0 Jy/beam. For the ^{13}CO data we define the intensity integrated over the velocity range of component i as $I^{\rm gas}(v_i) = \int_{v_i} T_{\rm mb}(v)\, dv$, where $T_{\rm mb}(v)$ is the main beam temperature, and v_i is the velocity interval of one

component as defined before. Also, for the correlation we do not apply any threshold. We use for the scaling the maximum and minimum value within the dilation box of the sum over the integrated intensity maps of all velocity components,

$$I_s^{\rm gas}(v_i) = \frac{I^{\rm gas}(v_i) - \min(\sum_i I^{\rm gas}(v_i))}{\max(\sum_i I^{\rm gas}(v_i)) - \min(\sum_i I^{\rm gas}(v_i))} \tag{5.3}$$

where $I_s^{\rm gas}(v_i)$ are the scaled ^{13}CO intensities of the velocity component i, and $I^{\rm gas}(v_i)$ are the original ones. Assuming a constant gas-to-dust ratio, the ATLASGAL maps should correlate with the molecular line emission integrated over all velocity components. We perform pixel-to-pixel correlation between the scaled ATLASGAL maps and the scaled integrated ^{13}CO maps of one velocity component using the same dilation box mask. Therefore, in cases of multiple components per candidate we will not find a one-to-one correlation, but we identify which velocity component shows the filamentary behaviour seen in dust emission. Additionally, noise in the observations and effects like CO depletion will affect the correlation plot. See Fig. 5.6 and appendix B.2 for examples.

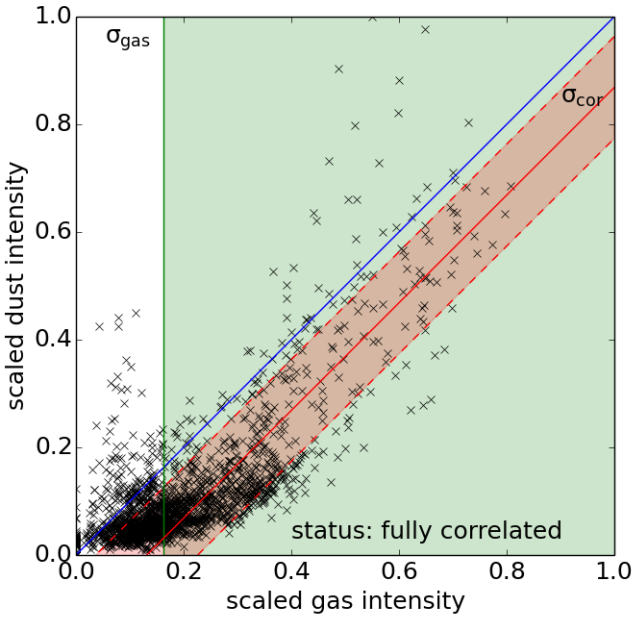

Figure 5.6: Gas-dust correlation plot of the brightest velocity component ("a" in the spectrum shown in Fig. 5.2) of the filament candidate G333.297+00.073. The blue line gives the one-to-one correlation. The green area indicates values above the $\sigma_{\rm gas}$ limit ($p_{\rm gas} = 0.51$). The red line shows the fitting result, and the area within the dashed red lines marks the $\pm\sigma_{\rm cor}$ surrounding ($p_{\rm cor} = 0.80$). $p_{\rm cor,\ gas} = 0.70$ is estimated from the overlap of these areas.

We analyze these correlation diagrams as follows. We calculate the standard deviation of the total (scaled) integrated intensities, $\sigma_{\rm gas} = \sigma(\sum_i I_s^{\rm gas}(v_i))$, presenting an

upper limit of the noise in the gas emission, and the standard deviation of the correlation, $\sigma_{\rm cor} = \sigma(I_s^{\rm dust} - \sum_i I_s^{\rm gas}(v_i))$. To estimate the intensity contribution of one velocity component, we perform a linear fit with a slope of 1 on the data points with $I_s^{\rm gas}(v_i) \geq \sigma_{\rm gas}$. We then derive the percentage of data points, which are above the $\sigma_{\rm gas}$ noise , $p_{\rm gas}$, which are within $\pm\sigma_{\rm cor}$ from the linear fit (red in Fig. 5.6), $p_{\rm cor}$, and which meet both conditions, $p_{\rm cor,\ gas}$. We then use these three parameters to characterize the different velocity components with the limiting values shown in Table 5.1.

Table 5.1: Limiting characterization parameters $p_{\rm gas}$, $p_{\rm cor}$, and $p_{\rm cor,\ gas}$ as described in Section 5.3.3. These parameters describe the population of three different areas in the correlation plots, see Fig. 5.6 and appendix B.2.

Status	$p_{\rm gas}$	$p_{\rm cor}$	$p_{\rm cor,\ gas}$
fully correlated	≥ 0.4		≥ 0.4
partially correlated	≥ 0.05		≥ 0.4
diffuse correlated	< 0.05	≥ 0.4	
uncorrelated (1)	≥ 0.05		< 0.4
uncorrelated (2)	< 0.05	< 0.4	

The limiting values for the characterization were obtained from the manual analysis of a test sample of filament candidates. This introduces a slight bias to the general analysis. The uncertainty of the characterization is difficult to determine, as the filament definition given by Li et al. (2016) can not be applied in a systematic way. Therefore, to get an objective, reproducible result, we decided to use this quantitative characterization over a visual approach as used by Li et al. (2016). A later visual inspection and different characterization will be possible, as all velocity components of all filament candidates, which are not uncorrelated, are handled in the same way in the subsequent analysis. Therefore, the characterization bias alters only the statistics of the characterization itself. However, the reliability of a filamentary shape decreases from fully correlated over partially correlated to diffuse structures, where partially correlated structures might not be continuous in position-position space, and diffuse structures might not show clearly enhanced emission from the surrounding. For simplicity we will still refer to all correlated structures as filaments. In total, we identified 422 filaments within the 283 filament candidates. More statistics of the characterization will be presented in Section 5.4.1 and 5.4.6.

5.3.4 Thermal and non-thermal motions

The unresolved kinematic motions in a molecular cloud can be estimated by the observed linewidth. The total velocity dispersion can be separated into a thermal and a non-thermal component. The thermal motions depend on the observed molecule and gas temperature. For the molecular gas temperature we assume a typical value of $T = 15$ K (Pillai et al., 2006; Wang et al., 2012, 2014), which is also in agreement with measured temperatures of ATLASGAL clumps (Urquhart et al., 2018). The non-thermal motions describe statistical motions of the gas, which are independent of the

kinetic temperature of the the gas. The non-thermal velocity dispersion, $\sigma_{\rm nt}$, is given by

$$\sigma_{\rm nt}^2 = \sigma_{\rm x}^2 - \frac{k_B T}{m_{\rm p} m_{\rm x}} \tag{5.4}$$

where $\sigma_{\rm x}$ is the measured second moment of ^{13}CO or C^{18}O, k_B the Boltzmann constant, $m_{\rm p}$ is the proton mass, and $m_{\rm x}$ is the molecular weight of the observed gas, here $m_{^{13}{\rm CO}} = 29$ and $m_{{\rm C}^{18}{\rm O}} = 30$. To derive the non-thermal velocity dispersion of the filament, $\sigma_{\rm nt}$, we average the measurements of each pixel along the skeleton, where we choose C^{18}O if it is detected and ^{13}CO otherwise. Therefore, this value is independent of velocity gradients along the skeleton, neglecting gradient effects within the beam, and it is less likely to be influenced by optical depth effects.

The thermal motion of the interstellar medium is given by the sound speed,

$$c_s = \frac{k_B T}{m_{\rm p} \mu} \tag{5.5}$$

where $\mu = 2.8$ is the mean molecular weight of the mean free particle (Kauffmann et al., 2008), and other parameters as previously defined. The total velocity dispersion of a filament is given by $\sigma_{\rm v} = \sqrt{c_s^2 + \sigma_{\rm nt}^2}$.

5.3.5 Mass and length of filaments

To calculate physical parameters of the 422 filaments it is crucial to estimate the distance towards them. However, estimating distances towards extended and diffuse structures, like these filaments, is difficult. Especially, solving the ambiguity of kinematic distances. Therefore, we use a method similar to that discussed by Li et al. (2016), but including additional measurements.

As a first step we identify all ATLASGAL clumps (Contreras et al., 2013; Urquhart et al., 2014) associated with the filaments. The distances towards these clumps have been estimated in Urquhart et al. (2018). As these estimates are based on kinematic distances, we must exclude the Galactic center region ($|\ell| < 5^\circ$), because of the large uncertainties. For filaments with an associated clump within the defined limits of the filament in position-position-velocity space) we simply assume the same distance. This provides distances for 222 filaments. In a second step we use friends-to-friends analysis to find adjacent clumps and adopt their distances for the filaments. This adds distances for another 114 filaments, but note the larger uncertainty for the distance estimate. For the friends-of-friends analysis we allow sources with a spatial offset of at most $10'$ (with 90% closer than $5'$) and a kinematic offset of at most 10 km s^{-1} (with 90% closer than 4 km s^{-1}). In total, we are able to assign a distance to 336 out of 422 filaments, including diffuse, partially correlated, and fully correlated ones. Additionally, we tested these estimates to be in agreement with (one of) the kinematic distances.

After we obtained the distances towards the filaments we can calculate their physical length. Here we take all pixels along the skeleton into account, towards which ^{13}CO was detected for the single filament. This allows us to get accurate measurements of the angular length for complex structures or partially correlated structures, including

the detected branches, by adding up the length over each relevant pixel. However, because of a possible inclination of the structures, the derived physical measurements represent lower limits to their true length.

For calculating the area and the mass of the filaments we again use a dilation box. With the distances in hand we are able to use a physical box-diameter. Here we take the box-diameter as a free parameter and in Section 5.5.1 we discuss the dependency between the filament mass and box-diameter. For calculating the filament mass we assume its diameter to be on the order of the star-forming size scale. For a first order approximation of the star-forming size scale we use the previously measured velocity dispersion within a filament, $\sigma_{\rm v}$, and assume a star formation time of $T_{\rm sf} = 2$ Myr (Evans II et al., 2009). The size scale is then given by $s_{\rm sf} = \sigma_{\rm v} \cdot T_{\rm sf}$. As box-diameters are limited to discrete multiples of pixels, we interpolate linearly the values from measurements of the next bigger and smaller box size.

We estimate the area covered by the filament, by summing over all pixels within the dilation box of the integrated intensity maps, within which we detect ^{13}CO emission (S/N > 5). The same positions are used to estimate the filament mass. Here we follow two different approaches: First we use the integrated ^{13}CO emission, $W(^{13}\mathrm{CO})$, in combination with the ^{13}CO X-factor, $X_{^{13}\mathrm{CO}(2-1)} = 1^{+1}_{-0.5} \times 10^{21}\mathrm{cm}^{-2}(\mathrm{K\,km\,s}^{-1})^{-1}$ derived by Schuller et al. (2017). This has the advantage of tracing only the emission within the specific velocity component. The molecular hydrogen column density, $N_i(\mathrm{H_2})$, in pixel i was then calculated by $N_i(\mathrm{H_2}) = W_i(^{13}\mathrm{CO})X_{^{13}\mathrm{CO}(2-1)}$. We then computed the mass using the equation

$$M(\mathrm{H_2}) = \sum_i N_i(\mathrm{H_2}) A_i \mu m_{\rm p} \tag{5.6}$$

where $N_i(\mathrm{H_2})$ is the $\mathrm{H_2}$ column density computed for pixel i, A_i its area, $\mu = 2.8$ the mean molecular weight per $\mathrm{H_2}$ molecule, and m_p the proton mass.

Second, we estimate the mass from dust emission maps of different surveys (ATLASGAL, ATLASGAL+PLANCK) using basic assumptions like a gas-dust ratio of $R = 100$, and a dust temperature of $T_D = 15\,\mathrm{K}$ (Urquhart et al., 2018). The mass of the filament candidate is then computed through the equation

$$M_\nu(\mathrm{H_2}) = \frac{S_\nu\, d^2 R}{B_\nu(T_D)\kappa_\nu} \tag{5.7}$$

where S_ν is the integrated flux density at the frequency ν of the used survey, d is the distance towards the structure, $B_\nu(T_D)$ is the Planck function at the given dust temperature, and κ_ν is the dust absorption coefficient, which is $\kappa_{870\mu\mathrm{m}} = 1.85\,\mathrm{cm^2\,g^{-1}}$ for the ATLASGAL emission (Schuller et al., 2009; Ossenkopf & Henning, 1994).

However, because of the contribution of the PLANCK data, the ATLASGAL+PLANCK survey traces not only the filament and the low column density gas around the filament, but also the diffuse Galactic dust emission, which ideally should be removed. To do so, we exclude the filament area of the maps using the inverse of the filament dilation box used previously. The remaining pixels should be dominated by non-filament emission. However, as the box has a width of three beams, we find a few cases in the most nearby (< 2kpc) filaments where the emission extends clearly

beyond the mask. Therefore, we use the 20th percentile value of the non filament pixels as estimate of the diffuse Galactic dust emission. We then correct the ATLASGAL+PLANCK maps for the diffuse emission and estimate the masses as shown previously. In Section 5.4.7 we discuss the differences of the these three mass estimates based on dust continuum emission and compare them to the ^{13}CO emission estimate.

5.4 Results

5.4.1 Final catalog

Using the methods described in the previous section we derived a large set of filament parameters. With these parameters we created a catalog of velocity coherent structures. The derived parameters of the catalog are shown in Table 5.2, and the complete catalog is shown in Tables B.1 and B.2. However, as several parameters are distance dependent, they cannot be calculated for the whole filament catalog. The following description of the derived parameters includes only the structures with a distance estimate. The catalog contains all 422 filaments of the 283 observed filament candidates, which show some correlation with the dust emission. In Table 5.3 we show the statistics of the characterization and the subsample for which we have distance estimates. The names of the structures are based on the initial filament candidate name from Li et al. (2016) and are extended by an integer starting from 0, indicating the velocity component.

5.4.2 Detection of filaments in ^{13}CO and C^{18}O

Out of the 283 ATLASGAL filament candidates within the SEDIGISM survey we detect correlated ^{13}CO emission for 260 filament candidates, which then show 422 velocity coherent (continuous kinematic structure, which cannot be resolved into separate components) filaments. We do not find a correlated ^{13}CO velocity component for 23 filament candidates, which is partially because of the sensitivity of the SEDIGISM survey, and partially because the candidates result from line-of-sight alignments of diffuse gas clouds. About 20% of the detected filaments show ^{13}CO emission at every position of the skeleton and for about 60% we detected ^{13}CO emission over at least half of the length of the skeleton. About 32% of the ^{13}CO detected filaments show no detection of C^{18}O on the skeleton, about 13% have C^{18}O detected over at least half of the skeleton, and for no filament C^{18}O is detected over its entire length; see Fig. 5.7.

This difference in the detection rate is very likely due to the different abundances of the molecules (^{13}CO/C^{18}O = 8.3; Miettinen, 2012). The C^{18}O line is expected to be weaker, resulting in a lower signal-to-noise ratio and the observed lower detection rate.

5.4.3 Galactic distribution

Using the distance estimates we can derive the Galactocentric coordinates and plot the positions onto a face-on artist's impression of the Milky Way (Fig. 5.8). We find

Table 5.2: Descriptions of the derived parameters. The complete catalog is shown in Tables B.1 (top) and B.2 (bottom).

Parameter	Unit	Description
		Table of measured parameters
Filament ID		
ℓ	$^\circ$	Galactic longitude of the center of the filament
b	$^\circ$	Galactic latitude of the center of the filament
Status		correlation with the ATLASGAL emission
N_c		number of detected velocity components in the original filament candidate
$v_{lsr}(^{13}CO)$	$km\,s^{-1}$	peak velocity derived from the ^{13}CO average spectrum
$v_{lsr}(C^{18}O)$	$km\,s^{-1}$	peak velocity from the $C^{18}O$ average spectrum
$\sigma(v_{^{13}CO})$	$km\,s^{-1}$	dispersion of the ^{13}CO peak velocities along the skeleton
$\sigma(v_{C^{18}O})$	$km\,s^{-1}$	dispersion of the $C^{18}O$ peak velocities along the skeleton
σ_v	$km\,s^{-1}$	average total velocity dispersion along the skeleton (derived from ^{13}CO and $C^{18}O$)
$\sigma_v(^{13}CO)$	$km\,s^{-1}$	average ^{13}CO velocity dispersion along the skeleton
$\sigma_v(C^{18}O)$	$km\,s^{-1}$	average $C^{18}O$ velocity dispersion along the skeleton
$\sigma_{v,t}(^{13}CO)$	$km\,s^{-1}$	^{13}CO velocity dispersion derived from the average spectrum
$\sigma_{v,t}(C^{18}O)$	$km\,s^{-1}$	$C^{18}O$ velocity dispersion derived from the average spectrum
		Table of derived parameters
Filament ID		
d	kpc	distance from the Sun
l	$^\circ$	angular length of the detected skeleton
$l(d)$	pc	physical length of the detected skeleton
M(ATG)	$M_\odot$	filament mass derived from ATLASGAL emission
M(ATG+P)	$M_\odot$	filament mass derived from ATLASGAL+PLANCK emission
M(dust)	$M_\odot$	filament mass derived from corrected ATLASGAL+PLANCK emission
$M(^{13}CO)$	$M_\odot$	filament mass derived from integrated ^{13}CO emission
$m_{crit,nt}$	$M_\odot\,pc^{-1}$	critical, non-thermal line-mass
m_{obs}	$M_\odot\,pc^{-1}$	observed line-mass
det. ^{13}CO		fraction of the skeleton detected in ^{13}CO
det. $C^{18}O$		fraction of the skeleton detected in $C^{18}O$
edge flag		skeleton truncated because of the edge of SEDIGISM
d flag		indicating the method for the distance estimate: 0 no distance; 1 inside ATLASGAL source; 2 nearby ATLASGAL source

that a large fraction of the filaments are likely to be associated with the near Scutum-Centaurus arm. We also find some filaments located in the near Sagittarius arm, the near and far 3-kpc arm, and the near Norma arm, but also in some inter-arm regions. We note that we do not have distance estimates for the Galactic center region ($|\ell| \leq 5^\circ$).

Histograms representing positions of the detected filaments with Galactic longitude and latitude are shown in Figs: 5.9 and 5.9, respectively. The distribution with Galactic longitude shows a peak around $l = -21^\circ$ with a strong decrease towards the outer Galaxy (only 14 structures for $l < -45^\circ$), and a decrease towards the Galactic center. As the filament candidates were identified in the ATLASGAL maps that trace only high column density dust emission, it is more unlikely to find filaments towards the outer Galaxy, which contains fewer dense molecular cloud regions. However, the number of filaments is also suppressed in the direction of the Galactic center, where identification is difficult because many structures along the line-of-sight are confused, and were categorized as networks, complexes or unclassified, such as the Galactic center region (Li et al., 2016). Nevertheless, comparing the distribution of filaments to the distribution of ATLASGAL clumps presented by (Beuther et al., 2012, Fig. 3) and (Csengeri et al., 2014, Fig. 16) shows similarities for the location of peaks, indicating

Table 5.3: Number of sources (with distance estimate) separated in different groups.

Groups	total	with dist.
filament candidates (Li et al., 2016)	517	
in SEDIGISM area	283	
≥ 1 correlated velocity component	260	
total velocity components	812	336
uncorrelated components	390	
filaments	422	336
fully correlated filaments	180	151
partially correlated filaments	191	148
diffuse component filaments	51	37

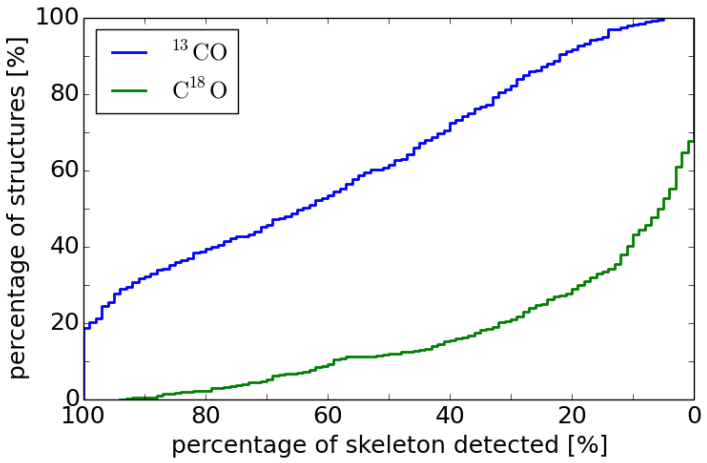

Figure 5.7: Cumulative histogram of the percentage of filament candidate skeletons detected in ^{13}CO (blue) and C^{18}O (green).

a possible correlation with active star-forming regions.

The distribution of the detected filaments with Galactic latitude (Fig. 5.9) shows a broad, almost flat behaviour similar to the findings of Li et al. (2016). However, we find the peak and mean ($\langle b \rangle = +0.02°$) of the distribution aligned with the Galactic mid-plane, which is in contrast to the general finding of more sources for $b < 0.0°$ than for $b > 0.0°$ (Beuther et al., 2012; Li et al., 2016). We note that our sample is not identical with that of Li et al. (2016), as we use only a sub-sample of their filament candidates and split some of these candidates in different velocity components, hence filaments.

5.4.4 Distributions of velocity dispersion, mass, length and distance

In the following, we give a short overview on the most interesting measured properties of the filaments, which are the non-thermal velocity dispersion along the skeleton, the

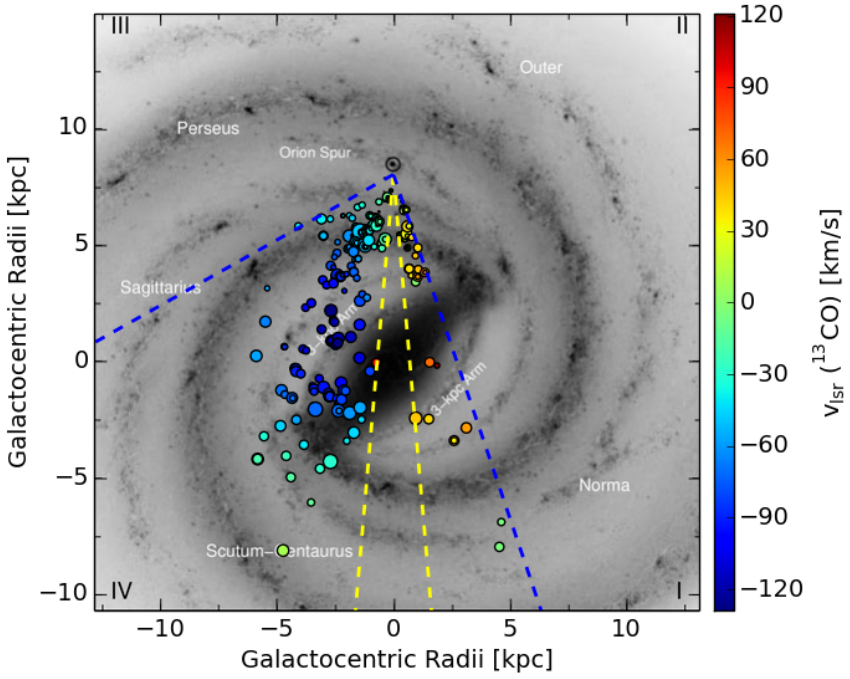

Figure 5.8: Filaments with distance estimated plotted onto an artist's impression of the Milky Way (Robert Hurt), the size is indicating the length of the filament, and the color indicates the ^{13}CO velocity. The yellow lines mark the range $|\ell| \leq 5°$, where distances are uncertain and the blue lines mark the SEDIGISM survey limits.

mass derived from the ^{13}CO emission, and the length of the filament, which we define as the sum over the detected parts of the skeleton.

For the calculation of the total velocity dispersion we assumed an isothermal medium of 15 K, see Section 5.3.4. The distribution of the resulting values is shown in Fig. 5.10. We find values reaching from about 0.5 km s^{-1} to 2.5 km s^{-1} with a relatively flat center between 0.8 km s^{-1} and 1.4 km s^{-1}, and a mean of about 1.17 km s^{-1}. Concentrating on the 180 fully correlated, hence, the most reliable filaments, we find a similar distribution with the mean at about 1.20 km s^{-1}. In general, these values are higher than what Arzoumanian et al. (2013) find in nearby filaments ($\sigma_v \approx 0.3$ km s^{-1}), but in agreement with studies of similar (more distant and more massive) objects like the DR21 filament (Schneider et al., 2010).

For the logarithmic distribution of the calculated masses, Fig. 5.10, we find a flat part between 1800 $M_\odot$ and 18000 $M_\odot$ with a mean mass of 8600 $M_\odot$. Again the distribution of the fully correlated filaments (151 with distance estimate) is similar to the complete distribution with a mean of 11000 $M_\odot$. For comparison we also show the mass ranges covered by other filament catalogs (Ragan et al., 2014; Wang et al., 2015; Zucker et al., 2015; Abreu-Vicente et al., 2016; Wang et al., 2016) and the study of Contreras et al. (2013). These studies report filaments with similar or higher masses.

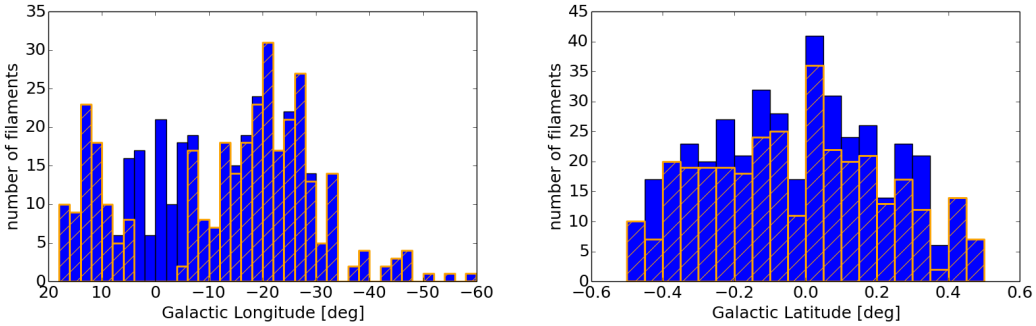

Figure 5.9: Distribution of the filament positions in Galactic Longitude **(left)** and Galactic Latitude **(right)**. The orange hatch marks the filaments with distance estimate.

However, several of these studies have tried to identify the largest structures in the Galaxy and therefore, are biased to larger structures. As a result, some filaments mentioned in this study are only parts of structures in the other catalogs. Also, we find filaments that are almost identical in several catalogs, like G11.046-00.069_2 (Snake) or G332.370-00.080_1.

We also find overlap between the catalogs for the lengths of the filaments (Fig. 5.10), where the shortest filaments of the other studies are as long as the mean of our sample (10.3 pc all, 11.1 pc fully correlated). In general, we cover the range from 2 pc to 100 pc with a peak around 8 pc.

Most filaments are found within 5 kpc from the Sun (Fig. 5.10), which is also the area where the other surveys found the long filaments. This area includes parts of the nearby Sagitarius and Scutum-Centaurus spiral arms. Another peak in the distance distribution is found at around 10 kpc, which is about the distance of the connection point of the Galactic bar with the Perseus spiral arm (see also Fig. 5.8).

Plotting the filament lengths against the estimated distances separated by the categories (Fig. 5.11), we find that especially the fully correlated filaments follow the distance distribution, while the others are more equally distributed. Also, we find no correlation between the longest filaments and the distance. This results in a larger scatter of lengths for a given distance. The shortest filaments reproduce our minimal length criteria of at least 10 pixels.

5.4.5 ^{13}CO – C^{18}O velocity comparison

As mentioned before, C^{18}O is less abundant than ^{13}CO and traces mainly the bright, dense parts of the filaments, where ^{13}CO is likely to be optically thick. However, to combine the kinematics of the two lines we need to be sure that both trace the same gas. Therefore, Fig. 5.12 shows the distribution of the absolute difference between the ^{13}CO and C^{18}O peak velocities of each filament derived from the average spectrum along the full skeleton, which is supposed to be zero if both istotopologues trace the same gas. The logarithmic distribution shows a plateau between 0.17 km s^{-1} and 1.0 km s^{-1} and

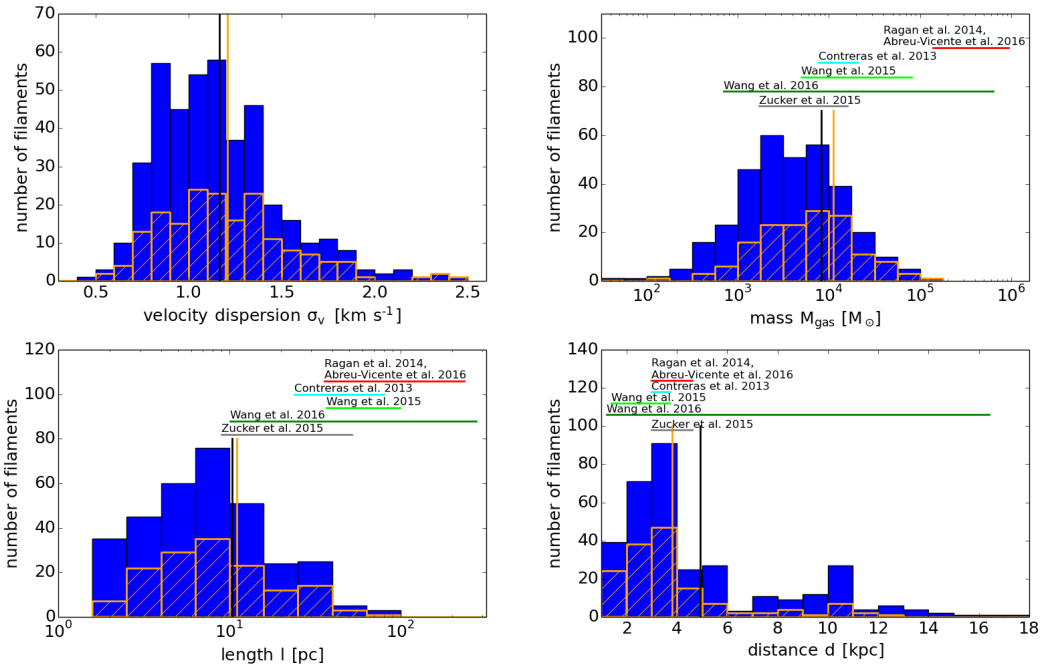

Figure 5.10: Distribution of the measured total velocity dispersion **(top left)**, mass **(top right)**, length **(bottom left)**, and distance **(bottom right)** of all filaments (blue). The fully correlated filaments are marked by the orange-colored hatched area. The vertical lines indicate the mean value for the complete (black) and the sub-sample (orange). The horizontal lines mark the ranges measured by the studies mentioned above the lines.

decreases steeply to both sides. Additionally, we find the largest difference in filaments with a signal-to-noise of the $C^{18}O$ average spectra of S/N < 5. In general, low S/N filaments peak at higher velocity differences (red).

We compare the observed distribution to a model distribution given by the mean velocity dispersion along the filament $\overline{\sigma}_\mathrm{v} = 1.17\ \mathrm{km\,s^{-1}}$ (see Section 5.4.4 and Fig. 5.10). Given the wide distribution of velocity dispersions this model gives only a first order impression of the expected distribution. We model the absolute difference between two velocities drawn from two Gaussian distributions. The dispersion of the differences is then given by $\sigma_{\delta v} = \sqrt{\overline{\sigma}_\mathrm{v}^2 + \overline{\sigma}_\mathrm{v}^2} = \sqrt{2}\,\overline{\sigma}_\mathrm{v}$. We generate an artificial difference distributions, using 10,000 draws to avoid statistical noise, bin the absolute values of the sample like the observed differences, and scale the height by 0.0373 to get a comparable total number of filaments as our sample. The resulting distribution (orange hatched in Fig. 5.12) does not agree with the observed one, as it is shifted to larger differences.

To further investigate this trend, we reduced the dispersion of the underlying velocity distribution until we found a distribution that matched the differences (black hatched) area. Its velocity dispersion is $\sigma_\mathrm{v}(\mathrm{model}) = 0.35\ \mathrm{km\,s^{-1}}$, which is about $\sqrt{2}$ times the channel width ($0.25\ \mathrm{km\,s^{-1}}$). We speculate therefore, that this distribution

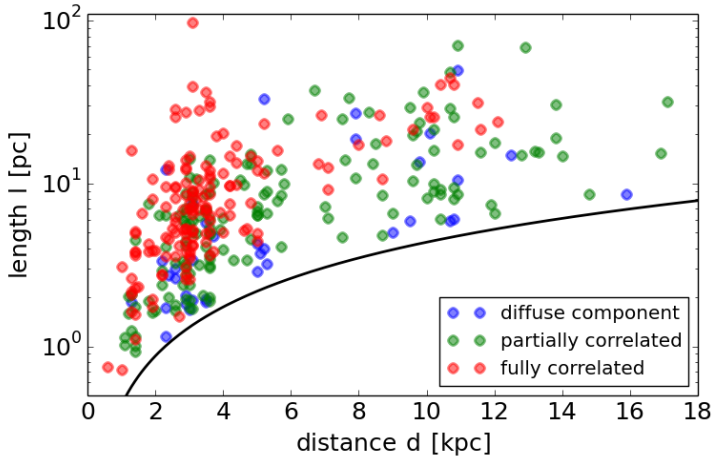

Figure 5.11: Filament length plotted against the estimated distance. The three filament categories are indicated by blue, green, and red for diffuse component, partially correlated, and fully correlated, respectively. The black line shows the criteria of a minimum length of 10 pixels.

is likely to arise from the sampling of the spectra.

However, we also see some filaments that show a larger difference between the ^{13}CO and C^{18}O peak velocities than can be expected by the channel-width introduced sampling issues. For these filaments we speculate that they show a gradient along the skeleton and are only partially detected in C^{18}O. To investigate this, we plot the velocity difference against the ^{13}CO velocity dispersion of the average spectrum (Fig. 5.12), as gradients along the skeleton result in a higher velocity dispersion. Additionally, filaments for which less than 10 % of the skeletons are detected in C^{18}O are marked in red. We find that almost all filaments fall below the one-to-one line and that all velocity differences are smaller than $2\sigma_{\rm v}(^{13}{\rm CO})$. We also see that 31 out of 43 filaments with a velocity difference larger than 1 km s^{-1} show low C^{18}O detection rates.

In summary we rule out systematic differences between the kinematic of the isotopologues. The observed differences are based on observational limitations, like the velocity resolution and sensitivity.

5.4.6 Multiplicity in velocity space

Filamentary structures are often identified in continuum emission maps. But it is unknown whether these structures are actual continuous filaments or only an effect of line-of-sight projection of multiple velocity components. We address this question with our data.

The 260 detected filament candidates split up in 422 velocity coherent filaments in total. Kinematic subcomponents are identified in single spectra for 14 of the filaments, but will not be discussed any further as more detailed studies will be needed. Analysis of the velocity components shows that about 58% of the filament candidates exhibit

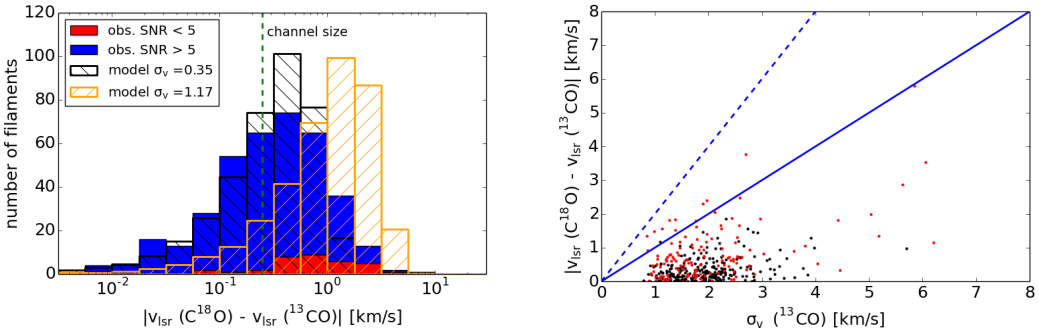

Figure 5.12: **Left:** Histogram of the absolute velocity difference. Sources with S/N < 5 are shown in red. On top the model difference distributions given by a underlying Gaussian velocity distribution with a dispersion of 1.17 km s^{-1} (orange) and 0.35 km s^{-1} (black) are shown. The green dashed line indicates the velocity channel size of the data. **Right:** Plot of the absolute velocity difference against the velocity dispersion of the filament, where filaments with a $C^{18}O$ detection rate below 10% are indicated in red. The blue lines show the one-to-one (1σ, solid) and two-to-one (2σ, dashed) relations.

one velocity component. Another significant fraction of the filaments, 27% and 12%, have 2 or 3 components, respectively. 6 filaments have 4 or more velocity components with a maximum of 7 components, seen in only one filament (Fig. 5.13).

The categorization of the velocity components shows that a filament candidate can have several velocity components even in the case of one component being fully correlated. This is shown in Fig. 5.13. However, a filament candidate with a single component does not necessarily have a fully correlated structure. In general, we find that filament candidates with fewer velocity components are more likely to have a fully correlated component, and candidates with an increasing number of velocity components are more likely to have partially correlated and diffuse components.

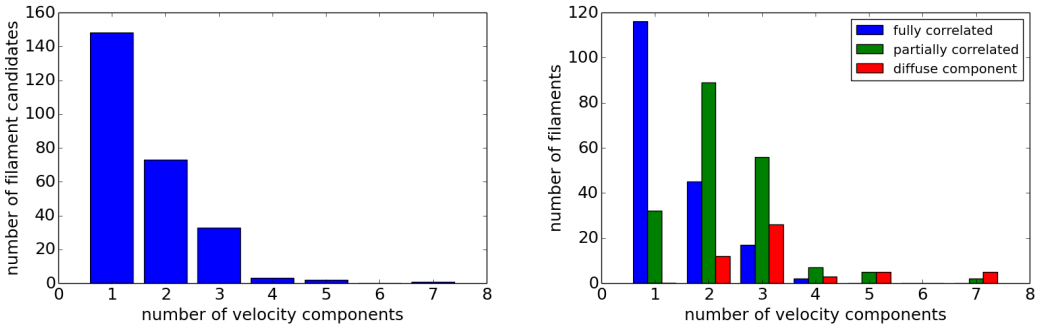

Figure 5.13: **Left:** Histogram of the number of velocity components per filament candidate. **Right:** Histogram of the number of velocity components for fully correlated (blue), partially correlated (green), and diffuse (red) structures.

Many structures are identified on continuum data that does not provide information about the velocity coherence. Therefore, we test whether there a correlation exists

between the intensities of 2D-data and the number of velocity components. With the known multiplicity of the filament candidates, we are able to show that filament candidates with several velocity components tend to be brighter (see Fig. 5.14). We do so as follows: we derive the mean and maximum intensity of the ATLASGAL dust emission and the ^{13}CO emission integrated over all velocity components. Because the statistical scatter of the intensity values shows a non-Gaussian distribution, we take the median and the 90th percentile value of the intensity distributions of each filament category (i.e. separated according to the number of components) as a qualitative measure. We also estimate the uncertainty of the median using a bootstrapping method. However, only the sample sizes of the filament categories with 1, 2, and 3 components are sufficient to use the bootstrapping method. In this method we draw new, random samples of intensities from among the observed values. We then calculate the median of these new, simulated samples. The resulting distribution of the median values then estimates the sampling function of the observed median and is used to estimate the uncertainty using the standard deviation. We find, that the medians of the ^{13}CO peak intensities increase outside their uncertainties as the number of velocity components increases. The same increase is also seen for the 90th percentile values (Fig. 5.14). Our data suggests a similar increase for the ATLASGAL peak intensities, but a flat behaviour is also consistent with the data. We could not find such a behaviour for the mean intensities of the filaments (not shown in figures).

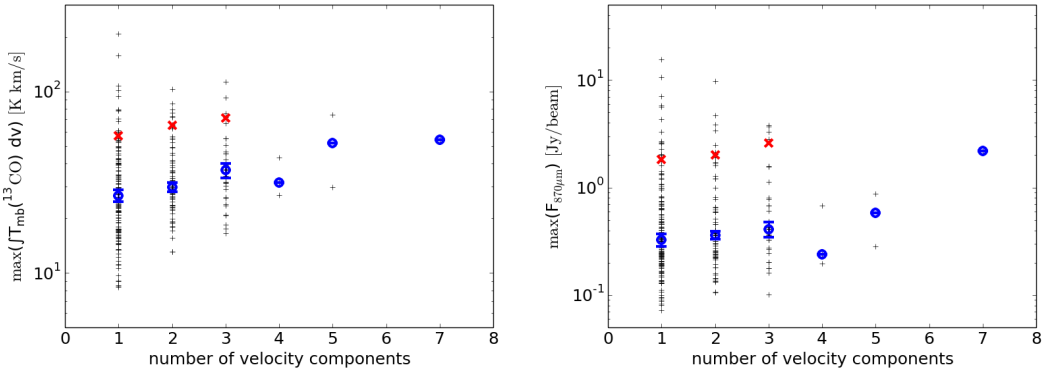

Figure 5.14: The peak integrated ^{13}CO intensity **(left)** and the peak ATLASGAL dust intensity **(right)** of a filament are plotted against the number of velocity components. The blue circles mark the median, and the red crosses mark the 90th percentile for each number of components. The error-bars show the uncertainty of the median derived by bootstrapping.

For filament candidates with multiple components we investigate whether two physically separate filaments can be located within the same spiral arm. Therefore, we show in Fig. 5.15 a histogram of the absolute peak-to-peak velocity difference (blue). The bins up to $\delta v = 10$ km s^{-1} are likely to be incomplete because of the component separation limit, as shown before (Fig. 5.3, Eq. 5.1). We compare the distribution of the observed velocity differences with model distributions (hatched) of

expected velocity difference from a spiral arm. We assume velocity dispersions of $\sigma_{v_1}(\mathrm{arm}) = 5\ \mathrm{km\,s^{-1}}$ and $\sigma_{v_2}(\mathrm{arm}) = 10\ \mathrm{km\,s^{-1}}$ following Reid et al. (2016) and Caldu-Primo et al. (2013). As we measure the absolute difference between two velocities drawn from a Gaussian distribution, the dispersion of the differences is given by $\sigma_{\delta v} = \sqrt{\sigma_v(\mathrm{arm})^2 + \sigma_v(\mathrm{arm})^2} = \sqrt{2}\sigma_v(\mathrm{arm})$. We sample the difference distributions with 10,000 draws to avoid statistical noise, bin the absolute values of the sample like the observed differences, and scale by 0.016 to get a comparable total number of filaments. We find, that the observed and the model distribution of $\sigma_{v_2}(\mathrm{arm})$ are similar for $\delta v \leq 30\ \mathrm{km\,s^{-1}}$, but we see more observed filaments for larger velocity separations. The model distribution for $\sigma_{v_1}(\mathrm{arm})$ does not describe the observed one. Therefore, we can conclude that a large fraction of separated filaments might be located in the same spiral arm with a velocity dispersion of $\sigma_{v_2}(\mathrm{arm})$, but we also see filaments from different Galactic structures along the line-of-sight. However, because of the kinematic distance ambiguity filaments located in different spiral arms can have similar line-of-sight velocities at specific Galactic Longitudes.

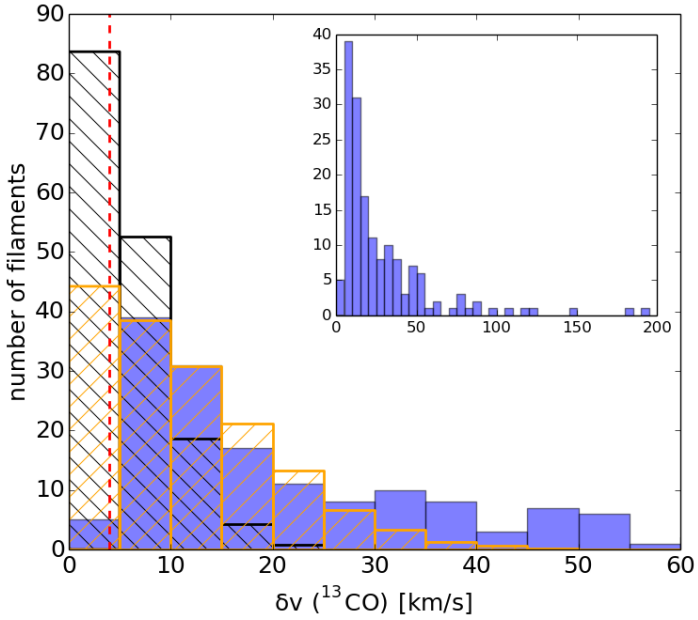

Figure 5.15: Histogram of the absolute difference in velocity between the neighboring velocity components of a filament. The upper right panel shows the complete distribution, while the main panel shows only the lower velocity separations. The black and orange hatched distributions indicate the models for spiral arm velocity dispersions of $5\ \mathrm{km\,s^{-1}}$ and $10\ \mathrm{km\,s^{-1}}$. The dashed red line indicates the average velocity separation limit of $3.5\ \mathrm{km\,s^{-1}}$ (see Eq. 5.1 and mean velocity dispersion of $1.17\ \mathrm{km\,s^{-1}}$)

5.4.7 Comparison of masses derived from gas and dust

Calculating the masses of the filaments is an important part of the analysis. However, it comes with some difficulties. Commonly, dust emission or dust extinction is used to calculate the mass of objects. However, because of the line-of-sight projection several filaments that may appear at the same position, and cannot be separated in the continuum data, this is not applicable here. Therefore, we need to use the CO emission to disentangle the projected emission from different structures in velocity space. For the mass estimate we then use the emission integrated over the velocity range of the filament. Specifically, we use the ^{13}CO emission as it has a higher signal-to-noise and traces the lower column density gas around the skeleton, and calculate the mass like described in Section 5.3.5.

We first have to test whether this X-factor is a good approximation for the whole survey area. To do so we take a sample of filaments, which show only one velocity component and are fully correlated with the ATLASGAL dust emission. We calculate the masses for this sample using the integrated ^{13}CO emission with Equation 5.6 and using the ATLASGAL and ATLASGAL+PLANCK dust emission with Equation 5.7. For all three data-sets we use the same mask around the skeleton. The comparison of the resulting masses is shown in Fig. 5.16.

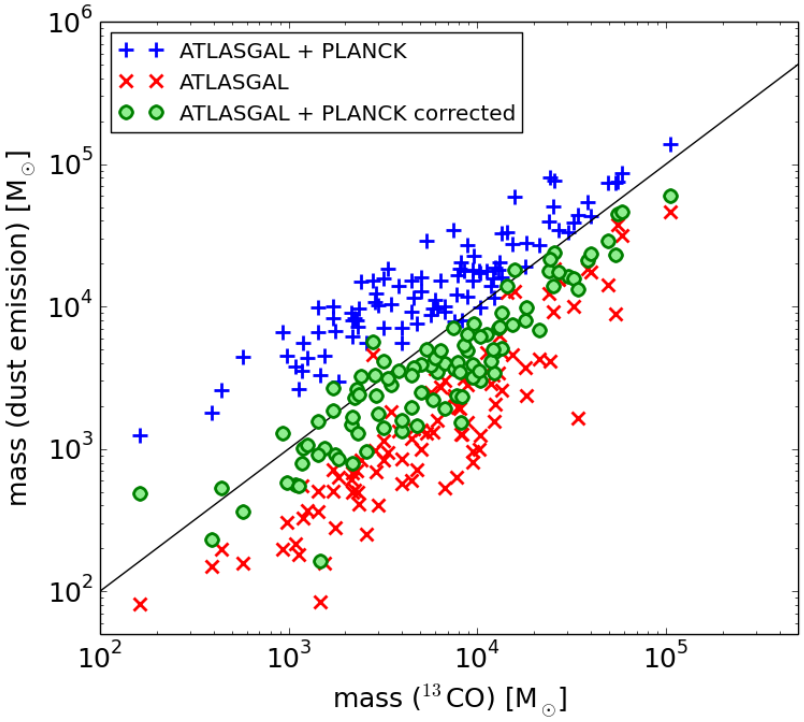

Figure 5.16: Mass per fully correlated filament derived from dust versus the mass derived from integrated ^{13}CO using an $X_{^{13}\mathrm{CO}(2-1)}$ factor from Schuller et al. (2017). The black line indicates the one-to-one ratio.

We find that masses derived from ^{13}CO are systematically larger than the masses derived from ATLASGAL, but systematically smaller than the masses derived from ATLASGAL+PLANCK. This behaviour is expected as the ATLASGAL maps are sensitive to the small scale (2.5′), high column density dust structures and extended emission from the diffuse surrounding gas is filtered out because of the observing technique (see Schuller et al. (2009)). Therefore, Csengeri et al. (2016) combined the ATLASGAL data with the PLANCK data, which traces the diffuse, large scale structures, but does not resolve the small scales because of the low resolution (4.8′). However, the combined data also traces the dust emission along the line-of-sight, i.e foreground and background. Thus, masses derived from ATLASGAL are likely to be underestimated while masses derived from ATLASGAL+PLANCK are likely to be overestimated.

As shown in Section 5.3.5, we corrected the ATLASGAL+PLANCK data for the line-of-sight emission towards every filament and used this data to derive another mass estimate. On average we find a mean Galactic emission of 0.52 Jy/beam (beam size of 21″). These corrected dust masses are in agreement with the ^{13}CO derived masses within a factor of 2. Therefore we conclude that the ^{13}CO X-factor derived from the SEDIGISM science demonstration field (Schuller et al., 2017) is a good approximation for the whole survey area.

5.5 Discussion

5.5.1 Radial filament profiles

Nearby (< 500 pc), low line-mass (< 100 $M_\odot\,pc^{-1}$) filaments have been found to have an FWHM size on the order of 0.1 pc (Arzoumanian et al., 2011). The corrected ATLASGAL+PLANCK and ^{13}CO data trace the wide range of column densities that is needed to study the filament profile. To ensure that we are looking only at true filaments we restrict our sample to the 151 fully correlated filaments with a distance estimate, but for completeness we show the results of the other filaments in Appendix B.3. However, measuring the filament profile is challenging as most filaments are not homogeneous, linear structures, but show branches and varying central densities.

Therefore, we do not extract the radial column density distribution directly from the data, but estimate the mass of the filaments within filament masks with increasing diameter, $s_{\rm box}$, using the same equations and assumptions as in Section 5.3.5. The mass, $M(R)$, is then given by

$$M(R) = 2l \int_0^R \Sigma(r)\, dr \tag{5.8}$$

where l is the length of the filament, $\Sigma(r)$ is the column density of the gas at distance r from the skeleton (to both sides, with the skeleton at $r = 0\,$pc), and $R = 0.5\, s_{\rm box}$ the maximum radius. We normalize the values with the mass from a box-diameter of $s_{\rm max} = 4$ pc, where the typically found radial profile is almost flat (Arzoumanian et al., 2011). The smallest box-diameter is given by the pixel size. The resulting mass curves of the ^{13}CO emission are shown in Fig. 5.17, and of the continuum emission

and less correlated filaments in Appendix B.3. As the physical resolution is changing with the distance towards the source, we group the filaments in four distance intervals d_i ($d_1 < 2$ kpc $< d_2 < 4$ kpc $< d_3 < 8$ kpc $< d_4$) and average the mass curves within these intervals (see Fig. 5.19).

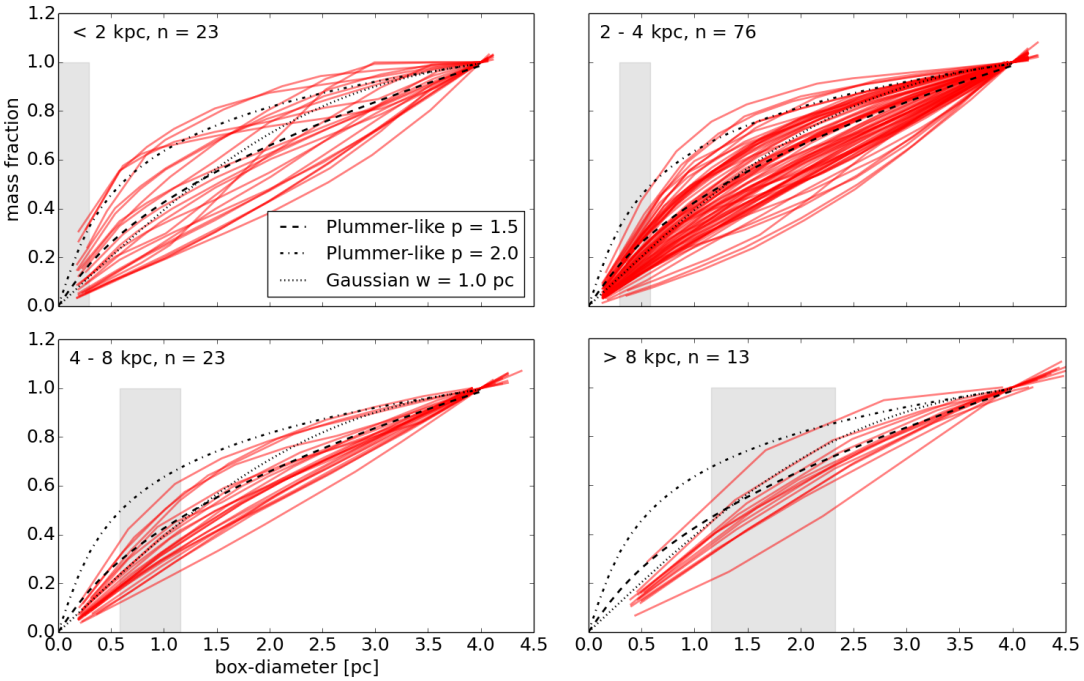

Figure 5.17: Fraction of the filament mass derived from ^{13}CO emission dependent on the box-diameter of the mask separated by distances. **Top left:** $d < 2$ kpc, **Top right:** 2 kpc $< d < 4$ kpc, **Bottom left:** 4 kpc $< d < 8$ kpc, **Bottom right:** $d > 8$ kpc. One curve describes one fully correlated filament at its distance estimate. The gray lines indicate the physical beamsize at distances of 2 kpc, 3 kpc, 6 kpc, and 8 kpc. The black lines show the integrated theoretical radial profiles, which describe a Plummer-like distribution $p = 1.5$ (dashed) or $p = 2.0$ (dash-dotted), and a Gaussian distribution with a dispersion of $w = 1.0$ (dotted).

The profiles of filamentary structures are found to be well described by a Plummer-like density distribution (Nutter et al., 2008; Arzoumanian et al., 2011; Contreras et al., 2013), which is given by

$$\rho(r) = \rho_c \left(1 + \left(\frac{r}{R_{\rm flat}}\right)^2\right)^{-p/2} \tag{5.9}$$

where ρ_c is the central density of the filament, and $R_{\rm flat}$ the characteristic radius of the flat inner part. The column density profile of the filament (Arzoumanian et al., 2011; Panopoulou et al., 2014) then is described by

$$\Sigma_p(r) = A_p \frac{\rho_c R_{\rm flat}}{[1 + (r/R_{\rm flat})^2]^{\frac{p-1}{2}}} \tag{5.10}$$

where $\Sigma = N(\mathrm{H_2})\mu m_p$, μ and m_p as previously defined, and $A_p = (\cos i)^{-1} \int_{-\infty}^{\infty} (1 + u^2)^{-p/2} du$, a finite constant for $p > 1$. Other studies (e.g., Arzoumanian et al., 2011) have shown that the inner part of the radial profile of a filament can also be well described by a Gaussian column density distribution. These two models are shown in Fig. 5.18, where they are normalized to an integrated intensity of 1.

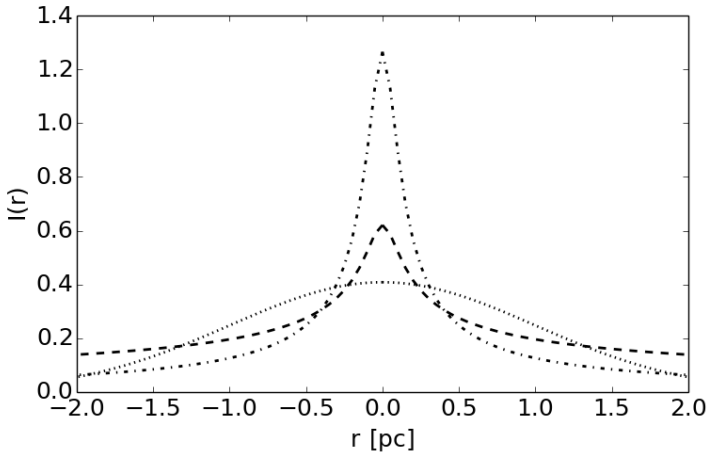

Figure 5.18: Theoretical filament profiles normalized to an integrated intensity of 1, which describe a Plummer-like function with $R_{\mathrm{flat}} = 0.1$ pc and $p = 1.5$ (dashed) or $p = 2.0$ (dash-dotted), and a Gaussian with a dispersion of $w = 1.0$ pc (dotted). The radial integration of these profiles is shown in Figs. 5.17 and 5.19.

The mass within a box around the theoretical filament is then given by Eq. 5.8. We plot the measured mass curves as well as the theoretical ones as $M(R)/M(2\ \mathrm{pc})$ and test different values for the exponent, p, and the inner radius, R_{flat}, of the Plummer-like distribution and for the dispersion, w, of the Gaussian (see Fig. 5.19).

A detailed analysis of the density structure of filaments is beyond the scope of this paper. Still, we perform a rough visual comparison between the observed radial column density profiles and modeled ones. We find that the Plummer-like distribution is in agreement with the average profile of the ^{13}CO and dust observations for $p \approx 1.5 \pm 0.5$ and $R_{\mathrm{flat}} \approx 0.1$ pc. Also the Gaussian column density distribution with a dispersion of $w = 1$ pc describes the observation within the uncertainties. However, the two fitting models lead to different $FWHMs$ for the filaments. While for a Plummer-like function the $FWHM_P = (2^{2/(p-1)} - 1)^{1/2} R_{\mathrm{flat}}$ ($FWHM_{2.0} \approx 0.17$ pc, $FWHM_{1.5} \approx 0.39$ pc (Heitsch, 2013a), for the Gaussian $FWHM_G = \sqrt{8 \ln 2}\, w \approx 2.36$ pc.

One possible interpretation is that the Gaussian traces only the low column density surrounding of the filament, but not the dense inner part, hence the actual filament. From previous studies (see Arzoumanian et al., 2011; Panopoulou et al., 2014) and the Plummer-like function we see measurements of the FWHM between 0.1 pc and 0.6 pc. The physical beam size of the SEDIGISM data at a distance of 2 kpc is about 0.3 pc and therefore, we are at the resolution limit for the dense filament spine, but note that the mass curves (integral over the radial profile) have a dependency on R_{flat} in the

Plummer-like case. However, we find that small changes of $R_{\rm flat}$ do not significantly change the agreement with the observation. Therefore, we conclude that the mass of the filament is dominated by the low column density gas surrounding the spine, and that the resolution of the SEDIGISM data is not sufficient to meaningfully fit the inner spine with a Gaussian radial profile.

The exponent of the average density profile is $p \approx 1.5$, which is in agreement with the lower limit found by Arzoumanian et al. (2011). The single profiles scatter between $p \approx 1.0$ and $p \approx 2.0$, with the scatter decreasing with more distant filaments most likely because of the smaller sample. Also, we tested the effect of the beam size to the theoretical radial profiles by convolving the profile with a Gaussian beam. The resulting theoretical mass curves are shallower with increasing distance, but not significantly, given the scatter of the single observed mass curves. The study of Arzoumanian et al. (2011) analyzes prominent filaments in nearby molecular clouds using dust continuum emission. This selection of prominent filaments might give a bias towards higher exponents. Theoretically, an isolated, isothermal, cylindrical filament in hydrostatic equilibrium would be expected to have an exponent of $p = 4$ (Ostriker, 1964). However, this exponent is typically not found in observations and models (Juvela et al., 2012; Kainulainen et al., 2015). Low resolution and signal-to-noise data explain only partially the observed exponents. Therefore, observations suggest that filaments are embedded in a surrounding molecular cloud (Fischera & Martin, 2012), not isothermal (Recchi et al., 2013) and/or not in hydrostatic equilibrium (Heitsch, 2013a,b).

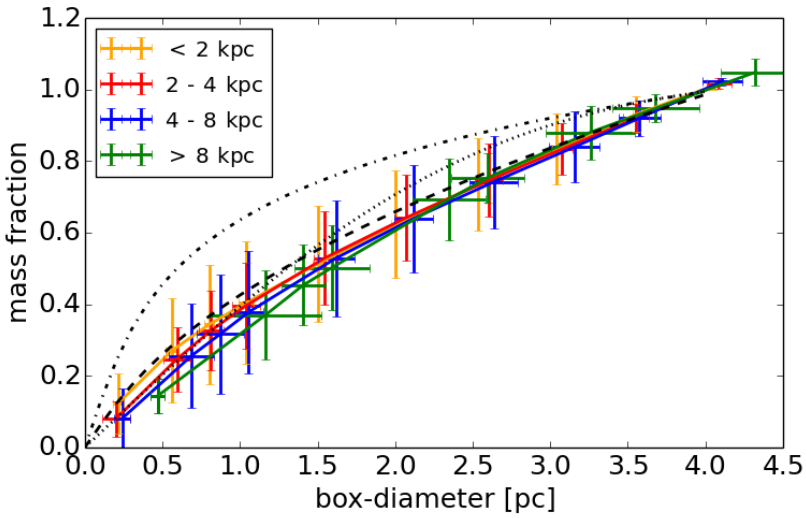

Figure 5.19: Average fraction of the filament mass derived from ^{13}CO emission dependent on the box-diameter of the mask. The color indicates the distance of the filament with d_1 orange, d_2 red, d_3 blue, and d_4 green. The errorbars indicate the dispersion of the measured mass fraction and box-diameter. The black lines are same as Fig. 5.17.

It is important to mention that for an exponent of $p < 2$ mathematically the mass diverges with an increasing radius. This can be seen in Fig. 5.18. As a result the

mass, M, and therefore, also the line-mass (mass per unit length), $m = M/l$, are not well-defined. However, filaments are not isolated structures, but surrounded by low density gas, which sets boundary conditions that are not considered in this model. As mentioned before, we decided to use a radius dependent on the velocity dispersion of the filament to estimate the mass of the filaments in this study.

5.5.2 Stability against collapse

Thermally supercritical filaments are commonly seen as star formation sites. Therefore, they need to build the connection between the diffuse gas of the molecular cloud and the dense gas in the star-forming cores. Inutsuka & Miyama (1992) showed that isothermal, infinitely long, self-gravitating cylinders will collapse radially if their line-mass (mass per unit length) exceed a critical value, and fragment along the axis in the sub-critical and equilibrium case. The critical line-mass is given by

$$m_{\rm crit,th} = \frac{2c_s^2}{G} \tag{5.11}$$

(Ostriker, 1964), where G is the gravitational constant and c_s is the sound speed of the medium, which is dependent on the gas temperature T (Eq. 5.5). Assuming a typical gas temperature of $T = 15$ K the critical line-mass is $m_{\rm crit} = 20\ {\rm M_\odot\,pc^{-1}}$.

Based on our observations and analysis we can estimate the line-mass for all the filaments with a distance estimate by $m_{\rm obs} = M/l$, where M is the mass estimated from the ^{13}CO emission, and l is the length along the velocity coherent skeleton. Because of the separation of the velocity components this length does no longer securely describe the linear shape (with small branches) of the original filament candidate sample, especially for the not fully correlated filaments. Therefore, we concentrate this discussion on the fully correlated filaments, but also perform the calculations for the others.

The line-masses we observe with our resolution are significantly above the critical thermal value (see Fig. 5.20). This leaves us with two possible conclusions: either the filaments are collapsing radially or they have a supporting mechanism additional to the thermal pressure. Moreover, we find that the linewidth of the molecular gas is significantly larger than the sound speed, $c_s = 0.21\ {\rm km\,s^{-1}}$. This increased linewidth can support both theories, as it can be interpreted as either structured motions, like collapse, or turbulent motions within the gas.

Assuming that non-thermal motions contribute to the supporting mechanism, equation 5.11 can be modified to

$$m_{\rm crit,tot} = \frac{2(c_s^2 + \sigma_{\rm nt}^2)}{G} \tag{5.12}$$

(Fiege & Pudritz, 2000), where $\sigma_{\rm nt}$ is the non-thermal velocity dispersion of the filament, and $m_{\rm crit,tot}$ is the critical, total (thermal and non-thermal) line-mass. After determining the velocity dispersion for all filaments, we can calculate the critical non-thermal line-mass and compare it with the observed one (Fig. 5.20).

The uncertainty of the critical line-mass is given by the observed velocity dispersion and therefore depends on the velocity resolution and the quality of the signal. The main

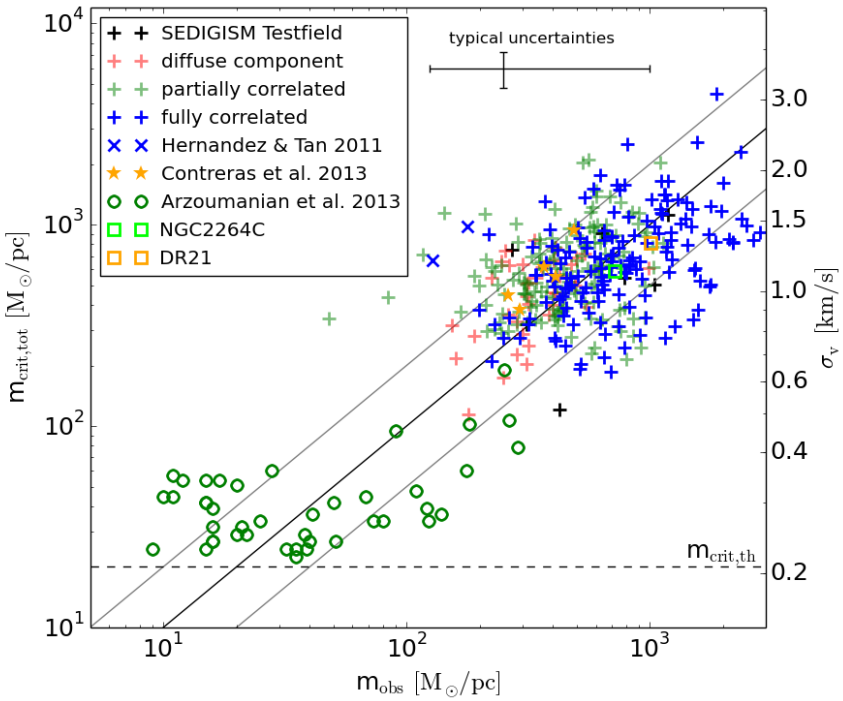

Figure 5.20: Critical, non-thermal line-mass derived from the velocity dispersion versus observed line-mass using integrated ^{13}CO. The fully correlated filaments are indicated in blue, and the other filaments of this study in a shaded green and red. The black solid line shows the one-to-one correlation, the gray lines indicate a factor 2 uncertainty, and the dashed line shows the critical thermal line-mass.

contributions for the uncertainties of the mass estimates are the X-factor (factor of 0.5–2), optically thick ^{13}CO emission (factor of 1–2), and the distance. As the length is also dependent on the distance estimate, the line-mass is only linearly dependent on the distance, which adds another factor of 0.8–1.2 to the uncertainty. Additionally, the length is measured as projection on the sky and therefore, the observed line-mass is an upper limit considering possible inclinations. The typical uncertainty is given by the black cross in Fig. 5.20. Additionally, it needs to be mentioned that based on the resolution of our data we are only able to derive global parameters. Higher resolution data (spatial and kinematic) could reveal substructures, which might lead to different results.

We find that the critical, non-thermal line-mass is, within the uncertainties, in agreement with the observed line-mass. Therefore, Eq. 5.12 seems to describe a common relation between the observed linewidth and line-mass in the form $m \propto (c_s^2 + \sigma_{\rm nt}^2)$. The sound speed, c_s, depends only on the temperature of the ISM, which can be assumed to be about constant. Hence, the line-mass is proportional to the non-thermal motion. We also find that partially correlated filaments and diffuse components follow

the same relation as the fully correlated filaments, but with a slightly wider spread.

We now want to investigate where this relation comes from. As we discussed before, one explanation might be infall motion. Inutsuka & Miyama (1992) showed that infinitely long, isothermal filaments with a line-mass above the critical value collapse radially. Heitsch et al. (2009) and Heitsch (2013a) determined the accretion velocity profile, $v(R)$, for gas in a steady-state free-fall onto the filament axis as

$$v(R) = 2\left(Gm \ln \frac{R_{\rm ref}}{R}\right)^{1/2} \tag{5.13}$$

where G is the gravitational constant, m is the line-mass of the filament, $R_{\rm ref}$ is the limiting, outer radius of the filament, and R is the radial position of the gas.

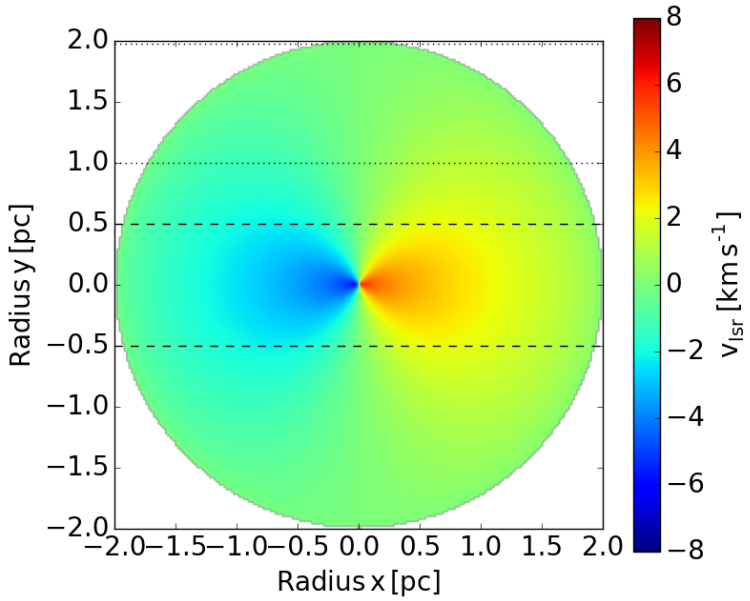

Figure 5.21: Line-of-sight velocity distribution across a slice of a filament based on Eq. 5.13 using a line-mass of $m = 500$ M$_\odot$ pc^{-1} and $R_{\rm ref} = 2.0$ pc. The observer is located on the right side, observing the whole slice, the inner part (dashed lines), and outer part (dotted lines), which where analyzed separately.

We use this radial velocity distribution, $v(R)$, to estimate the signal which would be observed from a collapsing filament, similar to Heitsch (2013a). First, we derive the line-of-sight velocities, v_{lsr}, across the filament for an observer looking edge on (see Fig. 5.21),

$$v_{lsr} = v(R) \cdot \frac{x}{R} \tag{5.14}$$

where R is the radial distance to the center, and x is the position in the x-axis direction of the Cartesian coordinate system. Second, we draw for each position in the filament 50 values from a Gaussian distribution centered on the derived velocities with a thermal

velocity dispersion of $c_s = 0.21$ km s^{-1}. Third, we plot a weighted histogram of the velocities with bins identical to the SEDIGISM channel width of 0.25 km s^{-1}, where we use the density at the position of the filament as weight. The density is given by a Plummer-like distribution (see Section 5.5.1). From the weighted histogram we calculate the standard deviation, hence the theoretically observed velocity dispersion.

Within this template we vary the line-mass, m, the exponent of the density profile, p, and the area of the filament we observe (complete, middle, edge) to study their effect on theoretical signal. We choose the outer radius $R_{\rm ref} = 2.0$ pc and the characteristic radius of the density distribution $R_0 = 0.1$ pc, see Section 5.5.1. The results are shown in Table 5.4 and Fig. 5.22.

Table 5.4: The three input parameters, the resulting velocity dispersion $\sigma_{\rm v}$, derived from the modeled collapse spectra, and the expected total velocity dispersion, following the found relation with m.

Fig. 5.22	m	p	area	$\sigma_{\rm v}$	$\sigma_{\rm crit,nt}$
	M$_\odot$ pc^{-1}			km s^{-1}	km s^{-1}
a	100	1.5	all	1.03	0.46
b	500	1.5	all	2.29	1.04
c	1000	1.5	all	3.23	1.47
d	500	2.0	all	2.65	1.04
e	500	3.0	all	3.24	1.04
f	500	1.5	middle	2.86	-
g	500	1.5	edge	0.62	-

We find that the infall motions indeed show the observed relation between line-mass and velocity dispersion, $m \propto \sigma_{\rm v}^2$ (Table 5.4, models a, b, c). However, the theoretical velocity dispersion is higher by a factor of 2 than the observed values. Additionally, we did not take turbulent motions into account, which would be caused by the infall (Heitsch, 2013a), and give a wider theoretical signal. To fit the observations, the collapse needs to be slowed down, which can be caused by the turbulence created by the collapse. Finding a combination of collapse and turbulent motions that would reproduce the observed kinematics is beyond the scope of this study.

Another way to identify ongoing collapse could be an analysis of the shape of the emission lines (Schneider et al., 2010). The theoretical line profiles show double-peaked shapes towards the center of the filament and for filaments with a steep density profile. However, a comparison of the theoretical line shapes with the observed ones is difficult as several other effects can alter the shape, like spatially unresolved motions of the filament within the beam, or self-absorption, also see Heitsch (2013a) for different inclination angles. In a few filaments we find some evidence for a double-peaked velocity profile (see Section 5.3.2). But a more detailed analysis of, preferably, geometrically simple filaments with higher spatial and kinematic resolution would be necessary to address the effects of complex kinematics.

Rapid radial collapse would lead to extremely narrow filaments, which rarely have

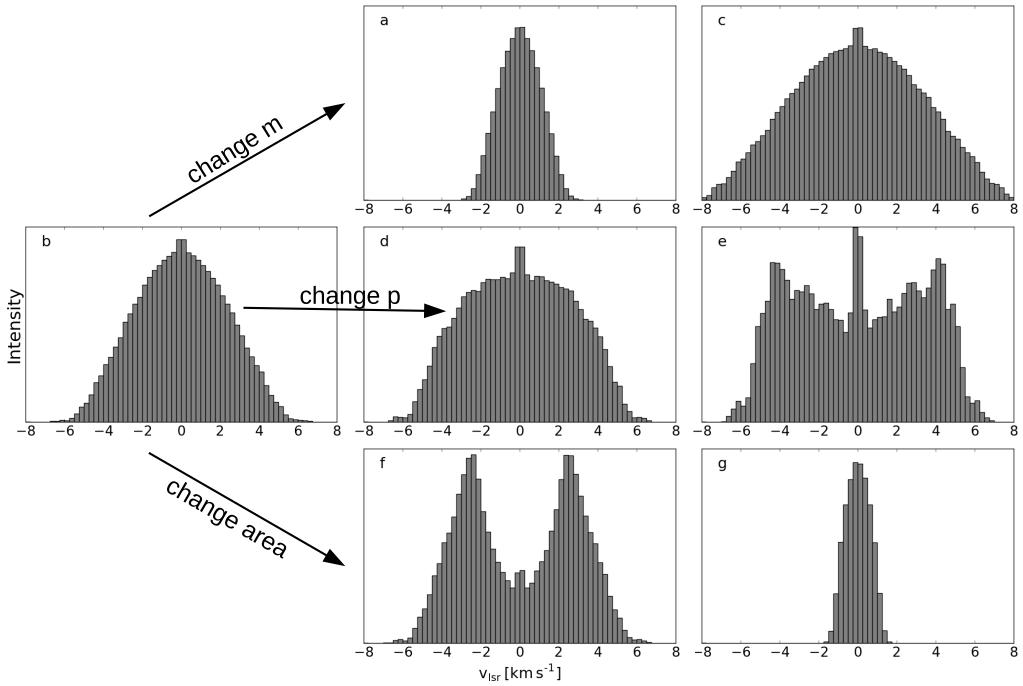

Figure 5.22: Theoretical molecular line profiles with varying parameters, see Table 5.4.

been observed up to now (e.g., Stutz & Gould, 2016). However, Heitsch (2013a) shows that the fragmentation timescales are shorter than the collapse timescales, which is supported by the fact that fragmentation is seen in almost all filaments (Jackson et al., 2010; Kainulainen et al., 2013; Takahashi et al., 2013; Wang et al., 2014; Beuther et al., 2015; Teixeira et al., 2016; Kainulainen et al., 2017). Our finding of slowed collapse would increase the difference between the timescales, which is still in agreement with the observations. Also, simulations of filament evolution by Chira et al. (2018) show a start of fragmentation before the filaments reach the critical mass for gravitational collapse.

However, we also cannot rule out the possibility that the observed velocity dispersion is mainly created by turbulent motions. These turbulent motions are discussed to increase the internal pressure and support the filament against gravitational collapse. Therefore, this theory is also in agreement with the observations.

5.6 Conclusions

In this study we studied spectral line emission from 283 filament candidates detected with ATLASGAL continuum dust emission from the catalog of Li et al. (2016) in the SEDIGISM ^{13}CO and C^{18}O survey. As these candidates can be the result of line-of-sight projection of multiple structures, we tested the candidates for coherence in velocity space and derived the mass, size, and a collection of kinematic properties. To do so we developed an automated analysis tool that finds the different velocity com-

ponents of a candidate, if existing, separates them and checks for correlation with the original ATLASGAL emission. We found 422 velocity-coherent filaments that correlate completely or partially with the original candidate. For these filaments we find the following:

- Two-thirds of the filament candidates are single velocity-coherent structures. The other candidates are line-of-sight projections of mainly two and three velocity components, and up to one candidate with seven velocity components. Also, we found a possible indication for a correlation between the maximum intensity within the filament candidate and the number of velocity components for the integrated ^{13}CO and ATLASGAL dust emission, but a flat behaviour is within the uncertainties.

- Comparing the kinematics of the filaments seen in ^{13}CO and C^{18}O , we could show that both isotopologues trace the same gas. Differences found in the comparison could be identified as biases arising from low signal-to-noise C^{18}O data.

- The filament profiles are on average in agreement with a Plummer-like density distribution with an exponent of $p \approx 1.5 \pm 0.5$. The inner radius cannot be constrained exactly because of the limited resolution of the data. This low exponent indicates that filaments are typically located within larger molecular clouds, and therefore, the outer radius of a filament cannot be well defined. For the mass estimates we chose a radius which includes the gas that can take part in star formation within the next 2 Myr.

- The observed line-mass of the filaments is in agreement with the critical non-thermal line-mass and significantly higher than the critical thermal line-mass. However, we do not know the source of the observed velocity dispersion. Comparing the relation we find between velocity dispersion and line-mass with the theoretical infall velocity profile based on Heitsch (2013a) generally does not reveal evidence for free-fall collapse. However, radial infall of the gas onto the skeleton can possibly explain the relation.

In this study we analyzed the kinematics of 283 filament candidates, finding 180 reliable velocity coherent filaments, 151 with distance estimates between 1 kpc and 13 kpc, and 242 other velocity coherent filamentary structures in the line-of-sight of the candidates, leading to the largest statistics of filament parameters so far. However, due to the spatial resolution of $30''$ and velocity resolution of 0.25 km s^{-1}, the derived parameters generally only describe global behaviour of the filaments. As the evolution and fragmentation of filaments is a hierarchical process it will be necessary to also study the smaller scales. High resolution observations to recover the small scales (< 0.1 pc) are essential, and this study can be the starting point for the selection of a representative sample for such higher resolution follow-ups.

Acknowledgments

We want to thank the anonymous referee for constructive and very detailed comments. Also, we thank Guang-Xing Li for supporting this study by offering additional data and information on the filament candidates. Also, we thank Prof. Kostas Tassis, Dr. Dario Colombo, Carsten König, and the rest of the SEDIGISM consortium for support and productive discussions.

M.M. is supported for this research through a stipend from the International Max Planck Research School (IMPRS) for Astronomy and Astrophysics at the Universities of Bonn and Cologne. T.Cs. acknowledges support from the *Deutsche Forschungsgemeinschaft, DFG* via the SPP (priority program) 1573 'Physics of the ISM'. H.B. acknowledges support from the European Research Council under the Horizon 2020 Framework Program via the ERC Consolidator Grant CSF-648505. L.B. acknowledges support by CONICYT project PFB-06. This work of J.K. has received funding from the European Union's Horizon 2020 research and innovation program under grant agreement No 639459 (PROMISE).

Chapter 6

Summary

In this thesis we investigated the physical properties of massive filamentary molecular clouds throughout the inner Galactic plane. In particular, we studied one extremely long filamentary cloud in more detail, commonly known as Nessie, and analyzed the properties of a large given sample of filaments and filament fragments identified using ATLASGAL dust emission data. As we expect the Nessie filament to be a special case of massive filaments, we summarize these studies independently and bring the results in context afterwards.

6.1 The long Nessie filamentary cloud

The Chapters 2 and 3 are dedicated to study the classical and the extended Nessie filament, respectively. In both Chapters we estimated the distance towards Nessie and found estimates of $d_{\rm cl} = 3.5 \pm 0.5$ kpc based on NIR source-counts (Chapter 2) and $d_{\rm ex} = 3.1 \pm 0.1$ kpc based on kinematic distance measurements (Chapter 3). These estimates are in agreement given their uncertainty, however the difference needs to be taken into account when comparing the results of these studies. Both estimates place Nessie in or close to the Scutum-Centaurs spiral arm as it was previously suggested by Goodman et al. (2014) and Ragan et al. (2014). Our main results are:

- Combined near- and mid-infrared dust extinction measurements allow us to derive a high-resolution (~ 0.03 pc), high dynamic range ($N(\mathrm{H_2}) = 3$ – 100×10^{21} cm^{-2}) column density map of the classical Nessie filament. Based on this map we calculated a mass of 4.2×10^4 M$_\odot$ (at 3.5 kpc), considering regions above $N(\mathrm{H_2}) \gtrsim 3 \times 10^{21}$ cm^{-2}, which leads to a mean line-mass of about 627 M$_\odot$ pc^{-1} for a length of 67 pc. Therefore, Nessie is a massive filament.

- Using a wavelet approach we analyzed the fragmentation of the filament across scales in the range from 0.1 pc to 10 pc and detected fragmentation at all scales. Assuming an ellipsoidal shape for the fragments, we calculated their masses, densities and nearest-neighbor separation. We find that their masses decrease and densities increase for smaller size-scales, where at the smallest scale, the typical masses of the fragments are 0.4 M$_\odot$ and mean densities are $\sim 10^4$ cm^{-3}. This describes the fragmentation of the large diffuse structure into small dense clumps. The fragmentation length is given by the median nearest-neighbor separation per size-scale and decreases for the smaller and denser fragments. This behavior can be approximated by a power-law with an exponent of -0.96 ± 0.05, which is also in agreement with the previous determination of the 4 pc fragmentation length by

Jackson et al. (2010). However, our data show that determining the fragmentation length at any particular scale does not capture the full, scale-dependent picture of fragmentation in the classical Nessie.

- Comparing the observed relation of fragmentation length and density to analytic gravitational fragmentation models, we find that at all scales the observed nearest-neighbor separations are within a factor of two of the Jeans' length. However, the slope of the scale-dependency of the Jeans' length is significantly steeper than the observed mean density – separation relationship. We do find agreement for the observed relationship with a gravitationally fragmenting near-equilibrium cylinder that is supported by non-thermal motions that exhibits a Larson-like velocity-size scaling, that is, a power-law with an exponent of 0.5. This scaling could result, for example, from turbulent motions in the cloud, which is supported by the finding of clearly non-thermal velocity dispersions (Jackson et al., 2010, and Chapter 3).

- We estimated the star formation rate (SFR) of Nessie based on different tracers. Based on the number of identified YSOs in the cloud we find the SFR to be 389 $M_\odot\,Myr^{-1}$, based on the number of $\sim$ 0.1 pc-scale column density "cores" we estimate 205 $M_\odot\,Myr^{-1}$, and based on the total amount of dense gas ($A_V > 7.3$ mag; Lada et al. 2012) in the cloud we estimate 400 $M_\odot\,Myr^{-1}$. These results suggest that the star-forming content of the classical Nessie can be approximated relatively well by the number of dense cores and the amount of dense gas above $A_V > 7.3$ mag. These numbers indicate that the star-forming content of Nessie is similar to the Solar neighborhood giant molecular clouds like Orion A.

- Analyzing the structure of ATLASGAL Gauss clumps (GCSC) identified in the classical Nessie we find typically two to three small-scale structures ($<$ 0.16 pc),which contain about 7 % of the mass of the parental clump. However, this is a lower limit as the extinction mapping is susceptible for incompleteness arising from MIR bright objects, such as foreground stars, and warm/hot gas.

- To investigate the larger extend of Nessie we used SEDIGISM ^{13}CO(2 – 1) and C^{18}O(2 – 1) data and obtained maps of the zeroth, first, and second order moments of the extended Nessie filamentary molecular cloud from the SEDIGISM ^{13}CO(2 – 1) and C^{18}O(2 – 1) emission with a spatial resolution of 40″. Based on the integrated ^{13}CO emission (zeroth order) over SNR of 5 we estimate the mass to be 1.89×10^6 $M_\odot$. With the total length of the visually identified skeleton of 283.1 pc we calculate a mean line-mass of 563 $M_\odot\,pc^{-1}$, which is similar to the value of the classical part (555 $M_o dot\,pc^{-1}$ at 3.1 kpc).

- The most striking result is that the velocity structure along the filamentary cloud is continuous, although the outer edges of two embedded HII regions cause two steep gradients. However, changes in the morphology, for example intensity, radial extend, or kinematic behavior, of the extended Nessie filament suggest that that the filament is not evolving as a single filament. We could identify 12 subparts

for the extended Nessie. Additionally, we find a difference in the distribution of ATLASGAL (CSC) and Hi-GAL high-mass clumps as well as compact and evolved HII regions, which indicate on-going massive star formation.

- In the shells around the evolved HII regions we find a slightly enhanced number of high-mass clumps, which have the tendency to appear at equally spaced distances. This finding may hint to a fragmentation of the compressed molecular shell and therefore, star formation triggered by the expanding shock front of the HII region.

6.2 Filamentary molecular clouds in the inner Galactic Plane

In the second part of the thesis we analyzed the continuity in ppv-space and the gas properties of filament candidates previously identified based on the ATLASGAL dust emission data by Li et al. (2016). Since the dust emission represents a 2D projection of all emission along the line-of-sight, it is crucial to use molecular line data to reveal whether the identified structures are single physical entities. This includes a small study on the SEDIGISM science demonstration field and a fully automated analysis on the entire SEDIGISM survey area. Our results are summarized in the following:

- A visual investigation of the SEDIGISM science demonstration field reveals a large number of filamentary structures from simple filaments to larger complexes. While the brightest structures are also identified in dust emission data (ATLASGAL and Hi-GAL), there are several more diffuse structures present.

- We detect 8 of 9 filaments and all 3 networks of filaments of the catalog of Li et al. (2016) in the SEDIGISM science demonstration field. While one filament candidate is the result of a projection of several velocity components, and one network is a product of two distinct velocity components seen in projection along the line-of-sight, all other structures show one velocity component tracing significant parts of the dust identified candidates.

- Comparing the observed line-mass of the velocity coherent filaments with their critical non-thermal (virial) value we find this ratio in the range from 0.4 to 3.5. We concluded from this result that filaments might not be gravitationally bound on the large scale but form stars in the inner denser parts.

- In the automated study of the filament candidates within the entire SEDIGISM survey we find that two-thirds of the candidates are single velocity-coherent structures. Other candidates are line-of-sight projections of mainly two or three velocity components, but at most seven velocity components in one candidate. Comparing the number of components with projected line-of-sight intensities, we found a tendentious correlation between the maximum integrated ^{13}CO intensity as well as ATLASGAL dust emission within the filament candidate and the number of velocity components, however, a flat behavior is within the uncertainties.

- Measuring the increasing filament mass with increasing radius we find that the filament profiles are on average in agreement with a Plummer-like density distribution with an exponent of $p \approx 1.5 \pm 0.5$. Because of the limited spatial resolution of the data the inner profile radius cannot be constrained. The shallow power-law exponent indicates that th studied filaments are typically located within larger molecular clouds, and therefore, the outer radius of a filament cannot be well defined using low density tracers like ^{13}CO. For further mass estimates we defined a radius which includes the gas that possibly can take part in star formation through accretion within the next 2 Myr.

- Similar to the findings in the test field, the observed line-mass of the filaments in the SEDIGISM survey is in agreement with the critical non-thermal line-mass and is significantly higher than the critical thermal line-mass. However, while turbulent motions are one possible explanation, we do not know the source of the observed velocity dispersion. Rotation, shear, and inflow of gas could contribute to the observed velocity dispersion. Comparing the found relation between velocity dispersion and line-mass with the theoretical infall velocity profile based on Heitsch (2013a) does not reveal evidence for free-fall collapse. However, radial infall motions of the gas onto the skeleton can possibly explain the relation.

6.3 Final conclusions

The results shown in the first part of the thesis are found for a single giant molecular filament and therefore, cannot be transferred to general statements. The finding of a continuous velocity structure over the 200 pc long spine without significant large scale curvature in position-position space suggests that this filamentary molecular cloud was not formed as a result of stellar feedback, but is rather a result of Galactic, large-scale mechanisms. Comparing our results to two proposed formation scenarios based on Galactic simulations (Smith et al., 2014; Duarte-Cabral & Dobbs, 2017) we see an agreement with both models. However, our results do not allow to distinguish between these models, and we cannot conclude a preferred scenario of giant molecular filament formation.

The found hierarchical fragmentation process has also be seen in other filamentary clouds like G11.11-0.12 (Kainulainen et al., 2013), the Taurus cloud (Hacar et al., 2013), and the integral-shaped filament in Orion (Teixeira et al., 2016; Kainulainen et al., 2017), which suggests that hierarchical fragmentation is a common processes, however with different characteristics, hence, power-law slopes. The found relation between the observed line-mass and the velocity dispersion supports two interpretations: the filament is globally in a near-equilibrium state, where turbulence supports the filament against gravitational collapse, or the filament is undergoing a radial collapse with infall speeds below the free-fall velocity.

Combining these results with the findings that denser structures (i.e. sub-filaments, clumps, cores) can collapse on smaller time-scales than the parent cloud (Pon et al., 2011) and that the fragmentation time-scale is comparable to the radial free-fall collapse

time-scale (Heitsch, 2013a) leads to a possible picture of massive filament evolution: gravitational super-critical parts of massive filaments collapse radially, while the diffuse surrounding molecular cloud might be in an equilibrium state. During the collapse the density of the filament will increase and therefore, the fragmentation scales will decrease following the sausage and Jeans' fragmentation models. This leads to the observed hierarchical fragmentation characteristics. Additional contributions from other processes like turbulence and magnetic fields might influence these relations and lead to the observed variations between massive filaments.

Chapter 7

Outlook

In this thesis we performed a detailed study on one of the most interesting filamentary molecular clouds, we developed an automated analysis method for massive filamentary clouds and we found a possible scenario for massive filament evolution and fragmentation. These results leave several open questions for further investigations.

7.1 Extension of the filament catalog

With the presented automated filament analysis tool in hand it will be straightforward to extend the study in other regions. The Galactic plane is the target of several molecular line surveys. While we used the SEDIGISM survey for our analysis, the rest of the inner Galactic plane ($18° < l < 60°$) is covered by the Galactic Ring Survey (Jackson et al., 2006), which observed the ^{13}CO(1 – 0) line with the SEQUOIA multi-pixel array receiver on the FCRAO 14 m telescope with a spatial resolution of $46''$, a spectral resolution of 0.2 $\mathrm{km\,s^{-1}}$, and a sensitivity of $< 0.4\ K$. This area is also covered by the filament candidate catalog of Li et al. (2016) and therefore, such an extension would increase the statistics in a consistent way. Additionally, surveys of different transitions of the same molecules, which are currently observed, will provide the possibility to derive the excitation temperature and opacity of the gas and therefore, improve our mass estimates.

Furthermore, to achieve a more complete picture of the distribution of filamentary structures in the Galaxy, it will be beneficial to include also more structures with more complex morphologies like the networks of filaments and complexes from the study of Li et al. (2016). While we ignored these objects for the final analysis during the manual test study shown in Chapter 4 because of their complexity, the developed algorithm is able to take care of such morphologies. These more complex objects will also include already well-known star-forming regions with much higher luminosity such as W43 and W49. Therefore, we will be able to investigate also the differences of star formation in varying surrounding conditions. Additionally, with a larger sample it will be more likely to identify a general structure of the Galaxy. Using an advanced friends-of-friends approach, including the orientation of the filaments, we can identify more of the giant molecular filaments like Nessie (Chapters 2 and 3). This selection of GMFs is likely to be less biased than visual identification methods, for example used in Ragan et al. (2014) and Abreu-Vicente et al. (2016).

7.2 Nessie and the origin of GMFs

Our study of the Nessie giant molecular filament in Chapter 3 showed that this is a spatially and velocity continuous object, whose formation process is currently not understood. Galactic modeling revealed two possible formation processes. While our study showed several properties which are expected from the proposed processes, the study could not provide conclusive evidence for either of them. Recently several catalogs of possible GMFs have been conducted (Ragan et al., 2014; Wang et al., 2014, 2015; Abreu-Vicente et al., 2016; Zucker et al., 2017), however, applying different criteria for the identification. These studies are aiming on finding the location and orientation of the GMFs in the spiral structure of the Galaxy. However, the uncertainties in both, the knowledge of the location of the spiral arm and the kinematic distance estimates, does not allow conclusive results.

One observable difference between the two models is the interaction with the surround material. The 'bones of the Milky Way' model of Smith et al. (2014) suggest steady infall of gas into the gravitational potential of the spiral arm, where the filament is located. However, the GMFs observed in the study of Duarte-Cabral & Dobbs (2017) are located in the inter-arm region and confined by an external pressure. With observations across the filament of different tracers can reveal the kinematics onto the filament. Here we are planning to observe the optically thick CO, neutral carbon, [CI], in the outer edge of the molecular filament and ionized carbon, [CII], which traces the surrounding gas. We then will analyze the data to identify infall signatures or external pressure.

7.3 Detailed study of massive filamentary molecular clouds

From the results of the studies presented in this thesis we drew a picture for massive filament evolution, where the filament is radially collapsing and fragmenting, and thereby creating a hierarchical sub-structure. However, we need additional informations to confirm this picture. In particular, we plan to select a sample of the most interesting filaments, that covers a large range of line-masses, morphologies, and distances from our catalog derived in Chapter 5. This sample would then be the ideal testbed for detailed studies. To allow more detailed studies it is necessary to select the bright sources from the catalog. Also, we want to include filaments with different global surrounding conditions like kinematic substructures, or alignment with HII regions. Therefore, it is possible to identify different filament formation processes and study their impact on the evolution and star formation content. Another approach to find the most interesting sources is to investigate whether there are correlations between parameters of filamentary molecular clouds and associated high-mass star formations clumps, like ATLASGAL or Hi-GAL clumps (Contreras et al., 2013; Urquhart et al., 2014; Molinari et al., 2016).

To investigate the cause of the observed line-mass velocity dispersion correlation high resolution molecular line emission observations are essential. With these data we will mainly focus on the following two questions: does the filament have substructures,

and does the filamentary cloud show evidence for radial collapse? From previous studies we expect to find one or several dense filaments in the center of the filamentary cloud (Hacar et al., 2013; Zhang et al., 2015; Hacar et al., 2018), which show a narrower fragmentation pattern than the parental cloud (Chapter 2 and Kainulainen et al., 2013; Pokhrel et al., 2018). However, the surrounding cloud provides a large reservoir of molecular gas, which is most likely responsible for the observed high line-masses, and therefore, the found correlation. As discussed in Chapter 5, theoretical models predict a radial collapse for such configurations (Inutsuka & Miyama, 1992; Heitsch, 2013a), which has not yet been observed. Therefore, we will search for collapse signatures, like radial gradients of the peak velocity and velocity dispersion, pronounced blue line profiles (e.g., Lu et al., 2018), and line shapes as predicted by models (Chapter 5 and Heitsch, 2013a). Finally, we will compare the results of the different sources to investigate the impact of the global conditions. In conclusion, this study will show for the first time the continuous path of molecular gas from the parsec-scale to the dense star-forming clump.

Appendix A

Appendix to Chapter 2

A.1 Used observations

For the calculation of the NIR extinction map of the Nessie filament we use observations conducted by the VVV (VISTA Variables in the Via Lactea) survey (Saito et al., 2012) in the JHK$_S$ photometric bands. These calibrated and reduced (science ready) data are publicly available in the ESO archive. The exact observations used in this study are listed in Table A.1.

A.2 Photometry of different observations

For the photometry of the NIR data, we use a set of different observations (see Appendix A.1), which show different spatial resolutions due to different conditions. Therefore, the point-spread-function (PSF) for point sources will be different in the single observations, and also effect the stacked data. This might be especially relevant in the K$_s$ filter where we use a larger set of observations. To test the significance of this quality difference we compare the results of photometry in the K$_S$ filter performed on tile 068 of the stacked data, one 80 s exposure (from 2010-05-09), and the lowest resolution 16 s exposure (from 2011-08-31). For all data-sets we used the same parameters as described before and also calibrated the found magnitudes with the 2MASS data (Skrutskie et al., 2006; Cutri et al., 2003). We then identified stars seen in the stacked and 16 s data, and stacked and 80 s data, and plotted the derived magnitudes against each other.

We find a good correlation for the three data-sets. However, there is a larger scatter for the 16 s data because of the lower sensitivity of the data. In general, we find a significantly increased number of stars for the longer exposure or stacked data. Specifically, more faint stars are detected because of the higher sensitivity of the data. As the number of sources is important for our applied method of NIR extinction measurement, we except small uncertainties introduced by the PSF fitting on the stacked data as they are not significant, which we were able to show here.

A.3 Reference color correction

For the estimation of the dust extinction of a molecular cloud we need to calculate the average color of the stars behind the cloud. In order to make accurate measurements, we need to address two problems. First the cloud itself causes a strong shift of the star colors. This is exactly the effect we want to measure, but a direct measure of the color on the farther side of the cloud is impossible. Therefore, we assume the

Table A.1: List of NIR observations.

Filter	RA	DEC	Exposure time	beamsize	date
	hh:mm:ss.ss	dd:mm:ss.ss	s	$''$	
near-infrared VVV tile d068					
J	16:40:50.52	-47:19:13.08	80	0.82	2010-03-27
J	16:40:50.52	-47:19:13.08	80	0.93	2010-05-09
H	16:40:50.52	-47:19:13.08	80	0.84	2010-03-27
H	16:40:50.52	-47:19:13.08	80	0.94	2010-05-09
K_S	16:40:50.52	-47:19:13.08	80	0.82	2010-03-27
K_S	16:40:50.52	-47:19:13.08	80	0.96	2010-05-09
K_S	16:40:50.52	-47:19:13.08	16	0.93	2010-03-06
K_S	16:40:50.52	-47:19:13.08	16	0.93	2010-06-26
K_s	16:40:50.52	-47:19:13.08	16	0.74	2011-05-14
K_S	16:40:50.52	-47:19:13.08	16	0.82	2011-05-15
K_S	16:40:50.52	-47:19:13.08	16	0.74	2011-05-16
K_S	16:40:50.52	-47:19:13.08	16	0.71	2011-05-16
K_S	16:40:50.52	-47:19:13.08	16	0.90	2011-05-18
K_S	16:40:50.52	-47:19:13.08	16	1.09	2011-08-31
K_S	16:40:50.52	-47:19:13.08	16	0.93	2011-09-01
K_S	16:40:50.52	-47:19:13.08	16	0.88	2011-09-05
K_S	16:40:50.52	-47:19:13.08	16	0.93	2011-09-17
K_S	16:40:50.52	-47:19:13.08	16	0.81	2011-09-21
near-infrared VVV tile d069					
J	16:46:25.56	-46:13:07.32	80	0.79	2010-03-27
J	16:46:25.56	-46:13:07.32	80	0.96	2010-05-09
H	16:46:25.56	-46:13:07.32	80	0.81	2010-03-27
H	16:46:25.56	-46:13:07.32	80	0.89	2010-05-09
K_S	16:46:25.56	-46:13:07.32	80	0.83	2010-03-27
K_S	16:46:25.56	-46:13:07.32	80	0.87	2010-05-09
K_S	16:46:25.56	-46:13:07.32	16	1.02	2010-03-06
K_S	16:46:25.56	-46:13:07.32	16	0.79	2010-08-18
K_S	16:46:25.56	-46:13:07.32	16	0.97	2011-06-15
K_S	16:46:25.56	-46:13:07.32	16	0.71	2011-05-14
K_S	16:46:25.56	-46:13:07.32	16	0.83	2011-05-15
K_S	16:46:25.56	-46:13:07.32	16	0.72	2011-05-16
K_S	16:46:25.56	-46:13:07.32	16	1.04	2011-08-09
K_S	16:46:25.56	-46:13:07.32	16	1.01	2011-09-06

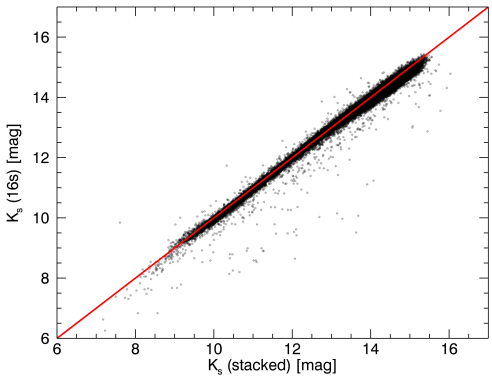

Figure A.1: Comparison of K_S magnitudes between the stacked and 16 s data. The red line indicates the one-to-one correlation. The shown stars have an photometric uncertainty lower than 0.05 mag.

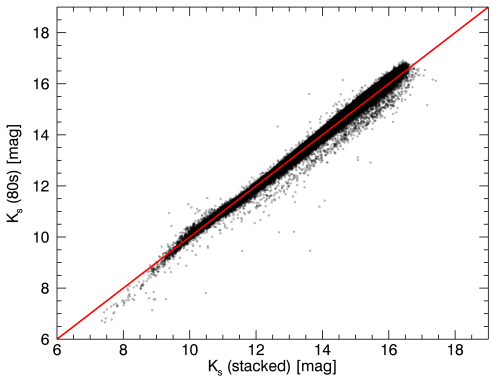

Figure A.2: Comparison of K_S magnitudes between the stacked and 80 s data. The red line indicates the one-to-one correlation. The shown stars have a photometric uncertainty lower than 0.05 mag.

colors of stars in a nearby cloud-free region are the same as behind the cloud. Second, diffuse dust in the Milky Way causes a steady dust reddening with distance from the observer. Therefore, stars located in between the cloud and the observer will confuse the measurement of the background color and need to be removed. We address this problem by statistical subtraction of foreground stars in the JHK_S color-color-space. We first bin the stars in the J-H and H-K_S colors and scale the numbers with the size of the reference field, which leads to a two-dimensional histogram shown in Fig. A.3. Then, we do the same for stars located towards the highest extinction regions of the cloud. These stars are either in front of the cloud and show almost no color excess or they are behind the cloud, in which case they show a strong color excess and can be ignored. Again, we scale the number of stars per bin with the area in which they were

observed. We subtract the number of stars per bin of foreground histogram from the number of stars in the corresponding bin of the reference field histogram. The resulting histogram is shown in Fig. A.4 and represents the distribution of star colors behind the cloud. Some bins show a negative number of stars, but neighboring bins show still 'unreddend' stars, so they cancel in deriving the average J-H, and H-K_S colors.

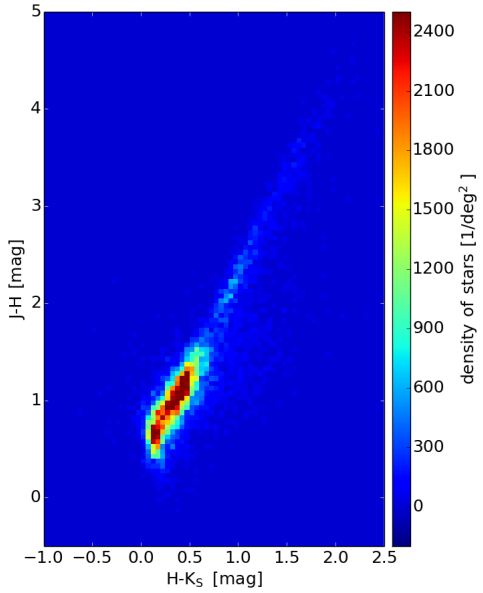

Figure A.3: JHK$_s$ color-color histogram of the reference field before correction.

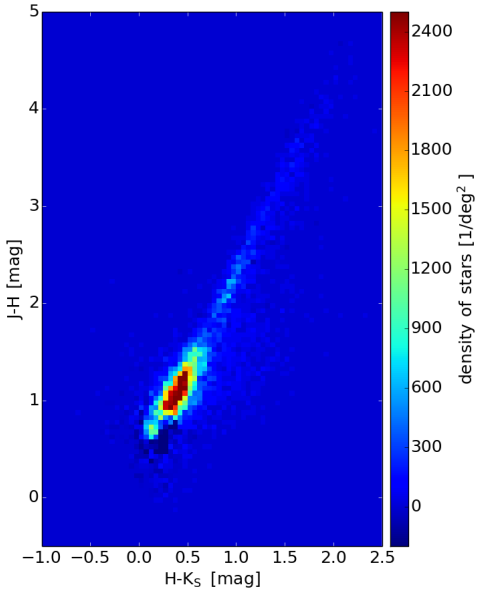

Figure A.4: JHK$_s$ color-color histogram of the reference field after correction.

A.4 Mid-infrared near-infrared correlation

For the combination of the 'NIR and MIR extinction maps we convolve the MIR data (FWHM = 2.4") to the significantly lower resolution of the NIR data (FWHM = 48"). Then, we perform a pixel-to-pixel comparison between the two maps to investigate their correlation. Figure A.5 shows only a poor correlation of the data and a large scatter. For $A_V^{NIR} \lesssim 10$ mag, the MIR extinction at most positions is underestimated by a factor of approximately five, but at some positions the data is correlated. This can be explained by the spatial filtering of the MIR mapping, which is not able to trace the diffuse cloud component. Therefore, the correlation arises only from the very inner parts of the filament. Additionally, at extinctions higher than $A_V^{NIR} \lesssim 5$ – 10 mag, the NIR data begin to underestimate the extinction, because of a lower number of background stars in the line-of-sight. A similar behavior of the correlation can be seen in the study of Kainulainen & Tan (2013).

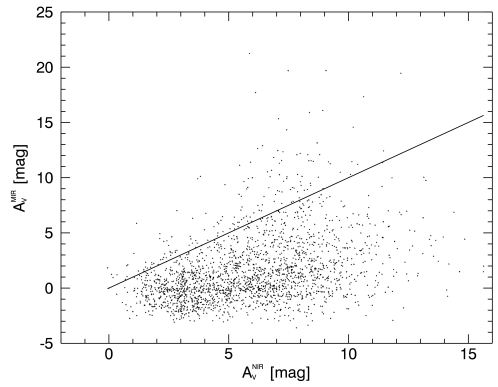

Figure A.5: Pixel-to-pixel comparison of the NIR and MIR extinction values restricted to the filament area (polygon in Fig. 2.5). The black line indicates the one-to-one correlation.

A.5 ATLASGAL clumps

Here we show cut-outs from the combined NIR and MIR extinction map of the 16 ATLASGAL GCSC sources contained in Nessie. In section 2.4.4 we describe how these parsec-scale structures identified from ATLASGAL (white contours) break down into possibly star-forming substructures. Therefore, we show the positions of identified scale $i = 2$ structures with black crosses.

A.6 Properties of the identified structures

Here we show the properties of the identified small-scale structures, which are likely to become star formation sites. The shown properties are the results of the clumpfind-2D algorithm applied to the column density map of scale ($i = 2$).

Table A.2: Structures identified on the $i = 2$ scale-map

ID	l [°]	b [°]	$N(H_2)_{peak}$ $[\frac{1}{cm^2}]$	$FWHM_x$ pix	$FWHM_y$ pix	R pix	$N(H_2)_{tot}$ $[\frac{1}{cm^2}]$	N_{pix}
9	338.11	-0.47	10.38	4.38	2.93	3.39	194.42	36
10	338.08	-0.45	9.78	4.96	6.44	3.95	224.46	49
11	338.09	-0.45	9.66	2.87	2.67	2.65	127.39	22
16	338.86	-0.47	8.71	10.33	3.52	4.62	232.36	67
17	338.70	-0.46	8.63	7.02	2.49	3.87	173.85	47
20	338.73	-0.47	8.38	3.43	3.19	3.14	126.11	31
24	338.09	-0.45	8.13	4.51	6.27	3.74	160.13	44
26	338.09	-0.45	8.01	3.21	2.67	2.82	113.50	25
29	338.65	-0.46	7.77	5.00	3.77	3.19	118.37	32

Continued on next page

Table A.2 – Continued from previous page

ID	l [°]	b [°]	$N(H_2)_{peak}$ $[\frac{1}{cm^2}]$	$FWHM_x$ pix	$FWHM_y$ pix	R pix	$N(H_2)_{tot}$ $[\frac{1}{cm^2}]$	N_{pix}
33	338.71	-0.46	7.55	4.21	2.61	3.09	108.18	30
36	338.11	-0.46	7.38	2.27	4.12	2.82	85.24	25
43	338.64	-0.46	7.14	2.93	2.09	2.33	82.64	17
44	338.73	-0.46	7.09	3.01	3.62	2.93	102.15	27
46	338.11	-0.47	6.95	4.01	4.30	3.52	134.24	39
48	338.08	-0.45	6.92	3.21	2.83	2.52	72.30	20
49	338.69	-0.46	6.89	5.20	3.13	3.61	125.90	41
50	338.87	-0.48	6.87	2.74	5.54	3.61	153.59	41
51	338.34	-0.50	6.84	3.37	2.89	2.88	89.20	26
53	338.09	-0.43	6.79	1.80	4.40	2.65	83.95	22
54	338.10	-0.45	6.73	3.88	1.90	2.52	80.81	20
56	338.08	-0.44	6.69	5.41	2.96	3.24	111.74	33
58	338.31	-0.51	6.66	3.01	2.54	2.71	76.39	23
59	338.11	-0.47	6.61	1.91	3.39	2.39	63.31	18
60	338.55	-0.42	6.45	6.23	4.03	3.61	133.05	41
67	338.09	-0.44	6.27	1.92	2.17	1.95	43.95	12
71	338.87	-0.48	6.15	2.36	3.23	2.46	67.43	19
77	338.08	-0.43	6.04	2.23	2.42	2.26	52.61	16
78	338.87	-0.47	6.01	5.25	2.75	3.19	95.52	32
79	338.08	-0.43	6.00	2.70	1.72	2.11	45.62	14
83	338.78	-0.46	5.92	2.34	3.13	2.33	50.45	17
85	338.87	-0.48	5.84	2.25	3.44	2.46	72.41	19
87	338.39	-0.40	5.79	2.66	3.43	2.65	65.60	22
88	338.62	-0.44	5.74	3.83	5.21	3.09	78.61	30
89	338.09	-0.45	5.74	2.60	2.47	2.33	53.72	17
90	338.32	-0.41	5.73	4.68	3.34	3.19	105.23	32
95	338.32	-0.51	5.67	8.75	2.10	3.57	115.17	40
96	338.19	-0.48	5.64	2.84	3.06	2.65	67.07	22
97	338.24	-0.44	5.63	2.63	4.44	3.04	88.73	29
100	338.13	-0.49	5.62	3.73	3.68	3.14	85.00	31
102	338.11	-0.45	5.60	2.71	2.89	2.65	66.99	22
103	338.10	-0.45	5.59	6.57	3.81	3.39	107.10	36
106	338.46	-0.43	5.50	5.86	2.02	3.04	85.06	29
108	338.10	-0.45	5.49	3.55	2.47	2.39	58.37	18
110	338.85	-0.47	5.47	2.49	2.68	2.46	59.34	19
111	338.33	-0.51	5.46	2.03	2.91	2.33	50.69	17
113	338.09	-0.44	5.45	3.26	2.60	2.65	70.43	22
116	338.20	-0.46	5.44	2.69	3.57	2.71	75.55	23
117	338.60	-0.44	5.44	1.83	5.45	2.82	79.80	25
118	338.64	-0.46	5.43	3.59	1.88	2.39	58.47	18

Continued on next page

Table A.2 – Continued from previous page

ID	l [°]	b [°]	$N(H_2)_{peak}$ [$\frac{1}{cm^2}$]	$FWHM_x$ pix	$FWHM_y$ pix	R pix	$N(H_2)_{tot}$ [$\frac{1}{cm^2}$]	N_{pix}
120	338.67	-0.45	5.40	4.36	2.46	2.71	63.15	23
121	338.08	-0.44	5.35	2.96	2.73	2.52	64.19	20
122	338.34	-0.40	5.33	6.25	3.01	3.24	89.47	33
125	338.82	-0.45	5.32	2.92	3.32	2.52	59.44	20
126	338.81	-0.48	5.31	3.19	2.31	2.59	60.68	21
129	338.69	-0.46	5.28	3.21	2.11	2.39	52.69	18
130	338.60	-0.44	5.27	3.64	2.43	2.71	75.71	23
134	338.82	-0.47	5.23	3.11	3.57	2.65	61.68	22
135	338.94	-0.42	5.22	2.34	4.97	2.99	83.16	28
136	338.27	-0.43	5.22	3.72	2.35	2.82	70.46	25
138	338.50	-0.42	5.21	3.78	3.16	2.71	69.47	23
139	338.33	-0.41	5.21	3.61	1.76	2.33	55.73	17
141	338.09	-0.46	5.19	3.75	6.70	2.99	73.09	28
145	338.61	-0.44	5.16	3.26	4.76	3.09	95.21	30
147	338.60	-0.44	5.12	3.34	2.18	2.46	65.92	19
148	338.78	-0.46	5.12	4.06	4.37	3.43	94.78	37
149	338.87	-0.48	5.12	3.81	1.96	2.39	48.98	18
154	338.85	-0.47	5.03	2.84	2.09	2.33	47.11	17
157	338.48	-0.43	4.95	4.17	2.94	3.14	87.01	31
159	338.29	-0.43	4.93	3.24	3.61	3.09	81.85	30
160	338.30	-0.52	4.92	3.00	4.62	3.29	98.33	34
161	338.62	-0.44	4.91	3.04	5.80	3.09	79.39	30
164	338.52	-0.43	4.89	2.45	2.04	2.11	38.29	14
168	338.62	-0.44	4.85	2.20	2.72	2.33	47.48	17
170	338.60	-0.44	4.83	3.11	2.49	2.46	56.86	19
173	338.30	-0.52	4.82	4.16	2.31	2.82	72.29	25
178	338.09	-0.44	4.78	4.77	2.31	2.88	77.22	26
179	338.50	-0.42	4.77	3.09	4.57	2.88	78.79	26
181	338.84	-0.45	4.76	7.52	3.05	3.57	100.89	40
182	338.75	-0.46	4.76	6.73	5.13	3.74	107.58	44
183	338.34	-0.51	4.75	2.98	2.28	2.33	51.20	17
184	338.76	-0.48	4.74	2.20	4.51	2.71	57.15	23
185	338.61	-0.44	4.73	6.08	3.39	3.57	104.06	40
189	338.70	-0.48	4.71	4.08	3.40	3.19	81.20	32
190	338.11	-0.46	4.71	3.54	1.95	2.33	42.64	17
191	338.61	-0.44	4.70	3.15	2.90	2.71	62.21	23
195	338.30	-0.52	4.66	2.44	6.96	3.14	80.88	31
196	338.09	-0.45	4.66	6.14	2.50	3.14	80.21	31
197	338.10	-0.46	4.66	2.83	2.30	2.26	45.35	16
199	338.73	-0.47	4.62	3.08	6.62	2.76	57.63	24

Continued on next page

Table A.2 – Continued from previous page

ID	l [°]	b [°]	$N(H_2)_{peak}$ $[\frac{1}{cm^2}]$	$FWHM_x$ pix	$FWHM_y$ pix	R pix	$N(H_2)_{tot}$ $[\frac{1}{cm^2}]$	N_{pix}
201	338.57	-0.44	4.61	3.60	2.26	2.46	50.63	19
202	338.65	-0.45	4.61	2.44	1.79	1.95	33.23	12
204	338.17	-0.47	4.59	2.19	2.51	2.19	39.57	15
208	338.18	-0.46	4.56	2.20	1.96	1.95	35.85	12
211	338.31	-0.52	4.56	5.37	2.54	2.71	57.95	23
213	338.10	-0.46	4.55	2.73	3.91	2.76	66.28	24
217	339.04	-0.39	4.54	4.51	2.87	3.14	85.78	31
218	338.33	-0.41	4.52	3.38	1.75	2.11	41.53	14
219	338.93	-0.49	4.52	2.79	4.27	3.14	84.45	31
220	338.31	-0.51	4.50	1.74	2.43	1.95	32.52	12
227	338.86	-0.47	4.47	4.71	3.95	3.48	86.50	38
228	338.08	-0.44	4.46	3.36	1.79	2.33	43.44	17
229	338.33	-0.41	4.46	2.90	1.84	2.11	38.98	14
231	338.81	-0.46	4.45	2.25	2.34	2.03	38.57	13
236	338.30	-0.52	4.43	3.76	3.27	2.82	62.30	25
239	338.20	-0.46	4.42	4.80	3.31	3.19	76.03	32
240	338.93	-0.43	4.42	2.64	2.19	2.26	42.37	16
242	338.77	-0.46	4.40	3.02	2.80	2.46	51.70	19
246	338.19	-0.46	4.37	3.46	2.83	2.71	64.63	23
248	338.24	-0.44	4.36	1.55	3.30	2.03	37.13	13
249	338.29	-0.43	4.36	2.86	2.19	2.26	41.10	16
252	338.31	-0.43	4.35	1.68	3.33	2.19	38.06	15
253	338.45	-0.42	4.35	7.54	2.76	3.29	78.07	34
256	338.20	-0.48	4.32	2.47	4.63	2.88	67.15	26
257	338.62	-0.44	4.31	2.13	2.44	1.95	34.91	12
259	338.09	-0.42	4.31	3.15	2.10	2.39	46.75	18
267	338.77	-0.46	4.27	3.16	2.20	2.26	45.37	16
269	338.21	-0.48	4.27	2.08	1.87	1.87	30.97	11
271	338.18	-0.48	4.26	4.38	3.80	2.93	69.68	27
272	338.33	-0.41	4.26	5.35	4.27	3.39	99.61	36
273	338.18	-0.46	4.25	3.00	2.82	2.52	56.71	20
276	338.87	-0.49	4.23	3.27	4.13	2.88	62.19	26
277	338.87	-0.48	4.22	4.13	2.40	2.46	48.62	19
279	338.63	-0.45	4.21	2.34	3.10	2.33	42.57	17
282	338.12	-0.47	4.20	3.42	3.57	3.09	72.84	30
285	338.90	-0.43	4.20	4.70	3.30	2.93	66.23	27
287	338.46	-0.43	4.18	1.89	2.47	1.95	31.58	12
288	338.47	-0.43	4.18	3.32	2.58	2.26	46.97	16
289	338.90	-0.43	4.18	2.82	2.09	2.19	39.80	15
290	338.51	-0.42	4.17	5.28	2.82	3.09	69.12	30

Continued on next page

Table A.2 – Continued from previous page

ID	l [°]	b [°]	$N(H_2)_{peak}$ [$\frac{1}{cm^2}$]	$FWHM_x$ pix	$FWHM_y$ pix	R pix	$N(H_2)_{tot}$ [$\frac{1}{cm^2}$]	N_{pix}
291	338.85	-0.47	4.17	2.92	3.41	2.82	66.00	25
293	338.87	-0.49	4.15	2.24	2.26	2.03	32.41	13
296	338.33	-0.51	4.13	2.07	2.52	2.11	38.05	14
298	338.26	-0.38	4.12	2.75	2.28	2.26	39.48	16
300	338.08	-0.45	4.12	2.29	5.21	2.19	34.42	15
303	338.19	-0.47	4.11	7.73	3.58	2.93	60.83	27
306	338.71	-0.47	4.09	2.51	2.26	2.11	38.51	14
307	338.09	-0.45	4.09	3.07	2.07	2.33	41.94	17
308	338.75	-0.47	4.09	2.99	3.47	2.88	67.70	26
310	338.81	-0.49	4.09	2.98	3.04	2.76	60.01	24
312	338.56	-0.44	4.08	5.54	2.29	3.04	74.99	29
315	338.34	-0.41	4.08	3.59	1.91	2.11	34.87	14
316	338.16	-0.48	4.08	1.99	3.17	2.26	41.14	16
317	338.93	-0.49	4.08	3.41	2.55	2.46	45.47	19
319	338.78	-0.46	4.07	2.91	4.07	2.76	58.32	24
326	338.32	-0.42	4.05	3.33	3.87	2.59	45.35	21
329	338.46	-0.43	4.05	3.33	1.96	2.39	43.65	18
330	338.93	-0.49	4.04	6.58	4.80	3.61	111.99	41
333	338.65	-0.45	4.03	4.66	2.04	2.65	54.46	22
337	338.86	-0.48	4.02	4.28	2.64	2.59	55.51	21
338	338.65	-0.45	4.02	3.83	4.01	2.88	60.45	26
339	338.58	-0.44	4.02	1.73	2.48	1.95	29.73	12
340	338.58	-0.43	4.02	1.65	5.11	2.59	52.32	21
342	338.24	-0.45	4.01	1.79	2.55	1.95	30.15	12
343	338.87	-0.49	4.01	1.77	2.60	2.03	31.81	13
344	338.54	-0.43	4.00	2.98	2.09	2.33	38.68	17
345	339.09	-0.41	3.99	3.68	2.49	2.59	53.84	21
346	338.71	-0.48	3.99	2.20	2.50	2.03	33.55	13
350	338.31	-0.42	3.97	3.38	2.09	2.19	39.75	15
353	338.72	-0.47	3.96	3.01	2.18	2.26	42.21	16
358	338.32	-0.41	3.94	3.42	3.18	2.46	47.99	19
360	338.13	-0.49	3.93	5.36	2.08	2.65	51.31	22
361	338.99	-0.40	3.93	5.93	3.47	3.39	90.02	36
363	338.87	-0.49	3.92	1.99	3.28	2.19	35.27	15
367	338.92	-0.50	3.91	1.74	3.51	2.33	43.16	17
368	338.62	-0.45	3.91	3.24	2.77	2.39	43.53	18
373	338.88	-0.49	3.88	3.06	2.38	2.33	39.56	17
374	338.95	-0.42	3.88	3.84	4.19	2.88	67.02	26
376	338.57	-0.44	3.87	2.86	2.99	2.46	44.64	19
379	338.13	-0.47	3.86	2.24	2.57	2.19	35.89	15

Continued on next page

Table A.2 – Continued from previous page

ID	l [°]	b [°]	$N(H_2)_{peak}$ $[\frac{1}{cm^2}]$	$FWHM_x$ pix	$FWHM_y$ pix	R pix	$N(H_2)_{tot}$ $[\frac{1}{cm^2}]$	N_{pix}
380	338.85	-0.47	3.85	3.28	2.52	2.39	42.99	18
386	338.86	-0.48	3.82	3.18	2.00	2.19	36.43	15
387	338.32	-0.41	3.82	2.75	2.72	2.39	46.55	18
389	338.11	-0.46	3.81	3.14	7.97	3.48	90.03	38
391	339.02	-0.40	3.81	5.29	2.79	3.14	79.56	31
393	338.68	-0.46	3.81	5.74	5.04	3.09	61.83	30
394	338.10	-0.46	3.81	2.87	3.85	2.93	70.69	27
397	338.85	-0.45	3.80	3.34	3.10	2.39	46.74	18
400	338.87	-0.47	3.79	2.38	2.87	2.33	40.43	17
402	338.78	-0.46	3.79	1.79	2.52	1.87	27.91	11
407	338.55	-0.42	3.77	3.22	2.70	2.39	44.22	18
408	338.78	-0.46	3.77	2.81	2.28	2.26	39.44	16
409	338.40	-0.40	3.76	2.31	2.37	2.03	34.17	13
410	338.50	-0.42	3.76	3.23	2.94	2.39	44.86	18
416	338.25	-0.44	3.74	4.34	3.55	2.65	51.41	22
418	338.94	-0.49	3.74	2.97	2.28	2.33	41.33	17
419	338.33	-0.40	3.74	2.52	1.93	2.03	31.91	13
424	338.11	-0.46	3.73	2.23	3.18	2.52	47.40	20
427	338.81	-0.46	3.73	2.21	2.09	1.95	29.11	12
430	338.41	-0.41	3.70	4.55	2.54	2.59	50.33	21
432	338.55	-0.43	3.70	1.62	3.16	2.11	30.81	14
435	338.94	-0.42	3.69	3.72	2.56	2.52	46.00	20
436	338.30	-0.48	3.69	8.93	3.74	3.24	67.69	33
437	338.42	-0.42	3.69	3.96	2.96	2.33	37.20	17
441	338.47	-0.43	3.68	4.43	6.44	3.19	70.14	32
443	338.94	-0.49	3.67	3.32	2.28	2.46	46.19	19
445	338.34	-0.51	3.66	3.00	1.76	2.11	33.98	14
447	338.92	-0.49	3.66	2.54	2.26	2.19	35.85	15
448	339.10	-0.40	3.66	5.58	2.93	2.76	51.35	24
455	338.87	-0.47	3.65	3.50	2.63	2.59	46.82	21
456	338.17	-0.47	3.64	2.70	2.84	2.33	42.97	17
458	338.11	-0.46	3.64	4.67	3.00	3.09	65.79	30
459	338.93	-0.42	3.63	4.40	2.19	2.65	51.21	22
464	338.41	-0.40	3.62	3.43	2.33	2.39	43.00	18
466	338.86	-0.50	3.62	4.56	2.46	2.82	59.96	25
467	338.64	-0.45	3.62	2.01	3.10	2.03	29.45	13
469	338.62	-0.44	3.62	2.80	2.32	2.33	40.72	17
472	338.38	-0.41	3.61	3.10	2.22	2.39	40.07	18
474	338.38	-0.40	3.60	8.46	1.77	3.52	85.07	39
476	338.43	-0.41	3.59	2.82	2.19	2.33	38.70	17

Continued on next page

Table A.2 – Continued from previous page

ID	l [°]	b [°]	$N(H_2)_{peak}$ [$\frac{1}{cm^2}$]	$FWHM_x$ pix	$FWHM_y$ pix	R pix	$N(H_2)_{tot}$ [$\frac{1}{cm^2}$]	N_{pix}
481	338.25	-0.42	3.59	6.31	4.20	2.88	51.53	26
482	338.73	-0.47	3.59	3.65	2.43	2.03	30.09	13
483	338.18	-0.46	3.58	3.29	2.87	2.26	39.31	16
484	339.09	-0.41	3.58	6.07	2.06	2.99	66.74	28
485	338.85	-0.47	3.58	1.73	2.72	1.87	27.13	11
487	338.28	-0.43	3.58	4.09	1.68	2.39	41.53	18
488	338.25	-0.44	3.58	7.14	5.04	3.19	78.22	32
494	338.63	-0.46	3.56	2.64	3.38	2.52	43.19	20
497	338.88	-0.54	3.56	2.31	1.74	1.87	25.55	11
499	338.32	-0.41	3.55	3.74	2.00	2.39	45.00	18
503	339.09	-0.41	3.53	3.84	1.94	2.46	44.86	19
504	338.16	-0.48	3.53	6.17	3.02	3.19	69.67	32
505	338.62	-0.45	3.53	4.27	6.16	3.19	64.71	32
508	338.26	-0.44	3.52	2.63	5.68	2.99	60.92	28
509	338.93	-0.42	3.52	3.87	2.86	2.52	41.61	20
510	338.39	-0.40	3.52	4.35	2.13	2.39	38.16	18
511	338.32	-0.42	3.52	3.86	2.65	2.19	33.45	15
512	338.15	-0.48	3.51	2.03	2.86	2.03	29.11	13
515	338.72	-0.46	3.51	2.39	3.91	2.52	47.61	20
516	338.84	-0.45	3.50	7.58	3.22	3.57	92.03	40
519	339.02	-0.40	3.50	2.39	1.71	1.87	26.38	11
525	338.31	-0.50	3.48	3.09	3.07	2.26	33.52	16
526	338.09	-0.46	3.48	3.13	1.74	2.11	32.44	14
527	338.21	-0.47	3.48	3.10	4.38	3.04	63.24	29
530	338.93	-0.49	3.47	3.38	2.63	2.46	43.78	19
534	338.15	-0.49	3.46	2.34	1.94	1.87	27.83	11
541	338.23	-0.49	3.45	2.19	2.79	2.26	35.14	16
548	338.32	-0.42	3.44	6.93	2.16	2.88	62.58	26
549	338.93	-0.49	3.44	2.35	3.64	2.19	34.08	15
551	339.08	-0.41	3.43	2.53	2.37	2.19	33.81	15
552	338.11	-0.48	3.43	2.75	2.52	2.39	41.90	18
555	338.42	-0.42	3.43	3.61	2.05	2.19	34.05	15
556	338.55	-0.42	3.43	5.50	6.00	2.93	49.09	27
558	338.93	-0.50	3.41	3.18	2.20	2.19	34.37	15
559	338.87	-0.48	3.41	1.92	3.23	2.19	33.82	15
563	338.41	-0.41	3.41	1.97	2.45	2.03	29.67	13
565	338.42	-0.41	3.40	4.76	6.13	3.34	71.32	35
569	338.15	-0.48	3.39	5.04	2.66	2.71	50.21	23
573	338.10	-0.46	3.38	2.86	1.95	2.19	35.27	15
575	338.96	-0.43	3.37	4.13	2.74	2.65	52.43	22

Continued on next page

Table A.2 – Continued from previous page

ID	l [°]	b [°]	$N(H_2)_{peak}$ $[\frac{1}{cm^2}]$	$FWHM_x$ pix	$FWHM_y$ pix	R pix	$N(H_2)_{tot}$ $[\frac{1}{cm^2}]$	N_{pix}
576	338.75	-0.46	3.37	2.31	3.18	2.26	38.80	16
581	338.28	-0.43	3.36	3.05	2.02	2.26	37.93	16
583	338.85	-0.45	3.36	3.12	1.62	1.87	25.73	11
584	338.93	-0.42	3.35	2.38	2.02	1.87	25.95	11
588	338.94	-0.48	3.35	3.08	3.71	2.82	55.20	25
593	339.03	-0.40	3.34	2.37	2.50	2.11	32.78	14
594	338.26	-0.43	3.34	3.57	2.11	2.39	41.79	18
595	338.24	-0.37	3.34	3.32	3.32	2.52	45.93	20
598	338.78	-0.45	3.34	2.18	2.80	2.03	29.06	13
605	338.25	-0.42	3.31	3.13	2.21	1.95	25.39	12
606	338.73	-0.46	3.30	2.62	2.71	2.26	35.77	16
608	338.65	-0.45	3.30	3.57	2.30	2.26	38.13	16
613	338.87	-0.48	3.30	2.60	1.69	1.87	24.71	11
616	338.65	-0.45	3.29	3.46	3.37	2.46	47.44	19
618	338.20	-0.47	3.29	2.53	3.00	2.46	39.80	19
620	338.09	-0.46	3.29	1.82	2.79	1.95	26.62	12
622	338.64	-0.45	3.28	2.54	3.15	2.52	46.68	20
623	338.30	-0.48	3.28	2.60	2.90	2.33	36.33	17
626	338.32	-0.42	3.27	1.61	4.58	2.33	42.92	17
627	338.09	-0.43	3.27	2.32	2.30	1.95	28.44	12
628	338.31	-0.42	3.27	2.62	2.46	2.11	32.06	14
632	338.67	-0.46	3.26	3.29	2.19	2.26	32.28	16
634	338.77	-0.46	3.26	3.01	4.47	2.93	61.89	27
636	338.13	-0.45	3.26	1.85	3.80	2.26	36.59	16
639	338.74	-0.47	3.25	3.64	4.05	2.76	55.48	24
641	338.82	-0.47	3.25	1.83	4.12	1.95	24.01	12
650	338.33	-0.41	3.23	3.26	2.43	2.11	31.07	14
654	338.76	-0.46	3.23	3.67	5.64	2.65	42.56	22
657	338.82	-0.46	3.22	2.36	3.43	2.19	33.18	15
662	338.89	-0.44	3.21	2.99	2.63	2.26	35.37	16
664	339.04	-0.43	3.21	3.53	1.70	2.19	29.72	15
670	338.19	-0.47	3.20	4.98	2.81	2.82	50.91	25
671	338.77	-0.46	3.20	4.11	3.46	2.93	53.53	27
672	338.92	-0.50	3.20	2.43	1.75	1.87	24.94	11
676	338.31	-0.42	3.19	2.05	2.11	1.87	24.23	11
677	338.30	-0.52	3.19	3.17	1.82	2.19	32.27	15
681	338.93	-0.42	3.18	2.06	2.65	1.95	26.58	12
689	338.94	-0.42	3.17	2.46	3.88	1.95	24.56	12
695	338.15	-0.49	3.17	1.87	2.40	1.87	23.86	11
700	338.81	-0.46	3.15	5.73	4.56	2.93	50.88	27

Continued on next page

Table A.2 – Continued from previous page

ID	l [°]	b [°]	$N(H_2)_{peak}$ [$\frac{1}{cm^2}$]	$FWHM_x$ pix	$FWHM_y$ pix	R pix	$N(H_2)_{tot}$ [$\frac{1}{cm^2}$]	N_{pix}
705	338.25	-0.44	3.14	2.55	3.53	2.11	27.85	14
706	338.63	-0.46	3.14	4.05	2.33	2.71	55.49	23
709	338.15	-0.48	3.14	2.35	2.85	1.87	26.52	11
714	338.11	-0.45	3.13	3.05	2.41	2.33	35.36	17
724	338.38	-0.40	3.10	3.01	2.46	2.26	34.84	16
730	338.94	-0.42	3.10	3.94	2.95	2.76	49.44	24
736	338.31	-0.42	3.09	4.75	1.54	2.19	36.73	15
738	338.09	-0.44	3.08	2.19	2.36	2.03	27.83	13
743	338.09	-0.43	3.04	1.58	4.01	2.19	31.44	15
747	338.32	-0.50	3.04	3.21	2.91	2.59	45.57	21
756	338.87	-0.49	3.03	1.79	3.62	2.26	33.49	16
757	339.10	-0.41	3.02	3.32	2.94	2.19	30.79	15
761	339.00	-0.41	3.01	2.80	2.12	2.11	28.16	14
762	338.39	-0.41	3.01	3.81	4.05	2.59	44.03	21
766	338.92	-0.51	3.00	2.51	4.78	2.93	58.06	27
767	338.32	-0.44	3.00	2.55	3.28	2.19	31.35	15
771	338.45	-0.42	2.99	4.15	4.00	2.71	43.32	23
780	338.93	-0.49	2.98	4.18	8.68	3.14	67.19	31
786	338.26	-0.43	2.97	4.00	4.10	2.71	48.26	23
787	338.91	-0.53	2.97	3.53	2.00	2.19	30.76	15
789	338.12	-0.50	2.96	2.54	2.13	2.11	29.34	14
790	338.37	-0.40	2.96	3.62	3.54	2.71	47.90	23
793	339.01	-0.40	2.96	2.62	7.07	2.82	48.46	25
794	338.14	-0.48	2.96	5.21	3.54	2.71	41.30	23
795	338.18	-0.46	2.96	3.52	1.74	2.11	27.88	14
796	338.64	-0.45	2.96	2.71	2.31	1.95	26.54	12
800	338.71	-0.47	2.95	2.10	2.36	1.95	26.85	12
801	338.95	-0.42	2.95	4.03	3.81	3.29	73.55	34
803	338.28	-0.43	2.95	4.34	2.31	2.52	38.05	20
805	338.52	-0.43	2.94	2.01	3.06	2.19	31.25	15
806	338.42	-0.41	2.94	2.43	2.17	2.03	25.85	13
809	338.63	-0.45	2.94	3.87	3.45	2.65	42.43	22
812	338.94	-0.49	2.94	2.39	2.75	2.26	33.87	16
819	338.11	-0.45	2.92	3.38	2.40	2.33	32.89	17
821	338.32	-0.41	2.92	2.78	4.96	2.52	37.38	20
822	338.55	-0.42	2.92	2.01	3.45	2.33	35.02	17
823	339.00	-0.40	2.92	2.54	3.53	2.52	39.96	20
824	338.09	-0.46	2.92	2.71	2.71	2.39	38.23	18
825	339.00	-0.41	2.92	2.37	2.88	1.95	25.02	12
826	338.86	-0.50	2.92	2.80	2.03	2.19	30.56	15

Continued on next page

Table A.2 – Continued from previous page

ID	l [°]	b [°]	$N(H_2)_{peak}$ $[\frac{1}{cm^2}]$	$FWHM_x$ pix	$FWHM_y$ pix	R pix	$N(H_2)_{tot}$ $[\frac{1}{cm^2}]$	N_{pix}
833	338.09	-0.44	2.91	2.07	3.41	2.03	25.15	13
835	338.85	-0.47	2.90	3.57	3.08	2.39	36.98	18
841	338.39	-0.40	2.90	3.31	3.20	2.52	41.88	20
843	338.41	-0.42	2.89	2.30	1.81	1.87	23.09	11
848	338.34	-0.41	2.89	3.28	1.57	2.03	26.28	13
851	338.09	-0.43	2.88	1.56	3.19	1.87	22.86	11
855	338.47	-0.42	2.88	3.92	2.29	2.39	39.05	18
860	338.91	-0.44	2.87	2.76	1.97	2.03	25.09	13
862	338.48	-0.43	2.87	1.82	3.44	2.03	24.75	13
868	339.00	-0.41	2.86	2.94	2.47	2.19	30.87	15
873	338.77	-0.46	2.86	4.29	2.22	2.59	44.53	21
875	338.78	-0.45	2.86	2.38	3.50	2.11	27.94	14
881	338.39	-0.41	2.85	4.44	3.62	2.99	56.27	28
882	338.41	-0.40	2.85	2.22	3.04	2.33	35.67	17
886	338.96	-0.41	2.84	2.74	2.40	2.03	26.13	13
889	339.07	-0.41	2.84	3.20	2.86	2.19	30.98	15
894	338.86	-0.50	2.83	2.99	1.41	1.87	23.21	11
896	338.13	-0.46	2.83	3.60	2.03	2.03	25.17	13
897	338.73	-0.47	2.82	2.46	3.07	2.26	30.70	16
898	338.38	-0.39	2.82	6.66	3.16	3.34	65.60	35
900	338.93	-0.48	2.82	2.71	2.23	2.11	29.19	14
909	338.35	-0.41	2.80	5.46	1.97	2.76	47.88	24
912	338.09	-0.44	2.80	1.64	3.50	2.03	25.88	13
921	338.33	-0.51	2.78	5.40	2.97	2.59	37.55	21
922	338.14	-0.48	2.78	2.09	3.20	2.19	29.89	15
923	339.04	-0.42	2.78	4.01	1.68	2.11	28.54	14
924	338.82	-0.45	2.78	2.70	3.66	2.59	39.57	21
927	338.31	-0.43	2.78	2.18	3.32	2.26	33.61	16
930	338.08	-0.42	2.77	2.29	2.81	2.03	26.13	13
931	338.93	-0.50	2.77	4.96	1.52	2.26	30.70	16
933	338.83	-0.46	2.77	2.47	3.37	2.59	41.85	21
934	338.32	-0.42	2.77	1.97	4.12	2.33	36.09	17
936	338.08	-0.45	2.76	1.66	2.60	1.87	21.71	11
939	338.19	-0.48	2.76	1.74	2.69	1.87	23.72	11
940	338.85	-0.47	2.76	2.98	3.87	2.39	37.16	18
941	338.18	-0.47	2.76	2.46	2.66	2.26	30.54	16
944	338.83	-0.45	2.75	6.34	7.60	3.74	85.64	44
949	338.82	-0.46	2.74	3.20	2.57	2.39	37.41	18
950	338.10	-0.46	2.74	3.28	2.50	2.33	36.22	17
953	338.78	-0.46	2.74	4.17	2.04	2.46	38.05	19

Continued on next page

Table A.2 – Continued from previous page

ID	l [°]	b [°]	$N(H_2)_{peak}$ $[\frac{1}{cm^2}]$	$FWHM_x$ pix	$FWHM_y$ pix	R pix	$N(H_2)_{tot}$ $[\frac{1}{cm^2}]$	N_{pix}
954	338.40	-0.40	2.74	6.99	3.35	2.99	47.57	28
956	338.81	-0.48	2.73	5.81	5.17	2.93	52.59	27
963	338.41	-0.41	2.73	2.17	2.39	1.87	21.75	11
970	338.69	-0.49	2.72	1.49	4.69	2.11	26.56	14
973	338.41	-0.40	2.72	1.57	3.93	2.11	26.85	14
980	338.37	-0.40	2.70	2.67	3.47	2.03	25.73	13
981	338.20	-0.47	2.70	3.26	5.64	2.65	44.85	22
987	338.31	-0.50	2.69	2.55	2.70	2.26	30.31	16
994	338.37	-0.40	2.69	2.56	4.04	2.19	30.63	15
1002	338.09	-0.46	2.68	4.93	2.33	2.39	35.03	18
1005	338.93	-0.48	2.68	2.58	2.44	2.19	29.21	15
1009	338.86	-0.47	2.68	2.71	3.94	2.26	29.48	16
1011	339.03	-0.40	2.67	2.44	3.07	2.26	31.96	16
1016	338.94	-0.42	2.66	3.65	3.96	2.82	49.61	25
1022	338.11	-0.47	2.65	1.75	3.64	2.26	32.96	16
1025	338.32	-0.40	2.65	5.67	3.46	2.59	40.37	21
1027	338.76	-0.46	2.64	2.44	2.77	2.19	28.37	15
1031	338.08	-0.42	2.63	4.11	3.86	2.03	24.55	13
1032	338.31	-0.52	2.63	2.77	1.89	2.03	26.27	13
1033	338.93	-0.47	2.63	3.04	3.09	2.26	28.61	16
1037	338.92	-0.47	2.63	3.53	2.26	2.11	25.46	14
1040	338.65	-0.46	2.62	1.73	3.97	2.11	25.92	14
1046	338.31	-0.40	2.62	4.60	2.31	2.65	39.79	22
1049	338.23	-0.46	2.61	2.09	2.92	2.19	27.37	15
1051	338.39	-0.40	2.61	2.43	2.66	1.95	21.65	12
1053	338.42	-0.41	2.60	2.34	2.28	1.95	22.77	12
1056	338.78	-0.50	2.60	4.00	2.24	2.46	36.40	19
1058	338.73	-0.48	2.60	2.31	2.08	1.87	20.14	11
1059	338.86	-0.49	2.60	2.60	3.83	2.33	32.30	17
1061	339.03	-0.42	2.59	2.68	3.08	2.26	30.22	16
1062	338.82	-0.45	2.59	3.55	2.87	2.39	36.06	18
1072	338.32	-0.51	2.57	6.73	3.80	2.65	39.47	22
1074	338.82	-0.48	2.57	2.42	3.00	2.33	33.41	17
1075	338.18	-0.46	2.57	2.87	2.45	2.03	23.19	13
1077	338.18	-0.47	2.57	1.88	3.66	2.03	22.67	13
1079	338.92	-0.52	2.56	2.09	6.18	2.59	38.36	21
1089	338.93	-0.50	2.54	2.79	1.70	1.95	22.25	12
1098	338.08	-0.42	2.53	2.58	4.52	2.52	37.33	20
1099	338.32	-0.51	2.53	6.36	2.29	2.39	31.33	18
1100	338.92	-0.49	2.53	4.13	2.46	2.65	40.62	22

Continued on next page

Table A.2 – Continued from previous page

ID	l [°]	b [°]	$N(H_2)_{peak}$ $[\frac{1}{cm^2}]$	$FWHM_x$ pix	$FWHM_y$ pix	R pix	$N(H_2)_{tot}$ $[\frac{1}{cm^2}]$	N_{pix}
1103	338.78	-0.47	2.53	1.82	2.66	1.95	23.11	12
1107	338.19	-0.47	2.52	4.23	4.07	2.46	35.50	19
1109	338.68	-0.46	2.52	3.00	3.41	2.59	37.29	21
1110	338.66	-0.46	2.52	2.36	3.03	2.33	30.75	17
1111	338.23	-0.54	2.51	2.72	2.88	2.33	31.96	17
1112	338.92	-0.49	2.51	3.51	1.76	2.19	29.06	15
1115	338.75	-0.47	2.51	2.49	3.75	2.19	27.81	15
1118	338.96	-0.44	2.50	2.76	2.17	1.87	20.08	11
1122	338.35	-0.41	2.50	3.72	3.95	2.33	31.33	17
1132	338.11	-0.47	2.48	3.15	1.93	1.95	22.37	12
1140	339.03	-0.40	2.47	2.94	4.73	2.33	28.47	17
1144	338.68	-0.48	2.46	2.10	2.74	2.03	23.67	13
1154	338.76	-0.48	2.45	3.15	2.07	2.03	23.77	13
1155	339.01	-0.41	2.45	3.40	2.87	2.03	23.04	13
1157	338.42	-0.41	2.45	3.02	2.06	2.11	24.91	14
1163	338.86	-0.48	2.44	3.54	3.71	2.52	34.61	20
1164	338.33	-0.51	2.44	2.79	1.77	1.95	21.37	12
1166	338.79	-0.45	2.44	3.51	2.96	2.26	29.53	16
1167	338.65	-0.45	2.44	2.83	4.72	2.52	37.71	20
1170	338.32	-0.40	2.44	3.62	2.71	2.46	34.45	19
1174	338.31	-0.41	2.43	1.76	3.56	2.11	25.21	14
1186	338.93	-0.44	2.41	2.16	2.09	1.87	20.10	11
1193	338.41	-0.43	2.40	2.91	4.72	2.76	43.26	24
1199	338.43	-0.41	2.38	3.00	2.42	2.26	28.97	16
1201	338.13	-0.47	2.38	2.13	3.51	2.26	29.05	16
1203	338.29	-0.46	2.38	2.15	2.94	1.87	19.95	11
1204	338.75	-0.50	2.38	2.94	1.66	1.95	22.68	12
1205	338.81	-0.47	2.38	4.46	2.38	2.33	28.46	17
1206	338.80	-0.46	2.38	4.55	1.80	2.11	23.51	14
1210	338.39	-0.41	2.37	2.82	1.63	1.87	19.66	11
1211	338.31	-0.44	2.37	2.29	3.39	2.19	28.20	15
1216	338.34	-0.50	2.36	1.40	3.81	1.95	23.55	12
1226	338.64	-0.44	2.34	2.71	1.73	1.95	21.87	12
1242	338.07	-0.43	2.33	4.49	4.30	2.59	37.37	21
1246	338.84	-0.48	2.32	1.62	2.74	1.87	19.24	11
1248	339.04	-0.41	2.32	1.74	2.79	1.95	21.91	12
1249	338.25	-0.44	2.32	2.62	3.13	2.03	22.78	13
1251	339.02	-0.40	2.32	3.15	4.01	2.39	31.33	18
1252	339.00	-0.41	2.32	3.96	1.93	2.11	25.44	14
1258	338.12	-0.47	2.31	2.82	2.50	2.19	25.60	15

Continued on next page

Table A.2 – Continued from previous page

ID	l [°]	b [°]	$N(H_2)_{peak}$ [$\frac{1}{cm^2}$]	$FWHM_x$ pix	$FWHM_y$ pix	R pix	$N(H_2)_{tot}$ [$\frac{1}{cm^2}$]	N_{pix}
1259	338.69	-0.48	2.31	1.80	2.68	1.87	18.46	11
1261	338.20	-0.48	2.31	2.76	7.84	2.39	30.11	18
1262	338.70	-0.46	2.31	4.21	3.62	1.95	20.75	12
1266	338.69	-0.46	2.30	3.16	1.71	1.95	22.74	12
1271	338.11	-0.46	2.30	3.51	1.85	2.03	23.63	13
1275	338.16	-0.47	2.29	1.88	2.94	2.03	23.12	13
1278	338.75	-0.50	2.29	2.67	9.65	3.04	48.86	29
1281	338.75	-0.46	2.29	2.75	2.76	2.26	29.68	16
1288	338.68	-0.46	2.28	3.35	1.92	2.19	26.11	15
1289	338.94	-0.48	2.28	5.99	1.85	2.19	25.31	15
1290	339.03	-0.40	2.27	3.28	2.19	2.11	23.38	14
1293	338.92	-0.43	2.27	6.72	4.35	2.76	42.14	24
1307	338.08	-0.44	2.24	5.37	1.44	2.03	23.45	13
1309	338.28	-0.43	2.24	3.77	1.77	2.03	22.34	13
1312	338.21	-0.49	2.24	2.75	2.46	1.87	20.47	11
1314	338.59	-0.45	2.23	3.06	4.20	2.26	27.29	16
1315	338.39	-0.40	2.23	3.21	2.08	2.03	22.14	13
1318	338.77	-0.47	2.23	4.02	2.83	2.03	20.97	13
1322	338.80	-0.48	2.22	4.08	1.91	2.19	26.50	15
1324	339.06	-0.42	2.22	1.77	2.95	2.03	22.86	13
1325	338.82	-0.47	2.22	4.72	1.58	2.03	23.03	13
1336	338.24	-0.46	2.21	3.37	2.03	2.11	23.68	14
1341	338.24	-0.45	2.20	2.75	6.28	2.59	35.06	21
1343	338.33	-0.54	2.19	2.78	3.55	1.95	21.35	12
1346	338.61	-0.44	2.19	2.50	2.28	1.87	18.92	11
1348	338.31	-0.49	2.19	2.14	5.71	2.39	29.30	18
1351	338.90	-0.43	2.18	2.04	2.78	1.87	18.29	11
1357	339.06	-0.41	2.18	2.29	2.16	1.95	21.11	12
1359	338.58	-0.45	2.17	1.87	4.60	2.46	31.17	19
1361	339.05	-0.41	2.17	2.60	2.69	2.03	22.80	13
1363	338.55	-0.42	2.17	1.68	2.79	1.87	19.69	11
1364	338.97	-0.41	2.17	2.00	3.08	1.87	19.79	11
1365	338.93	-0.49	2.17	5.81	11.05	2.88	44.12	26
1366	338.52	-0.43	2.17	1.89	2.52	1.95	21.52	12
1375	338.11	-0.46	2.16	3.46	4.06	2.19	26.28	15
1380	338.51	-0.41	2.15	5.56	2.41	2.52	32.87	20
1382	338.21	-0.48	2.15	2.33	3.05	1.95	20.87	12
1384	338.31	-0.46	2.14	2.61	2.04	1.87	18.32	11
1386	338.61	-0.45	2.14	1.82	2.42	1.87	19.15	11
1392	338.21	-0.46	2.13	7.33	1.18	2.52	33.94	20

Continued on next page

Table A.2 – Continued from previous page

ID	l [°]	b [°]	$N(H_2)_{peak}$ $[\frac{1}{cm^2}]$	$FWHM_x$ pix	$FWHM_y$ pix	R pix	$N(H_2)_{tot}$ $[\frac{1}{cm^2}]$	N_{pix}
1396	338.18	-0.49	2.12	2.00	2.43	1.87	18.83	11
1399	338.39	-0.40	2.12	2.20	2.23	1.87	18.85	11
1400	338.93	-0.48	2.12	3.15	2.78	1.87	18.96	11
1405	338.12	-0.46	2.11	2.77	2.00	1.87	19.07	11
1408	338.13	-0.49	2.10	7.10	5.57	2.46	31.00	19
1411	339.02	-0.40	2.10	8.15	3.09	2.93	44.73	27
1419	338.72	-0.46	2.08	2.14	3.05	2.11	24.18	14
1421	339.09	-0.41	2.08	6.14	1.73	2.03	22.01	13
1426	338.66	-0.45	2.07	3.70	1.57	1.95	18.95	12
1428	339.05	-0.41	2.07	4.41	1.95	2.33	28.24	17
1438	338.76	-0.46	2.05	2.26	2.87	1.87	19.42	11
1442	338.12	-0.50	2.05	2.24	2.15	1.87	18.54	11
1444	338.80	-0.48	2.04	3.64	2.13	1.87	18.07	11
1454	338.93	-0.50	2.03	4.36	5.94	2.76	39.36	24
1460	338.93	-0.48	2.02	2.78	1.75	1.87	18.35	11
1464	338.95	-0.42	2.01	5.24	3.37	2.59	34.32	21
1466	339.10	-0.41	2.01	2.80	3.20	1.87	17.33	11
1473	338.24	-0.45	2.00	2.75	2.79	1.95	20.27	12
1474	338.92	-0.50	1.99	3.29	1.73	1.87	18.02	11
1475	338.63	-0.46	1.99	1.68	3.27	1.87	19.41	11
1478	338.75	-0.48	1.98	3.83	4.53	2.19	25.00	15
1485	338.92	-0.47	1.97	2.21	2.50	1.95	19.61	12
1492	338.25	-0.41	1.95	1.55	4.60	1.95	18.79	12
1495	338.91	-0.45	1.94	5.13	1.67	2.11	22.28	14
1513	338.79	-0.50	1.90	3.47	3.03	1.95	18.84	12
1515	338.68	-0.46	1.89	3.22	2.39	1.95	18.85	12
1517	338.16	-0.48	1.89	3.66	2.43	1.87	18.60	11
1522	338.97	-0.41	1.86	3.08	2.27	1.87	17.50	11
1527	338.83	-0.46	1.85	3.54	4.50	1.95	19.37	12
1535	338.61	-0.45	1.79	2.29	3.22	1.87	17.12	11
1538	338.80	-0.48	1.77	3.13	2.48	1.87	17.05	11
1539	338.79	-0.47	1.76	4.52	1.12	1.87	17.07	11
1540	338.09	-0.43	1.76	4.58	3.86	1.95	17.82	12
1546	338.80	-0.49	1.73	5.75	1.51	2.11	20.86	14

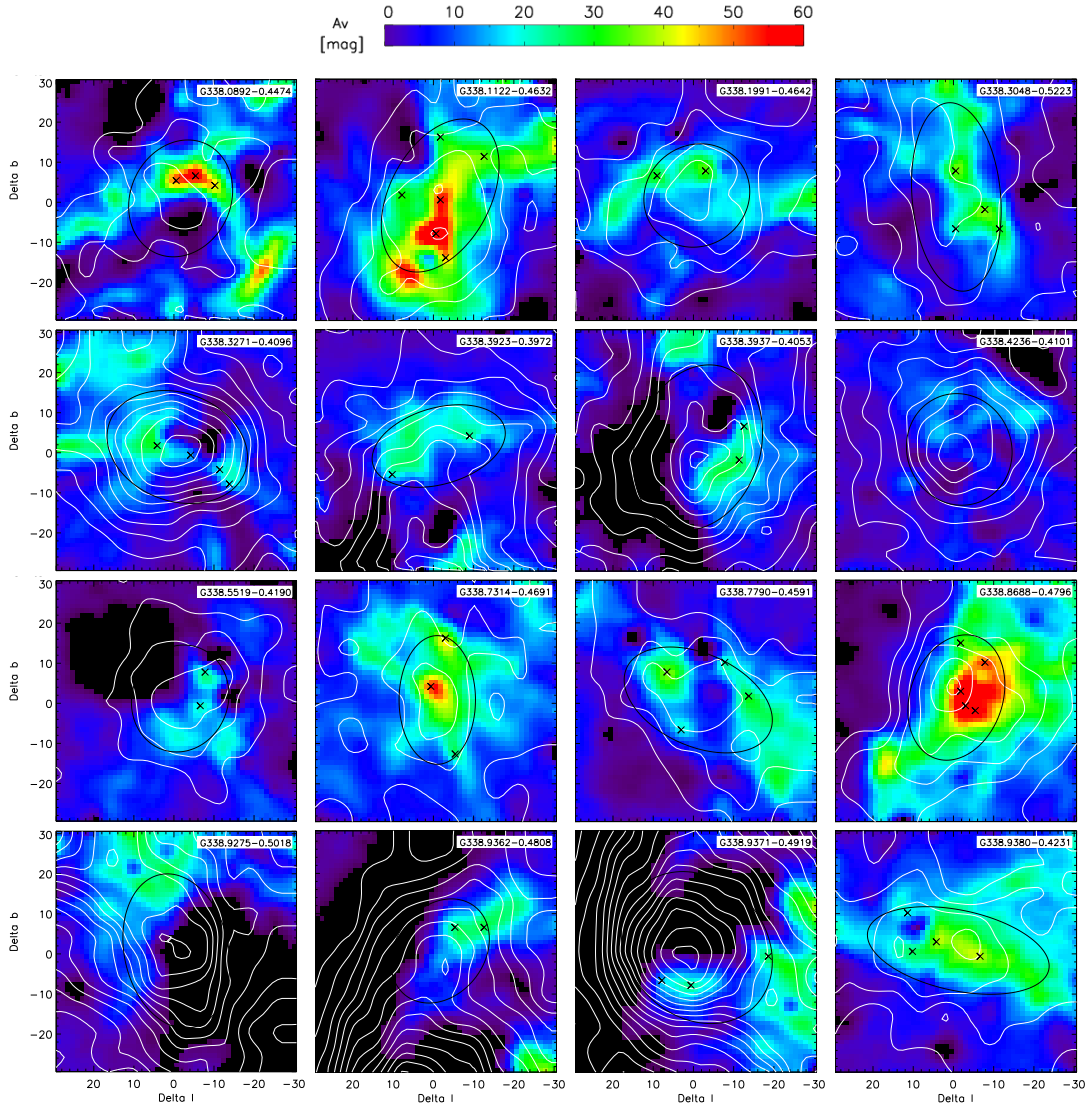

Figure A.6: Half-power ellipses of 16 GCSC ATLASGAL sources (black) overlaid on combined NIR and MIR extinction maps. The crosses mark the position of substructures detected on a scale-map ($s = 2$) by the clumpfind-2D algorithm within the ATLASGAL sources. The white lines indicate the contours of the ATLASGAL emission.

Appendix B

Appendix to Chapter 5

B.1 Tables of Filament properties

Table B.1: Measured parameters of all filaments.

Filament ID	ℓ °	b °	Status	N_c	$v_{lsr}(^{13}CO)$ km s^{-1}	$v_{lsr}(C^{18}O)$ km s^{-1}	$\sigma(v_{^{13}CO})$ km s^{-1}	$\sigma(v_{C^{18}O})$ km s^{-1}	σ_v km s^{-1}	$\sigma_v(^{13}CO)$ km s^{-1}	$\sigma_v(C^{18}O)$ km s^{-1}	$\sigma_{v,t}(^{13}CO)$ km s^{-1}	$\sigma_{v,t}(C^{18}O)$ km s^{-1}
G000.615-00.448_0	0.61	-0.45	full. cor.	1	15.69	15.75	0.56	7.18	0.84	0.95	0.5	1.19	1.16
G000.675+00.310_0	0.67	0.31	part. cor.	1	136.44	-	1.33	0.0	1.72	1.73	-	3.79	-
G000.914+00.308_0	0.91	0.31	part. cor.	1	174.07	173.73	1.99	0.0	1.94	1.95	-	4.46	4.88
G001.717+00.359_0	1.72	0.36	part. cor.	3	3.07	2.34	0.36	0.53	0.79	0.92	0.46	1.24	0.81
G001.717+00.359_1	1.72	0.36	part. cor.	3	8.93	-	0.44	1.19	0.97	1.07	0.61	1.76	-
G001.717+00.359_2	1.72	0.36	part. cor.	3	-17.3	-	3.17	0.0	1.73	1.74	-	4.65	-
G002.128+00.295_0	2.13	0.3	full. cor.	1	3.86	2.85	0.36	1.66	1.13	1.23	0.71	1.98	-
G002.210-00.049_0	2.21	-0.05	part. cor.	2	11.27	8.39	2.05	0.0	2.77	2.77	-	5.62	5.95
G002.210-00.049_1	2.21	-0.05	part. cor.	2	127.35	126.52	1.42	0.0	1.72	1.73	-	3.03	3.81
G002.370+00.069_0	2.37	0.07	dif. comp.	3	1.21	0.45	0.5	0.0	0.79	0.81	-	1.05	1.03
G002.370+00.069_1	2.37	0.07	full. cor.	3	7.56	7.67	0.89	1.36	1.38	1.41	0.64	2.17	2.18
G002.370+00.069_2	2.37	0.07	part. cor.	3	15.97	15.61	0.24	0.0	0.98	1.0	-	1.53	1.31
G002.420+00.205_0	2.42	0.21	part. cor.	1	6.68	7.05	0.75	2.5	0.91	1.1	0.71	2.14	2.05
G002.476-00.120_0	2.48	-0.12	part. cor.	2	6.99	6.28	1.13	0.0	1.31	1.33	-	2.56	2.75
G002.476-00.120_1	2.48	-0.12	part. cor.	2	14.93	13.99	0.84	0.0	0.94	0.97	-	1.83	-
G002.585-00.000_0	2.59	-0.0	part. cor.	2	-5.58	-5.49	0.76	1.59	1.13	1.17	1.0	1.7	1.62
G002.585-00.000_1	2.59	-0.0	dif. comp.	2	5.5	-	0.58	0.0	1.38	1.4	-	2.31	-
G002.687+00.106_0	2.69	0.11	full. cor.	1	10.68	9.69	1.35	4.43	1.25	2.01	0.64	3.98	-
G003.321-00.097_0	3.32	-0.1	part. cor.	2	3.61	3.69	0.81	0.54	1.27	1.34	0.7	1.91	1.68
G003.321-00.097_1	3.32	-0.1	part. cor.	2	10.24	9.79	1.13	3.48	1.35	1.56	1.15	2.09	1.45
G003.387+00.185_0	3.39	0.18	part. cor.	1	66.94	72.73	1.98	0.0	1.96	1.97	-	5.85	9.2
G003.446-00.223_0	3.45	-0.22	part. cor.	1	-23.25	-22.61	0.93	0.0	0.95	0.97	-	1.6	-
G003.456+00.006_0	3.46	0.01	full. cor.	1	5.11	5.07	0.62	2.17	1.05	1.33	0.61	1.94	-
G004.180-00.010_0	4.18	-0.01	part. cor.	3	6.22	5.23	0.53	1.6	0.69	0.76	0.5	1.46	1.24
G004.180-00.010_1	4.18	-0.01	full. cor.	3	14.61	14.51	1.03	3.66	1.27	1.37	0.57	2.13	2.46
G004.180-00.010_2	4.18	-0.01	part. cor.	3	27.11	26.08	0.78	9.62	0.99	1.21	0.85	1.66	-
G004.583-00.109_0	4.58	-0.11	part. cor.	2	13.79	13.71	0.74	4.35	1.2	1.39	0.59	2.2	1.73
G004.583-00.109_1	4.58	-0.11	part. cor.	2	25.1	23.24	1.55	0.0	1.32	1.33	-	2.33	-

Table B.1: Measured parameters of all filaments continued.

Filament ID	ℓ	b	Status	N_c	$v_{lsr}(^{13}CO)$	$v_{lsr}(C^{18}O)$	$\sigma(v_{^{13}CO})$	$\sigma(v_{C^{18}O})$	σ_v	$\sigma_v(^{13}CO)$	$\sigma_v(C^{18}O)$	$\sigma_{v,t}(^{13}CO)$	$\sigma_{v,t}(C^{18}O)$
	°	°			km s^{-1}	km s^{-1}	km s^{-1}	km s^{-1}	km s^{-1}	km s^{-1}	km s^{-1}	km s^{-1}	km s^{-1}
G004.705+00.001_0	4.7	0.0	full. cor.	1	10.32	10.54	0.52	5.03	1.74	2.81	0.58	3.24	2.2
G004.711-00.440_0	4.71	-0.44	full. cor.	1	5.91	5.47	0.24	1.52	0.7	0.76	0.41	0.98	0.99
G004.794-00.284_0	4.79	-0.28	full. cor.	2	6.77	6.67	0.25	0.0	0.74	0.77	-	1.07	0.73
G004.794-00.284_1	4.79	-0.28	part. cor.	2	12.15	11.76	0.37	0.0	1.05	1.07	-	1.4	1.11
G004.950-00.076_0	4.95	-0.08	full. cor.	1	11.01	11.33	0.73	3.3	1.13	1.23	1.02	1.95	1.09
G005.101-00.104_0	5.1	-0.1	full. cor.	1	45.0	44.99	0.81	16.57	1.07	1.21	0.7	1.61	1.66
G005.357+00.101_0	5.36	0.1	full. cor.	1	10.98	11.18	0.82	5.21	0.75	1.13	0.58	2.13	1.17
G005.454+00.167_0	5.45	0.17	full. cor.	1	12.92	13.24	0.32	0.0	1.09	1.11	-	1.6	1.7
G005.704-00.306_0	5.7	-0.31	full. cor.	1	7.54	7.41	0.28	0.0	1.27	1.29	-	1.45	1.15
G005.912+00.283_0	5.91	0.28	part. cor.	1	57.99	-	1.93	0.0	1.52	1.54	-	3.27	-
G005.930-00.095_0	5.93	-0.09	part. cor.	1	15.3	15.78	0.26	3.95	0.7	0.74	0.58	0.92	0.61
G006.589-00.106_0	6.59	-0.11	part. cor.	2	5.05	6.37	0.78	0.42	1.13	1.19	0.78	1.57	1.38
G006.589-00.106_1	6.59	-0.11	part. cor.	2	15.35	15.46	2.55	5.55	1.71	1.96	1.09	3.6	2.99
G006.849+00.151_0	6.85	0.15	part. cor.	2	18.46	18.48	0.76	0.0	1.04	1.06	-	2.07	2.02
G006.849+00.151_1	6.85	0.15	part. cor.	2	-17.1	-16.98	0.86	0.0	1.12	1.14	-	1.75	2.34
G007.250-00.120_0	7.25	-0.12	part. cor.	2	18.21	18.68	0.37	2.5	0.86	0.9	0.68	0.96	0.27
G007.250-00.120_1	7.25	-0.12	part. cor.	2	22.76	22.85	0.63	10.2	1.02	1.28	0.62	1.57	1.34
G008.000-00.272_0	8.0	-0.27	full. cor.	1	40.72	40.56	0.48	15.76	1.01	1.5	0.88	1.71	1.22
G008.255+00.165_0	8.25	0.16	full. cor.	1	18.87	19.03	0.27	0.34	0.79	1.36	0.71	1.41	1.21
G008.800-00.359_0	8.8	-0.36	full. cor.	2	38.18	38.35	0.64	18.79	1.15	1.45	0.66	1.77	0.61
G008.800-00.359_1	8.8	-0.36	part. cor.	2	20.21	20.15	0.36	7.51	0.85	0.94	0.55	1.29	1.47
G008.914-00.318_0	8.91	-0.32	full. cor.	1	38.03	38.1	0.49	19.21	1.06	1.3	0.63	1.56	-
G009.230+00.157_0	9.23	0.16	full. cor.	1	16.97	17.22	0.35	4.59	0.7	1.04	0.61	1.14	0.89
G009.280-00.152_0	9.28	-0.15	full. cor.	1	40.97	41.75	0.28	0.29	0.74	1.36	0.64	1.56	-
G009.970-00.024_0	9.97	-0.02	part. cor.	3	49.46	48.9	0.83	21.86	1.12	1.43	0.83	2.25	1.43
G009.970-00.024_1	9.97	-0.02	part. cor.	3	11.12	10.87	0.44	0.0	1.21	1.23	-	2.03	2.53
G009.970-00.024_2	9.97	-0.02	dif. comp.	3	17.51	15.94	0.36	0.0	0.67	0.7	-	1.13	-
G010.531-00.024_0	10.53	-0.02	part. cor.	1	69.23	69.18	1.51	18.22	1.53	1.63	0.98	2.68	2.75

Table B.1: Measured parameters of all filaments continued.

Filament ID	ℓ	b	Status	N_c	$v_{lsr}(^{13}CO)$	$v_{lsr}(C^{18}O)$	$\sigma(v_{^{13}CO})$	$\sigma(v_{C^{18}O})$	σ_v	$\sigma_v(^{13}CO)$	$\sigma_v(C^{18}O)$	$\sigma_{v,t}(^{13}CO)$	$\sigma_{v,t}(C^{18}O)$
	°	°			km s^{-1}	km s^{-1}	km s^{-1}	km s^{-1}	km s^{-1}	km s^{-1}	km s^{-1}	km s^{-1}	km s^{-1}
G010.682-00.161_0	10.68	-0.16	full. cor.	4	29.52	29.75	0.78	14.62	1.73	2.23	0.87	2.83	1.96
G010.682-00.161_1	10.68	-0.16	dif. comp.	4	42.6	-	0.87	0.0	0.95	0.97	-	2.16	-
G010.682-00.161_2	10.68	-0.16	part. cor.	4	51.4	51.9	0.41	17.38	0.97	1.25	0.75	1.31	-
G010.682-00.161_3	10.68	-0.16	dif. comp.	4	-8.08	-	3.32	0.0	0.85	0.88	-	3.88	-
G010.694+00.034_0	10.69	0.03	part. cor.	3	18.92	19.07	0.79	5.3	1.36	1.6	0.6	2.13	2.28
G010.694+00.034_1	10.69	0.03	full. cor.	3	30.81	31.21	2.24	9.87	2.34	2.52	0.81	3.77	3.74
G010.694+00.034_2	10.69	0.03	part. cor.	3	39.19	-	0.43	0.0	0.97	0.99	-	1.15	-
G010.809-00.393_0	10.81	-0.39	part. cor.	2	-0.26	-1.13	0.9	0.54	1.31	1.42	1.01	1.96	1.98
G010.809-00.393_1	10.81	-0.39	part. cor.	2	30.82	29.2	0.47	0.0	0.98	1.0	-	1.78	-
G010.878-00.468_0	10.88	-0.47	part. cor.	2	32.77	33.07	0.63	9.55	1.45	1.65	0.6	2.97	0.86
G010.878-00.468_1	10.88	-0.47	part. cor.	2	-0.63	0.06	1.65	0.17	1.21	1.26	0.61	2.08	1.99
G010.971-00.363_0	10.97	-0.36	full. cor.	2	-1.01	-0.94	0.71	0.29	1.32	1.39	0.67	1.69	1.24
G010.971-00.363_1	10.97	-0.36	part. cor.	2	33.91	34.53	0.6	0.0	1.61	1.63	-	2.42	2.05
G011.046-00.069_0	11.05	-0.07	dif. comp.	3	10.99	8.69	0.63	0.68	1.07	1.09	0.46	1.89	-
G011.046-00.069_1	11.05	-0.07	part. cor.	3	19.72	21.03	1.83	4.65	1.24	1.44	0.76	2.53	2.15
G011.046-00.069_2	11.05	-0.07	full. cor.	3	30.0	30.01	1.06	14.75	1.06	1.35	0.68	1.93	1.71
G011.612-00.383_0	11.61	-0.38	full. cor.	1	30.64	30.43	0.3	0.0	1.83	1.84	-	2.48	2.12
G012.405-00.138_0	12.41	-0.14	full. cor.	2	33.61	33.75	0.39	11.92	1.14	1.25	0.57	1.35	1.22
G012.405-00.138_1	12.41	-0.14	part. cor.	2	120.88	120.44	0.53	0.0	0.81	0.84	-	1.1	1.12
G012.529-00.314_0	12.53	-0.31	full. cor.	3	34.8	34.68	0.5	14.83	1.08	1.2	0.81	1.4	0.59
G012.529-00.314_1	12.53	-0.31	dif. comp.	3	40.27	40.49	0.53	0.0	0.58	0.61	-	0.93	0.93
G012.529-00.314_2	12.53	-0.31	dif. comp.	3	9.82	8.16	0.73	0.0	1.25	1.26	-	2.23	-
G012.543+00.011_0	12.54	0.01	part. cor.	2	45.69	45.49	0.44	8.38	1.27	1.32	0.8	2.06	1.42
G012.543+00.011_1	12.54	0.01	part. cor.	2	34.49	-	0.21	0.0	0.8	0.83	-	1.17	-
G012.543-00.092_0	12.54	-0.09	part. cor.	3	36.46	36.61	0.85	0.0	1.24	1.26	-	1.93	2.59
G012.543-00.092_1	12.54	-0.09	full. cor.	3	50.96	51.02	0.83	5.42	1.27	1.32	0.39	2.42	2.84
G012.543-00.092_2	12.54	-0.09	dif. comp.	3	21.5	21.15	1.1	0.0	1.06	1.08	-	1.77	-
G012.595+00.116_0	12.59	0.12	part. cor.	1	56.98	57.18	0.68	20.0	0.88	0.98	0.75	1.28	0.96

Table B.1: Measured parameters of all filaments continued.

Filament ID	ℓ	b	Status	N_c	$v_{lsr}(^{13}CO)$	$v_{lsr}(C^{18}O)$	$\sigma(v_{^{13}CO})$	$\sigma(v_{C^{18}O})$	σ_v	$\sigma_v(^{13}CO)$	$\sigma_v(C^{18}O)$	$\sigma_{v,t}(^{13}CO)$	$\sigma_{v,t}(C^{18}O)$
	°	°			km s^{-1}	km s^{-1}	km s^{-1}	km s^{-1}	km s^{-1}	km s^{-1}	km s^{-1}	km s^{-1}	km s^{-1}
G012.893+00.496_0	12.89	0.5	full. cor.	2	32.72	32.7	0.58	5.12	0.96	1.49	0.96	1.77	1.04
G012.893+00.496_1	12.89	0.5	full. cor.	2	18.39	19.06	0.45	0.0	0.86	0.89	-	1.05	-
G013.220+00.164_0	13.22	0.16	full. cor.	2	53.81	54.21	0.33	0.0	1.21	1.23	-	1.57	1.6
G013.220+00.164_1	13.22	0.16	part. cor.	2	17.92	18.55	0.82	0.0	1.21	1.23	-	2.26	2.53
G013.282-00.316_0	13.28	-0.32	full. cor.	2	39.44	40.1	0.89	19.77	1.87	2.2	0.8	3.14	2.53
G013.282-00.316_1	13.28	-0.32	part. cor.	2	17.53	18.22	1.45	3.91	2.08	2.19	0.5	3.46	2.43
G013.313+00.193_0	13.31	0.19	full. cor.	2	18.16	18.27	0.58	8.22	0.85	0.95	0.61	1.13	0.7
G013.313+00.193_1	13.31	0.19	part. cor.	2	53.13	54.95	0.37	8.89	0.84	0.9	0.66	1.27	-
G013.460+00.171_0	13.46	0.17	full. cor.	1	18.16	18.08	0.29	4.64	1.1	1.15	0.62	1.23	-
G013.700-00.072_0	13.7	-0.07	part. cor.	1	47.89	47.21	0.98	23.35	0.88	1.19	0.74	1.65	1.11
G013.893-00.129_0	13.89	-0.13	full. cor.	2	39.12	38.95	0.49	19.67	1.39	1.7	0.7	1.81	1.33
G013.893-00.129_1	13.89	-0.13	part. cor.	2	17.56	16.99	0.75	8.19	1.32	1.62	0.99	2.09	2.1
G014.005+00.311_0	14.01	0.31	full. cor.	1	46.14	45.3	0.77	12.36	1.16	1.25	0.58	1.86	1.83
G014.117-00.392_0	14.12	-0.39	full. cor.	2	38.38	38.03	0.6	15.46	1.68	1.78	0.68	2.45	1.33
G014.117-00.392_1	14.12	-0.39	full. cor.	2	20.83	-	0.64	0.0	1.67	1.69	-	2.61	-
G014.627-00.123_0	14.63	-0.12	full. cor.	1	40.59	40.46	0.65	19.94	1.55	1.76	0.87	2.28	2.07
G014.789-00.478_0	14.79	-0.48	full. cor.	1	22.0	21.15	0.67	8.88	1.11	1.25	0.4	1.72	1.37
G014.919-00.065_0	14.92	-0.06	full. cor.	1	28.3	28.44	0.75	0.0	1.31	1.33	-	2.52	2.12
G015.611-00.476_0	15.61	-0.48	full. cor.	2	16.21	15.91	1.05	7.41	0.63	0.72	0.63	1.27	1.25
G015.611-00.476_1	15.61	-0.48	part. cor.	2	-4.2	-	0.78	0.0	1.14	1.16	-	1.66	-
G015.653-00.224_0	15.65	-0.22	full. cor.	1	57.4	57.5	0.69	24.27	0.61	0.77	0.59	1.04	0.7
G016.609-00.069_0	16.61	-0.07	part. cor.	2	59.06	59.22	0.94	22.42	0.79	1.0	0.71	1.54	1.25
G016.609-00.069_1	16.61	-0.07	part. cor.	2	41.25	40.82	1.01	14.72	0.96	1.26	0.71	2.72	1.17
G016.661+00.121_0	16.66	0.12	full. cor.	1	15.23	15.21	0.28	5.42	0.64	0.7	0.55	0.8	0.5
G016.700-00.235_0	16.7	-0.24	part. cor.	2	55.93	56.71	0.61	8.44	0.89	0.92	0.69	1.44	-
G016.700-00.235_1	16.7	-0.24	part. cor.	2	28.4	28.12	1.1	0.0	1.17	1.19	-	1.89	1.63
G016.757+00.013_0	16.76	0.01	full. cor.	1	33.99	34.96	0.6	6.31	1.33	1.37	0.84	2.23	-
G016.919+00.275_0	16.92	0.27	full. cor.	1	24.3	24.34	0.3	8.62	1.13	1.39	0.76	1.4	1.14

Table B.1: Measured parameters of all filaments continued.

Filament ID	ℓ	b	Status	N_c	$v_{lsr}(^{13}CO)$	$v_{lsr}(C^{18}O)$	$\sigma(v_{^{13}CO})$	$\sigma(v_{C^{18}O})$	σ_v	$\sigma_v(^{13}CO)$	$\sigma_v(C^{18}O)$	$\sigma_{v,t}(^{13}CO)$	$\sigma_{v,t}(C^{18}O)$
	°	°			km s^{-1}	km s^{-1}	km s^{-1}	km s^{-1}	km s^{-1}	km s^{-1}	km s^{-1}	km s^{-1}	km s^{-1}
G016.929-00.082_0	16.93	-0.08	full. cor.	2	40.85	40.86	0.32	14.5	0.72	0.81	0.48	1.02	0.37
G016.929-00.082_1	16.93	-0.08	dif. comp.	2	-4.42	-4.91	0.98	0.0	1.13	1.15	-	1.54	2.03
G016.998+00.280_0	17.0	0.28	full. cor.	1	23.35	23.66	0.67	10.71	1.32	1.67	0.52	1.84	1.68
G301.638-00.239_0	301.64	-0.24	full. cor.	1	-37.2	-37.34	0.5	12.09	0.96	1.34	0.66	1.41	0.6
G305.560-00.003_0	305.56	-0.0	full. cor.	1	-38.53	-38.11	1.26	15.3	1.39	1.66	1.0	2.1	1.76
G309.161-00.358_0	309.16	-0.36	full. cor.	1	-41.7	-41.43	0.3	6.8	1.02	1.65	0.85	2.01	1.67
G313.703-00.181_0	313.7	-0.18	full. cor.	1	-44.49	-44.38	0.9	1.36	1.04	1.75	0.88	2.06	2.14
G313.717+00.103_0	313.72	0.1	part. cor.	3	-55.82	-56.33	0.65	27.19	0.75	0.97	0.63	1.11	0.87
G313.717+00.103_1	313.72	0.1	dif. comp.	3	-50.55	-49.07	0.27	0.0	0.76	0.78	-	0.99	-
G313.717+00.103_2	313.72	0.1	full. cor.	3	-44.87	-44.83	0.19	22.4	0.79	1.1	0.57	1.1	0.76
G314.219+00.266_0	314.22	0.27	full. cor.	1	-60.53	-60.7	1.36	11.61	1.31	1.95	1.04	2.43	2.5
G314.284+00.100_0	314.28	0.1	full. cor.	2	-56.6	-56.2	0.48	25.54	1.17	1.33	0.76	1.47	0.96
G314.284+00.100_1	314.28	0.1	full. cor.	2	-50.3	-50.24	0.85	17.16	1.1	1.86	1.01	2.14	1.62
G317.386+00.113_0	317.39	0.11	full. cor.	1	-43.42	-43.27	1.66	13.37	1.45	1.98	1.0	2.71	2.67
G317.889-00.256_0	317.89	-0.26	full. cor.	1	-36.53	-35.99	0.65	12.09	1.31	1.77	1.04	1.96	1.68
G320.240+00.027_0	320.24	0.03	full. cor.	1	-9.88	-10.4	0.5	4.36	1.37	1.64	0.76	1.75	1.4
G320.243+00.406_0	320.24	0.41	part. cor.	1	-32.72	-32.4	0.37	16.01	0.83	0.98	0.84	1.22	0.93
G320.270-00.299_0	320.27	-0.3	full. cor.	1	-65.81	-65.6	1.01	30.69	1.34	1.7	1.01	2.09	1.46
G320.883-00.392_0	320.88	-0.39	full. cor.	1	-45.1	-45.08	0.46	6.77	0.84	1.33	0.81	1.54	1.2
G323.179+00.149_0	323.18	0.15	full. cor.	1	-65.96	-65.91	0.73	25.98	0.83	1.18	0.81	1.39	1.31
G323.929+00.036_0	323.93	0.04	full. cor.	1	-57.18	-57.23	0.64	24.27	1.69	1.78	0.73	2.23	2.02
G326.552+00.165_0	326.55	0.16	full. cor.	1	-74.69	-74.51	0.74	37.17	1.36	1.6	0.92	1.91	1.28
G326.586+00.050_0	326.59	0.05	full. cor.	1	-75.73	-75.55	0.49	0.0	1.25	1.27	-	1.73	-
G326.722-00.099_0	326.72	-0.1	full. cor.	1	-58.65	-57.08	1.23	13.52	1.73	1.79	0.79	2.74	0.9
G326.790-00.119_0	326.79	-0.12	full. cor.	1	-56.53	-56.27	0.52	25.21	1.29	1.76	0.87	1.97	1.18
G327.036-00.408_0	327.04	-0.41	full. cor.	1	-63.89	-63.57	0.84	26.58	1.09	1.56	0.74	1.97	1.25
G327.042-00.169_0	327.04	-0.17	full. cor.	1	-60.1	-60.55	0.63	26.22	1.47	1.63	0.69	1.94	1.33
G327.157-00.256_0	327.16	-0.26	full. cor.	1	-61.49	-61.52	1.33	24.59	1.59	2.23	0.94	2.85	2.52

Table B.1: Measured parameters of all filaments continued.

Filament ID	ℓ	b	Status	N_c	$v_{lsr}(^{13}CO)$	$v_{lsr}(C^{18}O)$	$\sigma(v_{^{13}CO})$	$\sigma(v_{C^{18}O})$	σ_v	$\sigma_v(^{13}CO)$	$\sigma_v(C^{18}O)$	$\sigma_{v,t}(^{13}CO)$	$\sigma_{v,t}(C^{18}O)$
	°	°			km s^{-1}	km s^{-1}	km s^{-1}	km s^{-1}	km s^{-1}	km s^{-1}	km s^{-1}	km s^{-1}	km s^{-1}
G327.258-00.420_0	327.26	-0.42	full. cor.	1	-48.01	-48.14	0.45	23.36	1.18	1.34	0.72	1.43	1.54
G327.396+00.452_0	327.4	0.45	full. cor.	1	-79.89	-79.35	0.48	38.14	1.44	1.75	1.04	2.29	1.85
G327.870+00.157_0	327.87	0.16	part. cor.	2	-92.65	-92.01	1.76	37.96	1.13	1.33	1.04	2.32	1.88
G327.870+00.157_1	327.87	0.16	dif. comp.	2	-50.25	-49.27	0.92	14.87	1.02	1.36	0.59	2.13	2.19
G327.884+00.002_0	327.88	0.0	full. cor.	2	-97.17	-96.4	0.55	18.94	1.17	1.2	0.95	1.5	1.13
G327.884+00.002_1	327.88	0.0	part. cor.	2	-49.48	-48.14	0.51	0.0	0.78	0.81	-	0.86	-
G327.981-00.101_0	327.98	-0.1	full. cor.	1	-48.87	-48.63	0.85	20.19	1.49	1.78	0.86	2.22	2.11
G328.627+00.063_0	328.63	0.06	part. cor.	2	-85.69	-	0.28	0.0	0.81	0.84	-	1.06	-
G328.627+00.063_1	328.63	0.06	part. cor.	2	-56.59	-	0.48	0.0	1.07	1.09	-	1.6	-
G328.773+00.304_0	328.77	0.3	full. cor.	2	-101.44	-101.79	0.57	41.63	1.35	1.54	0.59	1.8	1.3
G328.773+00.304_1	328.77	0.3	dif. comp.	2	-86.01	-	0.2	0.0	0.75	0.78	-	1.31	-
G328.940+00.277_0	328.94	0.28	full. cor.	1	-88.82	-89.06	0.54	0.0	1.4	1.42	-	1.65	0.99
G330.348-00.122_0	330.35	-0.12	part. cor.	1	-95.97	-95.96	0.64	0.0	1.42	1.43	-	1.87	1.88
G330.760-00.306_0	330.76	-0.31	full. cor.	2	-63.07	-63.32	0.67	29.64	1.51	1.78	0.93	1.99	1.29
G330.760-00.306_1	330.76	-0.31	part. cor.	2	-53.2	-54.38	0.64	0.0	0.94	0.96	-	1.96	1.88
G330.973+00.076_0	330.97	0.08	part. cor.	3	-50.47	-50.37	0.59	12.48	1.11	1.23	0.64	1.67	0.94
G330.973+00.076_1	330.97	0.08	part. cor.	3	-61.5	-59.71	0.63	7.58	1.12	1.18	0.52	1.76	-
G330.973+00.076_2	330.97	0.08	part. cor.	3	-32.91	-33.82	0.38	5.56	0.75	0.81	0.65	0.87	-
G330.986+00.337_0	330.99	0.34	full. cor.	1	-55.7	-55.69	0.38	27.43	0.93	1.18	0.77	1.28	0.87
G331.533+00.241_0	331.53	0.24	dif. comp.	3	-62.31	-	0.31	0.0	1.04	1.06	-	1.43	-
G331.533+00.241_1	331.53	0.24	part. cor.	3	-55.63	-55.99	1.2	22.38	1.08	1.32	0.56	1.88	1.58
G331.533+00.241_2	331.53	0.24	part. cor.	3	-92.3	-92.12	0.56	15.41	1.13	1.2	0.53	1.63	1.46
G331.670-00.272_0	331.67	-0.27	full. cor.	3	-48.12	-48.17	0.67	15.48	0.66	0.93	0.64	1.18	1.06
G331.670-00.272_1	331.67	-0.27	dif. comp.	3	-99.78	-97.94	0.71	0.0	0.91	0.93	-	1.39	-
G331.670-00.272_2	331.67	-0.27	part. cor.	3	-94.07	-94.29	0.82	0.0	1.25	1.26	-	1.85	1.77
G331.973-00.378_0	331.97	-0.38	full. cor.	1	-60.3	-60.44	0.81	30.0	1.0	1.25	0.7	1.5	1.41
G332.000+00.011_0	332.0	0.01	full. cor.	2	-55.08	-54.18	1.68	8.97	2.32	2.4	0.52	3.6	2.38
G332.000+00.011_1	332.0	0.01	part. cor.	2	-87.04	-87.77	0.91	0.0	1.59	1.6	-	2.63	2.63

Table B.1: Measured parameters of all filaments continued.

Filament ID	ℓ °	b °	Status	N_c	$v_{lsr}(^{13}CO)$ km s^{-1}	$v_{lsr}(C^{18}O)$ km s^{-1}	$\sigma(v_{^{13}CO})$ km s^{-1}	$\sigma(v_{C^{18}O})$ km s^{-1}	σ_v km s^{-1}	$\sigma_v(^{13}CO)$ km s^{-1}	$\sigma_v(C^{18}O)$ km s^{-1}	$\sigma_{v,t}(^{13}CO)$ km s^{-1}	$\sigma_{v,t}(C^{18}O)$ km s^{-1}
G332.370-00.080_0	332.37	-0.08	dif. comp.	3	-58.92	-58.31	0.63	0.0	0.98	1.0	-	1.31	0.06
G332.370-00.080_1	332.37	-0.08	full. cor.	3	-48.2	-48.12	2.06	23.57	1.18	1.51	0.83	3.15	2.92
G332.370-00.080_2	332.37	-0.08	dif. comp.	3	-87.66	-88.02	1.57	16.15	1.27	1.39	0.76	2.71	2.53
G332.610+00.052_0	332.61	0.05	full. cor.	1	-94.91	-95.27	0.97	29.09	1.24	1.33	0.69	2.27	1.62
G332.852-00.214_0	332.85	-0.21	full. cor.	1	-42.06	-42.19	0.63	16.28	1.36	1.45	0.81	1.89	1.93
G333.007+00.452_0	333.01	0.45	full. cor.	1	-47.14	-	0.86	0.0	1.28	1.3	-	2.28	-
G333.063+00.181_0	333.06	0.18	full. cor.	1	-51.13	-50.78	1.06	21.78	1.94	2.2	0.96	3.23	2.87
G333.202-00.250_0	333.2	-0.25	part. cor.	3	-54.86	-55.42	1.37	0.0	0.97	0.99	-	1.67	1.63
G333.202-00.250_1	333.2	-0.25	part. cor.	3	-48.23	-49.39	2.03	0.0	1.13	1.15	-	2.5	1.48
G333.202-00.250_2	333.2	-0.25	part. cor.	3	-38.5	-	1.22	0.0	0.87	0.89	-	1.87	-
G333.297+00.073_0	333.3	0.07	full. cor.	2	-48.32	-48.42	1.09	23.89	1.59	1.85	1.01	2.38	1.67
G333.297+00.073_1	333.3	0.07	part. cor.	2	-70.21	-70.54	0.72	18.21	1.21	1.34	0.78	1.75	1.0
G333.481+00.165_0	333.48	0.16	full. cor.	1	-103.6	-103.82	0.29	30.98	0.84	0.88	0.79	0.88	0.91
G333.722+00.361_0	333.72	0.36	full. cor.	1	-33.99	-33.96	0.6	7.1	0.81	1.16	0.78	1.39	1.12
G333.868-00.312_0	333.87	-0.31	full. cor.	1	-46.4	-45.11	1.49	20.98	2.49	3.19	0.92	3.91	3.44
G333.899-00.106_0	333.9	-0.11	part. cor.	2	-93.62	-93.46	0.25	19.82	0.8	0.86	0.49	1.16	1.36
G333.899-00.106_1	333.9	-0.11	part. cor.	2	-41.82	-39.96	1.2	9.21	1.56	1.79	1.04	2.96	2.49
G333.985+00.224_0	333.98	0.22	part. cor.	5	-83.25	-82.64	0.38	12.38	0.76	0.8	0.31	1.22	1.1
G333.985+00.224_1	333.98	0.22	part. cor.	5	-48.13	-	1.04	9.73	0.97	1.02	0.44	1.77	-
G333.985+00.224_2	333.98	0.22	dif. comp.	5	-42.14	-	0.45	0.0	0.8	0.82	-	1.33	-
G333.985+00.224_3	333.98	0.22	part. cor.	5	-60.19	-60.08	1.9	16.15	1.02	1.1	0.54	2.09	1.93
G333.985+00.224_4	333.98	0.22	dif. comp.	5	-93.89	-	1.18	0.0	1.06	1.08	-	3.07	-
G333.992+00.058_0	333.99	0.06	full. cor.	3	-86.06	-86.01	0.68	24.2	1.78	1.89	0.7	2.86	2.73
G333.992+00.058_1	333.99	0.06	part. cor.	3	-44.96	-45.34	1.49	11.23	1.34	1.4	0.59	3.15	2.66
G333.992+00.058_2	333.99	0.06	part. cor.	3	-60.56	-60.18	0.8	18.22	0.9	1.03	0.75	1.28	0.99
G334.056+00.489_0	334.06	0.49	full. cor.	1	-59.72	-60.27	0.59	0.0	1.66	1.68	-	2.52	0.84
G334.070-00.257_0	334.07	-0.26	part. cor.	2	-48.76	-48.16	0.31	0.0	0.95	0.98	-	1.39	1.0
G334.070-00.257_1	334.07	-0.26	part. cor.	2	-43.63	-42.7	0.49	0.0	1.17	1.19	-	1.9	2.27

Table B.1: Measured parameters of all filaments continued.

Filament ID	ℓ	b	Status	N_c	$v_{lsr}(^{13}CO)$	$v_{lsr}(C^{18}O)$	$\sigma(v_{^{13}CO})$	$\sigma(v_{C^{18}O})$	σ_v	$\sigma_v(^{13}CO)$	$\sigma_v(C^{18}O)$	$\sigma_{v,t}(^{13}CO)$	$\sigma_{v,t}(C^{18}O)$
	°	°			km s^{-1}	km s^{-1}	km s^{-1}	km s^{-1}	km s^{-1}	km s^{-1}	km s^{-1}	km s^{-1}	km s^{-1}
G334.202+00.156_0	334.2	0.16	full. cor.	2	-89.28	-88.54	0.83	29.13	1.83	1.96	0.61	2.86	2.39
G334.202+00.156_1	334.2	0.16	part. cor.	2	-40.47	-39.8	1.08	0.0	1.36	1.37	-	2.47	2.58
G334.267-00.107_0	334.27	-0.11	full. cor.	2	-86.23	-86.01	0.85	9.93	1.21	1.24	0.67	1.75	1.17
G334.267-00.107_1	334.27	-0.11	part. cor.	2	-32.07	-32.8	1.5	3.61	1.29	1.34	0.74	2.58	-
G334.442+00.050_0	334.44	0.05	part. cor.	3	-90.46	-91.13	0.47	36.5	0.84	1.04	0.6	1.8	1.26
G334.442+00.050_1	334.44	0.05	part. cor.	3	-106.95	-108.36	1.36	0.0	1.16	1.18	-	1.97	-
G334.442+00.050_2	334.44	0.05	part. cor.	3	-70.86	-71.56	1.13	0.0	0.94	0.97	-	2.36	2.57
G334.617-00.270_0	334.62	-0.27	full. cor.	1	-46.18	-45.46	0.67	22.15	1.33	1.78	0.71	2.24	0.9
G334.640+00.426_0	334.64	0.43	full. cor.	1	-64.73	-64.55	0.39	31.84	1.02	1.24	0.81	1.52	0.82
G334.684+00.024_0	334.68	0.02	part. cor.	3	-32.05	-31.71	0.83	7.0	0.89	0.95	0.56	1.49	1.37
G334.684+00.024_1	334.68	0.02	dif. comp.	3	-27.49	-	0.11	0.0	0.65	0.68	-	0.67	-
G334.684+00.024_2	334.68	0.02	dif. comp.	3	-85.75	-	0.51	0.0	0.82	0.84	-	1.28	-
G334.840-00.196_0	334.84	-0.2	part. cor.	2	-43.77	-44.07	1.17	17.4	1.09	1.27	0.55	2.19	1.67
G334.840-00.196_1	334.84	-0.2	part. cor.	2	-27.81	-28.41	0.84	0.0	1.18	1.2	-	1.56	1.51
G335.008-00.268_0	335.01	-0.27	part. cor.	2	-27.06	-25.39	1.74	3.02	1.46	1.5	0.36	2.57	1.92
G335.008-00.268_1	335.01	-0.27	part. cor.	2	-18.75	-18.83	1.34	0.0	1.14	1.16	-	1.84	1.76
G335.083+00.065_0	335.08	0.07	part. cor.	1	-73.22	-74.25	0.79	0.0	1.11	1.13	-	1.86	0.57
G335.251-00.033_0	335.25	-0.03	full. cor.	1	-44.47	-44.59	0.43	10.95	1.02	1.07	0.65	1.75	1.72
G335.814+00.061_0	335.81	0.06	part. cor.	1	-89.59	-88.06	0.74	0.0	0.83	0.85	-	1.38	-
G336.060+00.040_0	336.06	0.04	part. cor.	1	-118.02	-118.41	0.52	38.31	0.98	1.1	0.53	1.41	-
G336.062-00.271_0	336.06	-0.27	full. cor.	1	-39.23	-39.52	0.43	12.74	0.8	0.88	0.7	1.11	1.03
G336.194-00.457_0	336.19	-0.46	full. cor.	1	-87.77	-87.82	0.22	26.29	0.88	0.94	0.63	1.2	0.88
G336.248+00.310_0	336.25	0.31	part. cor.	2	-73.37	-72.87	1.5	10.76	1.01	1.07	0.64	1.85	1.94
G336.248+00.310_1	336.25	0.31	part. cor.	2	-44.94	-45.01	0.6	14.29	0.75	1.05	0.52	1.41	0.96
G336.376+00.204_0	336.38	0.2	full. cor.	2	-45.82	-46.26	0.88	7.58	1.07	1.1	0.72	1.8	1.51
G336.376+00.204_1	336.38	0.2	dif. comp.	2	-68.41	-68.73	1.05	12.53	0.97	1.07	0.7	1.78	1.65
G336.391+00.012_0	336.39	0.01	part. cor.	2	-128.65	-128.26	1.21	40.86	1.36	1.48	1.36	2.24	2.0
G336.391+00.012_1	336.39	0.01	dif. comp.	2	-39.03	-	0.39	3.38	0.89	0.98	0.45	2.14	-

Table B.1: Measured parameters of all filaments continued.

Filament ID	ℓ °	b °	Status	N_c	$v_{lsr}(^{13}CO)$ km s^{-1}	$v_{lsr}(C^{18}O)$ km s^{-1}	$\sigma(v_{^{13}CO})$ km s^{-1}	$\sigma(v_{C^{18}O})$ km s^{-1}	σ_v km s^{-1}	$\sigma_v(^{13}CO)$ km s^{-1}	$\sigma_v(C^{18}O)$ km s^{-1}	$\sigma_{v,t}(^{13}CO)$ km s^{-1}	$\sigma_{v,t}(C^{18}O)$ km s^{-1}
G336.846+00.282_0	336.85	0.28	part. cor.	2	-77.16	-78.1	1.43	16.6	1.45	1.5	0.57	2.77	2.48
G336.846+00.282_1	336.85	0.28	part. cor.	2	-66.88	-67.05	0.76	22.57	0.92	1.13	0.72	1.33	1.01
G337.148-00.387_0	337.15	-0.39	full. cor.	2	-20.68	-20.61	0.65	0.0	0.74	0.77	-	1.17	1.29
G337.148-00.387_1	337.15	-0.39	part. cor.	2	-40.45	-41.11	0.52	6.81	0.87	0.94	0.72	1.2	0.86
G337.409-00.400_0	337.41	-0.4	part. cor.	2	-41.24	-41.42	0.48	20.23	1.01	1.26	1.1	1.78	1.37
G337.409-00.400_1	337.41	-0.4	dif. comp.	2	-54.26	-	0.21	10.05	0.7	0.77	0.51	0.78	-
G337.744-00.346_0	337.74	-0.35	full. cor.	1	-41.56	-41.58	0.6	19.85	0.99	1.22	0.72	1.69	1.16
G337.850+00.087_0	337.85	0.09	full. cor.	1	-54.82	-53.84	1.85	14.01	3.09	3.15	0.51	5.7	6.23
G338.181-00.477_0	338.18	-0.48	full. cor.	1	-36.88	-36.5	0.78	13.93	1.41	1.55	0.59	2.28	1.73
G338.279-00.295_0	338.28	-0.29	part. cor.	2	-13.54	-13.91	0.99	4.41	1.43	1.61	0.71	2.78	2.92
G338.279-00.295_1	338.28	-0.29	part. cor.	2	-122.35	-121.63	0.46	0.0	1.13	1.15	-	1.33	1.62
G338.291-00.119_0	338.29	-0.12	part. cor.	2	-91.93	-92.07	0.33	15.36	0.88	0.93	0.54	1.01	0.96
G338.291-00.119_1	338.29	-0.12	part. cor.	2	-116.16	-117.14	1.16	0.0	1.27	1.29	-	2.25	2.27
G338.528+00.214_0	338.53	0.21	part. cor.	1	-36.06	-35.78	0.64	12.04	1.34	1.48	0.86	2.12	2.11
G338.680-00.455_0	338.68	-0.45	full. cor.	2	-38.02	-39.32	0.37	13.01	1.17	1.28	0.62	2.17	-
G338.680-00.455_1	338.68	-0.45	part. cor.	2	-46.93	-	0.49	5.2	1.01	1.06	0.62	1.3	-
G338.708-00.328_0	338.71	-0.33	full. cor.	2	-45.24	-43.78	0.57	12.56	1.04	1.11	0.65	1.89	1.14
G338.708-00.328_1	338.71	-0.33	full. cor.	2	-31.77	-31.63	0.63	12.4	1.27	1.46	0.59	2.05	1.34
G338.749+00.159_0	338.75	0.16	full. cor.	1	-33.31	-34.75	0.74	15.59	1.79	1.99	1.0	2.92	-
G338.773+00.492_0	338.77	0.49	full. cor.	1	-62.87	-63.13	0.85	23.46	1.5	2.14	1.03	2.49	1.99
G338.806+00.111_0	338.81	0.11	full. cor.	1	-33.54	-34.6	0.68	9.56	1.7	1.84	0.67	2.66	-
G338.941-00.058_0	338.94	-0.06	part. cor.	2	-55.67	-56.54	0.84	12.33	0.92	0.96	0.76	1.42	-
G338.941-00.058_1	338.94	-0.06	part. cor.	2	-44.83	-45.54	1.37	22.96	1.23	1.6	1.0	2.6	2.02
G338.953+00.278_0	338.95	0.28	full. cor.	2	-55.15	-55.67	0.59	17.77	0.8	0.88	0.57	1.12	-
G338.953+00.278_1	338.95	0.28	part. cor.	2	-25.92	-25.32	1.14	3.48	1.31	1.32	0.42	2.46	2.23
G338.993+00.110_0	338.99	0.11	part. cor.	1	-28.15	-25.66	1.46	0.0	1.31	1.33	-	2.58	-
G339.077+00.153_0	339.08	0.15	part. cor.	2	-79.91	-79.84	1.27	33.74	1.31	1.5	1.03	2.28	2.49
G339.077+00.153_1	339.08	0.15	dif. comp.	2	-26.26	-22.5	1.55	0.0	1.15	1.17	-	2.7	-

Table B.1: Measured parameters of all filaments continued.

Filament ID	ℓ °	b °	Status	N_c	$v_{lsr}(^{13}CO)$ km s^{-1}	$v_{lsr}(C^{18}O)$ km s^{-1}	$\sigma(v_{^{13}CO})$ km s^{-1}	$\sigma(v_{C^{18}O})$ km s^{-1}	σ_v km s^{-1}	$\sigma_v(^{13}CO)$ km s^{-1}	$\sigma_v(C^{18}O)$ km s^{-1}	$\sigma_{v,t}(^{13}CO)$ km s^{-1}	$\sigma_{v,t}(C^{18}O)$ km s^{-1}
G339.113-00.203_0	339.11	-0.2	full. cor.	3	-117.57	-117.98	1.59	38.08	1.38	1.57	0.73	2.6	2.34
G339.113-00.203_1	339.11	-0.2	part. cor.	3	-30.48	-30.66	0.71	4.0	1.02	1.05	0.69	1.72	1.66
G339.113-00.203_2	339.11	-0.2	part. cor.	3	-42.98	-43.04	0.31	13.21	0.98	1.1	0.69	1.28	1.37
G339.116-00.405_0	339.12	-0.41	full. cor.	1	-37.2	-37.35	0.78	16.3	1.05	1.4	0.7	1.73	1.73
G339.260+00.117_0	339.26	0.12	part. cor.	1	-72.43	-72.56	1.15	35.35	1.12	1.3	0.97	1.93	1.86
G339.385-00.414_0	339.38	-0.41	full. cor.	1	-38.69	-38.86	0.35	17.96	1.0	1.18	0.63	1.28	1.03
G339.586-00.119_0	339.59	-0.12	full. cor.	2	-33.49	-33.94	1.35	13.95	1.3	2.01	0.89	2.78	2.19
G339.586-00.119_1	339.59	-0.12	part. cor.	2	-23.07	-23.82	1.09	2.82	1.11	1.14	0.96	1.93	1.02
G339.692+00.291_0	339.69	0.29	part. cor.	1	-92.69	-92.75	0.51	33.77	1.13	1.22	0.92	1.55	1.53
G339.988-00.165_0	339.99	-0.16	full. cor.	2	-51.65	-51.69	0.8	22.57	1.28	1.68	0.83	2.02	2.0
G339.988-00.165_1	339.99	-0.16	part. cor.	2	-36.58	-36.05	0.45	4.75	0.86	0.88	0.59	1.17	0.79
G340.301-00.387_0	340.3	-0.39	full. cor.	3	-48.24	-48.04	1.77	19.32	1.58	2.65	1.12	3.85	3.4
G340.301-00.387_1	340.3	-0.39	dif. comp.	3	-122.84	-122.58	1.6	0.0	1.13	1.15	-	2.18	2.21
G340.301-00.387_2	340.3	-0.39	dif. comp.	3	-91.41	-91.75	0.65	0.0	1.02	1.04	-	1.44	1.6
G340.316+00.079_0	340.32	0.08	part. cor.	2	-111.48	-111.5	1.44	53.62	0.83	1.01	0.67	1.74	1.9
G340.316+00.079_1	340.32	0.08	dif. comp.	2	-28.75	-28.58	0.36	0.0	1.05	1.08	-	1.62	1.85
G340.482-00.306_0	340.48	-0.31	part. cor.	3	-88.7	-88.84	0.44	40.35	0.83	1.14	0.66	1.28	1.07
G340.482-00.306_1	340.48	-0.31	part. cor.	3	-45.58	-45.78	0.71	0.0	1.78	1.79	-	2.4	1.97
G340.482-00.306_2	340.48	-0.31	part. cor.	3	-39.19	-38.55	0.39	11.57	1.19	1.32	0.62	1.59	1.63
G340.511-00.471_0	340.51	-0.47	full. cor.	1	-43.75	-43.09	1.18	18.62	1.85	2.04	0.86	2.52	1.5
G340.630-00.093_0	340.63	-0.09	part. cor.	3	-101.52	-	0.73	0.0	0.87	0.89	-	1.23	-
G340.630-00.093_1	340.63	-0.09	part. cor.	3	-48.1	-	1.34	0.0	1.71	1.73	-	2.41	-
G340.630-00.093_2	340.63	-0.09	part. cor.	3	-38.23	-	0.68	0.0	1.66	1.67	-	2.88	-
G340.981-00.013_0	340.98	-0.01	full. cor.	4	-47.06	-46.86	0.4	0.0	1.08	1.1	-	1.23	1.09
G340.981-00.013_1	340.98	-0.01	part. cor.	4	-40.29	-39.66	0.61	12.38	0.77	0.84	0.52	1.21	-
G340.981-00.013_2	340.98	-0.01	part. cor.	4	-32.25	-31.44	0.61	3.88	0.93	0.98	0.57	1.3	-
G340.981-00.013_3	340.98	-0.01	part. cor.	4	-27.51	-28.6	0.65	0.0	1.07	1.1	-	1.69	0.68
G341.244-00.265_0	341.24	-0.27	full. cor.	1	-43.55	-43.41	0.77	13.58	1.37	2.35	1.02	2.84	2.4

Table B.1: Measured parameters of all filaments continued.

Filament ID	ℓ °	b °	Status	N_c	$v_{lsr}(^{13}CO)$ km s^{-1}	$v_{lsr}(C^{18}O)$ km s^{-1}	$\sigma(v_{^{13}CO})$ km s^{-1}	$\sigma(v_{C^{18}O})$ km s^{-1}	σ_v km s^{-1}	$\sigma_v(^{13}CO)$ km s^{-1}	$\sigma_v(C^{18}O)$ km s^{-1}	$\sigma_{v,t}(^{13}CO)$ km s^{-1}	$\sigma_{v,t}(C^{18}O)$ km s^{-1}
G341.415+00.244_0	341.42	0.24	full. cor.	3	-37.04	-37.51	0.23	13.61	1.01	1.1	0.6	1.3	-
G341.415+00.244_1	341.42	0.24	full. cor.	3	-24.03	-25.5	1.2	0.0	1.87	1.89	-	2.83	-
G341.415+00.244_2	341.42	0.24	part. cor.	3	-76.96	-78.13	0.41	15.5	0.81	0.86	0.5	1.09	-
G341.674+00.184_0	341.67	0.18	part. cor.	2	-15.77	-16.91	1.65	5.92	1.19	1.3	0.77	2.21	1.12
G341.674+00.184_1	341.67	0.18	part. cor.	2	-74.79	-	0.35	0.0	1.05	1.07	-	1.42	-
G341.938+00.054_0	341.94	0.05	full. cor.	2	-121.32	-121.24	0.65	31.92	0.83	0.88	0.6	1.11	-
G341.938+00.054_1	341.94	0.05	part. cor.	2	-22.61	-21.44	0.26	0.0	0.83	0.85	-	1.46	-
G342.100+00.399_0	342.1	0.4	part. cor.	7	-119.73	-119.75	0.56	50.34	0.88	1.16	0.73	1.37	1.19
G342.100+00.399_1	342.1	0.4	dif. comp.	7	-84.23	-83.93	0.56	0.0	0.63	0.66	-	0.98	0.78
G342.100+00.399_2	342.1	0.4	dif. comp.	7	-77.6	-77.38	0.62	14.7	1.15	1.21	0.71	1.61	1.61
G342.100+00.399_3	342.1	0.4	part. cor.	7	-71.36	-71.13	0.93	32.7	1.31	1.7	1.06	2.16	1.99
G342.100+00.399_4	342.1	0.4	dif. comp.	7	-25.5	-25.49	0.51	4.1	1.03	1.11	0.55	1.51	0.4
G342.100+00.399_5	342.1	0.4	dif. comp.	7	-40.7	-	0.26	0.0	0.9	0.93	-	1.08	-
G342.100+00.399_6	342.1	0.4	dif. comp.	7	-19.4	-	0.36	0.0	0.45	0.5	-	0.62	-
G342.345-00.005_0	342.34	-0.01	part. cor.	1	-6.41	-6.25	0.6	2.11	1.22	1.31	0.82	1.6	1.63
G342.357+00.113_0	342.36	0.11	part. cor.	5	-93.48	-93.72	0.65	45.65	0.77	0.93	0.72	1.3	1.05
G342.357+00.113_1	342.36	0.11	dif. comp.	5	-128.8	-128.03	1.44	0.0	1.32	1.34	-	2.27	2.31
G342.357+00.113_2	342.36	0.11	part. cor.	5	-7.08	-7.76	1.51	2.3	1.14	1.4	1.24	2.01	1.65
G342.357+00.113_3	342.36	0.11	dif. comp.	5	-68.57	-69.02	1.78	0.0	1.09	1.11	-	2.38	1.97
G342.357+00.113_4	342.36	0.11	dif. comp.	5	-28.97	-	1.6	4.26	1.22	1.26	0.5	2.71	-
G342.478-00.167_0	342.48	-0.17	full. cor.	2	-24.64	-24.84	0.49	11.23	1.08	1.26	0.65	1.43	1.29
G342.478-00.167_1	342.48	-0.17	full. cor.	2	-19.66	-	0.56	0.0	0.8	0.83	-	1.03	-
G342.823+00.129_0	342.82	0.13	full. cor.	1	-24.46	-26.87	0.86	0.0	0.92	0.94	-	1.97	-
G343.579-00.170_0	343.58	-0.17	full. cor.	1	-27.53	-26.86	0.38	11.41	0.95	1.04	0.52	1.64	0.96
G343.776-00.149_0	343.78	-0.15	full. cor.	1	-26.74	-26.29	2.26	13.13	1.12	1.62	0.79	3.32	3.12
G343.908+00.113_0	343.91	0.11	part. cor.	1	9.4	9.23	1.1	1.24	1.28	1.32	0.6	1.77	1.73
G343.998-00.143_0	344.0	-0.14	part. cor.	1	-21.73	-22.73	0.28	0.0	0.96	0.99	-	1.69	1.1
G344.043-00.373_0	344.04	-0.37	full. cor.	1	-87.92	-87.77	0.6	43.91	0.93	1.13	0.63	1.34	0.97

Table B.1: Measured parameters of all filaments continued.

Filament ID	ℓ	b	Status	N_c	$v_{lsr}(^{13}CO)$	$v_{lsr}(C^{18}O)$	$\sigma(v_{^{13}CO})$	$\sigma(v_{C^{18}O})$	σ_v	$\sigma_v(^{13}CO)$	$\sigma_v(C^{18}O)$	$\sigma_{v,t}(^{13}CO)$	$\sigma_{v,t}(C^{18}O)$
	°	°			km s^{-1}	km s^{-1}	km s^{-1}	km s^{-1}	km s^{-1}	km s^{-1}	km s^{-1}	km s^{-1}	km s^{-1}
G344.340-00.227_0	344.34	-0.23	full. cor.	1	-85.75	-85.8	1.07	42.56	0.89	1.05	0.53	1.54	1.12
G344.447-00.186_0	344.45	-0.19	part. cor.	2	-86.35	-86.15	0.26	40.63	0.67	0.85	0.54	0.94	0.85
G344.447-00.186_1	344.45	-0.19	part. cor.	2	-46.42	-	0.59	0.0	0.75	0.78	-	1.87	-
G344.592-00.026_0	344.59	-0.03	part. cor.	1	-1.71	-1.87	0.39	0.3	1.55	1.63	1.18	2.03	1.73
G345.345-00.060_0	345.34	-0.06	full. cor.	2	-18.04	-18.51	0.37	0.0	0.89	0.91	-	1.48	1.95
G345.345-00.060_1	345.34	-0.06	part. cor.	2	-1.14	-0.0	0.32	0.0	0.83	0.86	-	1.31	-
G345.433-00.143_0	345.43	-0.14	full. cor.	1	-16.2	-16.37	0.96	7.58	1.13	1.37	0.76	1.71	1.55
G345.493+00.337_0	345.49	0.34	full. cor.	1	-16.89	-16.69	0.74	5.03	1.3	1.9	1.14	2.32	1.71
G345.635+00.358_0	345.64	0.36	full. cor.	1	-16.3	-16.6	0.77	8.13	1.65	2.09	0.83	2.49	2.33
G345.873+00.292_0	345.87	0.29	full. cor.	1	-15.2	-14.97	0.76	3.32	1.35	1.45	0.4	1.95	1.34
G345.879+00.021_0	345.88	0.02	part. cor.	3	-114.93	-115.01	0.62	53.56	0.7	0.93	0.59	1.12	1.11
G345.879+00.021_1	345.88	0.02	part. cor.	3	-80.76	-80.65	1.17	29.49	1.18	1.38	0.73	2.11	1.39
G345.879+00.021_2	345.88	0.02	part. cor.	3	-4.57	-4.35	0.82	1.05	1.46	1.53	1.0	2.86	2.79
G346.177+00.029_0	346.18	0.03	part. cor.	4	-77.21	-77.42	0.47	13.18	1.09	1.14	0.66	1.34	1.47
G346.177+00.029_1	346.18	0.03	part. cor.	4	-89.45	-	0.66	0.0	1.37	1.38	-	1.8	-
G346.177+00.029_2	346.18	0.03	part. cor.	4	-12.45	-	1.15	1.77	1.15	1.16	0.84	1.97	-
G346.177+00.029_3	346.18	0.03	dif. comp.	4	-99.71	-98.15	0.62	0.0	1.17	1.19	-	2.24	0.55
G346.293+00.109_0	346.29	0.11	part. cor.	3	-97.88	-97.6	0.33	48.32	1.09	1.32	0.87	1.47	1.22
G346.293+00.109_1	346.29	0.11	dif. comp.	3	-34.04	-34.29	0.83	6.41	1.14	1.22	0.51	1.57	1.64
G346.293+00.109_2	346.29	0.11	part. cor.	3	-28.13	-28.12	0.34	11.88	0.65	0.78	0.59	0.91	0.89
G346.483+00.144_0	346.48	0.14	part. cor.	1	-8.89	-8.45	0.62	3.97	1.55	1.73	1.1	1.93	1.47
G346.951-00.155_0	346.95	-0.16	part. cor.	3	-82.94	-82.55	0.61	13.7	1.01	1.07	0.51	1.31	1.45
G346.951-00.155_1	346.95	-0.16	part. cor.	3	-76.65	-77.93	1.34	0.0	1.37	1.39	-	2.06	1.77
G346.951-00.155_2	346.95	-0.16	part. cor.	3	-70.55	-70.32	0.62	0.0	1.03	1.05	-	1.46	1.19
G347.216+00.026_0	347.22	0.03	full. cor.	1	-70.43	-70.53	1.22	35.11	2.22	2.57	1.05	3.41	2.7
G347.390+00.266_0	347.39	0.27	part. cor.	3	-91.67	-92.15	1.94	0.0	1.56	1.57	-	2.76	2.65
G347.390+00.266_1	347.39	0.27	part. cor.	3	-81.8	-82.03	1.33	17.71	1.39	1.44	0.79	2.23	2.23
G347.390+00.266_2	347.39	0.27	dif. comp.	3	-64.12	-	0.22	0.0	0.85	0.88	-	1.27	-

Table B.1: Measured parameters of all filaments continued.

Filament ID	ℓ °	b °	Status	N_c	$v_{lsr}(^{13}CO)$ km s^{-1}	$v_{lsr}(C^{18}O)$ km s^{-1}	$\sigma(v_{^{13}CO})$ km s^{-1}	$\sigma(v_{C^{18}O})$ km s^{-1}	σ_v km s^{-1}	$\sigma_v(^{13}CO)$ km s^{-1}	$\sigma_v(C^{18}O)$ km s^{-1}	$\sigma_{v,t}(^{13}CO)$ km s^{-1}	$\sigma_{v,t}(C^{18}O)$ km s^{-1}
G347.870-00.318_0	347.87	-0.32	full. cor.	1	-94.39	-93.95	0.97	43.66	1.11	1.62	0.83	2.06	1.2
G347.894+00.035_0	347.89	0.03	part. cor.	2	-28.62	-	1.53	9.86	1.39	1.52	1.29	2.71	-
G347.894+00.035_1	347.89	0.03	dif. comp.	2	-77.96	-76.9	3.62	0.0	1.2	1.21	-	3.8	4.88
G348.034+00.439_0	348.03	0.44	full. cor.	1	-8.4	-7.35	0.4	1.32	1.22	1.26	0.49	1.47	1.08
G348.232+00.462_0	348.23	0.46	full. cor.	1	-7.4	-7.23	0.44	2.49	1.14	1.62	0.75	1.77	1.14
G348.492+00.346_0	348.49	0.35	part. cor.	2	-62.67	-62.06	0.94	25.79	1.44	1.69	0.78	2.16	-
G348.492+00.346_1	348.49	0.35	full. cor.	2	-8.3	-7.51	0.37	0.0	1.06	1.08	-	1.27	-
G349.876+00.099_0	349.88	0.1	part. cor.	3	-61.44	-61.14	1.05	12.67	1.56	1.65	0.66	2.48	2.09
G349.876+00.099_1	349.88	0.1	part. cor.	3	-108.2	-109.39	1.22	36.54	1.46	1.6	0.89	2.57	-
G349.876+00.099_2	349.88	0.1	dif. comp.	3	16.35	-	3.35	0.0	1.18	1.2	-	3.89	-
G350.299+00.237_0	350.3	0.24	part. cor.	1	-40.01	-41.35	2.23	0.0	2.11	2.12	-	5.18	5.79
G350.522-00.255_0	350.52	-0.25	full. cor.	1	-21.65	-21.81	0.59	10.75	1.56	1.84	0.79	2.1	0.99
G350.781+00.492_0	350.78	0.49	full. cor.	1	-1.63	-1.16	0.41	0.78	0.7	0.9	0.56	1.01	-
G351.022-00.343_0	351.02	-0.34	full. cor.	1	-17.49	-17.08	0.46	7.33	0.97	1.52	0.83	1.9	1.34
G351.498+00.254_0	351.5	0.25	full. cor.	1	-44.11	-43.79	1.39	0.0	1.43	1.44	-	2.29	2.14
G351.731+00.446_0	351.73	0.45	part. cor.	1	-3.26	-	0.37	0.0	0.9	0.93	-	1.01	-
G351.928-00.245_0	351.93	-0.25	part. cor.	2	-22.41	-23.15	0.61	3.8	1.22	1.26	0.7	1.91	1.71
G351.928-00.245_1	351.93	-0.25	full. cor.	2	-11.97	-12.35	0.6	5.15	1.52	1.67	0.69	2.3	2.0
G352.030+00.069_0	352.03	0.07	full. cor.	1	-4.55	-5.09	0.48	2.3	0.74	1.15	0.44	1.54	1.07
G352.062-00.257_0	352.06	-0.26	full. cor.	1	-11.32	-11.05	0.57	5.58	1.2	1.46	0.94	1.93	1.13
G352.107+00.184_0	352.11	0.18	full. cor.	3	-55.9	-56.53	1.54	25.79	1.57	1.83	1.27	3.09	2.5
G352.107+00.184_1	352.11	0.18	dif. comp.	3	-43.83	-41.95	0.86	0.0	1.63	1.64	-	2.44	1.64
G352.107+00.184_2	352.11	0.18	dif. comp.	3	-37.3	-	0.18	0.0	0.8	0.82	-	1.05	-
G352.208+00.354_0	352.21	0.35	full. cor.	1	-1.16	-1.14	0.23	0.44	0.6	0.78	0.56	0.8	0.54
G352.308-00.447_0	352.31	-0.45	full. cor.	1	-12.21	-11.86	1.3	5.94	1.19	1.67	0.98	2.4	2.1
G352.781-00.050_0	352.78	-0.05	part. cor.	1	-44.87	-44.61	0.79	0.0	1.02	1.04	-	1.74	1.34
G352.883+00.464_0	352.88	0.46	full. cor.	1	-4.11	-4.36	0.62	1.66	1.62	1.72	0.8	1.98	1.68
G353.201-00.242_0	353.2	-0.24	full. cor.	1	-17.4	-17.35	0.37	7.3	0.76	1.25	0.61	1.49	0.94

Table B.1: Measured parameters of all filaments continued.

Filament ID	ℓ	b	Status	N_c	$v_{lsr}(^{13}CO)$	$v_{lsr}(C^{18}O)$	$\sigma(v_{^{13}CO})$	$\sigma(v_{C^{18}O})$	σ_v	$\sigma_v(^{13}CO)$	$\sigma_v(C^{18}O)$	$\sigma_{v,t}(^{13}CO)$	$\sigma_{v,t}(C^{18}O)$
	°	°			km s^{-1}	km s^{-1}	km s^{-1}	km s^{-1}	km s^{-1}	km s^{-1}	km s^{-1}	km s^{-1}	km s^{-1}
G353.294+00.312_0	353.29	0.31	part. cor.	3	-1.09	-1.12	0.35	0.06	0.77	0.83	0.35	0.89	0.34
G353.294+00.312_1	353.29	0.31	part. cor.	3	-21.94	-22.1	0.35	0.0	0.95	0.97	-	1.11	1.32
G353.294+00.312_2	353.29	0.31	part. cor.	3	-17.05	-16.38	0.48	0.0	1.03	1.06	-	1.35	1.25
G353.389-00.340_0	353.39	-0.34	full. cor.	1	-16.95	-17.21	0.79	8.51	1.44	1.79	1.24	2.31	1.93
G353.418-00.208_0	353.42	-0.21	full. cor.	1	-82.43	-82.46	0.76	35.73	1.2	1.33	0.75	1.77	1.61
G353.477-00.160_0	353.48	-0.16	full. cor.	1	-16.29	-16.46	0.18	5.59	0.97	1.02	0.66	1.02	-
G353.564-00.464_0	353.56	-0.46	full. cor.	1	-17.01	-16.5	0.44	3.14	0.88	1.59	0.71	1.86	0.55
G353.949+00.252_0	353.95	0.25	full. cor.	1	2.78	3.21	0.33	1.46	1.01	1.25	0.61	1.51	1.05
G353.992+00.321_0	353.99	0.32	full. cor.	1	2.63	3.17	0.6	1.18	0.93	0.95	0.54	1.62	1.22
G354.991+00.421_0	354.99	0.42	part. cor.	1	96.9	95.75	2.87	0.0	2.09	2.1	-	6.2	4.75
G355.211-00.496_0	355.21	-0.5	full. cor.	1	-4.15	-4.86	0.5	2.56	1.24	1.53	0.64	1.91	1.04
G355.257-00.260_0	355.26	-0.26	full. cor.	1	-2.23	-2.09	0.46	0.67	1.15	1.65	0.93	2.02	1.43
G355.265+00.339_0	355.26	0.34	part. cor.	3	55.68	53.86	3.52	0.0	2.15	2.16	-	4.42	3.03
G355.265+00.339_1	355.26	0.34	dif. comp.	3	103.08	103.15	1.3	0.0	0.94	0.96	-	2.47	2.71
G355.265+00.339_2	355.26	0.34	dif. comp.	3	71.21	-	1.64	7.5	1.35	1.41	0.52	2.22	-
G355.564+00.279_0	355.56	0.28	full. cor.	2	-80.75	-80.53	1.06	18.57	0.84	0.9	0.48	2.23	2.69
G355.564+00.279_1	355.56	0.28	part. cor.	2	111.01	-	0.9	0.0	1.16	1.18	-	1.55	-
G355.619-00.049_0	355.62	-0.05	full. cor.	1	-19.78	-19.76	0.72	6.01	1.48	1.54	0.97	2.18	2.09
G355.635+00.302_0	355.64	0.3	part. cor.	2	111.26	111.0	0.38	17.32	0.95	0.97	0.51	1.22	1.12
G355.635+00.302_1	355.64	0.3	part. cor.	2	-71.54	-70.29	0.47	11.17	1.02	1.09	0.54	1.78	-
G355.673+00.089_0	355.67	0.09	full. cor.	2	4.15	4.17	0.42	0.91	0.83	0.86	0.71	1.23	0.95
G355.673+00.089_1	355.67	0.09	part. cor.	2	-72.38	-71.63	0.71	0.0	1.41	1.43	-	2.54	1.61
G355.742-00.252_0	355.74	-0.25	full. cor.	2	-24.6	-24.33	1.11	11.95	1.15	1.4	0.96	2.26	2.33
G355.742-00.252_1	355.74	-0.25	part. cor.	2	4.16	3.92	0.28	0.0	0.77	0.8	-	0.93	1.03
G355.743+00.135_0	355.74	0.13	part. cor.	1	17.33	16.61	0.86	2.36	1.38	1.4	0.4	2.38	-
G355.836+00.317_0	355.84	0.32	part. cor.	1	-3.19	-3.05	0.47	0.35	0.85	0.93	0.44	1.59	1.39
G355.991-00.414_0	355.99	-0.41	full. cor.	1	-0.87	-1.12	0.39	0.37	0.75	1.05	0.72	1.15	0.73
G356.416+00.088_0	356.42	0.09	full. cor.	1	-5.4	-5.38	1.03	2.93	0.97	1.22	0.64	1.91	1.78

Table B.1: Measured parameters of all filaments continued.

Filament ID	ℓ °	b °	Status	N_c	$v_{lsr}(^{13}CO)$ km s^{-1}	$v_{lsr}(C^{18}O)$ km s^{-1}	$\sigma(v_{^{13}CO})$ km s^{-1}	$\sigma(v_{C^{18}O})$ km s^{-1}	σ_v km s^{-1}	$\sigma_v(^{13}CO)$ km s^{-1}	$\sigma_v(C^{18}O)$ km s^{-1}	$\sigma_{v,t}(^{13}CO)$ km s^{-1}	$\sigma_{v,t}(C^{18}O)$ km s^{-1}
G356.495+00.198_0	356.5	0.2	full. cor.	1	-4.83	-4.34	0.53	1.48	0.91	1.04	0.59	1.24	0.54
G356.874-00.021_0	356.87	-0.02	full. cor.	1	-9.04	-8.92	0.92	4.22	1.14	1.31	0.61	1.87	1.8
G357.033+00.193_0	357.03	0.19	full. cor.	1	-7.97	-7.8	0.42	1.36	0.95	0.98	0.77	1.24	0.96
G357.420+00.356_0	357.42	0.36	full. cor.	1	-13.92	-13.68	0.41	0.0	0.9	0.92	-	1.07	0.69
G357.637-00.325_0	357.64	-0.33	part. cor.	3	-11.44	-10.94	1.29	0.87	1.13	1.16	0.62	2.29	2.1
G357.637-00.325_1	357.64	-0.33	dif. comp.	3	-2.97	-	0.72	0.39	0.96	1.05	0.8	1.64	-
G357.637-00.325_2	357.64	-0.33	full. cor.	3	4.38	5.09	0.7	2.27	1.38	1.73	0.9	1.81	-
G357.956-00.160_0	357.96	-0.16	part. cor.	2	-6.28	-6.29	1.22	2.14	1.83	2.12	1.21	2.81	1.65
G357.956-00.160_1	357.96	-0.16	part. cor.	2	8.12	10.18	0.63	2.95	1.09	1.37	0.56	2.12	-
G358.017-00.041_0	358.02	-0.04	full. cor.	2	9.06	8.9	1.41	3.34	1.31	1.55	0.67	2.64	2.63
G358.017-00.041_1	358.02	-0.04	part. cor.	2	-136.3	-	0.59	0.0	1.25	1.27	-	1.69	-
G358.101-00.128_0	358.1	-0.13	dif. comp.	2	-3.7	-4.18	1.09	0.83	0.94	1.03	0.71	2.18	1.47
G358.101-00.128_1	358.1	-0.13	full. cor.	2	8.11	8.4	0.73	3.4	1.42	2.09	0.92	2.31	1.91
G358.243-00.425_0	358.24	-0.43	full. cor.	2	4.25	4.43	0.93	1.49	0.91	1.41	0.86	1.77	1.32
G358.243-00.425_1	358.24	-0.43	part. cor.	2	-6.65	-6.15	0.41	0.0	1.15	1.17	-	1.69	1.83
G358.245+00.010_0	358.24	0.01	part. cor.	1	-34.78	-34.26	2.96	0.0	1.88	1.89	-	4.04	4.1
G358.377-00.211_0	358.38	-0.21	full. cor.	2	-0.57	-	1.52	0.54	1.41	1.43	0.31	2.68	-
G358.377-00.211_1	358.38	-0.21	part. cor.	2	-48.28	-50.27	2.56	10.28	2.97	3.13	0.77	5.03	5.14
G358.451-00.422_0	358.45	-0.42	full. cor.	3	-4.24	-4.34	0.63	2.04	1.19	1.57	1.14	1.95	1.67
G358.451-00.422_1	358.45	-0.42	part. cor.	3	6.17	6.23	0.46	2.93	0.8	1.14	0.77	1.52	1.54
G358.451-00.422_2	358.45	-0.42	dif. comp.	3	16.18	16.27	0.74	3.54	0.89	0.99	0.62	1.29	1.56
G359.232+00.329_0	359.23	0.33	part. cor.	1	0.68	0.17	0.34	0.0	0.84	0.87	-	1.03	-
G359.372-00.437_0	359.37	-0.44	full. cor.	1	14.28	14.26	0.26	4.9	0.6	0.98	0.48	1.07	0.43
G359.404+00.308_0	359.4	0.31	full. cor.	2	6.66	6.95	1.22	2.41	1.03	1.17	0.56	2.23	1.7
G359.404+00.308_1	359.4	0.31	dif. comp.	2	16.61	16.69	0.67	0.0	0.82	0.84	-	1.24	1.95
G359.564-00.451_0	359.56	-0.45	full. cor.	1	13.33	13.28	0.41	6.12	0.96	1.14	0.68	1.44	0.53
G359.863-00.248_0	359.86	-0.25	dif. comp.	3	-2.43	-	2.2	0.0	1.86	1.87	-	3.36	-
G359.863-00.248_1	359.86	-0.25	part. cor.	3	17.28	16.35	2.47	7.53	1.38	1.55	0.62	3.34	-

Table B.1: Measured parameters of all filaments continued.

Filament ID	ℓ °	b °	Status	N_c	$v_{lsr}(^{13}CO)$ km s^{-1}	$v_{lsr}(C^{18}O)$ km s^{-1}	$\sigma(v_{^{13}CO})$ km s^{-1}	$\sigma(v_{C^{18}O})$ km s^{-1}	σ_v km s^{-1}	$\sigma_v(^{13}CO)$ km s^{-1}	$\sigma_v(C^{18}O)$ km s^{-1}	$\sigma_{v,t}(^{13}CO)$ km s^{-1}	$\sigma_{v,t}(C^{18}O)$ km s^{-1}
G359.863-00.248_2	359.86	-0.25	dif. comp.	3	-127.04	-130.57	2.86	0.0	2.16	2.17	-	6.06	6.46
G359.896-00.316_0	359.9	-0.32	full. cor.	1	16.16	16.32	0.6	7.12	1.04	1.4	0.79	1.78	1.53

Table B.2: Distance dependent parameters of all filaments.

Filament ID	d	l	$l(d)$	M(ATG)	M(ATG + P)	M(dust)	M(gas)	$m_{\mathrm{crit,nt}}$	m_{obs}	det. ^{13}CO	det. C^{18}O	edge flag	d flag
	kpc	°	pc	$M_\odot$	$M_\odot$	$M_\odot$	$M_\odot$	$M_\odot\,\mathrm{pc}^{-1}$	$M_\odot\,\mathrm{pc}^{-1}$				
G000.615-00.448_0	-	0.11	-	-	-	-	-	351	-	1.0	0.28	0	0
G000.675+00.310_0	-	0.03	-	-	-	-	-	1397	-	0.18	0.0	0	0
G000.914+00.308_0	-	0.04	-	-	-	-	-	1769	-	0.25	0.0	0	0
G001.717+00.359_0	-	0.03	-	-	-	-	-	312	-	0.12	0.03	0	0
G001.717+00.359_1	-	0.06	-	-	-	-	-	459	-	0.18	0.02	0	0
G001.717+00.359_2	-	0.06	-	-	-	-	-	1410	-	0.22	0.0	0	0
G002.128+00.295_0	-	0.06	-	-	-	-	-	613	-	1.0	0.19	0	0
G002.210-00.049_0	-	0.04	-	-	-	-	-	3576	-	0.5	0.0	0	0
G002.210-00.049_1	-	0.04	-	-	-	-	-	1397	-	0.46	0.0	0	0
G002.370+00.069_0	-	0.02	-	-	-	-	-	307	-	0.19	0.0	0	0
G002.370+00.069_1	-	0.12	-	-	-	-	-	900	-	0.88	0.02	0	0
G002.370+00.069_2	-	0.05	-	-	-	-	-	466	-	0.4	0.0	0	0
G002.420+00.205_0	-	0.04	-	-	-	-	-	405	-	0.5	0.14	0	0
G002.476-00.120_0	-	0.06	-	-	-	-	-	824	-	0.45	0.0	0	0
G002.476-00.120_1	-	0.03	-	-	-	-	-	435	-	0.22	0.0	0	0
G002.585-00.000_0	-	0.06	-	-	-	-	-	613	-	0.56	0.08	0	0
G002.585-00.000_1	-	0.03	-	-	-	-	-	912	-	0.31	0.0	0	0
G002.687+00.106_0	-	0.14	-	-	-	-	-	752	-	0.98	0.68	0	0
G003.321-00.097_0	-	0.07	-	-	-	-	-	768	-	0.31	0.02	0	0
G003.321-00.097_1	-	0.1	-	-	-	-	-	863	-	0.36	0.12	0	0
G003.387+00.185_0	-	0.08	-	-	-	-	-	1811	-	0.22	0.0	0	0
G003.446-00.223_0	-	0.03	-	-	-	-	-	439	-	0.25	0.0	0	0
G003.456+00.006_0	-	0.12	-	-	-	-	-	535	-	0.62	0.18	0	0
G004.180-00.010_0	-	0.08	-	-	-	-	-	244	-	0.32	0.06	0	0
G004.180-00.010_1	-	0.16	-	-	-	-	-	767	-	0.7	0.05	0	0
G004.180-00.010_2	-	0.09	-	-	-	-	-	474	-	0.4	0.13	0	0
G004.583-00.109_0	-	0.11	-	-	-	-	-	695	-	0.69	0.09	0	0
G004.583-00.109_1	-	0.13	-	-	-	-	-	825	-	0.79	0.0	0	0

Table B.2: Distance dependent parameters of all filaments continued.

Filament ID	d	l	$l(d)$	M(ATG)	M(ATG + P)	M(dust)	M(gas)	$m_{\rm crit,nt}$	$m_{\rm obs}$	det. ^{13}CO	det. C^{18}O	edge flag	d flag
	kpc	°	pc	$M_\odot$	$M_\odot$	$M_\odot$	$M_\odot$	$M_\odot\,pc^{-1}$	$M_\odot\,pc^{-1}$				
G004.705+00.001_0	-	0.08	-	-	-	-	-	1423	-	1.0	0.5	0	0
G004.711-00.440_0	-	0.09	-	-	-	-	-	252	-	0.86	0.08	0	0
G004.794-00.284_0	2.9	0.06	3.07	299	5649	1065	894	274	291	0.49	0.0	0	2
G004.794-00.284_1	2.9	0.06	3.05	334	8754	1505	834	533	274	0.47	0.0	0	2
G004.950-00.076_0	2.9	0.05	2.57	280	6760	914	1774	619	689	0.83	0.08	0	2
G005.101-00.104_0	10.8	0.21	40.51	18402	76880	24043	25629	551	633	0.71	0.14	0	1
G005.357+00.101_0	2.9	0.1	5.28	720	7662	1461	4799	283	908	1.0	0.58	0	1
G005.454+00.167_0	2.9	0.05	2.77	214	3816	564	1082	572	391	1.0	0.0	0	2
G005.704-00.306_0	3.0	0.07	3.47	254	5603	954	2577	771	742	1.0	0.0	0	2
G005.912+00.283_0	-	0.04	-	-	-	-	-	1102	-	0.27	0.0	0	0
G005.930-00.095_0	3.0	0.03	1.72	348	4573	955	1018	246	592	0.43	0.07	0	2
G006.589-00.106_0	3.0	0.05	2.38	6187	27235	9665	1322	610	556	0.14	0.01	0	1
G006.589-00.106_1	3.0	0.21	10.98	6619	43684	12875	7499	1377	683	0.64	0.12	0	1
G006.849+00.151_0	3.0	0.04	1.93	536	6399	1717	891	521	462	0.42	0.0	0	2
G006.849+00.151_1	-	0.02	-	-	-	-	-	608	-	0.33	0.0	0	0
G007.250-00.120_0	3.0	0.05	2.8	2220	10619	3372	1176	366	420	0.32	0.02	0	1
G007.250-00.120_1	3.0	0.11	5.73	2455	15984	4343	3392	508	591	0.68	0.25	0	1
G008.000-00.272_0	10.9	0.09	17.26	15870	33100	16262	30342	493	1758	1.0	0.73	0	1
G008.255+00.165_0	3.0	0.13	7.05	1535	11756	4903	8897	314	1262	1.0	0.88	0	1
G008.800-00.359_0	4.4	0.22	17.07	2380	27776	9217	14098	640	826	1.0	0.39	0	1
G008.800-00.359_1	3.1	0.14	7.3	1197	14241	4700	2971	356	407	0.63	0.16	0	1
G008.914-00.318_0	4.4	0.17	13.36	2049	18719	4839	12420	539	929	1.0	0.39	0	1
G009.230+00.157_0	3.1	0.09	5.05	567	5528	1336	3958	246	784	1.0	0.77	0	1
G009.280-00.152_0	4.7	0.06	5.28	1579	9755	3464	6130	274	1161	1.0	0.8	0	1
G009.970-00.024_0	3.5	0.11	6.88	1593	16507	2535	2512	603	365	0.78	0.24	0	1
G009.970-00.024_1	3.5	0.07	4.09	1572	15282	2418	1327	698	325	0.42	0.0	0	2
G009.970-00.024_2	3.5	0.03	1.87	1446	8604	1822	530	228	283	0.22	0.0	0	2
G010.531-00.024_0	8.5	0.12	17.54	4360	48903	9008	14489	1103	826	0.98	0.07	0	1

Table B.2: Distance dependent parameters of all filaments continued.

Filament ID	d	l	$l(d)$	M(ATG)	M(ATG + P)	M(dust)	M(gas)	$m_{\mathrm{crit,nt}}$	m_{obs}	det. ^{13}CO	det. C^{18}O	edge flag	d flag
	kpc	°	pc	$M_\odot$	$M_\odot$	$M_\odot$	$M_\odot$	$M_\odot\,\mathrm{pc}^{-1}$	$M_\odot\,\mathrm{pc}^{-1}$				
G010.682-00.161_0	2.9	0.28	14.04	3783	49461	13992	16062	1418	1144	1.0	0.34	0	1
G010.682-00.161_1	5.0	0.03	2.87	6010	45787	15349	896	442	312	0.11	0.0	0	1
G010.682-00.161_2	5.0	0.07	6.38	6275	51055	16800	2768	462	434	0.28	0.12	0	1
G010.682-00.161_3	5.0	0.05	4.28	5752	40890	13982	1653	360	386	0.18	0.0	0	2
G010.694+00.034_0	2.9	0.08	4.17	2733	31686	11257	2765	885	663	0.38	0.07	0	1
G010.694+00.034_1	2.9	0.2	10.06	3143	52917	18674	15780	2573	1569	0.97	0.09	0	1
G010.694+00.034_2	2.9	0.04	1.96	2087	19936	7256	594	458	304	0.19	0.0	0	1
G010.809-00.393_0	5.0	0.07	6.41	1465	14267	2872	4020	816	627	0.81	0.09	0	1
G010.809-00.393_1	2.9	0.06	3.2	537	6408	1199	1139	468	356	0.66	0.0	0	2
G010.878-00.468_0	2.9	0.11	5.68	965	16112	1932	3742	999	659	0.66	0.08	0	2
G010.878-00.468_1	5.0	0.08	7.26	2188	22926	3565	3806	701	525	0.41	0.06	0	2
G010.971-00.363_0	5.0	0.14	12.07	4626	25295	6767	9341	833	774	0.92	0.06	0	1
G010.971-00.363_1	2.9	0.14	6.99	1727	17290	3306	4049	1230	579	0.92	0.0	0	2
G011.046-00.069_0	2.9	0.04	1.81	8349	49178	15981	774	557	427	0.05	0.0	0	1
G011.046-00.069_1	2.9	0.17	8.73	8704	61658	18562	4090	740	468	0.24	0.05	0	1
G011.046-00.069_2	2.9	0.54	27.35	8411	51454	16451	12878	543	471	0.76	0.28	0	1
G011.612-00.383_0	3.0	0.07	3.81	401	10230	1759	2999	1579	788	1.0	0.0	0	2
G012.405-00.138_0	2.6	0.21	9.43	807	18099	3927	7804	622	827	0.97	0.12	0	1
G012.405-00.138_1	8.7	0.03	4.82	4563	38064	10563	1727	329	358	0.15	0.0	0	2
G012.529-00.314_0	2.6	0.18	8.14	1177	13178	3543	5601	561	688	0.88	0.2	0	1
G012.529-00.314_1	2.6	0.07	3.0	964	7160	2163	754	174	251	0.33	0.0	0	1
G012.529-00.314_2	1.3	0.08	1.88	404	7353	1799	479	741	254	0.39	0.0	0	2
G012.543+00.011_0	12.0	0.08	17.74	6570	46716	9427	7198	776	406	0.84	0.03	0	1
G012.543+00.011_1	12.0	0.03	6.6	5071	28427	6550	2752	316	417	0.34	0.0	0	1
G012.543-00.092_0	2.6	0.07	3.25	832	19478	4223	2541	734	782	0.36	0.0	0	2
G012.543-00.092_1	4.8	0.18	14.84	2500	38102	8831	8142	767	548	0.81	0.01	0	2
G012.543-00.092_2	2.6	0.06	2.62	791	16469	3602	585	543	223	0.28	0.0	0	1
G012.595+00.116_0	4.8	0.05	4.59	1104	12478	2920	1830	382	398	0.49	0.13	0	2

Table B.2: Distance dependent parameters of all filaments continued.

Filament ID	d	l	$l(d)$	M(ATG)	M(ATG + P)	M(dust)	M(gas)	$m_{\rm crit,nt}$	$m_{\rm obs}$	det. ^{13}CO	det. C^{18}O	edge flag	d flag
	kpc	°	pc	$M_\odot$	$M_\odot$	$M_\odot$	$M_\odot$	$M_\odot\,pc^{-1}$	$M_\odot\,pc^{-1}$				
G012.893+00.496_0	2.5	0.12	5.3	3616	8374	4483	5040	446	951	1.0	0.93	1	1
G012.893+00.496_1	1.8	0.12	3.82	1882	4842	2428	2129	367	558	1.0	0.0	1	1
G013.220+00.164_0	2.6	0.08	3.56	305	8704	2115	2463	701	692	1.0	0.0	0	1
G013.220+00.164_1	1.9	0.05	1.61	232	7220	1815	1193	702	742	0.62	0.0	0	2
G013.282-00.316_0	2.6	0.57	25.67	3464	70003	18554	30486	1653	1188	0.99	0.28	0	1
G013.282-00.316_1	1.8	0.24	7.51	2559	51664	14625	8304	2032	1106	0.41	0.04	0	2
G013.313+00.193_0	1.9	0.32	10.64	837	12003	4864	4697	355	441	0.98	0.21	0	1
G013.313+00.193_1	2.6	0.04	1.79	1470	16418	6757	1698	346	949	0.14	0.03	0	2
G013.460+00.171_0	1.9	0.06	1.95	159	4496	1013	1540	581	789	1.0	0.05	0	2
G013.700-00.072_0	4.5	0.13	10.55	3280	22978	5657	8288	385	786	0.76	0.39	0	1
G013.893-00.129_0	3.1	0.08	4.22	1065	20126	3925	12025	918	2850	1.0	0.42	0	2
G013.893-00.129_1	1.8	0.06	1.89	564	11761	2190	854	825	452	0.77	0.27	0	1
G014.005+00.311_0	3.9	0.1	6.66	986	10736	3271	2866	647	430	0.8	0.08	0	1
G014.117-00.392_0	3.1	0.09	4.72	823	13483	1232	4793	1332	1015	0.97	0.16	0	2
G014.117-00.392_1	1.5	0.09	2.32	306	8194	838	2727	1321	1176	1.0	0.0	0	2
G014.627-00.123_0	3.1	0.13	7.21	1268	20376	1537	8135	1136	1128	1.0	0.31	0	1
G014.789-00.478_0	2.0	0.11	3.89	517	8317	2296	2225	590	572	0.93	0.14	1	1
G014.919-00.065_0	2.6	0.13	5.81	1136	15895	4127	3189	822	549	0.71	0.0	0	1
G015.611-00.476_0	1.8	0.14	4.27	1419	5858	2288	2213	203	519	0.83	0.28	1	1
G015.611-00.476_1	16.9	0.05	15.26	41765	89265	50118	9715	622	637	0.32	0.0	1	1
G015.653-00.224_0	11.6	0.11	21.58	4745	17675	6356	11165	193	517	1.0	0.61	0	1
G016.609-00.069_0	4.7	0.16	13.28	8860	39024	13367	9764	314	735	0.39	0.17	0	1
G016.609-00.069_1	3.6	0.14	8.78	5908	39790	11396	2725	453	310	0.38	0.14	0	1
G016.661+00.121_0	1.9	0.05	1.75	149	1804	233	392	211	224	0.65	0.12	0	1
G016.700-00.235_0	4.7	0.04	3.39	1375	15250	2568	1483	392	437	0.33	0.02	0	2
G016.700-00.235_1	3.6	0.09	5.38	973	15778	2275	2089	659	388	0.67	0.0	0	2
G016.757+00.013_0	3.6	0.09	5.93	1327	13873	3523	3840	844	647	0.82	0.03	0	1
G016.919+00.275_0	1.9	0.24	8.06	1576	11469	3421	12341	610	1532	1.0	0.71	0	1

Table B.2: Distance dependent parameters of all filaments continued.

Filament ID	d	l	$l(d)$	M(ATG)	M(ATG + P)	M(dust)	M(gas)	$m_{\mathrm{crit,nt}}$	m_{obs}	det. ^{13}CO	det. C^{18}O	edge flag	d flag
	kpc	°	pc	$M_\odot$	$M_\odot$	$M_\odot$	$M_\odot$	$M_\odot\,\mathrm{pc}^{-1}$	$M_\odot\,\mathrm{pc}^{-1}$				
G016.929-00.082_0	3.6	0.19	12.03	2001	15687	3393	4923	265	409	0.82	0.11	0	1
G016.929-00.082_1	15.9	0.03	8.63	23180	102276	29452	8535	609	990	0.14	0.0	0	1
G016.998+00.280_0	1.9	0.12	3.88	1251	9789	3034	10342	836	2663	1.0	0.43	0	2
G301.638-00.239_0	4.8	0.09	7.6	2491	8737	3874	5637	450	742	1.0	0.69	0	1
G305.560-00.003_0	3.8	0.29	19.5	12255	39279	17799	23893	919	1225	0.97	0.65	0	1
G309.161-00.358_0	3.5	0.11	6.7	2896	13887	4116	11882	505	1774	1.0	0.92	0	1
G313.703-00.181_0	3.0	0.07	3.61	1308	9620	2195	5821	526	1612	1.0	0.87	0	1
G313.717+00.103_0	7.5	0.04	4.69	3144	12401	4505	3990	281	851	0.5	0.38	0	1
G313.717+00.103_1	3.0	0.03	1.68	644	3954	1143	506	286	301	0.46	0.0	0	1
G313.717+00.103_2	3.0	0.05	2.59	696	5560	1410	1926	314	742	0.71	0.46	0	1
G314.219+00.266_0	4.2	0.2	14.77	10074	38592	15690	32319	820	2188	1.0	0.75	0	1
G314.284+00.100_0	4.2	0.13	9.73	8443	23633	11840	8855	661	910	1.0	0.24	0	1
G314.284+00.100_1	4.2	0.13	9.73	8611	25278	12335	11649	582	1198	1.0	0.84	0	1
G317.386+00.113_0	2.8	0.11	5.21	3399	18166	7068	13011	995	2498	1.0	0.69	0	1
G317.889-00.256_0	2.3	0.18	7.23	2572	16165	5089	13494	822	1866	1.0	0.69	0	1
G320.240+00.027_0	0.6	0.07	0.75	82	1239	489	163	896	217	1.0	0.54	0	1
G320.243+00.406_0	2.1	0.17	6.36	2297	5753	2966	4051	340	637	0.98	0.41	0	1
G320.270-00.299_0	8.6	0.18	26.37	37328	74991	44456	55758	854	2114	0.95	0.66	0	1
G320.883-00.392_0	2.8	0.14	6.95	3019	10049	4020	6689	348	963	1.0	0.88	0	1
G323.179+00.149_0	4.0	0.07	5.05	2362	7883	3657	7578	339	1502	1.0	0.74	0	1
G323.929+00.036_0	10.0	0.17	29.45	18472	54410	21140	38513	1344	1308	1.0	0.2	0	1
G326.552+00.165_0	4.4	0.13	9.85	3117	17795	5341	8525	885	865	1.0	0.36	0	1
G326.586+00.050_0	4.6	0.06	5.16	608	9069	1481	2146	749	416	0.95	0.0	0	2
G326.722-00.099_0	3.5	0.07	4.39	991	15912	3946	5068	1419	1155	0.96	0.04	0	1
G326.790-00.119_0	3.5	0.12	7.23	3143	17259	6190	10318	799	1427	1.0	0.6	0	1
G327.036-00.408_0	3.5	0.08	4.97	858	7042	1599	3995	578	803	0.97	0.57	0	1
G327.042-00.169_0	3.5	0.12	7.07	811	17955	3924	9478	1019	1340	1.0	0.19	0	1
G327.157-00.256_0	3.5	0.59	36.25	8940	73455	23085	54139	1200	1494	1.0	0.59	0	1

Table B.2: Distance dependent parameters of all filaments continued.

Filament ID	d	l	$l(d)$	M(ATG)	M(ATG + P)	M(dust)	M(gas)	$m_{\rm crit,nt}$	$m_{\rm obs}$	det. ^{13}CO	det. C^{18}O	edge flag	d flag
	kpc	°	pc	$M_\odot$	$M_\odot$	$M_\odot$	$M_\odot$	$M_\odot\,pc^{-1}$	$M_\odot\,pc^{-1}$				
G327.258-00.420_0	3.0	0.15	7.6	957	15264	3195	9413	671	1238	1.0	0.43	0	2
G327.396+00.452_0	5.0	0.16	13.85	12620	33115	13902	14448	985	1043	0.94	0.3	0	1
G327.870+00.157_0	5.7	0.12	12.24	8511	48707	17401	12673	614	1035	0.61	0.2	0	1
G327.870+00.157_1	3.1	0.06	3.38	2945	22080	7109	1049	508	311	0.31	0.1	0	2
G327.884+00.002_0	7.1	0.07	9.24	1792	19563	4110	6464	660	700	1.0	0.03	0	2
G327.884+00.002_1	3.1	0.03	1.71	384	5793	1097	395	304	230	0.47	0.0	0	2
G327.981-00.101_0	3.1	0.17	9.07	2824	26926	6362	8813	1053	972	1.0	0.59	0	1
G328.627+00.063_0	9.0	0.04	6.54	2574	15397	5281	1576	327	241	0.54	0.0	0	1
G328.627+00.063_1	3.4	0.03	2.06	562	8458	2188	966	548	469	0.54	0.0	0	2
G328.773+00.304_0	6.8	0.11	13.27	3453	27220	4990	9253	871	697	1.0	0.17	0	1
G328.773+00.304_1	9.0	0.03	5.04	3635	18056	4410	959	282	190	0.29	0.0	0	2
G328.940+00.277_0	5.0	0.05	4.46	694	12265	2390	2896	937	649	0.9	0.0	0	2
G330.348-00.122_0	5.8	0.1	10.0	1903	25812	4436	4653	956	466	0.69	0.0	0	1
G330.760-00.306_0	4.0	0.17	11.6	2233	32090	8461	16253	1074	1402	1.0	0.41	0	1
G330.760-00.306_1	4.0	0.06	3.95	1794	18910	5325	1577	430	399	0.37	0.0	0	1
G330.973+00.076_0	2.9	0.09	4.45	901	15132	2872	1021	591	230	0.43	0.06	0	2
G330.973+00.076_1	3.9	0.08	5.21	1561	22150	4404	3221	605	618	0.37	0.01	0	2
G330.973+00.076_2	-	0.06	-	-	-	-	-	283	-	0.27	0.03	0	0
G330.986+00.337_0	3.4	0.14	8.25	1814	10419	2829	3502	426	425	0.98	0.45	0	1
G331.533+00.241_0	3.5	0.03	1.96	1202	15198	4298	933	520	476	0.16	0.0	0	1
G331.533+00.241_1	3.5	0.11	6.97	1228	17574	4824	2887	561	414	0.59	0.19	0	1
G331.533+00.241_2	5.3	0.07	6.6	2635	25796	7781	2702	611	409	0.33	0.03	0	1
G331.670-00.272_0	3.1	0.15	8.33	1469	9835	2860	5407	220	649	0.96	0.85	0	1
G331.670-00.272_1	5.3	0.03	3.21	3743	18969	6237	1018	406	317	0.23	0.0	0	2
G331.670-00.272_2	5.3	0.1	9.0	4154	25715	7726	3600	743	400	0.6	0.0	0	2
G331.973-00.378_0	3.6	0.18	11.29	1370	12687	2512	5068	482	449	0.94	0.42	0	1
G332.000+00.011_0	3.1	0.17	8.94	1691	37862	5996	7211	2530	807	0.94	0.03	0	2
G332.000+00.011_1	5.3	0.13	12.02	1423	35153	4338	4906	1194	408	0.75	0.0	0	2

Table B.2: Distance dependent parameters of all filaments continued.

Filament ID	d	l	$l(d)$	M(ATG)	M(ATG + P)	M(dust)	M(gas)	$m_{\mathrm{crit,nt}}$	m_{obs}	det. ^{13}CO	det. C^{18}O	edge flag	d flag
	kpc	°	pc	$M_\odot$	$M_\odot$	$M_\odot$	$M_\odot$	$M_\odot\,\mathrm{pc}^{-1}$	$M_\odot\,\mathrm{pc}^{-1}$				
G332.370-00.080_0	3.1	0.14	7.63	25736	132180	48379	3077	464	403	0.07	0.0	0	1
G332.370-00.080_1	3.1	1.81	97.78	27338	174920	59182	80571	665	824	0.97	0.51	0	1
G332.370-00.080_2	5.2	0.36	33.02	69299	313946	120785	13501	772	409	0.2	0.03	0	1
G332.610+00.052_0	5.6	0.16	16.04	2259	34359	7143	7452	735	465	0.94	0.1	0	1
G332.852-00.214_0	3.6	0.1	6.38	600	15318	1958	4459	879	698	0.97	0.15	0	2
G333.007+00.452_0	3.6	0.06	3.62	506	9781	1554	1432	788	396	0.49	0.0	0	2
G333.063+00.181_0	3.6	0.14	8.59	1296	28891	4984	5392	1762	628	0.89	0.2	0	1
G333.202-00.250_0	3.6	0.03	1.89	641	12909	881	942	455	498	0.24	0.0	0	2
G333.202-00.250_1	3.6	0.03	2.0	658	14319	937	447	618	224	0.24	0.0	0	2
G333.202-00.250_2	3.6	0.06	3.46	632	12204	853	577	371	167	0.35	0.0	0	2
G333.297+00.073_0	3.6	0.47	29.71	11172	73991	22262	32686	1193	1100	0.99	0.37	0	1
G333.297+00.073_1	10.7	0.15	28.87	63610	196640	82882	20024	700	694	0.33	0.07	0	1
G333.481+00.165_0	8.7	0.07	10.61	4629	15205	5694	2802	345	264	0.86	0.07	0	1
G333.722+00.361_0	2.3	0.24	9.56	3667	11091	4360	5969	326	624	1.0	0.79	0	1
G333.868-00.312_0	3.6	0.15	9.64	1648	43775	13246	34310	2893	3561	1.0	0.35	0	1
G333.899-00.106_0	9.6	0.12	19.81	6419	36293	6610	5634	320	284	0.58	0.04	0	2
G333.899-00.106_1	3.6	0.05	3.06	1770	28740	2546	2772	1151	904	0.23	0.06	0	1
G333.985+00.224_0	5.2	0.1	8.64	3615	23103	8974	2126	289	246	0.34	0.02	0	2
G333.985+00.224_1	3.1	0.15	8.3	1728	17026	6124	2540	455	306	0.53	0.04	0	1
G333.985+00.224_2	3.1	0.04	1.93	1620	13698	5034	296	316	153	0.14	0.0	0	1
G333.985+00.224_3	3.7	0.16	10.05	2370	21204	7728	4137	502	412	0.56	0.06	0	1
G333.985+00.224_4	5.2	0.04	4.0	4153	30656	11549	1364	543	341	0.14	0.0	0	1
G333.992+00.058_0	5.2	0.26	23.2	3852	57212	14491	17355	1500	748	0.96	0.07	0	1
G333.992+00.058_1	3.6	0.22	13.97	1919	30542	7612	5497	856	394	0.82	0.05	0	2
G333.992+00.058_2	4.0	0.09	6.13	2127	25333	6777	2088	398	341	0.33	0.09	0	1
G334.056+00.489_0	3.7	0.06	3.85	362	6554	914	1425	1308	370	0.85	0.0	0	2
G334.070-00.257_0	3.6	0.08	4.93	639	12927	2487	1849	444	375	0.57	0.0	0	2
G334.070-00.257_1	3.1	0.09	5.01	546	14131	2591	1794	657	358	0.65	0.0	0	2

Table B.2: Distance dependent parameters of all filaments continued.

Filament ID	d	l	$l(d)$	M(ATG)	M(ATG + P)	M(dust)	M(gas)	$m_{\rm crit,nt}$	$m_{\rm obs}$	det. ^{13}CO	det. C^{18}O	edge flag	d flag
	kpc	°	pc	$M_\odot$	$M_\odot$	$M_\odot$	$M_\odot$	$M_\odot\,pc^{-1}$	$M_\odot\,pc^{-1}$				
G334.202+00.156_0	9.6	0.13	21.65	7931	61758	19401	15805	1572	730	1.0	0.11	0	1
G334.202+00.156_1	2.8	0.05	2.39	1396	14335	4148	2286	877	956	0.4	0.0	0	2
G334.267-00.107_0	5.2	0.13	11.62	3242	36560	9429	6894	698	593	0.54	0.01	0	1
G334.267-00.107_1	12.8	0.07	15.02	14140	104867	30747	8024	795	534	0.32	0.01	0	1
G334.442+00.050_0	9.7	0.12	20.82	7852	51946	14536	8654	349	416	0.53	0.17	0	1
G334.442+00.050_1	8.7	0.06	8.53	8018	57847	15705	2985	644	350	0.25	0.0	0	2
G334.442+00.050_2	10.8	0.05	9.46	9332	61013	17142	4223	434	446	0.21	0.0	0	2
G334.617-00.270_0	3.1	0.12	6.46	1949	16660	4036	7906	843	1225	1.0	0.52	0	1
G334.640+00.426_0	4.0	0.29	20.51	6301	20543	7171	13038	503	636	0.91	0.32	0	1
G334.684+00.024_0	2.3	0.16	6.36	1450	14495	3268	2063	391	324	0.49	0.05	0	1
G334.684+00.024_1	2.3	0.03	1.15	1334	10857	2641	184	217	160	0.1	0.0	0	1
G334.684+00.024_2	5.1	0.04	3.71	5663	34208	9420	1050	330	283	0.14	0.0	0	1
G334.840-00.196_0	3.1	0.16	8.78	1019	17938	2058	3969	570	452	0.72	0.18	0	1
G334.840-00.196_1	2.3	0.1	4.08	622	13939	1653	861	671	211	0.47	0.0	0	2
G335.008-00.268_0	13.8	0.13	30.74	19077	141611	45245	18720	1008	609	0.47	0.01	0	1
G335.008-00.268_1	13.8	0.08	18.95	16000	114062	36884	13217	629	697	0.29	0.0	0	1
G335.083+00.065_0	-	0.05	-	-	-	-	-	589	-	0.85	0.0	0	0
G335.251-00.033_0	2.9	0.1	4.9	496	7192	1294	2336	507	476	0.97	0.06	0	1
G335.814+00.061_0	9.7	0.08	13.02	3578	34398	6766	5313	338	408	0.36	0.0	0	2
G336.060+00.040_0	7.6	0.11	14.05	5373	29222	9503	6845	470	487	0.59	0.1	0	1
G336.062-00.271_0	2.9	0.08	3.8	329	5598	1004	1198	319	316	0.69	0.1	0	2
G336.194-00.457_0	5.0	0.06	4.97	306	4538	585	983	378	198	0.95	0.1	0	2
G336.248+00.310_0	10.8	0.14	25.59	16099	84815	28092	14781	496	578	0.3	0.02	0	2
G336.248+00.310_1	3.2	0.09	4.98	2056	20226	5286	2358	279	473	0.21	0.1	0	1
G336.376+00.204_0	12.1	0.11	23.97	10792	59185	16817	12126	556	506	0.42	0.02	0	1
G336.376+00.204_1	10.8	0.03	6.03	9257	52280	14643	2472	456	410	0.14	0.03	0	1
G336.391+00.012_0	6.7	0.32	37.36	25696	97969	35723	27166	886	727	0.7	0.1	0	1
G336.391+00.012_1	2.9	0.04	2.06	5270	26094	8211	1133	390	551	0.08	0.01	0	1

Table B.2: Distance dependent parameters of all filaments continued.

Filament ID	d	l	$l(d)$	M(ATG)	M(ATG + P)	M(dust)	M(gas)	$m_{\mathrm{crit,nt}}$	m_{obs}	det. ^{13}CO	det. C^{18}O	edge flag	d flag
	kpc	°	pc	$M_\odot$	$M_\odot$	$M_\odot$	$M_\odot$	$M_\odot\,\mathrm{pc}^{-1}$	$M_\odot\,\mathrm{pc}^{-1}$				
G336.846+00.282_0	4.6	0.12	9.79	3272	21084	6044	4825	1002	493	0.95	0.05	0	1
G336.846+00.282_1	4.3	0.05	3.41	2547	13091	4178	1998	413	586	0.35	0.12	0	1
G337.148-00.387_0	1.6	0.24	6.6	1609	10541	3155	1648	276	250	0.53	0.0	0	1
G337.148-00.387_1	2.8	0.12	6.01	4566	22947	7622	2622	374	436	0.27	0.03	0	1
G337.409-00.400_0	3.0	0.27	14.23	8944	29287	12783	13517	499	950	0.8	0.33	0	1
G337.409-00.400_1	3.7	0.07	4.78	12449	26816	14574	1522	251	318	0.22	0.03	0	1
G337.744-00.346_0	3.0	0.28	14.7	3671	22759	7633	9541	476	649	0.96	0.44	0	1
G337.850+00.087_0	3.5	0.21	12.96	4124	81314	21544	24395	4461	1882	1.0	0.06	0	1
G338.181-00.477_0	2.9	0.09	4.41	715	10061	2684	1710	945	388	0.86	0.11	0	1
G338.279-00.295_0	1.1	0.06	1.13	418	8969	3431	642	968	566	0.59	0.12	0	1
G338.279-00.295_1	7.0	0.06	7.25	2964	23829	4778	3211	610	443	0.59	0.0	0	2
G338.291-00.119_0	5.7	0.04	4.12	1148	17246	2379	1766	377	429	0.36	0.03	0	2
G338.291-00.119_1	7.1	0.05	6.15	1878	31224	4121	3313	775	539	0.44	0.0	0	2
G338.528+00.214_0	2.7	0.14	6.39	1760	15105	4387	2238	853	351	0.65	0.11	0	1
G338.680-00.455_0	2.9	0.24	12.3	1124	14025	2508	4588	652	373	0.95	0.1	0	1
G338.680-00.455_1	2.9	0.05	2.73	1078	11938	2227	540	499	198	0.22	0.01	0	1
G338.708-00.328_0	3.2	0.14	7.91	668	10417	2000	3155	525	399	0.88	0.07	0	2
G338.708-00.328_1	2.9	0.1	5.22	653	11615	2077	1709	776	328	0.66	0.12	0	2
G338.749+00.159_0	2.7	0.09	4.15	830	14933	3270	2425	1512	584	1.0	0.24	0	1
G338.773+00.492_0	4.2	0.1	7.52	3755	19029	7955	17964	1070	2387	1.0	0.7	1	1
G338.806+00.111_0	2.6	0.14	6.21	939	18538	3126	3362	1367	542	0.71	0.07	0	1
G338.941-00.058_0	11.6	0.08	15.54	22161	72798	31414	8379	411	539	0.3	0.05	0	1
G338.941-00.058_1	3.2	0.19	10.73	3170	25865	7320	6992	723	652	0.8	0.4	0	1
G338.953+00.278_0	4.2	0.09	6.41	857	11740	2982	3094	320	483	0.56	0.11	0	2
G338.953+00.278_1	2.2	0.08	2.91	575	10247	2261	1032	814	355	0.46	0.02	0	2
G338.993+00.110_0	2.4	0.05	1.99	214	6310	918	573	820	288	0.79	0.0	0	2
G339.077+00.153_0	4.8	0.18	15.19	4665	34627	10216	8996	822	592	0.67	0.21	0	1
G339.077+00.153_1	2.2	0.09	3.37	1098	12318	3199	1007	634	299	0.33	0.0	0	2

Table B.2: Distance dependent parameters of all filaments continued.

Filament ID	d	l	$l(d)$	M(ATG)	M(ATG + P)	M(dust)	M(gas)	$m_{\rm crit,nt}$	$m_{\rm obs}$	det. ^{13}CO	det. C^{18}O	edge flag	d flag
	kpc	°	pc	$M_\odot$	$M_\odot$	$M_\odot$	$M_\odot$	$M_\odot\,pc^{-1}$	$M_\odot\,pc^{-1}$				
G339.113-00.203_0	7.1	0.1	12.56	4853	55503	19462	13591	906	1082	0.56	0.1	0	2
G339.113-00.203_1	2.9	0.13	6.68	1061	15224	4979	1581	507	237	0.73	0.02	0	2
G339.113-00.203_2	3.1	0.11	5.86	1140	15870	5257	1968	469	336	0.58	0.1	0	1
G339.116-00.405_0	2.9	0.25	12.51	1918	18365	3450	8029	529	642	1.0	0.57	0	1
G339.260+00.117_0	4.8	0.16	13.2	3533	23282	6960	7818	599	592	0.95	0.32	0	1
G339.385-00.414_0	2.9	0.17	8.48	1385	11559	3740	4603	486	543	0.97	0.23	0	1
G339.586-00.119_0	2.6	0.21	9.61	4320	27985	11442	9357	809	974	0.99	0.62	0	1
G339.586-00.119_1	13.2	0.07	15.72	56501	127084	77114	7884	591	502	0.32	0.01	0	1
G339.692+00.291_0	10.0	0.05	8.15	2794	21031	6418	6317	612	775	0.57	0.13	0	1
G339.988-00.165_0	3.6	0.17	10.84	2007	26026	7685	12737	778	1175	1.0	0.6	0	1
G339.988-00.165_1	2.8	0.07	3.34	1101	11687	3624	828	363	248	0.38	0.02	0	1
G340.301-00.387_0	3.6	0.51	31.82	20468	85311	34770	62867	1176	1976	0.95	0.69	0	1
G340.301-00.387_1	7.9	0.2	27.05	68757	153410	84425	9723	618	359	0.37	0.0	0	2
G340.301-00.387_2	10.1	0.12	20.49	89615	185554	106355	10079	501	492	0.21	0.0	0	2
G340.316+00.079_0	7.9	0.08	10.8	2040	23973	3674	6145	342	569	0.69	0.33	0	2
G340.316+00.079_1	-	0.05	-	-	-	-	-	537	-	0.38	0.0	0	0
G340.482-00.306_0	10.2	0.05	8.94	4905	23156	4087	7625	344	853	0.46	0.29	0	2
G340.482-00.306_1	3.6	0.1	6.05	1032	15540	890	3636	1485	601	0.89	0.0	0	1
G340.482-00.306_2	3.6	0.08	4.89	933	10792	755	1967	682	403	0.71	0.09	0	1
G340.511-00.471_0	3.6	0.08	5.09	1003	17777	3530	10213	1612	2005	1.0	0.18	1	1
G340.630-00.093_0	9.6	0.06	10.38	1482	12983	2507	3011	370	290	1.0	0.0	0	2
G340.630-00.093_1	3.6	0.06	3.65	472	12461	1591	2201	1388	604	0.91	0.0	0	2
G340.630-00.093_2	3.6	0.05	3.13	468	12173	1564	2370	1297	758	0.82	0.0	0	2
G340.981-00.013_0	3.3	0.16	9.21	812	16660	3492	3122	564	339	0.82	0.0	0	1
G340.981-00.013_1	3.3	0.11	6.32	757	12716	2815	1352	298	214	0.57	0.1	0	1
G340.981-00.013_2	3.3	0.05	3.15	786	14595	3144	1031	420	327	0.28	0.01	0	1
G340.981-00.013_3	2.2	0.06	2.38	416	11523	2231	450	558	189	0.29	0.0	0	2
G341.244-00.265_0	3.3	0.49	28.23	14242	74596	28981	49166	895	1741	1.0	0.79	0	1

Table B.2: Distance dependent parameters of all filaments continued.

Filament ID	d	l	$l(d)$	M(ATG)	M(ATG + P)	M(dust)	M(gas)	$m_{\mathrm{crit,nt}}$	m_{obs}	det. ^{13}CO	det. C^{18}O	edge flag	d flag
	kpc	°	pc	$M_\odot$	$M_\odot$	$M_\odot$	$M_\odot$	$M_\odot\,\mathrm{pc}^{-1}$	$M_\odot\,\mathrm{pc}^{-1}$				
G341.415+00.244_0	2.2	0.07	2.77	239	4833	736	1281	490	463	1.0	0.11	0	2
G341.415+00.244_1	2.2	0.07	2.72	420	10471	1730	3015	1654	1110	0.96	0.0	0	2
G341.415+00.244_2	10.8	0.04	8.04	2518	14184	3705	2526	327	314	0.56	0.04	0	2
G341.674+00.184_0	14.0	0.06	14.77	5453	48378	14825	10009	674	678	0.5	0.13	0	2
G341.674+00.184_1	5.0	0.08	6.78	894	15058	4072	2067	528	305	0.61	0.0	0	1
G341.938+00.054_0	8.0	0.12	17.36	4054	29276	7358	5535	342	319	0.69	0.06	0	1
G341.938+00.054_1	2.0	0.05	1.67	398	7344	1308	561	340	337	0.28	0.0	0	2
G342.100+00.399_0	7.7	0.25	33.61	47791	143249	60722	25252	380	751	0.39	0.22	0	1
G342.100+00.399_1	10.9	0.06	10.6	52561	134087	62627	3308	203	312	0.08	0.0	0	1
G342.100+00.399_2	10.9	0.26	49.87	80893	223829	99440	23705	634	475	0.4	0.04	0	1
G342.100+00.399_3	10.9	0.37	70.18	94022	278989	118953	79406	813	1131	0.55	0.28	0	1
G342.100+00.399_4	2.3	0.31	12.25	5780	30924	9648	3876	518	316	0.46	0.03	0	1
G342.100+00.399_5	12.5	0.07	14.95	77227	198714	92312	5964	398	399	0.09	0.0	0	2
G342.100+00.399_6	2.3	0.04	1.72	4886	16464	6539	309	115	179	0.06	0.0	0	1
G342.345-00.005_0	1.2	0.1	2.02	390	8213	2068	237	712	117	0.6	0.11	0	1
G342.357+00.113_0	9.9	0.21	36.18	19188	88037	27960	27428	297	758	0.63	0.36	0	1
G342.357+00.113_1	7.9	0.14	18.69	17042	99136	28094	6284	836	336	0.4	0.0	0	2
G342.357+00.113_2	1.2	0.08	1.6	836	13048	2269	394	628	246	0.22	0.11	0	1
G342.357+00.113_3	-	0.16	-	-	-	-	-	575	-	0.45	0.0	0	0
G342.357+00.113_4	2.4	0.07	2.74	2114	26129	5174	1480	718	541	0.17	0.02	0	2
G342.478-00.167_0	2.3	0.12	4.7	396	7231	1644	1603	564	341	1.0	0.2	0	1
G342.478-00.167_1	2.3	0.09	3.57	360	4840	1166	820	319	230	0.77	0.0	0	1
G342.823+00.129_0	2.7	0.03	1.54	157	4420	365	575	413	374	0.55	0.0	0	2
G343.579-00.170_0	2.6	0.11	5.01	680	8019	1677	2184	443	436	0.95	0.16	0	1
G343.776-00.149_0	2.6	0.63	28.73	9132	50422	14012	25245	606	879	0.99	0.48	0	1
G343.908+00.113_0	17.1	0.11	31.93	32107	128729	47790	32660	777	1023	0.47	0.01	0	1
G343.998-00.143_0	2.6	0.04	1.66	270	4731	985	420	452	253	0.48	0.0	0	1
G344.043-00.373_0	10.1	0.15	25.8	4717	32520	8963	13408	419	520	0.93	0.37	0	1

Table B.2: Distance dependent parameters of all filaments continued.

Filament ID	d	l	$l(d)$	M(ATG)	M(ATG + P)	M(dust)	M(gas)	$m_{\rm crit,nt}$	$m_{\rm obs}$	det. ^{13}CO	det. C^{18}O	edge flag	d flag
	kpc	°	pc	$M_\odot$	$M_\odot$	$M_\odot$	$M_\odot$	$M_\odot\,pc^{-1}$	$M_\odot\,pc^{-1}$				
G344.340-00.227_0	10.2	0.14	25.78	4285	27090	6865	21249	392	824	1.0	0.36	0	1
G344.447-00.186_0	10.2	0.09	15.92	4180	20945	5622	9179	231	577	0.62	0.27	0	2
G344.447-00.186_1	-	0.03	-	-	-	-	-	280	-	0.25	0.0	0	0
G344.592-00.026_0	1.1	0.05	1.02	217	4705	1349	145	1142	143	1.0	0.05	0	1
G345.345-00.060_0	1.4	0.05	1.11	89	2641	184	504	388	454	0.67	0.0	0	2
G345.345-00.060_1	1.4	0.04	1.0	86	2471	176	48	342	48	0.62	0.0	0	2
G345.433-00.143_0	1.4	0.15	3.62	708	7953	2638	2292	611	633	1.0	0.62	0	1
G345.493+00.337_0	2.4	0.29	12.18	15468	34737	17632	26787	810	2199	1.0	0.76	0	1
G345.635+00.358_0	2.4	0.31	12.87	2358	28203	9874	18175	1292	1412	1.0	0.41	0	1
G345.873+00.292_0	2.4	0.11	4.59	411	9666	2399	2371	862	516	0.9	0.05	0	2
G345.879+00.021_0	7.5	0.19	24.88	19133	77043	31344	22821	245	917	0.44	0.3	0	1
G345.879+00.021_1	5.9	0.24	24.82	15692	78027	29208	12464	669	502	0.58	0.15	0	1
G345.879+00.021_2	1.4	0.18	4.48	1389	17994	5452	1259	1013	281	0.45	0.04	0	1
G346.177+00.029_0	5.6	0.08	7.81	1707	17128	3944	2259	576	289	0.72	0.03	0	2
G346.177+00.029_1	10.2	0.06	10.03	4965	41025	10177	6775	888	676	0.44	0.0	0	2
G346.177+00.029_2	14.8	0.03	8.54	7359	47552	13062	5198	630	608	0.36	0.03	0	1
G346.177+00.029_3	9.5	0.04	5.88	4076	31259	7985	1450	657	246	0.33	0.0	0	2
G346.293+00.109_0	9.5	0.18	29.15	22134	57231	22207	17934	569	615	0.92	0.32	0	1
G346.293+00.109_1	3.5	0.09	5.77	4011	17588	4531	1525	628	265	0.51	0.03	0	1
G346.293+00.109_2	13.3	0.07	15.65	23110	51740	22558	12584	216	804	0.32	0.23	0	1
G346.483+00.144_0	1.3	0.09	2.09	875	7475	2435	436	1131	209	0.97	0.26	0	1
G346.951-00.155_0	10.4	0.05	9.25	5225	19096	8013	3480	492	376	0.43	0.03	0	1
G346.951-00.155_1	10.4	0.05	8.56	6204	24235	9881	4275	893	500	0.49	0.0	0	1
G346.951-00.155_2	10.4	0.03	6.06	5145	18742	7876	2069	516	341	0.3	0.0	0	1
G347.216+00.026_0	10.7	0.24	44.39	46471	139034	60578	105279	2303	2371	1.0	0.35	0	1
G347.390+00.266_0	9.8	0.14	23.75	7917	51391	21931	13574	1153	571	0.73	0.0	0	2
G347.390+00.266_1	10.2	0.12	21.48	8059	49703	21490	12688	924	591	0.62	0.05	0	1
G347.390+00.266_2	10.7	0.03	5.93	6292	32706	14771	1555	360	262	0.17	0.0	0	2

Table B.2: Distance dependent parameters of all filaments continued.

Filament ID	d	l	$l(d)$	M(ATG)	M(ATG + P)	M(dust)	M(gas)	$m_{\mathrm{crit,nt}}$	m_{obs}	det. ^{13}CO	det. C^{18}O	edge flag	d flag
	kpc	°	pc	$M_\odot$	$M_\odot$	$M_\odot$	$M_\odot$	$M_\odot\,\mathrm{pc}^{-1}$	$M_\odot\,\mathrm{pc}^{-1}$				
G347.870-00.318_0	6.9	0.22	26.21	17433	43034	23512	39838	597	1520	0.95	0.59	0	1
G347.894+00.035_0	12.9	0.31	68.93	56255	171650	79834	66881	918	970	0.69	0.1	0	1
G347.894+00.035_1	9.8	0.08	13.61	35425	112024	51227	6757	686	497	0.2	0.0	0	2
G348.034+00.439_0	1.3	0.09	2.08	85	3305	163	1473	710	707	1.0	0.03	0	2
G348.232+00.462_0	1.3	0.7	15.94	3323	15729	4972	12082	627	758	1.0	0.7	1	1
G348.492+00.346_0	5.7	0.09	8.47	2025	17797	5214	4962	986	586	0.78	0.19	0	2
G348.492+00.346_1	1.3	0.1	2.17	151	3334	814	987	545	455	0.86	0.0	0	2
G349.876+00.099_0	10.7	0.26	48.39	38002	142702	53273	41081	1155	849	0.72	0.04	0	1
G349.876+00.099_1	8.3	0.19	27.39	25488	102875	36938	24430	1012	892	0.55	0.11	0	1
G349.876+00.099_2	22.1	0.04	15.3	70826	224169	91886	6137	667	401	0.11	0.0	0	2
G350.299+00.237_0	11.9	0.04	7.37	5673	39212	9603	4123	2098	559	0.4	0.0	0	2
G350.522-00.255_0	3.3	0.12	6.92	629	12239	2356	7750	1152	1119	1.0	0.29	0	1
G350.781+00.492_0	1.3	0.12	2.62	555	3521	787	1173	251	448	0.77	0.35	1	2
G351.022-00.343_0	3.3	0.18	10.54	2734	15104	4905	6417	461	609	1.0	0.64	0	1
G351.498+00.254_0	11.5	0.16	31.37	12708	59454	18081	15852	968	505	0.89	0.0	0	1
G351.731+00.446_0	1.3	0.06	1.26	77	2441	226	265	401	211	0.73	0.0	0	2
G351.928-00.245_0	3.5	0.14	8.54	2082	23029	5317	2989	717	350	0.65	0.03	0	1
G351.928-00.245_1	1.4	0.2	4.92	769	14656	3282	3996	1094	812	0.92	0.17	0	1
G352.030+00.069_0	1.4	0.09	2.29	199	6592	1282	933	275	408	0.57	0.24	0	2
G352.062-00.257_0	1.4	0.16	3.84	504	8351	1871	1730	689	450	0.91	0.32	0	1
G352.107+00.184_0	10.4	0.22	40.6	30749	132607	54065	28866	1160	711	0.84	0.24	0	1
G352.107+00.184_1	-	0.05	-	-	-	-	-	1256	-	0.19	0.0	0	0
G352.107+00.184_2	-	0.05	-	-	-	-	-	316	-	0.19	0.0	0	0
G352.208+00.354_0	1.3	0.07	1.64	181	2619	553	1137	186	693	1.0	0.87	0	1
G352.308-00.447_0	1.4	0.21	5.09	833	7057	1404	3182	684	625	0.99	0.59	0	1
G352.781-00.050_0	10.9	0.05	8.63	6024	39824	11177	2681	504	311	0.28	0.0	0	1
G352.883+00.464_0	1.4	0.15	3.77	534	9267	1930	6707	1239	1779	1.0	0.12	1	1
G353.201-00.242_0	3.1	0.13	6.81	1177	9209	3303	4458	286	654	0.92	0.62	0	1

Table B.2: Distance dependent parameters of all filaments continued.

Filament ID	d	l	$l(d)$	M(ATG)	M(ATG + P)	M(dust)	M(gas)	$m_{\rm crit,nt}$	$m_{\rm obs}$	det. ^{13}CO	det. C^{18}O	edge flag	d flag
	kpc	°	pc	$M_\odot$	$M_\odot$	$M_\odot$	$M_\odot$	$M_\odot\,pc^{-1}$	$M_\odot\,pc^{-1}$				
G353.294+00.312_0	1.4	0.07	1.75	222	5616	1165	458	296	261	0.27	0.01	0	2
G353.294+00.312_1	1.4	0.04	0.93	247	6863	1463	77	436	84	0.17	0.0	0	2
G353.294+00.312_2	1.4	0.05	1.15	261	7439	1609	348	518	304	0.23	0.0	0	2
G353.389-00.340_0	3.1	0.73	39.48	31847	87054	46500	58559	983	1483	0.99	0.43	0	1
G353.418-00.208_0	8.8	0.12	18.23	4620	27338	7485	15398	692	845	1.0	0.16	0	1
G353.477-00.160_0	3.1	0.08	4.13	493	6119	788	2179	461	528	0.93	0.11	0	1
G353.564-00.464_0	3.1	0.1	5.24	1270	7954	2341	8275	377	1578	1.0	0.82	0	1
G353.949+00.252_0	1.0	0.18	3.07	371	4353	1068	1253	495	408	0.97	0.32	0	1
G353.992+00.321_0	1.0	0.04	0.72	198	2609	533	438	419	613	0.29	0.06	0	1
G354.991+00.421_0	8.4	0.09	13.21	4056	51840	11728	7021	2043	532	0.55	0.0	0	2
G355.211-00.496_0	1.4	0.06	1.57	633	2985	848	1828	738	1166	1.0	0.27	1	2
G355.257-00.260_0	-	0.11	-	-	-	-	-	637	-	1.0	0.67	0	0
G355.265+00.339_0	-	0.13	-	-	-	-	-	2160	-	0.51	0.0	0	0
G355.265+00.339_1	-	0.04	-	-	-	-	-	432	-	0.14	0.0	0	0
G355.265+00.339_2	-	0.03	-	-	-	-	-	864	-	0.15	0.01	0	0
G355.564+00.279_0	-	0.07	-	-	-	-	-	351	-	0.46	0.04	0	0
G355.564+00.279_1	-	0.04	-	-	-	-	-	643	-	0.3	0.0	0	0
G355.619-00.049_0	-	0.1	-	-	-	-	-	1037	-	0.94	0.09	0	0
G355.635+00.302_0	-	0.05	-	-	-	-	-	441	-	0.41	0.02	0	0
G355.635+00.302_1	-	0.05	-	-	-	-	-	508	-	0.41	0.02	0	0
G355.673+00.089_0	-	0.11	-	-	-	-	-	342	-	0.45	0.05	0	0
G355.673+00.089_1	-	0.07	-	-	-	-	-	944	-	0.29	0.0	0	0
G355.742-00.252_0	-	0.12	-	-	-	-	-	640	-	0.87	0.26	0	0
G355.742-00.252_1	-	0.03	-	-	-	-	-	299	-	0.26	0.0	0	0
G355.743+00.135_0	-	0.05	-	-	-	-	-	907	-	0.45	0.02	0	0
G355.836+00.317_0	-	0.06	-	-	-	-	-	357	-	0.17	0.02	0	0
G355.991-00.414_0	-	0.09	-	-	-	-	-	285	-	1.0	0.94	0	0
G356.416+00.088_0	-	0.13	-	-	-	-	-	455	-	0.88	0.3	0	0

Table B.2: Distance dependent parameters of all filaments continued.

Filament ID	d	l	$l(d)$	M(ATG)	M(ATG + P)	M(dust)	M(gas)	$m_{\mathrm{crit,nt}}$	m_{obs}	det. ^{13}CO	det. C^{18}O	edge flag	d flag
	kpc	°	pc	$M_\odot$	$M_\odot$	$M_\odot$	$M_\odot$	$M_\odot\,\mathrm{pc}^{-1}$	$M_\odot\,\mathrm{pc}^{-1}$				
G356.495+00.198_0	-	0.13	-	-	-	-	-	402	-	0.76	0.12	0	0
G356.874-00.021_0	-	0.1	-	-	-	-	-	621	-	0.97	0.24	0	0
G357.033+00.193_0	-	0.13	-	-	-	-	-	439	-	0.64	0.03	0	0
G357.420+00.356_0	-	0.05	-	-	-	-	-	393	-	0.85	0.0	0	0
G357.637-00.325_0	-	0.32	-	-	-	-	-	614	-	0.45	0.0	0	0
G357.637-00.325_1	-	0.07	-	-	-	-	-	445	-	0.12	0.03	0	0
G357.637-00.325_2	-	0.7	-	-	-	-	-	901	-	1.0	0.48	0	0
G357.956-00.160_0	-	0.21	-	-	-	-	-	1570	-	0.82	0.23	0	0
G357.956-00.160_1	-	0.12	-	-	-	-	-	568	-	0.4	0.13	0	0
G358.017-00.041_0	-	0.11	-	-	-	-	-	820	-	0.77	0.19	0	0
G358.017-00.041_1	-	0.09	-	-	-	-	-	749	-	0.6	0.0	0	0
G358.101-00.128_0	-	0.1	-	-	-	-	-	435	-	0.42	0.04	0	0
G358.101-00.128_1	-	0.23	-	-	-	-	-	954	-	1.0	0.63	0	0
G358.243-00.425_0	-	0.32	-	-	-	-	-	406	-	1.0	0.79	0	0
G358.243-00.425_1	-	0.15	-	-	-	-	-	632	-	0.46	0.0	0	0
G358.245+00.010_0	-	0.21	-	-	-	-	-	1660	-	0.56	0.0	0	0
G358.377-00.211_0	-	0.05	-	-	-	-	-	950	-	0.57	0.03	0	0
G358.377-00.211_1	-	0.06	-	-	-	-	-	4124	-	0.63	0.03	0	0
G358.451-00.422_0	-	0.54	-	-	-	-	-	675	-	0.88	0.63	1	0
G358.451-00.422_1	-	0.22	-	-	-	-	-	317	-	0.37	0.29	1	0
G358.451-00.422_2	-	0.13	-	-	-	-	-	389	-	0.22	0.05	1	0
G359.232+00.329_0	-	0.04	-	-	-	-	-	348	-	0.4	0.0	0	0
G359.372-00.437_0	-	0.16	-	-	-	-	-	186	-	1.0	0.73	0	0
G359.404+00.308_0	-	0.31	-	-	-	-	-	510	-	0.91	0.18	0	0
G359.404+00.308_1	-	0.04	-	-	-	-	-	330	-	0.11	0.0	0	0
G359.564-00.451_0	-	0.13	-	-	-	-	-	446	-	0.61	0.26	0	0
G359.863-00.248_0	-	0.05	-	-	-	-	-	1622	-	0.29	0.0	0	0
G359.863-00.248_1	-	0.11	-	-	-	-	-	909	-	0.75	0.27	0	0

Table B.2: Distance dependent parameters of all filaments continued.

Filament ID	d	l	$l(d)$	M(ATG)	M(ATG + P)	M(dust)	M(gas)	$m_{\mathrm{crit,nt}}$	m_{obs}	det. ^{13}CO	det. C^{18}O	edge flag	d flag
	kpc	°	pc	$M_\odot$	$M_\odot$	$M_\odot$	$M_\odot$	$M_\odot\,\mathrm{pc}^{-1}$	$M_\odot\,\mathrm{pc}^{-1}$				
G359.863-00.248_2	-	0.04	-	-	-	-	-	2180	-	0.29	0.0	0	0
G359.896-00.316_0	-	0.17	-	-	-	-	-	526	-	0.97	0.59	0	0

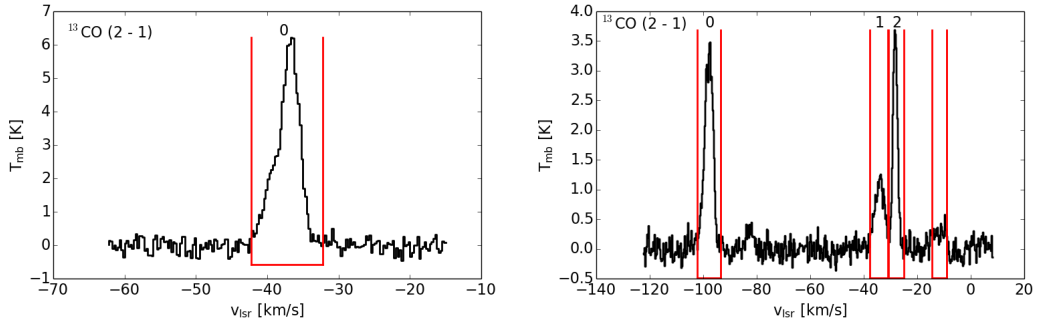

Figure B.1: Average ^{13}CO spectrum over the skeleton of filament candidate "G339.116-00.405" (top) and "G346.293+00.109" (bottom). The red lines mark the identified emission intervals named by letters.

B.2 gas dust correlation examples

In section 5.3.3 we are describing the method of comparing the ATLASGAL dust intensities with the integrated ^{13}CO intensity maps to identify the spatially correlated velocity components. Based on this correlation we assign one of four categories to the structure, which are: uncorrelated, completely correlated, partially correlated, and diffuse component. To visualize this categorization we show one example in the section 5.3.3 (Figs. 5.5, 5.6). To give a complete picture we present here the correlation plots of the other components of the filament candidate "G333.297+00.073" (Fig. B.2, for intensity maps see Fig. 5.5), and ^{13}CO spectra (Fig. B.1), integrated intensity maps and the corresponding correlation plots for the filament candidates "G339.116-00.405" (Fig. B.3) and "G346.293+00.109" (Figs. B.4 and B.5).

B.3 Filament profiles

In Section 5.5.1 we showed how the gas mass of correlated filaments is increasing with increasing radius. To be complete, we also show the mass curves of the correlated filaments based on the corrected ATLASGAL+PLANCK data (Fig. B.6), and the mass curves of the partially correlated (blue, Fig. B.7) and diffuse component filaments (red, Fig. B.7) based on the integrated ^{13}CO observations.

The mass curves of of the correlated filaments are in mostly in agreement with ^{13}CO observations. However, for the most nearby filaments (< 2 kpc), and especially in the continuum data, we find profiles indicating a slope of $p < 0$. This can be explained by line-of-sight confusion within the large boxes around the filament skeleton. As the dust continuum data traces all emission along the line-of-site it is possible that strong emission, which is not related to the filament but located nearby, is taken into account for the mass estimate for larger radii. Therefore, the masses will be overestimated. This effect is more likely for nearby filaments, as larger angular sizes are taken into account for the same physical size. The gas mass curves of the partially correlated and diffuse component filaments show on average similar results as the correlated filaments,

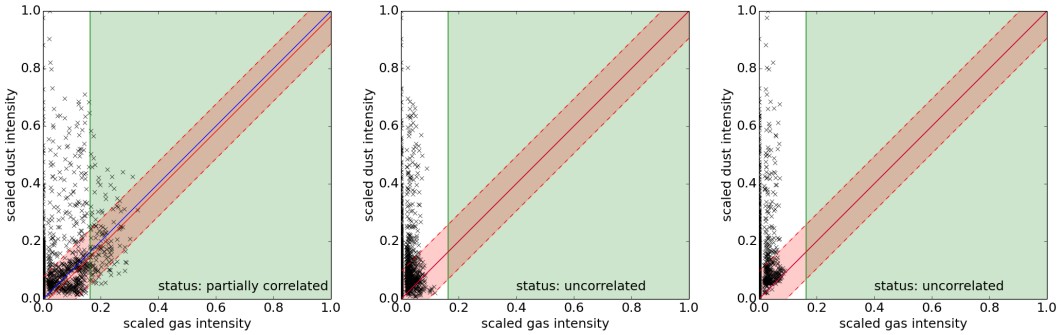

Figure B.2: Gas-dust correlation plots of the velocity components "b","c", and "d" of the filament candidate G333.297+00.073 (see Figs. 5.2, 5.4, and 5.5). The blue line gives the one-to-one correlation. The green area indicates values above the $\sigma_{\rm gas}$ limit. The red line shows the fitting result, and the area within the dashed red lines marks the $\pm\sigma_{\rm cor}$ surrounding. $p_{\rm cor,\,gas}$ is estimated from the overlap of these areas.

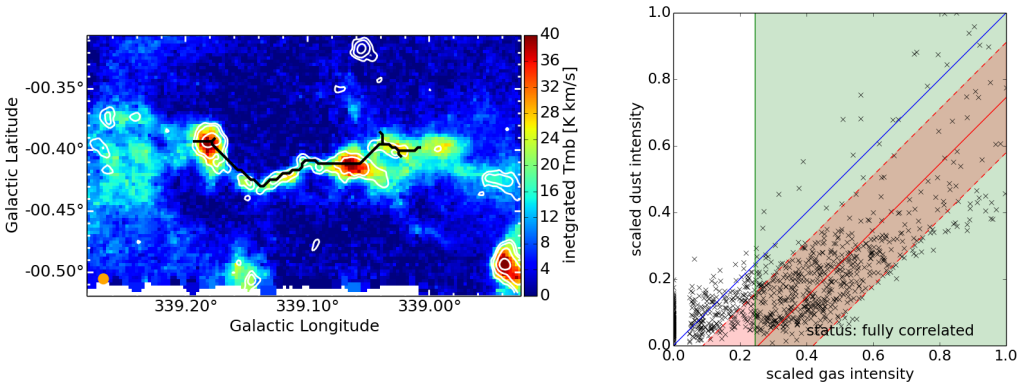

Figure B.3: Integrated ^{13}CO intensity map (left) and gas-dust correlation plot (right, description as in Fig. B.2) of the single velocity component filament candidate "G339.116-00.405". Because of the good correlation between the only identified velocity component with the ATLASGAL emission, it was categorized as fully correlated filament and can be found as "G339.116-00.405_0" in the final catalog.

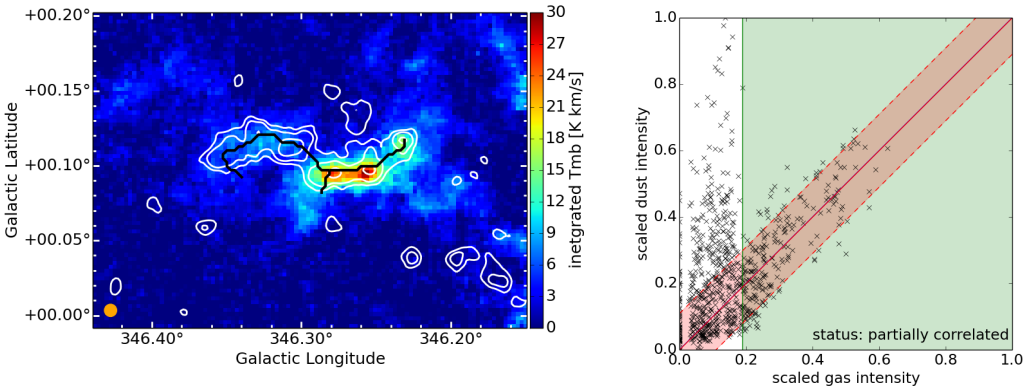

Figure B.4: Integrated ^{13}CO intensity map (left) and gas-dust correlation plot (right), description as in Fig. B.2)) of the first velocity component of the filament candidate "G346.293+00.109". The partially correlated filament is listed as "G346.293+00.109_0". The other three velocity components of the candidate are shown in Fig. B.5.

but with a larger scatter, as the skeleton no longer necessarily represents the shape of the structure.

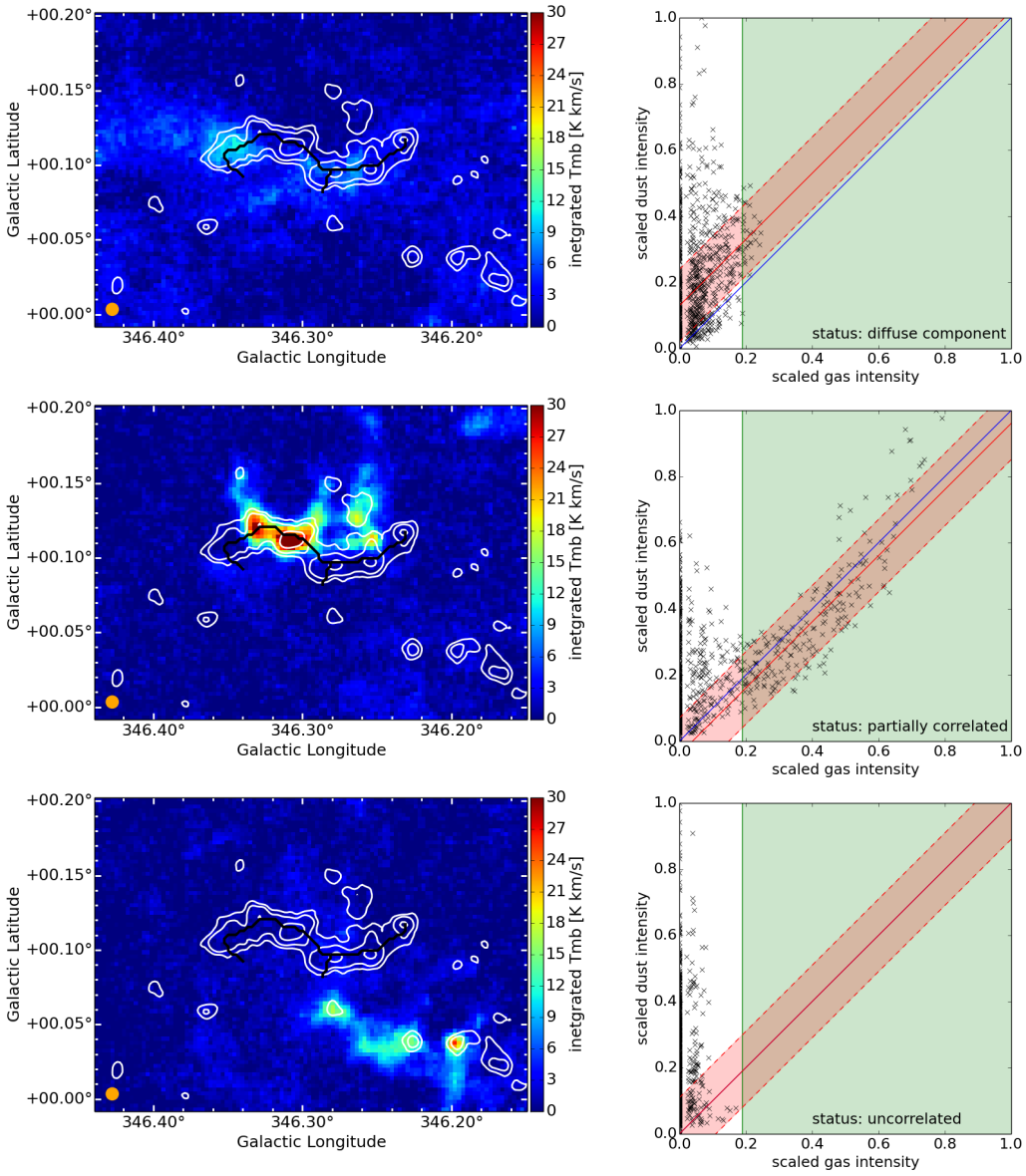

Figure B.5: Integrated ^{13}CO intensity maps (left) and gas-dust correlation plots (right, description as in Fig. B.2)) of the second (top), third (middle), and fourth (bottom) velocity component of the filament candidate "G346.293+00.109". The second, diffuse component is listed as "G346.293+00.109_1" and the third, partially correlated component is listed as "G346.293+00.109_2". The uncorrelated component is not listed in the catalog. The first velocity components of the candidate is shown in Fig. B.4.

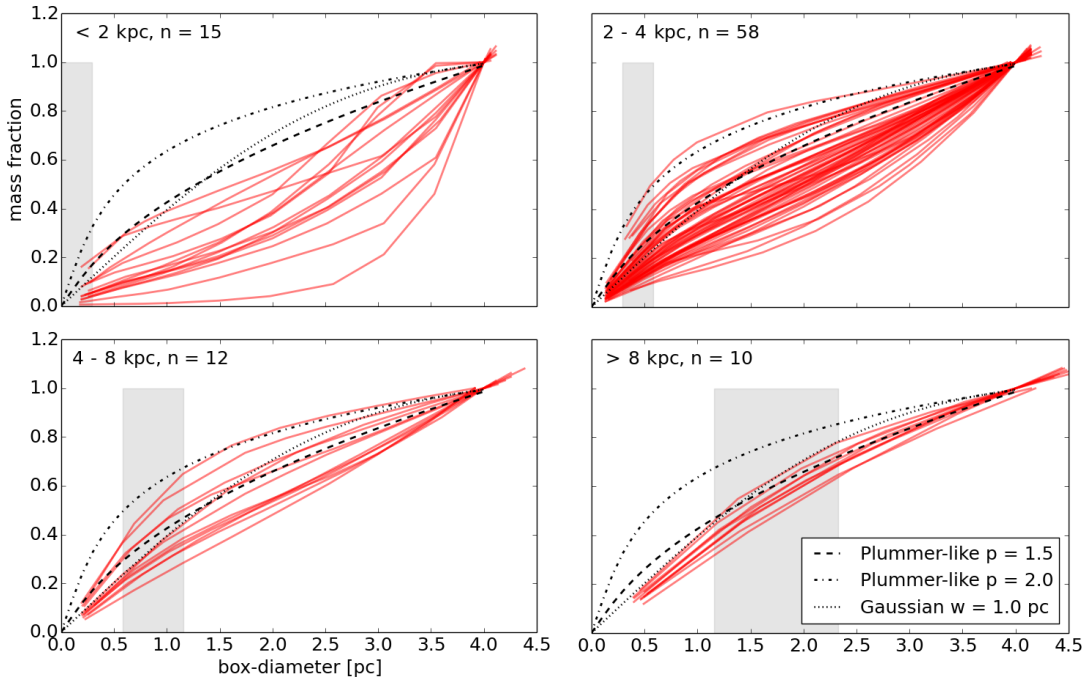

Figure B.6: Fraction of the filament mass derived from corrected ATLASGAL+PLANCK dust continuum emission dependent on the box-diameter of the mask separated with distances. *Top left:* $d < 2$ kpc, *Top right:* 2 kpc $< d < 4$ kpc, *Bottom left:* 4 kpc $< d < 8$ kpc, *Bottom right:* $d > 8$ kpc. The gray lines indicate the physical beam size at these distances. The black lines show the theoretical profiles, which describe a Plummer-like $p = 1.5$ (dashed) or $p = 2.0$ (dash-dotted), and a Gaussian with $w = 1.0$ (dotted).

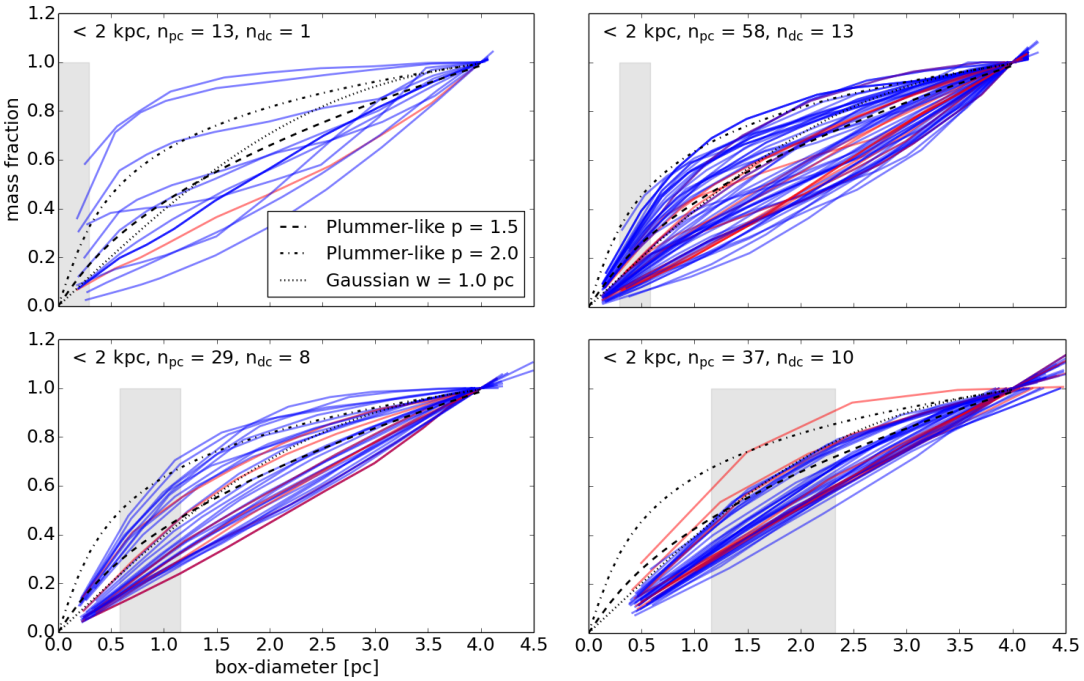

Figure B.7: Fraction of the filament mass for partially correlated (blue) and diffuse component (red) filaments derived from ^{13}CO emission dependent on the box-diameter of the mask separated with distances. *Top left:* $d < 2$ kpc, *Top right:* 2 kpc $< d <$ 4 kpc, *Bottom left:* 4 kpc $< d < 8$ kpc, *Bottom right:* $d > 8$ kpc. The vertical gray lines indicate the physical beam size at these distances. The black lines show the theoretical profiles, which describe a Plummer-like $p = 1.5$ (dashed) or $p = 2.0$ (dash-dotted), and a Gaussian with $w = 1.0$ (dotted).

Bibliography

Abergel A., Boulanger F., Mizuno A., Fukui Y., 1994, ApJ, 423, L59 (Cited on page 4.)

Abreu-Vicente J., Ragan S., Kainulainen J., Henning T., Beuther H., Johnston K., 2016, A&A, 590, A131 (Cited on pages 4, 5, 7, 16, 45, 75, 76, 91, 117 and 118.)

Alves J., Lombardi M., Lada C. J., 2007, A&A, 462, L17 (Cited on page 42.)

Anderson L. D., Bania T. M., Balser D. S., Cunningham V., Wenger T. V., Johnstone B. M., Armentrout W. P., 2014, ApJS, 212, 1 (Cited on pages 46, 52, 54, 59 and 63.)

André P., Di Francesco J., Ward-Thompson D., Inutsuka S.-I., Pudritz R. E., Pineda J. E., 2014, Protostars and Planets VI: From Filamentary Networks to Dense Cores in Molecular Clouds : Toward a New Paradigm for Star Formation. University of Arizona Press (Cited on pages 4, 5 and 15.)

André P., Men'shchikov A., Bontemps S., Könyves V., Motte F., Schneider N., Didelon P., Minier V., Henning T., Royer P., Merín B., Vavrek R., Attard M., Arzoumanian D., Wilson C. D., Ade P., Aussel H., Men A., Bontemps S., Könyves V., Motte F., Schneider N., Didelon P., Minier V., Henning T., Royer P., Merín B., Vavrek R., Attard M., Arzoumanian D., Wilson C. D., Ade P., Aussel H., 2010, A&A, 518, 1 (Cited on pages 4, 5, 42 and 75.)

Arzoumanian D., André P., Didelon P., Könyves V., Schneider N., Men'shchikov A., Sousbie T., Zavagno A., Bontemps S., Di Francesco J., Griffin M., Hennemann M., Hill T., Kirk J., Martin P., Minier V., Molinari S., Motte F., Peretto N., Pezzuto S., Spinoglio L., Ward-Thompson D., White G., Wilson C. D., Men A., Sousbie T., Zavagno A., Motte F., Peretto N., Pezzuto S., Spinoglio L., White G., Wilson C. D., Men'shchikov A., Sousbie T., Zavagno A., Bontemps S., Di Francesco J., Griffin M., Hennemann M., Hill T., Kirk J., Martin P., Minier V., Molinari S., Motte F., Peretto N., Pezzuto S., Spinoglio L., Ward-Thompson D., White G., Wilson C. D., 2011, A&A, 529, L6 (Cited on pages vii, 4, 5, 11, 15, 75, 77, 99, 100, 101 and 102.)

Arzoumanian D., André P., Könyves V., Palmeirim P., Roy A., Schneider N., Benedettini M., Didelon P., Di Francesco J., Kirk J., Ladjelate B., 2018, ArXiv e-prints (Cited on page 5.)

Arzoumanian D., André P., Peretto N., Könyves V., 2013, A&A, 553, A119 (Cited on pages 5 and 91.)

Ballesteros-Paredes J., Hartmann L., Vázquez-Semadeni E., 1999, ApJ, 527, 285 (Cited on pages 3 and 6.)

Bally J., Stark A. A., Wilson R. W., Langer W. D., Stark A. A., Wilson R. W., Langer W. D., 1987, ApJ, 312, L45 (Cited on pages 4, 7 and 75.)

Benjamin R. A., Churchwell E., Babler B. L., Bania T. M., Clemens D. P., Cohen M., Dickey J. M., Indebetouw R., Jackson J. M., Kobulnicky H. A., Lazarian A., Marston A. P., Mathis J. S., Meade M. R., Seager S., Stolovy S. R., Watson C., Whitney B. A., Wolff M. J., Wolfire M. G., 2003, PASP, 115, 953 (Cited on pages 17, 35 and 38.)

Bertin E., Arnouts S., 1996, A&AS, 117, 393 (Cited on page 12.)

Bessell J., Brett M., 1988, PASP, vol. 100, 1134 (Cited on pages 18, 38 and 39.)

Beuther H., Ragan S. E., Johnston K., Henning T., Hacar A., Kainulainen J. T., 2015, A&A, 584, A67 (Cited on pages 4, 16, 36, 75 and 107.)

Beuther H., Tackenberg J., Linz H., Henning T., Schuller F., Wyrowski F., Schilke P., Menten K., Robitaille T. P., Walmsley C. M., Bronfman L., Motte F., Nguyen-Luong Q., Bontemps S., 2012, ApJ, 747, 43 (Cited on pages 89 and 90.)

Bohlin R. C., Savage B. D., Drake J. F., 1978, ApJ, 224, 132 (Cited on page 23.)

Bolatto A., Wolfire M., Leroy A., 2013, ARA&A, 51, 207 (Cited on page 8.)

Bonnell I., Bate M., Vine S., 2003, MNRAS, 343, 413 (Cited on page 6.)

Brand J., Blitz L., 1993, A&A, 275, 67 (Cited on page 50.)

Busquet G., Zhang Q., Palau A., Liu H., Sánchez-Monge Á., Estalella R., Ho P., de Gregorio-Monsalvo I., Pillai T., Wyrowski F., Girart J., Santos F., Franco G., 2013, ApJ, 764, L26 (Cited on pages 16 and 36.)

Butler M. J., Tan J. C., 2012, ApJ, 754, 5 (Cited on pages 16, 19, 21, 22 and 23.)

Caldu-Primo A., Schruba A., Walter F., Leroy A., Sandstrom K., de Blok W. J. G., Ianjamasimanana R., Mogotsi K. M., 2013, AJ, 146, 150 (Cited on page 97.)

Cardelli J. A., Clayton G. C., Mathis J. S., 1989, ApJ, 345, 245 (Cited on page 23.)

Carey S. J., Noriega-Crespo A., Mizuno D. R., Shenoy S., Paladini R., Kraemer K. E., Price S. D., Flagey N., Ryan E., Ingalls J. G., Kuchar T. A., Pinheiro Gonçalves D., Indebetouw R., Billot N., Marleau F. R., Padgett D. L., Rebull L. M., Bressert E., Ali B., Molinari S., Martin P. G., Berriman G. B., Boulanger F., Latter W. B., Miville-Deschenes M. A., Shipman R., Testi L., 2009, PASP, 121, 76 (Cited on page 38.)

Chandrasekhar S., Fermi E., 1953, ApJ, 118, 116C (Cited on pages 6, 32 and 37.)

Chen H., Myers P. C., Ladd E. F., Wood D. O. S., 1995, ApJ, 445, 377 (Cited on page 38.)

Chira R. A., Kainulainen J., Ibàñez-Mejía J. C., Henning T., Mac Low M. M., 2018, A&A, 610, A62 (Cited on page 107.)

Churchwell E., Babler B. L., Meade M. R., Whitney B. A., Indebetouw R., Cyganowski C., Robitaille T. P., Povich M., Watson C., Bracker S., 2009, PASP, 121 (Cited on pages 7, 17, 38 and 52.)

Clarke S., Whitworth A., Spowage R., Duarte-Cabral A., Suri S., Jaffa S., Walch S., Clark P., 2018, MNRAS, 479, 1722 (Cited on pages 45 and 73.)

Clarke S. D., Whitworth A. P., Duarte-Cabral A., Hubber D. A., 2017, MNRAS, 468, 2489 (Cited on page 37.)

Colombo D., Rosolowsky E., Ginsburg A., Duarte-Cabral A., Hughes A., 2015, MNRAS, 454, 2067 (Cited on pages 34 and 37.)

Contreras Y., Rathborne J., Garay G., 2013, MNRAS, 433, 251 (Cited on pages 91 and 100.)

Contreras Y., Schuller F., Urquhart J. S., Csengeri T., Wyrowski F., Beuther H., Bontemps S., Bronfman L., Henning T., Menten K. M., Schilke P., Walmsley C. M., Wienen M., Tackenberg J., Linz H., 2013, A&A, 549, A45 (Cited on pages 12, 46, 73, 86 and 118.)

Csengeri T., Urquhart J. S., Schuller F., Motte F., Bontemps S., Wyrowski F., Menten K. M., Bronfman L., Beuther H., Henning T., Testi L., Zavagno A., Walmsley M., 2014, A&A, 565, A75 (Cited on pages 12, 16, 18, 34, 35, 51 and 89.)

Csengeri T., Weiss A., Wyrowski F., Menten K. M., Urquhart J. S., Leurini S., Schuller F., Beuther H., Bontemps S., Bronfman L., Henning T., Schneider N., 2016, A&A, 585, A104 (Cited on pages 7, 10, 77 and 99.)

Cutri R. M., Skrutskie M. F., van Dyk S., Beichman C. A., Carpenter J. M., Chester T., Cambresy L., Evans T., Fowler J., Gizis J., Howard E., Huchra J., Jarrett T., Kopan E. L., Kirkpatrick J. D., Light R. M., Marsh K. A., McCallon H., Schneider S., Stiening R., Sykes M., Weinberg M. D., Wheaton W. A., Wheelock S., Zacarias N., 2003, "The IRSA 2MASS All-Sky Point Source Cat. (Cited on pages 17 and 121.)

Dent W., Matthews H., Ward-Thompson D., 1998, MNRAS, 301, 1049 (Cited on page 9.)

Dobbs C., Krumholz M., Ballesteros-Paredes J., Bolatto A., Fukui Y., Heyer M., Low M.-M., Ostriker E., Vázquez-Semadeni E., 2014, Protostars and Planets VI, pp 3–26 (Cited on page 3.)

Dobbs C. L., 2015, MNRAS, 447, 3390 (Cited on pages 45 and 46.)

Dobbs C. L., Pringle J. E., 2013, MNRAS, 432 (Cited on page 5.)

Duarte-Cabral A., Dobbs C. L., 2016, MNRAS, 458, 3667 (Cited on pages 5 and 46.)

Duarte-Cabral A., Dobbs C. L., 2017, MNRAS, 470, 4261 (Cited on pages 5, 6, 46, 61, 114 and 118.)

Dunham M., Crapsi A., Evans II N., Bourke T., Huard T., Myers P., Kauffmann J., 2008, ApJS, 179, 249 (Cited on page 40.)

Dunham M. M., Allen L. E., Evans N. J., Broekhoven-Fiene H., Cieza L., Di Francesco J., Gutermuth R. A., Harvey P. M., Hatchell J., Heiderman A., Huard T., Johnstone D., Kirk J. M., Matthews B. C., Miller J. F., Peterson D. E., Young K. E., 2015, ApJS, 220, 26 pp (Cited on page 40.)

Elia D., Molinari S., Schisano E., Pestalozzi M., Pezzuto S., Merello M., Noriega-Crespo A., Moore T. J. T., Russeil D., Mottram J. C., Paladini R., Strafella F., Benedettini M., Bernard J. P., Di Giorgio A., Eden D. J., Fukui Y., Plume R., Bally J., Martin P. G., Ragan S. E., Jaffa S. E., Motte F., Olmi L., Schneider N., Testi L., Wyrowski F., Zavagno A., Calzoletti L., Faustini F., Natoli P., Palmeirim P., Piacentini F., Piazzo L., Pilbratt G. L., Polychroni D., Baldeschi A., Beltrán M. T., Billot N., Cambrésy L., Cesaroni R., García-Lario P., Hoare M. G., Huang M., Joncas G., Liu S. J., Maiolo B. M. T., Marsh K. A., Maruccia Y., Mège P., Peretto N., Rygl K. L. J., Schilke P., Thompson M. A., Traficante A., Umana G., Veneziani M., Ward-Thompson D., Whitworth A. P., Arab H., Bandieramonte M., Becciani U., Brescia M., Buemi C., Bufano F., Butora R., Cavuoti S., Costa A., Fiorellino E., Hajnal A., Hayakawa T., Kacsuk P., Leto P., Li Causi G., Marchili N., Martinavarro-Armengol S., Mercurio A., Molinaro M., Riccio G., Sano H., Sciacca E., Tachihara K., Torii K., Trigilio C., Vitello F., Yamamoto H., 2017, MNRAS, 471, 100 (Cited on pages 13, 46, 52 and 54.)

Evans II N. J., Dunham M. M., Jørgensen J. K., Enoch M. L., Merín B., van Dishoeck E. F., Alcalá J. M., Myers P. C., Stapelfeldt K. R., Huard T. L., Allen L. E., Harvey P. M., van Kempen T., Blake G. A., Koerner D. W., Mundy L. G., Padgett D. L., Sargent A. I., 2009, ApJ, 181, 321 (Cited on pages 40 and 87.)

Fang M., Kim J. S., van Boekel R., Sicilia-Aguilar A., Henning T., Flaherty K., 2013, ApJS, 207, 39 pp (Cited on pages 38 and 41.)

Federrath C., 2016, MNRAS, 457, 375 (Cited on page 75.)

Fiege J. D., Pudritz R. E., 2000, MNRAS, 311, 85 (Cited on page 103.)

Field G., 1965, ApJ, 142, 531 (Cited on page 3.)

Fischera J., Martin P. G., 2012, A&A, 542, A77 (Cited on page 102.)

Froebrich D., Murphy G. C., Smith M. D., Walsh J., Del Burgo C., 2007, MNRAS, 378, 1447 (Cited on page 19.)

Giannetti A., Leurini S., Wyrowski F., Urquhart J., Csengeri T., Menten K., König C., Güsten R., 2017, A&A, 603, A33 (Cited on page 8.)

Goldreich P., Lynden-Bell D., 1965, MNRAS, 130, 125 (Cited on page 3.)

Goldsmith P. F., Heyer M., Narayanan G., Snell R., Li D., Brunt C., 2008, ApJ, 680, 428 (Cited on page 15.)

Gonzalez R. C., Woods R. E., 1992, Reading, MA Addison-Wesley, 1992 (Cited on page 79.)

Goodman A. A., Alves J., Beaumont C. N., Benjamin R. A., Borkin M. A., Burkert A., Dame T. M., Jackson J., Kauffmann J., Robitaille T., Smith R. J., 2014, ApJ, 797, 53 (Cited on pages 5, 16, 24, 45, 46, 52 and 111.)

Goodman A. A., Pineda J. E., Schnee S. L., 2009, ApJ, 692, 91 (Cited on pages 15 and 19.)

Greene T. P., Wilking B. A., Andre P., Young E. T., Lada C. J., 1994, ApJ, 434, 614 (Cited on page 38.)

Gritschneder M., Heigl S., Burkert A., 2017, ApJ, 834, 202 (Cited on page 37.)

Güsten R., Nyman L. A., Schilke P., Menten K., Cesarsky C., Booth R., 2006, A&A, 454, L13 (Cited on pages 9 and 77.)

Gutermuth R., Heyer M., 2015, AJ, 149, 64 (Cited on page 38.)

Gutermuth R. A., Megeath S. T., Myers P. C., Allen L. E., Pipher J. L., Fazio G. G., 2009, ApJS, 184, 18 (Cited on page 38.)

Hacar A., Kainulainen J., Tafalla M., Beuther H., Alves J., 2016, A&A, 587, A97 (Cited on pages 7 and 75.)

Hacar A., Tafalla M., Forbrich J., Alves J., Meingast S., Grossschedl J., Teixeira P. S., 2018, A&A, 610, A77 (Cited on pages 5, 75 and 119.)

Hacar A., Tafalla M., Kauffmann J., Kovács A., 2013, A&A, 554, A55 (Cited on pages 4, 5, 15, 37, 75, 81, 114 and 119.)

Heitsch F., 2013a, ApJ, 769, 115 (Cited on pages 101, 102, 105, 106, 107, 108, 114, 115 and 119.)

Heitsch F., 2013b, ApJ, 776, 62 (Cited on page 102.)

Heitsch F., Ballesteros-Paredes J., Hartmann L., 2009, ApJ, 704, 1735 (Cited on page 105.)

Hennebelle P., Falgarone E., 2012, A&A Rev., 20, 55 (Cited on page 15.)

Henshaw J., Caselli P., Fontani F., Jiménez-Serra I., Tan J., Longmore S., Pineda J., Parker R., Barnes A., 2016, MNRAS, 463, 146 (Cited on page 16.)

Henshaw J. D., Caselli P., Fontani F., Jimenez-Serra I., Tan J. C., 2014, MNRAS, 440, 2860 (Cited on pages 6, 7, 75 and 76.)

Hernandez A. K., Tan J. C., Caselli P., Butler M. J., Jiménez-Serra I., Fontani F., Barnes P., Jimenez-Serra I., Fontani F., Barnes P., Jiménez-Serra I., Fontani F., Barnes P., 2011, ApJ, 738, 11 (Cited on page 73.)

Hernandez A. K., Tan J. C., Kainulainen J., Caselli P., Butler M. J., Jimenez-Serra I., Fontani F., Jiménez-Serra I., Fontani F., 2012, ApJ, 756, L13 (Cited on pages 4, 16, 36 and 75.)

Heyer M., Brunt C., 2004, ApJ, 615, L45 (Cited on pages 34 and 37.)

Hill T., Motte F., Didelon P., Bontemps S., Minier V., Hennemann M., Schneider N., André P., Men'shchikov A., Anderson L. D., Arzoumanian D., Bernard J.-P., di Francesco J., Elia D., Giannini T., Griffin M. J., Könyves V., Kirk J., Marston A. P., Martin P. G., Molinari S., Nguyen Luong Q., Peretto N., Pezzuto S., Roussel H., Sauvage M., Sousbie T., Testi L., Ward-Thompson D., White G. J., Wilson C. D., Zavagno A., 2011, A&A, 533, A94 (Cited on pages 11 and 77.)

Inutsuka S., Miyama S. M., 1997, ApJ, 480, 681 (Cited on page 73.)

Inutsuka S.-I., Miyama S. M., 1992, ApJ, 388, 392 (Cited on pages 6, 32, 37, 103, 105 and 119.)

Ioannidis G., Froebrich D., 2012, MNRAS, 425, 1380 (Cited on page 24.)

Jackson J. M., Finn S. C., Chambers E. T., Rathborne J. M., Simon R., 2010, ApJ, 719, L185 (Cited on pages 4, 5, 7, 16, 24, 25, 31, 33, 36, 37, 43, 45, 52, 75, 76, 107 and 112.)

Jackson J. M., Rathborne J. M., Shah R. Y., Simon R., Bania T. M., Clemens D. P., Chambers E. T., Johnson A. M., Dormody M., Lavoie R., Heyer M. H., 2006, ApJS, 163, 145 (Cited on pages 9 and 117.)

Jeans J. H., 1902, Philos. Trans. R. Soc. A Math. Phys. Eng. Sci., 199, 1 (Cited on pages 6, 32 and 37.)

Johnstone D., Jason D. F., Redman R. O., Feldman P. A., Carey S. J., Fiege J., Redman R. O., Feldman P. A., Carey S. J., Jason D. F., Redman R. O., Feldman P. A., Carey S. J., 2003, ApJ, 588, L37 (Cited on pages 7, 21, 22 and 76.)

Juvela M., Malinen J., Lunttila T., 2012, A&A, 544, 11 pp (Cited on page 102.)

Juvela M., Pelkonen V.-M., Padoan P., Mattila K., 2008, A&A, 480, 445 (Cited on page 19.)

Kainulainen J., Alves J., Beuther H., Henning T., Schuller F., 2011, A&A, 536, A48 (Cited on pages 16, 19, 24 and 32.)

Kainulainen J., Beuther H., Henning T., Plume R., 2009, A&A, 508, L35 (Cited on pages 19 and 42.)

Kainulainen J., Federrath C., Henning T., 2014, Science, 344, 183 (Cited on pages 25 and 30.)

Kainulainen J., Hacar A., Alves J., Beuther H., Bouy H., Tafalla M., Kainulainen J., Hacar A., Alves J., Beuther H., Bouy H., Tafalla M., 2015, A&A, 586, A27 (Cited on pages 7, 75 and 102.)

Kainulainen J., Ragan S. E., Henning T., Stutz A., 2013, A&A, 557, A120 (Cited on pages 4, 7, 16, 34, 37, 75, 76, 107, 114 and 119.)

Kainulainen J., Stutz A. M., Stanke T., Abreu-Vicente J., Beuther H., Henning T., Johnston K. G., Megeath S. T., 2017, A&A, 600, A141 (Cited on pages 4, 7, 15, 16, 37, 75, 107 and 114.)

Kainulainen J., Tan J. C., 2013, A&A, 549, A53 (Cited on pages 16, 19, 23, 32 and 124.)

Kauffmann J., Bertoldi F., Bourke T. L., Evans N. J., Lee C. W., 2008, A&A, 487, 993 (Cited on pages 18, 25, 50 and 86.)

Kirk H., Myers P. C., Bourke T. L., Gutermuth R. A., Hedden A., Wilson G. W., 2013, ApJ, 766, 115 (Cited on pages 4 and 75.)

Klessen R., Burkert A., 2000, ApJS, 128, 287 (Cited on page 6.)

Koch E. W., Rosolowsky E. W., 2015, MNRAS, 452, 3435 (Cited on pages 7 and 76.)

Koenig X., Leisawitz D., 2014, ApJ, 791, 27 pp (Cited on page 38.)

Koyama H., Inutsuka S.-I., 2000, ApJ, 532, 980 (Cited on page 3.)

Kramer C., Stutzki J., Rohrig R., Corneliussen U., 1998, A&A, 329, 249 (Cited on page 13.)

Kroupa P., 2001, MNRAS, 322, 231 (Cited on page 40.)

Kroupa P., 2002, Science, 295, 82 (Cited on page 42.)

Krumholz M., Klein R., McKee C., 2007, ApJ, 656, 959 (Cited on page 6.)

Kryukova E., Megeath S. T., Gutermuth R. A., Pipher J., Allen T. S., Allen L. E., Myers P. C., Muzerolle J., 2012, AJ, 144, 28 pp (Cited on page 40.)

Lada C. J., Forbrich J., Lombardi M., Alves J. F., 2012, ApJ, 745, 190 (Cited on pages 43 and 112.)

Lada C. J., Lombardi M., Alves J. F., 2010, ApJ, 724, 687 (Cited on page 42.)

Lamarre J.-M., Puget J.-L., Ade P. A. R., Bouchet F., Guyot G., Lange A. E., Pajot F., Arondel A., Benabed K., Beney J.-L., Benoît A., Bernard J.-P., Bhatia R., Blanc Y., Bock J. J., Bréelle E., Bradshaw T. W., Camus P., Catalano A., Charra J., Charra M., Church S. E., Couchot F., Coulais A., Crill B. P., Crook M. R., Dassas K., de

Bernardis P., Delabrouille J., de Marcillac P., Delouis J.-M., Désert F.-X., Dumesnil C., Dupac X., Efstathiou G., Eng P., Evesque C., Fourmond J.-J., Ganga K., Giard M., Gispert R., Guglielmi L., Haissinski J., Henrot-Versillé S., Hivon E., Holmes W. A., Jones W. C., Koch T. C., Lagardère H., Lami P., Landé J., Leriche B., Leroy C., Longval Y., Macías-Pérez J. F., Maciaszek T., Maffei B., Mansoux B., Marty C., Masi S., Mercier C., Miville-Deschênes M.-A., Moneti A., Montier L., Murphy J. A., Narbonne J., Nexon M., Paine C. G., Pahn J., Perdereau O., Piacentini F., Piat M., Plaszczynski S., Pointecouteau E., Pons R., Ponthieu N., Prunet S., Rambaud D., Recouvreur G., Renault C., Ristorcelli I., Rosset C., Santos D., Savini G., Serra G., Stassi P., Sudiwala R. V., Sygnet J.-F., Tauber J. A., Torre J.-P., Tristram M., Vibert L., Woodcraft A., Yurchenko V., Yvon D., 2010, A&A, 520, A9 (Cited on pages 10 and 77.)

Larson R. B., 1981, MNRAS, 194, 809 (Cited on pages 34 and 37.)

Li G.-X., Urquhart J. S., Leurini S., Csengeri T., Wyrowski F., Menten K. M., Schuller F., 2016, Astron. Astrophys. Vol. 591, id.A5, 24 pp., 591, A5 (Cited on pages vii, 4, 7, 11, 12, 15, 16, 62, 63, 70, 71, 73, 75, 76, 77, 78, 85, 86, 88, 89, 90, 107, 113 and 117.)

Lombardi M., 2005, A&A, 438, 169 (Cited on page 19.)

Lombardi M., Alves J., 2001, A&A, 377, 1023 (Cited on pages 15, 16, 19 and 20.)

Lombardi M., Alves J., Lada C. J., 2006, A&A, 454, 781 (Cited on page 19.)

Low M. M. M., Klessen R. R. S., Mac Low M.-M., Klessen R. R. S., 2004, Rev. Mod. Phys., 76, 125 (Cited on page 6.)

Lu X., Zhang Q., Liu H., Sanhueza P., Tatematsu K., Feng S., Smith H., Myers P., Sridharan T., Gu Q., 2018, ApJ, 855, 9 (Cited on page 119.)

Lumsden S. L., Hoare M. G., Urquhart J. S., Oudmaijer R. D., Davies B., Mottram J. C., Cooper H. D. B., Moore T. J. T., 2013, ApJS, 208, 17 (Cited on page 38.)

McKee C., Ostriker J., 1977, ApJ, 218, 148 (Cited on page 3.)

McKee C. F. C., Ostriker E. C. E., 2007, ARA&A, 45, 565 (Cited on page 15.)

Marsh K., Kirk J., André P., Griffin M., Könyves V., Palmeirim P., Men'shchikov A., Ward-Thompson D., Benedettini M., Bresnahan D., di Francesco J., Elia D., Motte F., Peretto N., Pezzuto S., Roy A., Sadavoy S., Schneider N., Spinoglio L., White G., 2016, MNRAS, 459, 342 (Cited on page 42.)

Marshall D. J., Robin A. C., Reyle C., Schultheis M., Picaud S., Reylé C., Schultheis M., Picaud S., Reyle C., Schultheis M., Picaud S., 2006, A&A, 453, 635 (Cited on pages 24 and 39.)

Mattern M., Kainulainen J., Zhang M., Beuther H., 2018, A&A, 616, A78 (Cited on pages 47, 50, 51, 52 and 76.)

Mattern M., Kauffmann J., Csengeri T., Urquhart J., Leurini S., Wyrowski F., Giannetti A., Barnes P., Beuther H., Bronfman L., Duarte-Cabral A., Henning T., Kainulainen J., Menten K., Schisano E., Schuller F., 2018, A&A, 619, A166 (Cited on pages 47, 50 and 73.)

Menten K. M., Reid M. J., Forbrich J., Brunthaler A., 2007, Astron. Astrophys. Vol. 474, Issue 2, Novemb. I 2007, pp.515-520, 474, 515 (Cited on page 16.)

Meyer M., Calvet N., Hillenbrand L., 1997, AJ, 114, 288 (Cited on pages 38 and 39.)

Miettinen O., 2012, A&A, 545, A3 (Cited on pages 52, 81 and 88.)

Molinari S., Consortium t. H.-G., Bally J., Barlow M., Bernard J.-P., Martin P., Moore T., Noriega-Crespo A., Plume R., Testi L., Zavagno A., Abergel A., Ali B., André P., Baluteau J.-P., Benedettini M., Berné O., Billot N. P., Blommaert J., Bontemps S., Boulanger F., Brand J., Brunt C., Burton M., Campeggio L., Carey S., Caselli P., Cesaroni R., Cernicharo J., Chakrabarti S., Chrysostomou A., Codella C., Cohen M., Compiegne M., Davis C. J., de Bernardis P., de Gasperis G., Di Francesco J., di Giorgio A. M., Elia D., Faustini F., Fischera J. F., Fukui Y., Fuller G. A., Ganga K., Garcia-Lario P., Giard M., Giardino G., Glenn J., Goldsmith P., Griffin M., Hoare M., Huang M., Jiang B., Joblin C., Joncas G., Juvela M., Kirk J., Lagache G., Li J. Z., Lim T. L., Lord S. D., Lucas P. W., Maiolo B., Marengo M., Marshall D., Masi S., Massi F., Matsuura M., Meny C., Minier V., Miville-Deschênes M.-A., Montier L., Motte F., Müller T. G., Natoli P., Neves J., Olmi L., Paladini R., Paradis D., Pestalozzi M., Pezzuto S., Piacentini F., Pomarès M., Popescu C. C., Reach W. T., Richer J., Ristorcelli I., Roy A., Royer P., Russeil D., Saraceno P., Sauvage M., Schilke P., Schneider-Bontemps N., Schuller F., Schultz B., Shepherd D. S., Sibthorpe B., Smith H. A., Smith M. D., Spinoglio L., Stamatellos D., Strafella F., Stringfellow G., Sturm E., Taylor R., Thompson M. A., Tuffs R. J., Umana G., Valenziano L., Vavrek R., Viti S., Waelkens C., Ward-Thompson D., White G., Wyrowski F., Yorke H. W., Zhang Q., Swinyard B., Bally J., Barlow M., Bernard J.-P., Martin P., Moore T., Noriega-Crespo A., Plume R., Testi L., Zavagno A., Abergel A., Ali B., André P., Baluteau J.-P., Benedettini M., Berné O., Billot N. P., Blommaert J., Bontemps S., Boulanger F., Brand J., Brunt C., Burton M., Campeggio L., Carey S., Caselli P., Cesaroni R., Cernicharo J., Chakrabarti S., Chrysostomou A., Codella C., Cohen M., Compiegne M., Davis C. J., de Bernardis P., de Gasperis G., Di Francesco J., di Giorgio A. M., Elia D., Faustini F., Fischera J. F., Fukui Y., Fuller G. A., Ganga K., Garcia-Lario P., Giard M., Giardino G., Glenn J., Goldsmith P., Griffin M., Hoare M., Huang M., Jiang B., Joblin C., Joncas G., Juvela M., Kirk J., Lagache G., Li J. Z., Lim T. L., Lord S. D., Lucas P. W., Maiolo B., Marengo M., Marshall D., Masi S., Massi F., Matsuura M., Meny C., Minier V., Miville-Deschênes M.-A., Montier L., Motte F., Müller T. G., Natoli P., Neves J., Olmi L., Paladini R., Paradis D., Pestalozzi M., Pezzuto S., Piacentini F., Pomarès M., Popescu C. C.,

Reach W. T., Richer J., Ristorcelli I., Roy A., Royer P., Russeil D., Saraceno P., Sauvage M., Schilke P., Schneider-Bontemps N., Schuller F., Schultz B., Shepherd D. S., Sibthorpe B., Smith H. A., Smith M. D., Spinoglio L., Stamatellos D., Strafella F., Stringfellow G., Sturm E., Taylor R., Thompson M. A., Tuffs R. J., Umana G., Valenziano L., Vavrek R., Viti S., Waelkens C., Ward-Thompson D., White G., Wyrowski F., Yorke H. W., Zhang Q., 2010, PASP, 122, 314 (Cited on pages 4, 5, 7, 13, 38 and 75.)

Molinari S., Schisano E., Elia D., Pestalozzi M., Traficante A., Pezzuto S., Swinyard B. M., Noriega-Crespo A., Bally J., Moore T. J. T., Plume R., Zavagno A., di Giorgio A. M., Liu S. J., Pilbratt G. L., Mottram J. C., Russeil D., Piazzo L., Veneziani M., Benedettini M., Calzoletti L., Faustini F., Natoli P., Piacentini F., Merello M., Palmese A., Del Grande R., Polychroni D., Rygl K. L. J., Polenta G., Barlow M. J., Bernard J. P., Martin P. G., Testi L., Ali B., André P., Beltrán M. T., Billot N., Carey S., Cesaroni R., Compiègne M., Eden D., Fukui Y., Garcia-Lario P., Hoare M. G., Huang M., Joncas G., Lim T. L., Lord S. D., Martinavarro-Armengol S., Motte F., Paladini R., Paradis D., Peretto N., Robitaille T., Schilke P., Schneider N., Schulz B., Sibthorpe B., Strafella F., Thompson M. A., Umana G., Ward-Thompson D., Wyrowski F., Andrè P., Beltrán M. T., Billot N., Brunt C., Carey S., Cesaroni R., Compiègne M., Eden D., Fukui Y., Garcia-Lario P., Hoare M. G., Huang M., Joncas G., Lim T. L., Lord S. D., Martinavarro-Armengol S., Motte F., Paladini R., Paradis D., Peretto N., Robitaille T., Schilke P., Schneider N., Schulz B., Sibthorpe B., Strafella F., Thompson M. A., Umana G., Ward-Thompson D., Wyrowski F., 2016, A&A, 591, A149 (Cited on pages 13, 38 and 118.)

Molinari S., Swinyard B., Bally J., Barlow M., Bernard J., Martin P., Moore T., 2010, A&A, 518, L100 (Cited on pages 46 and 52.)

Motte F., Andre P., Neri R., 1998, A&A, 336, 150 (Cited on page 42.)

Myers P. C., 2009, ApJ, 700, 1609 (Cited on page 15.)

Nutter D., Kirk J. M., Stamatellos D., Ward-Thompson D., 2008, MNRAS, 384, 755 (Cited on page 100.)

Oort J., 1954, Bull. Astron. Inst. Netherlands, 12, 177 (Cited on page 3.)

Ossenkopf V., Henning T., 1994, A&A, 291, 943 (Cited on pages 18, 23 and 87.)

Ostriker E., Gammie C., Stone J., 1999, ApJ, 513, 259 (Cited on page 6.)

Ostriker J., 1964, ApJ, 140, 1056 (Cited on pages 5, 73, 102 and 103.)

Padoan P., Haugbølle T., Nordlund A., Nordlund Å., 2014, ArXiv e-prints, 797 (Cited on page 15.)

Padoan P., Juvela M., Goodman A. A., Nordlund A., 2001, ApJ, 553, 227 (Cited on pages 6 and 75.)

Palmeirim P., André P., Kirk J., Ward-Thompson D., Arzoumanian D., Könyves V., Didelon P., Schneider N., Benedettini M., Bontemps S., Di Francesco J., Elia D., Griffin M., Hennemann M., Hill T., Martin P. G., Men'shchikov A., Molinari S., Motte F., Nguyen Luong Q., Nutter D., Peretto N., Pezzuto S., Roy A., Rygl K. L. J., Spinoglio L., White G. L., Men'shchikov a., Molinari S., Motte F., Nguyen Luong Q., Nutter D., Peretto N., Pezzuto S., Roy A., Rygl K. L. J., Spinoglio L., White G. L., 2013, A&A, 550, A38 (Cited on pages 4 and 75.)

Panopoulou G. V., Tassis K., Goldsmith P. F., Heyer M. H., 2014, MNRAS, 444, 2507 (Cited on pages 100 and 101.)

Parker E., 1966, ApJ, 145, 811 (Cited on page 3.)

Peretto N., Fuller G. A., 2009, A&A, 505, 405 (Cited on pages 19, 21 and 22.)

Peretto N., Fuller G. A., André P., Arzoumanian D., Rivilla V. M., Bardeau S., Duarte Puertas S., Guzman Fernandez J. P., Lenfestey C., Li G.-X., Olguin F. A., Röck B. R., de Villiers H., Williams J., 2014, A&A, 561, A83 (Cited on pages 6 and 75.)

Peretto N., Fuller G. a., Duarte-Cabral A., Avison A., Hennebelle P., Pineda J. E., André P., Bontemps S., Motte F., Schneider N., Molinari S., 2013, A&A, 555, A112 (Cited on pages 6 and 75.)

Pettitt A., Dobbs C., Acreman D., Price D., 2014, MNRAS, 444, 919 (Cited on page 69.)

Pillai T., Wyrowski F., Carey S. J., Menten K. M., 2006, A&A, 450, 569 (Cited on pages 34 and 85.)

Pillai T., Wyrowski F., Menten K. M., Krügel E., 2006, A&A, 447, 929 (Cited on pages 7 and 76.)

Planck Collaboration P., Ade P. A. R., Aghanim N., Alves M. I. R., Armitage-Caplan C., Arnaud M., Ashdown M., Atrio-Barandela F., Aumont J., Aussel H., Baccigalupi C., Banday A. J., Barreiro R. B., Barrena R., Bartelmann M., Bartlett J. G., Bartolo N., Basak S., Battaner E., Battye R., Benabed K., Benoît A., Benoit-Lévy A., Bernard J. P., Bersanelli M., Bertincourt B., Bethermin M., Bielewicz P., Bikmaev I., Blanchard A., Bobin J., Bock J. J., Böhringer H., Bonaldi A., Bonavera L., Bond J. R., Borrill J., Bouchet F. R., Boulanger F., Bourdin H., Bowyer J. W., Bridges M., Brown M. L., Bucher M., Burenin R., Burigana C., Butler R. C., Calabrese E., Cappellini B., Cardoso J. F., Carr R., Carvalho P., Casale M., Castex G., Catalano A., Challinor A., Chamballu A., Chary R. R., Chen X., Chiang H. C., Chiang L. Y., Chon G., Christensen P. R., Churazov E., Church S., Clemens M., Clements D. L., Colombi S., Colombo L. P. L., Combet C., Comis B., Couchot F., Coulais A., Crill B. P., Cruz M., Curto A., Cuttaia F., Da Silva A., Dahle H., Danese L., Davies R. D., Davis R. J., de Bernardis P., de Rosa A., de Zotti G., Déchelette T., Delabrouille J., Delouis J. M., Démoclès J., Désert F. X., Dick J., Dickinson C., Diego J. M., Dolag K., Dole H., Donzelli S., Doré O., Douspis M., Ducout A., Dunkley J., Dupac X., Efstathiou G., Elsner F., Enßlin T. A., Eriksen H. K., Fabre O., Falgarone E., Falvella

M. C., Fantaye Y., Fergusson J., Filliard C., Finelli F., Flores-Cacho I., Foley S., Forni O., Fosalba P., Frailis M., Fraisse A. A., Franceschi E., Freschi M., Fromenteau S., Frommert M., Gaier T. C., Galeotta S., Gallegos J., Galli S., Gandolfo B., Ganga K., Gauthier C., Génova-Santos R. T., Ghosh T., Giard M., Giardino G., Gilfanov M., Girard D., Giraud-Héraud Y., Gjerløw E., González-Nuevo J., Górski K. M., Gratton S., Gregorio A., Gruppuso A., Gudmundsson J. E., Haissinski J., Hamann J., Hansen F. K., Hansen M., Hanson D., Harrison D. L., Heavens A., Helou G., Hempel A., Henrot-Versillé S., Hernández-Monteagudo C., Herranz D., Hildebrandt S. R., Hivon E., Ho S., Hobson M., Holmes W. A., Hornstrup A., Hou Z., Hovest W., Huey G., Huffenberger K. M., Hurier G., Ilić S., Jaffe A. H., Jaffe T. R., Jasche J., Jewell J., Jones W. C., Juvela M., Kalberla P., Kangaslahti P., Keihänen E., Kerp J., Keskitalo R., Khamitov I., Kiiveri K., Kim J., Kisner T. S., Kneissl R., Knoche J., Knox L., Kunz M., Kurki-Suonio H., Lacasa F., Lagache G., Lähteenmäki A., Lamarre J. M., Langer M., Lasenby A., Lattanzi M., Laureijs R. J., Lavabre A., Lawrence C. R., Jeune M. L., Leach S., Leahy J. P., Leonardi R., León-Tavares J., Leroy C., Lesgourgues J., Lewis A., Li C., Liddle A., Liguori M., Lilje P. B., Linden-Vørnle M., Lindholm V., López-Caniego M., Lowe S., Lubin P. M., Macías-Pérez J. F., MacTavish C. J., Maffei B., Maggio G., Maino D., Mandolesi N., Mangilli A., Marcos-Caballero A., Marinucci D., Maris M., Marleau F., Marshall D. J., Martin P. G., Martínez-González E., Masi S., Massardi M., Matarrese S., Matsumura T., Matthai F., Maurin L., Mazzotta P., McDonald A., McEwen J. D., McGehee P., Mei S., Meinhold P. R., Melchiorri A., Melin J. B., Mendes L., Menegoni E., Mennella A., Migliaccio M., Mikkelsen K., Millea M., Miniscalco R., Mitra S., Miville-Deschênes M. A., Molinari D., Moneti A., Montier L., Morgante G., Morisset N., Mortlock D., Moss A., Munshi D., Murphy J. A., Naselsky P., Nati F., Natoli P., Negrello M., Nesvadba N. P. H., Netterfield C. B., Nørgaard-Nielsen H. U., North C., Noviello F., Novikov D., Novikov I., O'Dwyer I. J., Orieux F., Osborne S., O'Sullivan C., Oxborrow C. A., Paci F., Pagano L., Pajot F., Paladini R., Pandolfi S., Paoletti D., Partridge B., Pasian F., Patanchon G., Paykari P., Pearson D., Pearson T. J., Peel M., Peiris H. V., Perdereau O., Perotto L., Perrotta F., Pettorino V., Piacentini F., Piat M., Pierpaoli E., Pietrobon D., Plaszczynski S., Platania P., Pogosyan D., Pointecouteau E., Polenta G., Ponthieu N., Popa L., Poutanen T., Pratt G. W., Prézeau G., Prunet S., Puget J. L., Pullen A. R., Rachen J. P., Racine B., Rahlin A., Räth C., Reach W. T., Rebolo R., Reinecke M., Remazeilles M., Renault C., Renzi A., Riazuelo A., Ricciardi S., Riller T., Ringeval C., Ristorcelli I., Robbers G., Rocha G., Roman M., Rosset C., Rossetti M., Roudier G., Rowan-Robinson M., Rubiño-Martín J. A., Ruiz-Granados B., Rusholme B., Salerno E., Sandri M., Sanselme L., Santos D., Savelainen M., Savini G., Schaefer B. M., Schiavon F., Scott D., Seiffert M. D., Serra P., Shellard E. P. S., Smith K., Smoot G. F., Souradeep T., Spencer L. D., Starck J. L., Stolyarov V., Stompor R., Sudiwala R., Sunyaev R., Sureau F., Sutter P., Sutton D., Suur-Uski A. S., Sygnet J. F., Tauber J. A., Tavagnacco D., Taylor D., Terenzi L., Texier D., Toffolatti L., Tomasi M., Torre J. P., Tristram M., Tucci M., Tuovinen J., Türler M., Tuttlebee M., Umana G., Valenziano L., Valiviita J., Van Tent B., Varis J., Vibert L., Viel M., Vielva P., Villa F., Vittorio N., Wade

L. A., Wandelt B. D., Watson C., Watson R., Wehus I. K., Welikala N., Weller J., White M., White S. D. M., Wilkinson A., Winkel B., Xia J. Q., Yvon D., Zacchei A., Zibin J. P., Zonca A., 2014, A&A, 571, A1 (Cited on pages 10 and 77.)

Pokhrel R., Myers P., Dunham M., Stephens I., Sadavoy S., Zhang Q., Bourke T., Tobin J., Lee K., Gutermuth R., Offner S., 2018, ApJ, 853, 5 (Cited on page 119.)

Pon A., Johnstone D., Heitsch F., 2011, ApJ, 740, 88 (Cited on pages 37 and 114.)

Pudritz R., Kevlahan N.-R., 2013, Philos. Trans. R. Soc. London Ser. A, 371, 20120248 (Cited on page 6.)

Purcell C., Longmore S., Walsh A., Whiting M., Breen S., Britton T., Brooks K., Burton M., Cunningham M., Green J., Harvey-Smith L., Hindson L., Hoare M., Indermuehle B., Jones P., Lo N., Lowe V., Phillips C., Thompson M., Urquhart J., Voronkov M., White G., 2012, MNRAS, 426, 1972 (Cited on page 45.)

Rachford B., Snow T., Tumlinson J., Shull J., Blair W., Ferlet R., Friedman S., Gry C., Jenkins E., Morton D., Savage B., Sonnentrucker P., Vidal-Madjar A., Welty D., York D., 2002, ApJ, 577, 221 (Cited on page 23.)

Ragan S. E., Bergin E. A., Gutermuth R. A., 2009, ApJ, 698, 324 (Cited on page 22.)

Ragan S. E., Henning T., Beuther H., Linz H., Zahorecz S., 2015, A&A, 573, A119 (Cited on page 7.)

Ragan S. E., Henning T., Tackenberg J., Beuther H., Johnston K. G., Kainulainen J., Linz H., 2014, A&A, 568, A73 (Cited on pages 4, 5, 16, 24, 45, 75, 76, 91, 111, 117 and 118.)

Rathborne J. M., Lada C. J., Muench A. A., Alves J., Kainulainen J., Lombardi M., 2009, ApJ, 699, 742 (Cited on page 42.)

Reach W. T., Rho J., Tappe A., Pannuti T. G., Brogan C. L., Churchwell E. B., Meade M. R., Babler B., Indebetouw R., Whitney B. A., 2005, AJ, 131, 1479 (Cited on page 23.)

Recchi S., Hacar A., Palestini A., 2013, A&A, 558, A27 (Cited on page 102.)

Reid M. J., Dame T. M., Menten K. M., Brunthaler A., 2016, ApJ, 823, 77 (Cited on page 97.)

Roberts W., 1969, ApJ, 158, 123 (Cited on page 3.)

Robin A. C., Reyl C., Derri S., 2003, A&A, 409, 523 (Cited on page 24.)

Robitaille T. P., Meade M. R., Babler B. L., Whitney B. A., Johnston K. G., Indebetouw R., Cohen M., Povich M. S., Sewilo M., Benjamin R. A., Churchwell E., 2008, AJ, 136, 2413 (Cited on page 38.)

Robitaille T. P., Whitney B. A., Indebetouw R., Wood K., Denzmore P., 2006, ApJS, 167, 256 (Cited on pages 40 and 41.)

Rohlfs K., Wilson T., 2004, Tools of radio astronomy, 4 edn. Berlin: Springer, 2004 (Cited on page 7.)

Saito R. K., Hempel M., Minniti D., Lucas P. W., Rejkuba M., Toledo I., Gonzalez O. A., 2012, A&A, 537, A107, 1 (Cited on pages 17, 38 and 121.)

Saral G., Hora J. L., Willis S. E., Koenig X. P., Gutermuth R. A., Saygac A. T., 2015, ApJ, 813, 21 pp (Cited on page 38.)

Savage B. D., Bohlin R. C., Drake J. F., Budich W., 1977, ApJ, 216, 291 (Cited on page 23.)

Schisano E., Rygl K. L. J., Molinari S., Busquet G., Elia D., Pestalozzi M., Polychroni D., Billot N., Carey S., Paladini R., Noriega-Crespo A., Moore T. J. T., Plume R., Glover S. C. O., Vázquez-Semadeni E., 2014, ApJ, 791, 27 (Cited on pages 4, 7, 15, 73, 75 and 76.)

Schneider N., Csengeri T., Bontemps S., Motte F., Simon R., Hennebelle P., Federrath C., Klessen R., 2010, A&A, 520, A49 (Cited on pages 6, 7, 75, 76, 91 and 106.)

Schneider S., Elmegreen B. G., 1979, ApJ, 41, 87 (Cited on pages 4, 15 and 75.)

Schuller F., Csengeri T., Urquhart J. S., Duarte-Cabral A., Barnes P. J., Giannetti A., Hernandez A. K., Leurini S., Mattern M., Medina S. N. X., Agurto C., Azagra F., Anderson L. D., Beltrán M. T., Beuther H., Bontemps S., Bronfman L., Dobbs C. L., Dumke M., Finger R., Ginsburg A., Gonzalez E., Henning T., Kauffmann J., Mac-Auliffe F., Menten K. M., Montenegro-Montes F. M., Moore T. J. T., Muller E., Parra R., Perez-Beaupuits J. P., Pettitt A., Russeil D., Sánchez-Monge Á., Schilke P., Schisano E., Suri S., Testi L., Torstensson K., Venegas P., Wang K., Wienen M., Wyrowski F., Zavagno A., 2017, A&A, 601, A124 (Cited on pages 7, 8, 45, 50, 69, 71, 72, 76, 77, 79, 81, 87, 98 and 99.)

Schuller F., Menten K. M., Contreras Y., Wyrowski F., Schilke P., Bronfman L., Henning T., Walmsley C. M., Beuther H., Bontemps S., Cesaroni R., Deharveng L., Garay G., Herpin F., Lefloch B., Linz H., Mardones D., Minier V., Molinari S., Motte F., Nyman L.-Å., Reveret V., Risacher C., Russeil D., Schneider N., Testi L., Troost T., Vasyunina T., Wienen M., Zavagno A., Kovacs A., Kreysa E., Siringo G., Weiß A., 2009, A&A, 504, 415 (Cited on pages 7, 9, 17, 18, 34, 52, 62, 76, 77, 87 and 99.)

Schultz G., Wiemer W., 1975, A&A, 43, 133 (Cited on page 23.)

Shetty R., Beaumont C. N., Burton M. G., Kelly B. C., Klessen R. S., 2012, MNRAS, 425, 720 (Cited on pages 34 and 37.)

Skrutskie M. F., Cutri R. M., Stiening R., Weinberg M. D., Schneider S., Carpenter J. M., Beichman C., Capps R., Chester T., Elias J., Huchra J., Liebert J., Lonsdale C., Monet D. G., Price S., Seitzer P., Jarrett T., Kirkpatrick J. D., Gizis J. E., Howard E., Evans T., Fowler J., Fullmer L., Hurt R., Light R., Kopan E. L., Marsh K. A., McCallon H. L., Tam R., Van Dyk S., Wheelock S., 2006, AJ, 131, 1163 (Cited on pages 17 and 121.)

Smith R. J., Glover S. C. O., Clark P. C., Klessen R. S., Springel V., 2014, MNRAS, 441, 1628 (Cited on pages 5, 45, 61, 114 and 118.)

Smith R. J., Glover S. C. O., Klessen R. S., Fuller G. A., Smith R. J., Glover S. C. O., Klessen R. S., Fuller G. A., 2015, MNRAS, 455, 3640 (Cited on pages 6 and 75.)

Solomon P. M., Rivolo A. R., Barrett J., Yahil A., 1987, ApJ, 319, 730 (Cited on pages 34 and 37.)

Sousbie T., 2011, MNRAS, 414, 350 (Cited on pages vii, 7, 11, 12, 62 and 77.)

Starck J.-L. J.-L., Murtagh F., 2002, Astronomical image and data analysis. Springer-Verlag Berlin Heidelberg GmbH (Cited on page 30.)

Stetson P. B., 1987, PASP, 99, 191 (Cited on page 17.)

Stutz A. M., Gould A., 2016, A&A, 590, A2 (Cited on pages 15 and 107.)

Stutzki J., Guesten R., 1990, ApJ, 356, 513 (Cited on page 13.)

Takahashi S., Ho P. T. P., Teixeira P. S., Zapata L. A., Su Y.-N., 2013, ApJ, 763, 57 (Cited on pages 7, 16, 32, 75 and 107.)

Teixeira P. S., Takahashi S., Zapata L. A., Ho P. T. P., Ho P. T. P., 2016, A&A, 587, A47 (Cited on pages 16, 37, 107 and 114.)

Tilley D., Pudritz R., 2004, MNRAS, 353, 769 (Cited on page 6.)

Urquhart J. S., Csengeri T., Wyrowski F., Schuller F., Bontemps S., Bronfman L., Menten K. M., Walmsley C. M., Contreras Y., Beuther H., Wienen M., Linz H., 2014, A&A, 568, A41 (Cited on pages 12, 46, 86 and 118.)

Urquhart J. S., König C., Giannetti A., Leurini S., Moore T. J. T., Eden D. J., Pillai T., Thompson M. A., Braiding C., Burton M. G., Csengeri T., Dempsey J. T., Figura C., Froebrich D., Menten K. M., Schuller F., Smith M. D., Wyrowski F., 2018, MNRAS, 473, 1059 (Cited on pages 12, 46, 52, 54, 85, 86 and 87.)

Vassilev V., Meledin D., Lapkin I., Belitsky V., Nyström O., Henke D., Pavolotsky A., Monje R., Risacher C., Olberg M., Strandberg M., Sundin E., Fredrixon M., Ferm S.-E., Desmaris V., Dochev D., Pantaleev M., Bergman P., Olofsson H., 2008, A&A, 490, 1157 (Cited on pages 8 and 77.)

Vazquez-Semadeni E., 1994, ApJ, 423, 681 (Cited on page 6.)

Veneziani M., Elia D., Noriega-Crespo A., Paladini R., Carey S., Faimali A., Molinari S., Pestalozzi M., Piacentini F., Schisano E., Tibbs C., 2013, A&A, 549, 8 pp (Cited on page 38.)

Wang K., Testi L., Burkert A., Walmsley C. M., Beuther H., Henning T., 2016, ApJS, 226, 9 (Cited on pages 5, 7, 16, 45, 76 and 91.)

Wang K., Testi L., Ginsburg A., Walmsley C. M., Molinari S., Schisano E., 2015, MNRAS, 450, 4043 (Cited on pages 5, 7, 45, 76, 91 and 118.)

Wang K., Zhang Q., Testi L., Tak F. v. d., Wu Y., Zhang H., Pillai T., Wyrowski F., Carey S., Ragan S. E., Henning T., 2014, MNRAS, 439, 3275 (Cited on pages 16, 85, 107 and 118.)

Wang K., Zhang Q., Wu Y., Li H. B., Zhang H., 2012, ApJ, 745 (Cited on page 85.)

Weiß A., Neininger N., Hüttemeister S., Klein U., 2001, A&A, 365, 571 (Cited on page 10.)

Wienen M., Wyrowski F., Menten K. M., Urquhart J. S., Csengeri T., Walmsley C. M., Bontemps S., Russeil D., Bronfman L., Koribalski B. S., Schuller F., 2015, eprint arXiv:1503.00007, 579, A91 (Cited on pages 24 and 72.)

Williams J. P., de Geus E. J., Blitz L., 1994, ApJ, 428, 693 (Cited on page 30.)

Wilson T. L., Rood R. T., 1994, ARA&A, 32, 191 (Cited on page 8.)

Wright E. L., Eisenhardt P. R. M., Mainzer A., Ressler M. E., Cutri R. M., Jarrett T., Kirkpatrick J. D., Padgett D., McMillan R. S., Skrutskie M., Stanford S. A., Cohen M., Walker R. G., Mather J. C., Leisawitz D., Gautier T. N., McLean I., Benford D., Lonsdale C. J., Blain A., Mendez B., Irace W. R., Duval V., Liu F., Royer D., Heinrichsen I., Howard J., Shannon M., Kendall M., Walsh A. L., Larsen M., Cardon J. G., Schick S., Schwalm M., Abid M., Fabinsky B., Naes L., Tsai C.-W., 2010, AJ, 140, 1868 (Cited on page 38.)

Xue M., Jiang B., Gao J., Liu J., Wang S., Li A., 2016, ApJS, 224, 23 (Cited on pages 38 and 39.)

Zhang M., Fang M., Wang H., Sun J., Wang M., Jiang Z., Anathpindika S., 2015, ApJS, 219, 21 pp (Cited on page 119.)

Zhang M., Kainulainen J., Mattern M., Fang M., Henning T., 2018, Submitt. to A&A (Cited on page 37.)

Zhang Q., Wang K., Lu X., Jimenez-Serra I., 2015, eprint arXiv:1503.03017 (Cited on page 38.)

Zucker C., Battersby C., Goodman A., 2015, ApJ, 815, 23 (Cited on pages 5, 7, 16, 45, 76 and 91.)

Zucker C., Battersby C., Goodman A., 2017, ArXiv e-prints (Cited on pages 4, 75 and 118.)